UNIVERSITY OF SOUTHAMPTON

FACULTY OF ENGINEERING AND THE ENVIRONMENT

Materials Research Group

The relations between thermodynamics, nanostructure, hardening and stability of an Al-Cu-Mg alloy processed by high pressure torsion

By

Ying Chen

October 2014

UNIVERSITY OF SOUTHAMPTON

Abstract

FACULTY OF ENGINEERING & THE ENVIROMENT
MATERIALS ENGINEERING

Doctor of Philosophy

THE RELATIONS BETWEEN THERMODYNAMICS, NANOSTRUCTURE, HARDENING AND STABILITY OF AN Al-Cu-Mg ALLOY PROCESSED BY HIGH PRESSURE TORSION

By Ying Chen

This thesis presents a study on microstructural evolutions of an ultrafine-grained (UFG) Al-Cu-Mg alloy processed by high-pressure torsion (HPT). This work aims to develop a physically based hardening model to predict the strength of cluster strengthened UFG ternary alloys, and to reveal the relation between thermodynamics and high strain in severe plastic deformation (SPD).

Experiments by means of Vickers hardness, differential scanning calorimetry (DSC), X-ray diffraction (XRD), transmission electron microscopy (TEM) and atom probe microscopy (APM) have been carried out to provide the relevant information for the calibration and validation of the models. Analysis of XRD line profile broadening using the Rietveld method and Williamson-Hall method shows that the dislocation density increases significantly due to severe plastic deformation, which contributes to the increase of strength. APM reveals the presence of nanoscale co-clusters and defect-solute clustering.

The relation between peak temperature for S phase formation and the equivalent strain for HPT was studied with the aid of a diffusion model. The model suggests that on increasing strain, the exothermic peaks correlated to S precipitation shift to lower temperatures. The model is consistent with the data from DSC thermographs of samples after different number of HPT rotations.

In both the strengthening model and the stored energy model, strengthening due to dislocations, grain refinement, co-clusters (due to short range order and modulus strengthening) and solute segregation are all incorporated to explain the multiple mechanisms. The models show good correspondences with measured microstructure data, measured hardness and measured enthalpy in DSC.

The thermal stability of nanostructures in the Al-Cu-Mg alloy obtained by HPT has been studied during DSC heating processes. A significant increase of crystallite size and a significant decrease of dislocation density are revealed from XRD profile broadening when heat treated up to 210 °C, which correlates with an exothermic peak in DSC thermographs. Clusters are thought to act as obstacles that hinder the movement of dislocations, stabilize the ultrafine microstructures.

In single reversal (SR) HPT, the hardness slightly decreases after 1/4 reversal turn; and increases again when the reversal rotations continue to increase. This phenomenon is thought to be due to the geometrically necessary dislocation (GND) density which decreases during the inverse straining.

This study introduces concepts of the solute-defect complexes and the multiple local interaction energies between solute and dislocations to explain the strengthening mechanisms. The understanding of the HPT processing and microstructural modification has been enhanced through construction of models.

Contents

Abbreviations

APM	atom probe microscopy
APT	atom probe tomography
ARB	accumulative roll-bonding
BF	bright field
CRSS	critically resolved shear stress
DSC	differential scanning calorimetry
ECAP	equal channel angular pressing
FWHM	full width at half maximum
GB	grain boundary
GND	geometrically necessary dislocation
GP	Guinier-Preston zones
GPB	Guinier-Preston-Bagaryatsky
HPT	high-pressure torsion
HRTEM	high resolution transmission electron microscopy
IADS	International Alloy Designation System
IVAS^{TM}	the Imago Visualization and Analysis Software
MAUD	Materials Analysis using Diffraction
MDF	multi-directional forging
PSF	Profile shape function
PV	Pseudo-Voigt
RH	rapid hardening
SAD	selected area diffraction
SPD	severe plastic deformation
SR-HPT	single reversal- HPT
SSD	statically stored dislocation
SSS	supersaturated solid solution
STD	standard deviation
TE	twist extrusion
TEM	transmission electron microscopy

TSRL	Transport Systems Research Laboratory
UFG	ultrafine grain
WQ	water quenched
XRD	X-ray diffraction

Nomenclature

A	a dimensionless constant, ~10
$A(L)$	the cosine Fourier coefficient
$A^{\text{size}}(L)$	the cosine Fourier coefficient in size compoent
$A^{\text{strain}}(L)$	the cosine Fourier coefficient in strain compoent
a_{DSC}	an parameter of a DSC baseline
$a_{\text{Al}}{}^{0}$	the lattice parameter of a pure Al sample
$a_{\text{Al}}{}^{\text{HPT}}$	the lattice parameter of a 5r-HPT sample
$a_{\text{Al}}{}^{\text{T351}}$	the lattice parameter of a T351 sample
$B(L)$	the sine Fourier coefficient
B_{exp}	the integral breadth of experimental profile
B_{ins}	the integral breadth of instrumental profile
B_{int}	the integral breadth of intrinsic profile
b	Burgers vector
b_{DSC}	an parameter of a DSC baseline
C	a constant, ~8
C_p	the heat capacity
c_{DSC}	an parameter of a DSC baseline
c	the universal constant in the Debye-Scherrer formula
c_j	the concentrations of the alloying elements (i.e. Cu and Mg) in solid solution
$c_{\text{p,ref}}$	the heat capacity of a reference
$c_{\text{p,s}}$	the heat capacity of a sample
D	the diffusion coefficient
D_0	the pre-exponential diffusion coefficient
D_{c}	the average crystallite size, related to coherently scattering domains
d	the average grain size
d_0	initial grain sizes
d_{hkl}	lattice spacing between the parallel *hkl* planes
d_{HV}	the measured average diameter of the indent
d_{SG}	the average subgrain diameter
E	the activation energy of the reaction of transformation
E_D	the activation energy of diffusion
E_{eff}	the effective activation energy of grain growth
E_{G}	the activation energy for grain growth

E_N	the activation energy for nucleation
E_{self}	the self-energy of a dislocation (per unit length)
e	the universal constant in the Debye-Scherrer formula
F	the applied load in hardness test
$f(\varepsilon)$	a defined function of microstrain
f	the volume fraction of the clusters
f_1	the fraction of A-B cluster
f_2	the fraction of A segregated to dislocations
f_3	the fraction of B segregated to dislocations
f_4	the fraction of A-B co-clusters segregated to dislocations
f_s	the volume fraction of cell walls
G	shear modulus
h	the disk thickness
HV	the vickers hardness
$I(hkl)$	the observed relative intensities in XRD
I_i^{calc}	the calculated peak intensities
I_i^{exp}	the experimental peak intensities
k	the Boltzmann's constant
k_1	the constant in estimating misorientation angle
k_2	a constant
K_A	a factor incorporates the contribution of the solid solute atoms
k_{HP}	the hardness coefficient
k_j	the factors describing the strengthening due to the individual elements (i.e. Cu and Mg)
l	a mean free path
L	Fourier length
L_k	Lorentz-Polarization factor
M	Taylor yield criterion
m	the universal constant in the Debye-Scherrer formula
N	the number of whole revolutions
N_A	Avogadro's number
N_{hkl}	the order of diffraction and λ is the wave length of X-ray
N_{HV}	the number of indentations
n	the stress exponent, 2
n_1	the exponent in estimating misorientation angle
P_k	the preferred orientation function
p_s	the grain size exponent (2 for lattice diffusion controlled flow and 3 for grain boundary diffusion controlled flow)
p	a constant, describing the strengthening due to solute atoms
p_{Cu}	the Vegard constant describing the effects of dissolved Cu on Al lattice parameter in binary alloys Al-Cu

$p_{Mg}(x_{Mg})$	the no-linear function describing the effect of dissolved Mg atoms on Al lattice parameter
p_{Si}	the Vegard constant describing the effects of dissolved Si on Al lattice parameter in binary alloys Al-Si
q	the heat flow in DSC
r	the radius of the disk
R	the gas constant
R_e	an outer cut-off radius
r_0	an inner cut-off radius
$S(2\theta_i - 2\theta_k)$	a profile shape function, which obeys Pseudo-Voigt function
s	the diffusion distance of solute atoms
T	temperature
T_e	the temperature in DSC
T_{iso}	the temperature of isothermal reactions
t	the diffusion time of precipitation in DSC heating
t_{eq}	the equivalent time of non-isothermal treatment (i.e. linearly heated at a constant heating rate in the heat flux DSC)
V	the active volume of the specimen
V_{atom}	the atomic volume
W_{pl}	specific plastic work
W_T	the total plastic work
$\bar{x}$	the average value of indentations
x'	the typical values of exponent in Hall-Petch equation
x_c	the occupied mole fractions of the solute atoms in the grains
x_{Cu}	the concentrations of Cu atoms in Al matrix
x_{gb}	the occupied mole fractions of the solute atoms at grain boundaries
x_i^{HV}	the value of individual indentation
x_{Mg}	the concentrations of Mg atoms in Al matrix
x_{Si}	the concentrations of Si atoms in Al matrix
y_A	the amount of A atoms in the co-clusters
y_B	the amount of B atoms in the co-clusters
y_{Cu}	the amount of Cu in the co-clusters
y_{Mg}	the amount of Mg in the co-clusters
α_1	an empirical constant ranging from 0.2-0.5, taken 0.3 in Al alloys
α_2	a constant to evaluate yield strength increment due to grain boundary
β	heating rate
γ_m	the boundary energy
γ_{SRO}	the change in energy per unit area on slip planes on the passing of one dislocation
$<\varepsilon^2(L)>$	the mean square strain

$<\varepsilon^2>^{1/2}$	the internal lattice microstrain
$\Delta a^{seg}_{Cu\text{-}Mg}$	the lattice parameter change due to Cu-Mg cluster segregation
$\Delta a^{seg}_{Mg\text{-}Si}$	the lattice parameter change due to Mg-Si cluster segregation
ΔE_{cl}	the enthalpy associated with the co-clusters (atomic short range order)
ΔE_{deg}	the enthalpy due to solute desegregation
ΔE_{dis}	the enthalpy due to dislocations annihilation
ΔE_{gb}	the enthalpy due to grain coarsening and grain rotation
ΔG	the Gibbs free energy of segregation per mole of solute atoms
$\Delta H_{(A\text{-}B)n\text{-}dis}$	the enthalpy of co-clusters located at dislocations
$\Delta H_{A\text{-}B}$	the enthalpy of the nearest neighbour bond
$\Delta H_{A\text{-}dis}$	the enthalpy of single atom A located at dislocations
$\Delta H_{B\text{-}dis}$	the enthalpy of single atom B located at dislocations
ΔH_{cl}	the enthalpy due to the clusters dissolution
ΔH_d	the energy stored in dislocations
ΔQ	the total evolved heat in DSC
$\Delta\mu$	the difference in shear modulus between surrounding metallic phase and clusters, with the average cluster ($M_mA_aB_b$) modulus
$\Delta\sigma_{gb}$	the yield strength increment due to the grain boundaries
$\Delta\tau_0$	the intrinsic CRSS
$\Delta\tau_{cl}$	the contribution due to co-clusters
$\Delta\tau_d$	the contribution due to dislocations
$\Delta\tau_m$	a modulus strengthening component
$\Delta\tau_{SRO}$	a short range order strengthening component
$\Delta\tau_{ss}$	the contribution due to solid solution contribution
$\Delta\tau_{tot}$	the overall CRSS of the grains
ε_v	an equivalent strain
η	the constant in estimating misorientation angle
η^b	the plastic strain gradient
θ	the glancing angle of diffraction, the Bragg angle
$\underline{\theta}$	the average misorientation angle
θ_m	the maximum misorientation angle of high-angle boundaries
κ	the fraction of screw or edge dislocations in the UFG sample
λ	the wavelength of X-ray
λ	the wavelength of X-ray
μ_A	the modulus of solute atom A
μ_A	the chemical potential of solute atom A dissolved in a constant number
μ_B	the modulus of solute atom B
μ_{cl}	the average cluster ($M_mA_aB_b$) modulus
μ_M	the modulus of matrix

γ	the plastic shear strain
ν	the Poisson's ratio
π	the universal constant in the Debye-Scherrer formula
ρ	the dislocation density
ρ_0	the initial dislocation density stored in the grain
$\rho_{A\text{-}B}(n=0)$	the area density of A-B nearest neighbour bonds crossing the slip plane before passage of one dislocation
$\rho_{A\text{-}B}(n=1)$	the area density of A-B nearest neighbour bonds crossing the slip plane after passage of one dislocation
ρ_G	the dislocation density mobile within grains
ρ_{GB}	the dislocation density accumulated in grain boundaries
ρ_{gen}	the dislocation density generated in grains
ρ_{ig}	the volume averaged dislocation density in the grains
ρ_S	the dislocation density immobile due to short range order phase particles
ρ_w	dislocation density in the cell interior
ρ_c	dislocation density in the cell walls
ρ_{GND}	dislocation density of geometrically necessary dislocations
ρ_{SSD}	dislocation density of statistically stored dislocations
σ	the tensile flow stress
σ_o	the instrinic yield strength
σ_{UTS}	the ultimate tensile strength
σ_y	the yield strength
τ	the shear flow stress
φ	the rotational angle
χ^2	the residual function

List of Figures

List of Tables

Declaration of Authorship

I, Ying Chen, declare that the thesis entitled

The Relations between Thermodynamics, Nanostructure, Hardening and Stability of an Al-Cu-Mg Alloy Processed by High Pressure Torsion

and the work presented in the thesis are both my own, and have been generated by me as result of my own original research.

I confirm that

This work was done wholly or mainly while in candidature for a research degree at this University;

Where any part of this thesis has previously been submitted for a degree or any other qualification at this University or any other institution, this has been clearly stated;

Where I have consulted the published work of others, this is always clearly attributed;

Where I have quoted from the work of others, the source is always given. With the exception of such quotations, this thesis is my own work with the help of my supervisors on writing and proof reading;

I have acknowledged all main sources of help;

Where the thesis is based on work done by myself jointly with others, I have made clear exactly what was done by others and what I have contributed myself;

Parts of this work have been published or to be published as:

1. Y. Chen, N. Gao, G. Sha, S. P. Ringer and M. J. Starink, Strengthening of an Al-Cu-Mg alloy processed by high-pressure torsion due to clusters, defects and defect-cluster complexes, Submitted to Acta Mater.
2. Y. Chen, N. Gao, G. Sha, S. P. Ringer and M. J. Starink, Microstructural evolution during linear heating of an ultrafine-grained Al-Cu-Mg alloy produced by high-pressure torsion' in preparation.

3. Y. Chen, N. Gao, G. Sha, S. P. Ringer and M. J. Starink, Solute segregation on structural defects in an ultrafine-grained Al-Cu-Mg alloy, 6th Nanomaterials by Severe Plastic Deformation, Metz, France, July 1-4, 2014
4. Y. Chen, N. Gao, M. J. Starink, Structural modification during linear heating of an Al-Cu-Mg alloy produced by high-pressure torsion, TMS 2013 Annual Meeting Exhibition, San Antonio, USA, March 3-7, 2013.
5. Y. Chen, N. Gao, M. J. Starink, Microstructural evolution of an UFG Al-2.1Cu-1.8Mg (at.%) alloy on DSC heating, Materials Research Exchange-Exhibition, Coventry, UK, February 24-25, 2014.
6. X.G. Qiao, Y. Zhao, W. Gan, Y. Chen, M. Zheng, K. Wu, N. Gao, M. J. Starink, Hardening mechanism of commercially pure Mg processed by high pressure torsion at room temperature, Materials Science & Engineering A, 619 (2014), 95-106.
7. X.G. Qiao, X. Zhang, Y. Chen, M. Zheng, K. Wu, N. Gao, M. J. Starink, Fabrication of ultrafine grained Al/Mg multilayered composite by high pressure torsion, The 5th Asian Symposium on Magnesium Alloys (ASMA5), Niigata, Japan, 6-8 Oct, 2013.

Signature:……

Acknowledgements

I would like to thank Professor Marco J Starink and Dr. Nong Gao for their excellent supervision on my PhD study. It is their patience and encouragement that inspire me to carry on. I am most appreciative of their comments and corrections on this thesis writing.

I am indebted to the Faculty of Engineering and the Environment, University of Southampton and the China Scholarship Council for financial support. I also would like to thank Institute of Physics and Armourers & Brasiers' Company for financial support to attend conferences.

I would like to acknowledge and thank to Dr. Shuncai Wang in Microscopy Centre, University of Southampton and to Dr. Zabeada Aslam in the Leeds EPSRC Nanoscience and nanotechnology facility for their assistance with TEM. My appreciation is also extended to Professor Sha Gang and Professor Simon P Ringer of Sydney University, Australia, for their help on APM experiments.

I take this opportunity to thank all the members of the Materials Research Group for their kind help. In particular thanks go to Professor Philippa Reed, Drs. Brian Mellor and Alex Zhilyaev for their important comments on my work. Thanks also to Dr. Mark Light, Dr. Xiaoguang Qiao, Dr. Fredrik Hage, Dr. Chuangting Wang, Mr. David Beckett, Mr. Yang He, Miss Xue Wang and Miss Nan Hu.

Finally, I wish to express my appreciation to my friends in Southampton who have made my life here much easier and happier, and in particular, to my family for their supports.

Chapter 1 Introduction

Metals with ultrafine grain (UFG) have many advantages over those with coarse grains, such as a higher strength and a superplastic potential [1]. The materials with UFG microstructures can be fabricated using two different procedures, which involve: "bottom-up" techniques (i.e. inert gas condensation [2], electro-deposition [3] and ball milling [4]) and "top-down" techniques (severe plastic deformation i.e. accumulative roll-bonding (ARB) [5] equal channel angular pressing (ECAP) [6], and high-pressure torsion (HPT) [1].)

One advantage of the "top-down" methods over their counterparts is that they avoid the introduction of either contaminants or porosity [1]. Further, these severe plastic deformation (SPD) processes impose a heavy straining and produce a very high dislocation density without any significant changes in the overall dimensions of a sample. HPT is a continuous process, and the basic concepts of HPT were first proposed by Bridgman in 1943 [7]. This process incorporates the compression as well as the torsional straining. An ultrahigh strength and the reasonable microstructural homogeneity can be obtained if the HPT processing is continued through a sufficient number of torsional revolutions. The feasibility of HPT has already been demonstrated in the lab, but so far its industrial application is still under consideration.

Because of the relatively high strength and low weight, Al and Al-based alloys are attractive to many engineering industries. For example, aluminium alloys have been of great importance in structural components of aircraft since 1930s [8]. The 2024 alloy is a specific Al-Cu-Mg alloy widely used in structural aerospace and other applications, not only because of its good combination of high strength, good fracture toughness and good fatigue crack growth resistance but also because it can be hardened by both precipitation and cold work [9-11].

The strength of Al alloys can be greatly improved by SPD [12-17]. To date, the research on the dissolved elements distribution after SPD processing in precipitation hardening Al alloys has attracted many worldwide attentions. During SPD processing, the pre-existing precipitations can be fragmented and partially dissolved (i.e. Al-Cu [18-21], Al-Cu-Mg [22], AA6060 [23]). On the other hand, dissolved atoms can be redistributed and segregated to grain/sub-grain boundaries or dislocations (i.e. AA7075 [24] AA6061 [25], AA7136 alloy [26]). A further increase of hardness was achieved by processing at elevated temperatures or artificial heat treatment after SPD [17, 23, 27, 28] by multiple strengthening mechanisms. However, up to now, there is no systematic study and clear explanation on the solute segregation effects on strengthening after SPD processes.

In this work, a range of experiments were performed on an Al-Cu-Mg alloy to gather data for the calibration and validation of the models. Hardness measurements were conducted to reveal property improvement on the macro-scale. Differential scanning calorimetry (DSC) was carried out at a constant heating rate from 50 to 540 °C. The stored energy due to deformation via HPT was measured by DSC. XRD was conducted on UFG Al-Cu-Mg alloy processed by HPT. Dislocation densities were evaluated from line profile broadening in the X-ray diffraction pattern, while the precipitates were detected, especially for samples isothermal heat treated at a range of temperature. Microstructural characterization and solute atom maps were carried out by transmission electron microscopy (TEM) and atom probe microscopy (APM). Most experiments were performed at the University of Southampton; APM analysis performed at the University of Sydney; some TEM micrographs were obtained at the Leeds EPSRC nanoscience and nanotechnology research equipment facility.

This PhD project involves extensive analysis of theory and models to reveal strengthening mechanisms for an Al-Cu-Mg alloy processed by HPT. The present work is part of a larger research effort at a range of universities worldwide aimed at improving our understanding of the fundamental processes in SPD, including the thermodynamics of deformation, with the ultimate aim of defining the capabilities and limitations of SPD. In this effort, the technologies and issues involved in upscaling need to be considered, but this is not the aim of the present work.

The first aim of present work is to develop a physically based hardening model to describe strengthening effects during HPT processing, which incorporates influence of dissolved atoms and the typical ultra-high strain effects in ultra-fine microstructures.

The second aim is to systematically analyse stored energy due to dislocation accumulation and grain refinement. Since the microstructure modifications and solid state reactions in metals always accompany with energy absorption and emission, the calorimetric study will help to explain the fundamental theory of plastic deformation, particularly at the very high strains employed in SPD.

The third aim is to investigate the microstructural stability of the UFG materials at elevated temperatures. The analysis on thermal stability of UFG materials makes it possible to improve the mechanical properties by artificial ageing.

The fourth aim is to clarify the reversal strain effects on hardening during single inverse HPT rotations. A model that captures the main mechanisms for the hardening due to geometrically necessary dislocations (GNDs), statically stored dislocations (SSDs) and grain refinement is developed and tested by comparison to experimental data.

The structure of this thesis is as follows: a literature review in Chapter 2 covers published experimental and theoretical studies of SPD and the hardening behaviour in Al-Cu-Mg based alloys. Chapter 3 describes the experimental techniques used in the present study. Then the results of the calorimetric studies are presented in Chapter 4, which also includes a model to predict S phase precipitation temperature for an Al-Cu-Mg alloy processed by HPT. In Chapter 5, microstructures of an UFG Al-Cu-Mg alloy processed by HPT for different rotations and a model for the increased strength are presented and discussed. Chapter 6 presents a study of thermal stability of the UFG materials using DSC linear heating, and a model predicting stored energy for an UFG Al-Cu-Mg alloy. The influence of reversal straining in HPT is presented in Chapter 7. Chapter 8 discusses on the solute atom effects in the UFG Al-Cu-Mg alloy, which involves the trends of solute segregation in thermodynamics, solute effects on thermal stability and the influence of trace Si addition. Finally, conclusions and suggestions for future work are outlined in Chapter 9.

Chapter 2 Literature Review

With an increasing knowledge on the microstructure evolution and its relationship to the properties in Al alloys processed by SPD, there has been an increasing interest in modelling of dislocation accumulations, grain refinement, solute redistribution and yield strength over the past 20 years. The ultra-high strength of UFG heat treatable Al alloys is derived from the multiple hardening mechanisms that involve clusters, precipitates and dislocations. This literature review contains six sections to show a full background for the present study on an HPT-deformed Al-Cu-Mg alloy. Firstly, the categorization of Al alloys and their temper nomenclatures are introduced in Section 2.1. Section 2.2 reviews the physical metallurgy of Al-Cu-Mg alloys, with an emphasis on solute co-clusters, GPB zones and precipitates. Section 2.3 presents the principles of HPT and properties of materials processed by HPT and other SPD techniques. The models for the dislocation generation, accumulation and annihilation of plastic deformation, and the models for GNDs and SSDs are summarized in Section 2.4. This thesis is based on substantial data from quantitative analysis of DSC and XRD, so the final section (Section 2.5) describes these quantitative analysis methods.

2.1 Introduction to aluminium alloys

2.1.1 Categorization of aluminium alloys

Aluminium alloys are widely used as structural components in the fields of transport, building, electrical engineering and packaging because of their advanced properties, such as low mass density, high thermal conductivity and electrical conductivity, good

corrosion resistance and a good potential of plastic formability. The properties are influenced by alloying elements, fabricated procedures, and heat treatment processes.

Based on the fabrication method, aluminium alloys can be classified into casting alloys and wrought alloys [29]. Wrought alloys refer to alloys which are shaped by plastic deformation; while casting alloys refer to those that are routinely produced by pressure-die, permanent-mould, green-and dry-sand, and plaster casting [29, 30].

Heat treatments are commonly used to adjust properties of Al alloys by precipitation. Both wrought and cast Al alloys can be classified as heat-treatable and non heat-treatable alloys. Non heat-treatable alloys include all types of commercial pure aluminium and all other alloys in which strengthening is mainly due to solid solution and strain hardening by temper [31]. The 3xxx (Al-Mn) series, 4xxx (Al-Si) series and 5xxx (Al-Mg) series alloys are generally non heat-treatable alloys. Heat treatable alloys refer to those contain a large amount of dissolved atoms (typical alloying elements, i.e. Cu, Mg, Mn, Si and Zn) at high temperature, but the dissolved atoms may decrease to a small degree at room temperature [31]. The strength and hardness of these alloys increase due to precipitation. According to phase diagrams, 2xxx (Al-Cu-Mg) series, 6xxx (Al-Mg-Si) series and 7xxx (Al-Zn) series are classified in this group.

The numbering system of these aluminium alloys is shown in Table 2-1, where the first digit generally specifies the main alloying elements, and the remaining numbers relate to the specific composition of the alloy. The last three digits have no or very limited special significance, but serve only to identify the different aluminium alloys in the group [30].

Table 2-1 Designation system of aluminium alloy [30]

Wrought alloys		
1xxx	Commercially pure Al (99%Al)	Not heat-treatable
2xxx	Al-Cu and Al-Cu-Li	Heat-treatable
3xxx	Al-Mn	Not heat-treatable
4xxx	Al-Si	Heat-treatable if Mg is presented
5xxx	Al-Mg	Not heat-treatable
6xxx	Al-Mg-Si	Heat-treatable
7xxx	Al-Mg-Zn	Heat-treatable
Cast alloys		
1xx.x.	Commercial pure Al	Not heat-treatable
2xx.x.	Al-Cu	Heat-treatable
3xx.x.	Al-Si-Cu or Al-Mg-Si	Some are heat-treatable
4xx.x.	Al-Si	Not heat-treatable
5xx.x.	Al-Mg	Not heat-treatable
7xx.x.	Al-Mg-Zn	Heat-treatable
8xx.x.	Al-Sn	Heat-treatable

2.1.2 Temper or heat-treatment nomenclatures

In heat-treatable Al alloys, the mechanical properties depend on the heat treatment tempers, so specific tempers are selected for alloys to optimize mechanical properties. Heat treatment to increase strength of Al alloys by a process comprising three steps [32]: (1) solution treatment, in which alloys are heated to a high temperature for dissolution of soluble phases; (2) quenching, in which a rapid cooling is applied to achieve a supersaturated solid solution (SSS) within the aluminium matrix; and (3) ageing, which leads to the formation of hardening precipitates from SSS.

The International Alloy Designation System (IADS) [31] deals with the temper designation to specify the mechanical properties of an alloy and the way to achieve these properties. The IADS list of the main tempers is provided in Table 2-2 [29, 33]. The temper designation T or H is given to classify the alloys subjected to age-hardening or strain-hardening. Other designations indicate whether the alloy is annealed (O), solution-treated (W), or used in the as-fabricated condition (F). Specific sets of additional digits have been assigned to stress-relieved wrought products. For example, the Tx51 applies specifically to plate, to rolled or cold finished rod and bar, with stress-relieved by stretching (0.5-3% for a plate) [31].

The IADS demonstrates all types of temper treatment that can be processed in Al alloys. It helps to achieve the best compromise between mechanical properties for alloys. For example, many 2xxx alloys show a significant strengthening response at room temperature and also have a strong response to artificial ageing at elevated temperature. The yield strength of 2024 (Al-Cu-Mg(-Mn,Si) alloy)-T3 is at least 30 MPa higher than 2024-T4, because the dislocations introduced by cold work enhance the alloy's response to subsequent natural ageing [8]. In the T8 temper, deformation is used to aid the nucleation of precipitates and reduce ageing time at temperature.

Table 2-2 Temper designation for aluminium alloy [29, 33].

Temper designations	
F	As-fabricated (hot-worked, forged, cast, etc.)
O	Annealed (in the softest possible condition)
H	Cold-worked
	H1x—cold worked only (x refers to the amount of cold work and strengthening)
	H2x—cold-worked and partly annealed.
	H3x—cold-worked and stabilized at a low temperature to prevent age hardening the structure.
W	Solution-treated
T	Age-hardened
	T1—cooled from the fabrication temperature and naturally aged.
	T2—cooled from the fabrication temperature, cold-worked, and naturally aged.
	T3—solution-treated, cold-worked, and naturally aged.
	T4—solution-treated and naturally aged.
	T5—cooled from the fabrication temperature and artificially aged.
	T6—solution –treated and artificially aged.
	T7—solution-treated and stabilized by overaging.
	T8—solution-treated, cold worked, and artificially aged.
	T9—solution-treated, and cold-worked.
	T10—cooled from the fabrication temperature, cool-worked and artificially aged.

2.2 Al-Cu-Mg alloys

Al-Cu-Mg alloys are widely applied as structural components in aircraft because of its high strength and low weight. The strength of heat treatable aluminium alloys is derived mainly from the fine precipitates. This section reviews the process of precipitation sequences.

2.2.1 Precipitation sequences

In 1911, the phenomenon of age hardening was first discovered in Al-(3.5-5.5%)Cu-Mg by Wilm [34]. In the early 1950s, Bagaryatsky [35] first proposed a four-stage precipitation sequence:

$$SSS \rightarrow GPB \quad zones \rightarrow S'' \,(GPB2) \rightarrow S' \rightarrow S \,(Al_2CuMg)$$

where GPB (Guinier-Preston-Bagaryatsky) are ordered Cu- and Mg- rich zones forming as thin rods along $<100>_{\alpha}$ directions [36]. Despite the extensive studies on Al-Cu-Mg alloys, details of the decomposition of the supersaturated solid solution and hardening mechanisms at the initial stage of ageing are controversial, and the precipitation sequences have been disputed for a long time.

With the aid of DSC and TEM, Shih et al [37] claimed the ageing sequences of an Al-1.8Cu-1.6Mg (at.%) alloy at different temperature should be revised as follows:

at 30 °C $\quad GPB \rightarrow GPB+GPB2 \rightarrow GPB2$;

at 110 to 190 °C $\quad GPB \rightarrow GPB+GPB2 \rightarrow GPB+GPB2+S' \rightarrow GPB2+S'+S \rightarrow S'+S \rightarrow S$

at 240 °C $\quad GPB+GPB2 \rightarrow GPB+GPB2+S' \rightarrow S'+S \rightarrow S$

Ringer et al. [38, 39] used atom probe together with field ion microscopy and observed the formation of co-clusters of Cu and Mg within the first 60s. Since no S'' or S' was

detected, the precipitation sequence of an Al-1.1Cu-1.7Mg (at.%) alloy at 150 °C was thought to be [39]

$$SSS \rightarrow \text{pre-precitate stage} \rightarrow GPB\ zones + S \rightarrow S$$

Using high resolution transmission electron microscopy (HRTEM) and TEM with selected area diffraction (SAD) [11], the existence of S" has been confirmed after ageing for more than 34 hours. The precipitation sequence of an Al-0.2Cu-5.1Mg (at. %) alloy at 180 °C was summarized as:

$$SSS \rightarrow Cu/Mg\ clusters\ (GPB\ zones) \rightarrow S'' \rightarrow S'\ (S\ phase)$$

But Charai et al. [40] observed the coexistence of clusters, GPB zones, S", S' and S phases in an Al-0.9Cu-1.4Mg (at. %) alloy. The formation of initial three dimensional ordered clusters was governed by vacancy enhanced Mg diffusion, providing nuclei for homogeneous S', which later transformed into the stable S phase; whilst the slower Cu atom diffusion may control the formation of GPB zones, which may transform into the semi-coherent S" phase [40].

The various interpretations of precipitation sequence was summarized by Wang and Starink as [10]:

$$SSS \rightarrow co\text{-}clusters\ /GPB\ zones \rightarrow GPB2/S'' \rightarrow S'\ /S\ phase$$

In interpreting this sequence, GPB2/S" was fully coherent with the Al-rich phase. GPB2/S" was thought to be formed either by ordering followed by long-range diffusion or by long-range diffusion followed by ordering. In the former mechanism, ordering would occur before composition variations occur, hence a co-clustering stage would not occur as part of GPB2/S" formation. But in the latter mechanism, the early stage of GPB2/S" phase would be expected to involve the formation and growth of clusters without distinct order. Thus, the co-clusters appear as a stage prior to the formation of GPB2/S".

In the study of an Al-4.2Cu-1.5Mg-0.6Mn-0.5Si and an Al-4.2Cu-1.5Mg-0.6Mn-0.08Si (wt. %) alloy, the combination of DSC and TEM indicated two types of S precipitates form in a sequence [41]. The sequence for the formation of S phase by homogeneous nucleation was suggested to be

SSS→ co-clusters/GPB zones→ GPB2/S"→ S (Type I) → S (Type II).

The classic orientated S precipitates were formed at lower peaks in DSC, while the S phase formed at a higher temperature had an orientation relationship that is rotated by ~4° to the classic one. The second type of S precipitates in Al-Cu-Mg alloys was confirmed to be rotated ~5° to ~7° by other investigators [42, 43]. In a recent paper by Styles et al. [44], using high-resolution synchrotron X-ray powder diffraction, both types of S phase were confirmed with different lattice parameters in a series of Al-2.5Cu-1.5Mg alloys, aged at temperatures from 200 to 400 °C for a period of time.

2.2.2 Co-clusters and GPB zones

Indications of the existence of GPB zones was first reported in interpretation of weak diffraction effects from diffuse X-ray scattering [36]. GPB zones were proposed to be small cylinders 1 to 2 nm in diameter and with length ranging from 4 nm to more than 8 nm. In this tetragonal structure of GPB zones, lattice parameter *a* equals to 0.55 nm and *c* equals to 0.404 nm [36]. The GPB zones were proposed to consist of one layer of Cu, one layer of Mg and two layers of Al, alternating along the <021> matrix direction by Monfoldo [45].

In the 1990s, a study on Al-1.1Cu-1.7Mg (at. %) aged at 150 °C using TEM and HRTEM by Ringer et al. [38, 46] showed that rod-like GPB zones formed along $<100>_{\alpha}$ directions near the end of the hardness plateau and correlated to the second-stage hardening. These zones possessed facets parallel to $\{120\}_{\alpha}$ and appeared to grow into the S phase on prolonged ageing [46]. Reich et al. [47] used atom probe combined with HRTEM and also found that GPB zones were formed after the rapid hardening reaction in an Al-1.1Cu-1.7Mg (at.%) alloy ageing for 480 minutes at 200 °C. In an Al-0.9Cu-1.4Mg (at.%) alloy aged at 200 °C, Charai et al. [40] found the lattice images of GPB zones which consist of thin, fully coherent plates on $\{100\}$Al matrix planes. Combined with experimental observations, the first principle energy calculation by Wolverton [48] suggested that GPB zones could correspond to a Cu or Mg monolayer along <100> as a result of GPB/matrix interfacial energy.

Co-clusters are metastable structures containing several distinct alloying atoms, numbers of which range from 2 to 100. The small Cu-Mg clusters were reported without any characteristic shape. Davin reported the 3DAP study on a stretched Al-1.2Cu-1.2Mg alloy and a stretched Al-1.9Cu-1.6Mg alloy [49]. The size of the Cu-Mg co-clusters was estimated from the radius of gyration as about 0.7 nm to 0.8 nm in two alloys. During natural ageing, the average measured composition of the Cu-Mg co-clusters varied with the ageing time, and no precipitates were observed for ageing time up to 6 months [49]. An example of the clusters as observed by APM is shown in Fig. 2.1 [50].

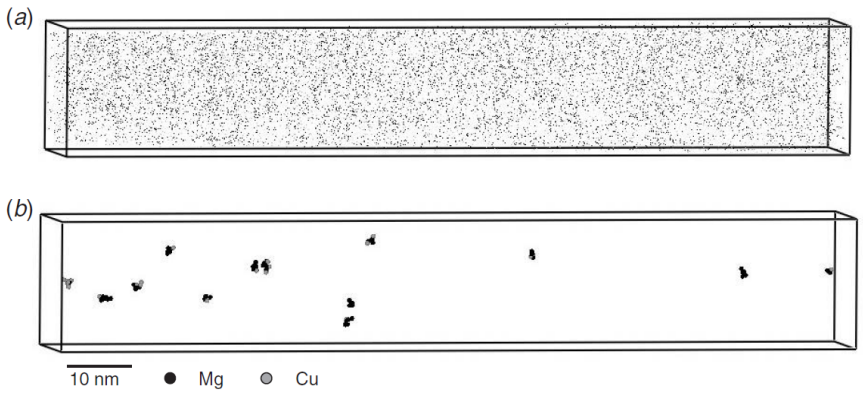

Fig. 2.1 Three dimensional atom map representing the distribution of the Mg and Cu atoms in the Al-1.2Cu-1.2Mg alloy aged at 25 °C for 2 hours before (a) and after (b) selection of the clusters [50].

Many investigations claimed the existence of GPB zones on artificial ageing from 150 °C to 200 °C, and GPB zones were thought to have the potential to explain the rapid hardening in Al-Cu-Mg alloys (e.g. [51, 52]). But atom probe data has conclusively shown that the rapid hardening phenomena is due to co-clusters rather than GPB zones [38, 39, 46, 53]. To respond comments by Zahra et al. [52], who suggested GPB zones were involved in the rapid hardening stage, Ringer et al. [54] re-examined the sample using APM after 5-minute ageing at 150 °C and maintained their finding of the formation of Cu-Mg co-clusters being responsible for the early stage of rapid hardening.

Reich et al. [47] found that the 5% deformation of the rapid hardened specimen caused further rapid hardening at 150 °C. Their studies suggested that solute-dislocation interaction is one of the main reasons for the rapid hardening. This effect was confirmed by similar studies by other authors [51, 55]. However, the study on ageing-deformation-ageing cycles at room temperature indicates on substantial additional age hardening occurs with the addition of deformation to the cycle [56]. It indicates a strengthening mechanism due to the shear modulus difference between zones of clusters and the surrounding metallic matrix. A thermodynamic model of co-clusters [57] shows the strengthening results from an extremely short ranged order phase, which involves 2 to 4 Cu and Mg atoms and hinder the dislocation movement.

The difference between GPB zones and Cu-Mg co-cluster is difficult to define. They are aggregates of both Cu and Mg atoms and are fully coherent with aluminium matrix. The distinction between Cu-Mg co-clusters and GPB zones was supposed to be made on the basis of size, shape, composition, degree of order, orientation structure [46]. However, in practice, such a criterion cannot provide useful information. A structure can only be identified with the complementary investigation using other experimental techniques such as TEM/SAD or HRTEM. The small Cu-Mg co-clusters cannot be detected in TEM or HRTEM. In addition, the GPB zones have proved difficult to be imaged and detected, as the GPB zones are complicated by the simultaneous presence of S phases in TEM/HRTEM. In some case, the GPB zones are termed to be large clusters.

2.2.3 S'' phase and GPB2

Monolayer GPB zones/Cu-Mg co-clusters may agglomerate and form the GPB2 zones or S" phase, just as in binary Al-Cu alloys GP zones transform into the θ" phase. The structure of S" has not been unambiguously proven.

Using TEM, Shih et al. [37] proposed a GPB2 zone oriented at a common $<001>_{Al}$ direction with a tetragonal structure. The lattice parameter, *a* equalled to 0.58 nm, and c equalled to 0.81 nm in an Al 2024-type alloy.

HREM studies confirmed the existence of metastable S'' phases but described them with different lattice parameters. A semi-coherent monoclinic structure of S'' precipitates were revealed by Charai et al [40], and the unit cell parameters were given as: $a_{S''}$= 0.320±0.008 nm, $b_{S''}$= a_{Al}, and $c_{S''}$= 0.254± 0.003 nm, β=91.7° [40].

However, in HRTEM work on Al-0.4Cu-3Mg-0.12Si(wt.%) alloy, Kovarik et al. [55] ascribed their observations of coherent particles after 4 and 8 hour ageing at 180 °C to be characteristic of the S'' phase. The GPB-II structure has an orthorhombic crystal C-cetred lattice, with lattice parameters: a=1.212 nm, b=0.404 nm, c=0.404 nm. And the space group is Cmmm.

Wang and Starink [58] assessed the structure for GPB2/S'' with the composition of $Al_{10}Cu_3Mg_3$. They proposed orthorhombic structure coherent with fcc Al matrix, and be formed by the replacement of some Al atoms with Cu or Mg atom, with lattice parameters: a=0.405 nm, b=1.62 nm, c=0.405 nm and space group Imm2.

The differences between S'' phase and GPB2 zones were discussed in the review paper [10]. The structure in Fig. 2.2 (a) shows many Mg-Mg or Cu-Cu neighbours [51]. The large local lattice distortions introduced by different atomic sizes between Mg, Cu, and Al provide another more stable range of atomic order. The structure in the red rectangle on the left was just the structure proposed by Wolverton [48]; whilst the structure in the orange rectangle on the right was the structure proposed by Cuisiat et al. [59]. In fact, they were supported to be the same with structure modification. The Fig. 2.2 (b) shows HREM simulation along $\left[001\right]$based on the proposed structure [58].

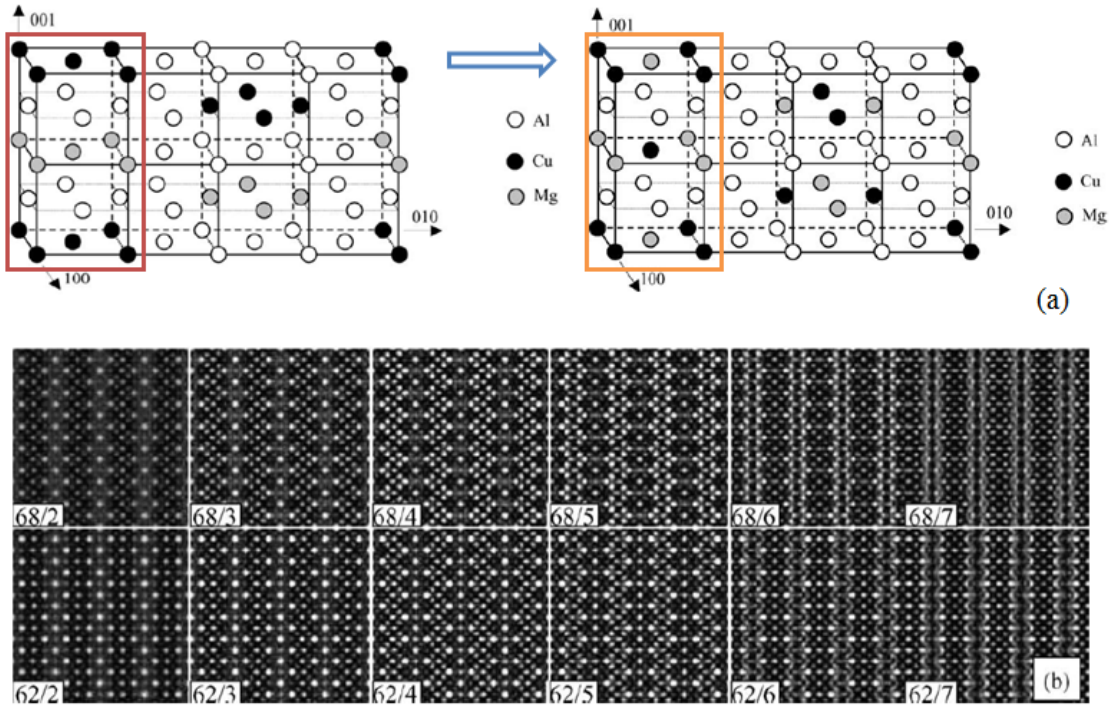

Fig. 2.2 (a) A possible GPB2/S" model [51] (b) HREM simulation along [001] based on the above structures. The numbers before and after the slash symbol "/" in the figures represented the defocus and the thickness (nm), respectively [58].

2.2.4 S' and S phases

Early (1960s) work [60] indicated that ageing of 2024-T4 alloy samples at elevated temperatures produces the transition phase S' (Al_2CuMg) precipitates, which are coherent on $\{021\}_{Al}$; whereas during the subsequent ageing, formation of equilibrium S phase occurs. That latter precipitates are incoherent with the Al rich matrix. XRD studies indicated that S (Al_2CuMg) has a Cmcm structure with lattice parameters a=0.400 nm, b=0.923 nm, c=0.714 nm [60]. Later HREM work [40] showed strain contrast accompanies the presence of semi-coherent S' particles.

Different structure models for the S phase have been reported. A generally accepted structure for S phase is Perlitz and Westgren (P-W) model, shown in Fig. 2.3 [61]. Radmilovic and Kilaas [62, 63] found their HREM images fit P-W model well with

space group Cmcm, and lattice parameters a=0.403 nm, b=0.930 nm, c=0.708 nm; a modification of the model by exchanging the positions of the Mg and Cu presented a better match. Charai et al. [40] reported HREM images of both S' and S phases; and suggested that the S' phase was semi-coherent orthorhombic with cell dimensions $b_{S'}$=0.89 nm, $c_{S'}$=0.76 nm whilst the S phase was incoherent orthorhombic with cell dimensions b_S=0.921 nm, c_S=0.719 nm.

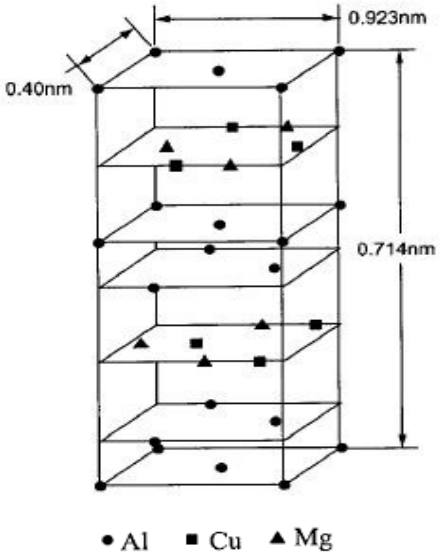

Fig. 2.3 Proposed structure of S phase by Perlitz and Westgren [61]

It has been reported the precipitates in Al-4.2Cu-1.5Mg (wt.%) alloys had classic orientation relationship (OR) for Type I S phase and had an OR rotated by ~4° for Type II S phase [41]. Since S' has the same structure as S phase with slight differences in their lattice parameters, it was regarded that there is no distinction between the S' and S phases [64]. The orientation relationship between S and the Al matrix was reported as [41, 65]

$$[100]_{Al}//[100]_S,[02\bar{1}]//[010]_S,[012]_{Al}//[001]_S$$

The morphology of S phase viewed on $<100>_{Al}$ with the elongated direction along $<100>_S$ shown in Fig. 2.4 [65].

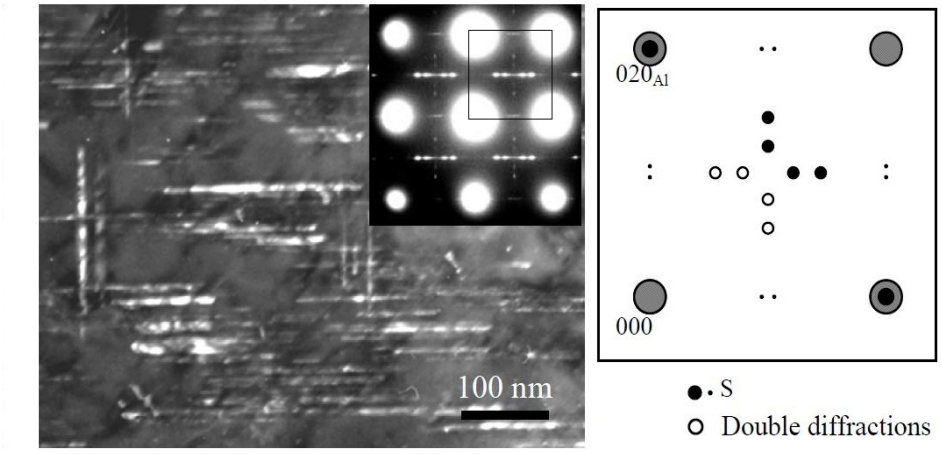

Fig. 2.4 TEM micrographs of precipitation in Al-1.21Cu-1.19Mg (at.%) alloy solution treated, stretched and subsequently aged for 12h at 190°C (dark field B=[001]) [65].

2.3 Severe plastic deformation via high-pressure torsion

High-pressure torsion is a very effective SPD process and has been applied to a number of metallic alloys to improve their mechanical properties [66-68]. A significant grain refinement and a large number of dislocations produced by SPD processing can lead to an increase of strength and simultaneously maintain the formability of materials [24]. In this section, works on metals or alloys processed by HPT is reviewed.

2.3.1 Principle of high-pressure torsion

The principle of modern HPT processing is illustrated schematically in Fig. 2.5 [1]. The sample, in the form of a thin disk about 0.85 mm, is placed between two anvils. High pressure up to several GPa, *P*, is applied on the disk. Simultaneously, the lower anvil rotates to impose a torsional strain on the disk. Due to the applied pressure and torsion, surface fictional forces deform the disk by shear. The deformation of the disk continues

under a condition of quasi-hydrostatic pressure. Since there is a small gap between the face of the two anvils, a small volume of materials can be forced outwards around the periphery of samples [1, 67].

The true accumulated strain is estimated as [1, 69]

$$\varepsilon = \ln(1 + \frac{\varphi^2 r^2}{h^2})^{\frac{1}{2}} \tag{2-1}$$

$$\varphi = 2\pi N \tag{2-2}$$

where the rotational angle is denoted as φ, r is the radius of the disk, N is the number of whole revolutions imposed on the disk and h is the disk thickness.

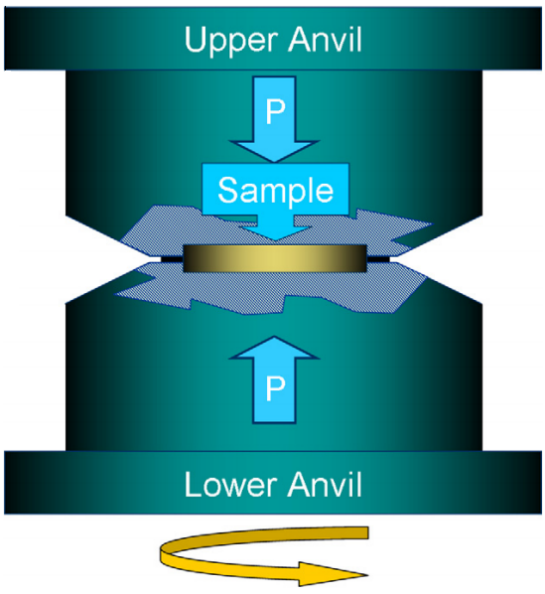

Fig. 2.5 Schematic illustration showing the principles of HPT [1].

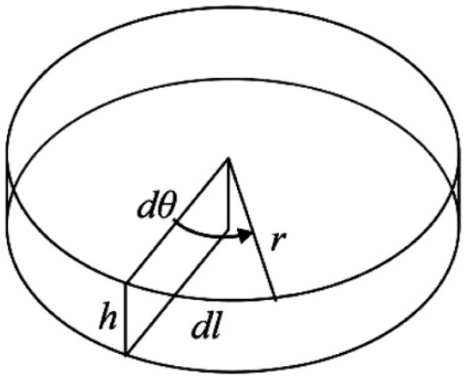

Fig. 2.6 Parameters used in estimating the total strain in HPT [1].

Using the parameters shown in Fig. 2.6 [1], the incremental shear strain dγ is defined as follows.

$$\mathrm{d}\gamma = \frac{\mathrm{d}l}{h} = \frac{r\mathrm{d}\theta}{h} \tag{2-3}$$

where h and r are denoted as before, θ is the rotation angle.

The integration of this shear strain is given by Eq. (2-3), as

$$\gamma = \frac{2\pi Nr}{h} \tag{2-4}$$

On the basis of von Mises yield criterion, the equivalent true strain of the small imposed shear strain is given by [66-68],

$$\varepsilon = \frac{\gamma}{\sqrt{3}} = \frac{2\pi N \cdot r}{\sqrt{3} \cdot h} \tag{2-5}$$

If the shear strain is larger ($\gamma \geqslant 0.8$), the equivalent strain can be calculated as [12, 14, 67]

$$\varepsilon = \frac{2}{\sqrt{3}} \ln[(1 + \frac{\gamma^2}{4})^{\frac{1}{2}} + \frac{\gamma}{2}] \quad (2\text{-}6)$$

A decrease in specimen thickness can be caused by the ultra-high pressure in the compression and the torsional deformation. When the reduction in sample thickness is taken into consideration [1], the equivalent strain can be:

$$\varepsilon = \ln[1 + (\frac{\theta \cdot r}{h})^2]^{\frac{1}{2}} + \ln(\frac{h_0}{h}) \quad (2\text{-}7)$$

where h_0 is the original thickness and h is the final thickness.

2.3.2 Microstructures and influence parameters in HPT

In HPT experiments, the induced strains are cylindrically symmetric and will linearly increase as the distance to the axis of rotation increases. The microstructures of samples processed by HPT are inhomogeneous. Hardness measurements often present a saturated value in the periphery areas of discs after processing by HPT, with the rotation number larger than 1.

In most HPT-processed alloys [12, 15, 16, 70, 71], higher hardness is observed in the peripheral areas of samples, as shown in Fig. 2.7 (a) [15]. By contrast, for alloys which show rapid dynamic recovery in the peripheral region, the hardness can be higher in the central area as compared to the peripheral area. An example is high purity aluminium, see Fig. 2.7 (b) (from [72]).

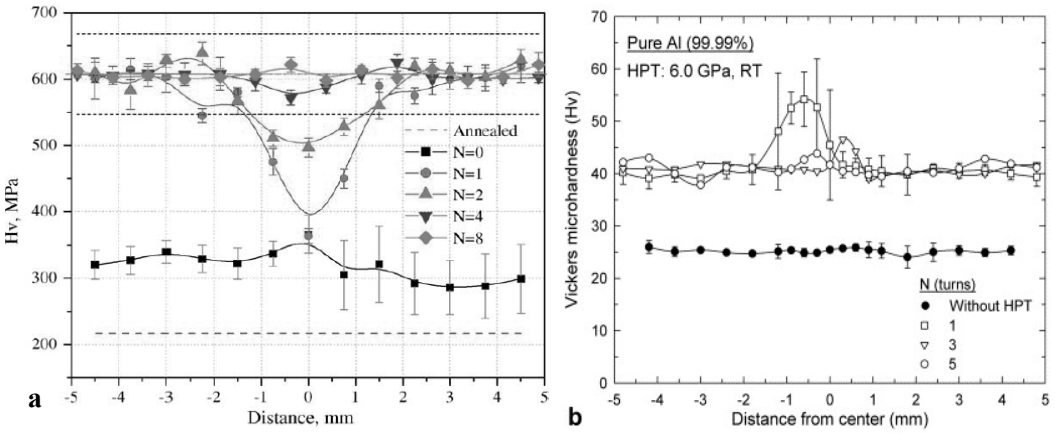

Fig. 2.7 Microhardness distributions across the diameters of (a) commercial pure Al (P=1GPa) [15]; (b) a high purity Al (99.99%) (P=6 GPa) [72].

Microstructures of samples processed by SPD are usually observed by TEM. The grain sizes of a commercial pure aluminium alloy after HPT were smaller than that of the initial samples [15]. A high dislocation density was observed at grain boundaries and inside some grains of samples in the central region (Fig. 2.8 (a) [12]), whilst free dislocation at boundaries, distortions and bending of the lattice fringes were observed in the peripheral region (Fig. 2.8 (b) [12]). This is thought to be due to the fast annihilation rate of dislocations in the periphery [12].

The applied pressure can play an important role in the microstructural evolution during HPT [72-76]. Bright-field TEM images in Fig. 2.9 [73] presents the microstructures of Ni processed by 5r-HPT under a pressure of 1, 3 or 9 GPa. The average grain size in the central region is larger than the grain size at the periphery. If the applied pressure is higher, the difference of grain sizes between the centre and the periphery becomes smaller. A significant difference in grain morphologies still exists. The grains tend to be reasonably equiaxed at the periphery and to be elongated in the centre.

Parameters that influence the hardness of HPT-processed metals were investigated by Edalati and Horita [74, 75]. In their work, the grain size at the steady state decreased by atomic bond energy, the specific heat capacity, the activation energy for self-diffusion and the homologous temperature, but the grain size was almost independent of stacking fault energy [75] (see Fig. 2.10 [74, 75]). The relation between the steady-state hardness

and its grain size was identified, indicating the great importance of grains having high angles of misorientation for HPT strengthening [75].

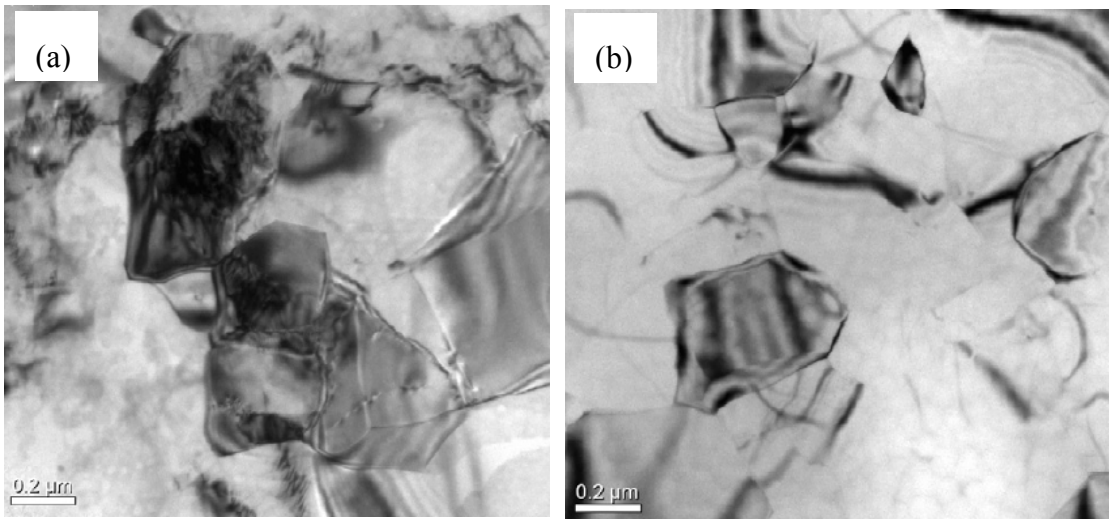

Fig. 2.8 TEM micrographs of 5 turns HPT under 3 GPa for commercial purity AA1050 alloy (a) centre region and (b) peripheral region [12].

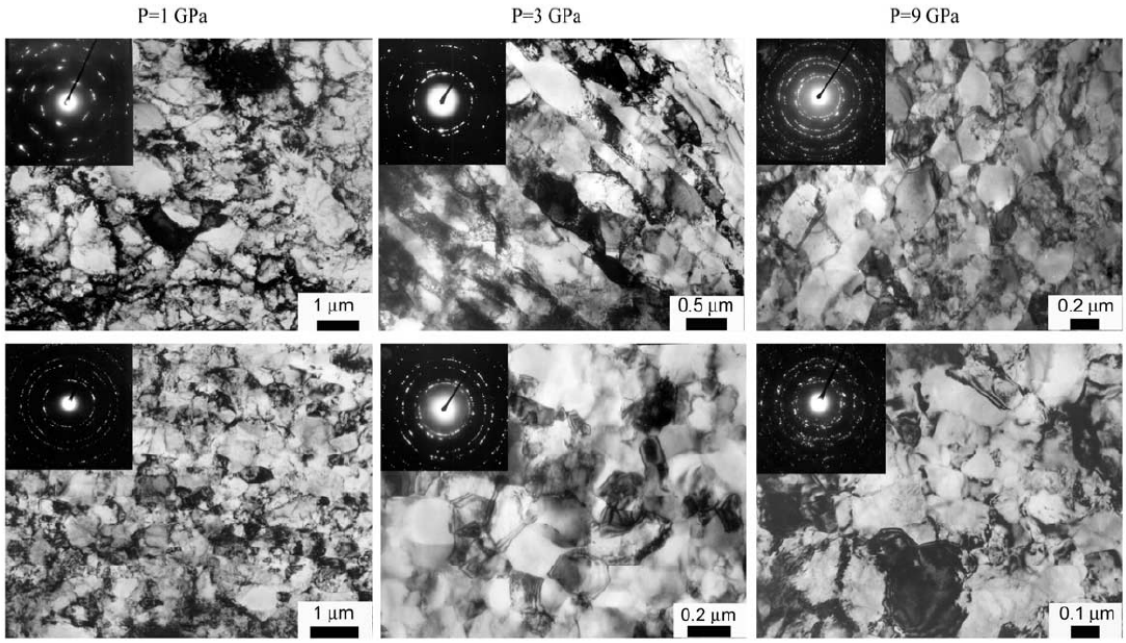

Fig. 2.9 Microstructures of pure Ni after HPT together with the associated SAED patterns: the upper row corresponds to the centers of the disks, the lower row to the peripheries of the disks and images are shown for N=5 whole revolutions at applied pressures of 1, 3 and 9 GPa from left to right, respectively [73].

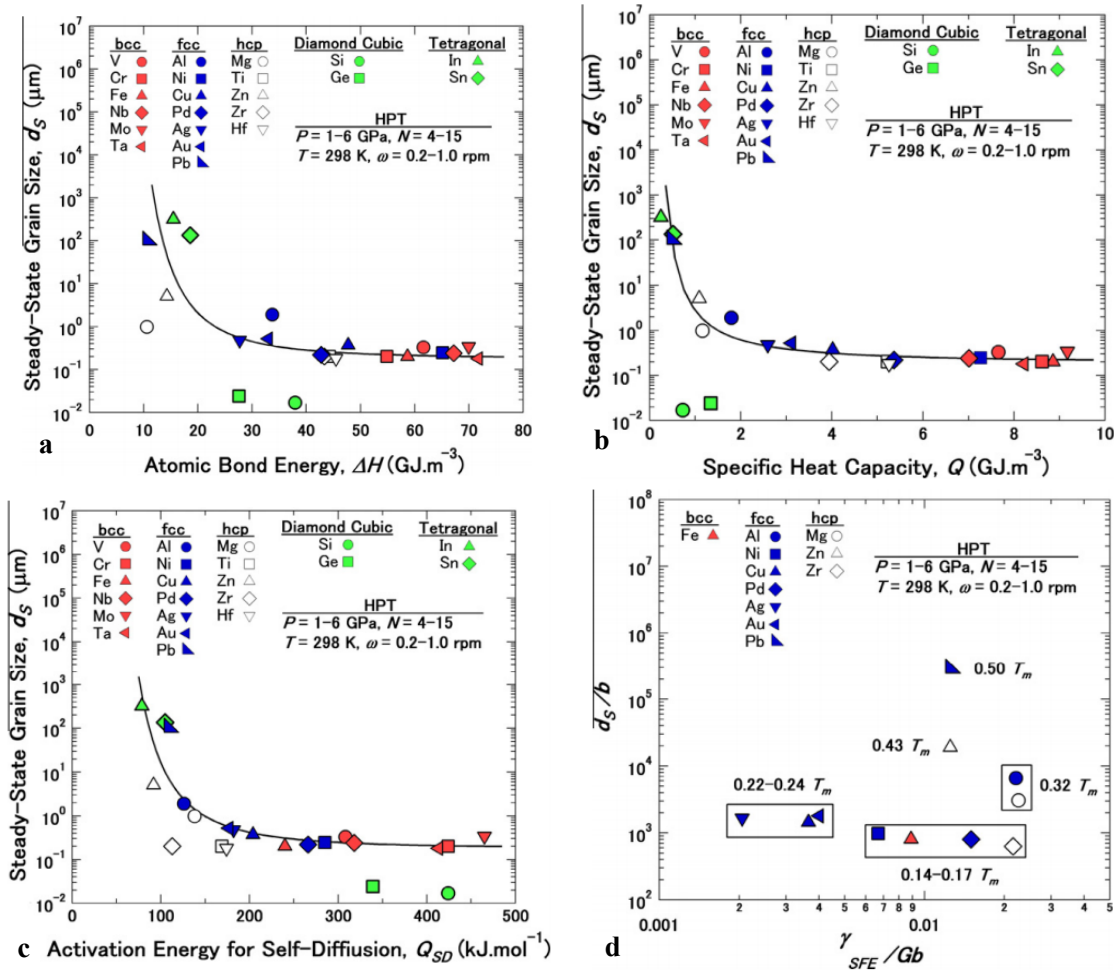

Fig. 2.10 Plots of steady state grain size against (a) atomic bond energy (b) specific heat capacity (c) activation energy for self-diffusion, and (d) steady state grain size normalized by Burgers vector *b* against stacking fault energy normalized by shear modulus and *b* [74, 75].

2.3.3 Mechanisms of strengthening in ultrafine-grained alloys

The strength of metals and alloys is essentially increased due to the presence of the various types of obstacles. The interaction between moving dislocations and obstacles cause an increased resistant force for a dislocation to pass by, leading to a higher strength of materials. In UFG Al based alloys, the obstacles include clusters, grain/subgrain boundaries, precipitates and other immobile dislocations. These strengthening mechanisms are summarized below.

Co-clusters involve two or more distinct alloying atoms and retain the structure of the host lattice. These co-clusters are shearable, so the strengthening mechanism is correlated to obstacle shearing [77] rather than Orowan strengthening [78]. For the case of strengthening due to co-clusters, the phases were considered to be extremely short ranged and hamper the individual dislocations when they passed through the co-clusters [57].

Grain boundaries are barriers for dislocation movement. The Hall-Petch equation [79] was established and fitted well with materials with coarse grain sizes. It demonstrates the yield stress increases as the grain size decreases:

$$\sigma_y = \sigma_0 + k_{HP} d^{-\frac{1}{2}} \tag{2-8}$$

where d is the average grain diameter. σ_0 is initial yield stress.

In the absence of appreciable work hardening, the hardness of materials is proportional to the yield stress $\sigma_y \approx Hv/3$ [80]. The Hall-Petch equation is then equivalent to

$$HV = HV_0 + k_{HP} d^{-\frac{1}{2}} \tag{2-9}$$

where HV_0 and k_{HP} are constants for particular materials. The Hall-Petch relationship may not hold when testing materials with ultrafine grain sizes. Some hardness data for ultrafine-grained materials are consistent with Eq. (2-9) but with a lower value of k_{HP} than that at the larger grain sizes [81-83]. If the grain size decreases to the nanoscale, the inverse Hall-Petch behaviours have been observed [84, 85]. So far, at least three main groups of theories and models have been derived to explain the breakdown of Hall-Petch equation: the classical dislocation pile-up model [86], the grain boundary sliding model [87] and the core and mantle models [88]. However, no clear experimental evidence has been able to support either model for all metals.

In terms of precipitation strengthening, Orowan by-passing [78] and obstacle shearing [89] are two main mechanisms in heat-treatable alloys during ageing. If the particles are small and shearable, the obstacle shearing mechanism is the dominant mechanism, which involves chemical, coherency, modulus mismatch, and anti-phase boundary (APB) strengthening [90, 91]. If the precipitates are large and non-shearable, dislocations cannot cut through the particles, but loop around the particles. In UFG microstructures, the precipitates are fragmented or partly dissolved [18-22], indicating shearing mechanism is more appropriate to explain the precipitation strengthening.

Dislocation hardening is thought to be the one of the dominant mechanisms for samples during SPD processing. In general, cold plastic deformation takes place in metals and alloys through dislocations generation, movement and storage. Two mechanisms are widely accepted for dislocation generation, the Frank-Read source [92] and the double-cross lip mechanism [93]. Both mechanisms depict dislocation generation from segment between two pinning agents. The localized source can operate repeatedly to emit a greater number of dislocations. The Frank-Read source emits many dislocations in the same plane, whilst in the double-cross lip mechanism only a single dislocation loop is emitted, moves on a plane parallel to the original one and leads to a growth of the width of the slip bands [94]. The moving dislocations may be blocked by obstacles, such as other dislocations, particles and grain boundaries, and stored in grains.

Due to the geometry of the HPT [1], strain is inhomogeneous and the equivalent (von Mises) strain increases with the distance from the centre to the near-edge regions. The strain gradients along the radius of the samples lead to inhomogeneous microstructures and the formation of geometrically necessary dislocations [95]. To date, very limited

work referring to GNDs during HPT are available. But the strain gradients have been incorporated to model HPT [14]. The counterpart of GNDs are statistically stored dislocations, which refer to dislocations accumulated as a result of random encounters in the crystal leading to mutual trapping [95]. Both GNDs and SSDs appear in central and peripheral parts of an HPT sample. The SSDs are correlated to the plastic shear and strain [96]; and the GNDs are derived from strain gradients and formed to release the local lattice curvature [95]. Hence, the proportions of GNDs and SSDs vary along the radius in an HPT disks.

The strengthening mechanisms in an UFG heat-treatable Al alloy are complex and correlated to each other, leading to an ultra-high strength. It is one of the aims of this project to investigate if a model based on the microstructural evolution for multiple mechanisms that can provide good description for the strengthening behaviours in heat-treatable Al-Cu-Mg alloy processed by HPT and the subsequent artificial ageing.

2.3.4 Thermal stability of HPT metals

The thermal stability of materials processed by HPT is of paramount importance, especially for industrial applications at elevated temperatures. When materials are heated, the UFG structures introduced by SPD coarsen through massive grain growth, and a high strength and other advanced features of materials will be lost.

Research on nanocrystalline or submicron grained Cu and Ni [97, 98] described that their grain sizes decreased to 107 nm and 114 nm after HPT, with a dislocation density of 10^{14} m^{-2}. In DSC heating, the grain sizes increased dramatically at 175 °C; simultaneously, the hardness of both samples decreased significantly. TEM, DSC, XRD and electrical resistance studies indicated thermal stability of UFG microstructure was associated with both grain growth and the relaxation of grain boundary structure [98].

A study on 7075 Al alloys processed by ECAP and DSC heating showed that the Vickers hardness of UFG alloys and the dislocation density decreased when heated at temperatures from 140 to 220 °C, and the crystallite size increased [99]. The

recrystallization started at 228 °C and completed at 300 °C, indicating a high thermal stability that was thought to be correlated with precipitates (i.e. η and η' phase).

In a study on structural evolution of bulk nanocrystalline Cu produced by HPT by Gubicza et al. [100], oxygen-free copper (99.97%) samples were processed by different SPD techniques, which involved multi-directional forging (MDF), twist extrusion (TE), ECAP and HPT. Despite their similar grain sizes (200 nm), the profile broadening analysis on XRD patterns indicated the thermal stability decreased in the order of MDF, TE, ECAP and HPT [100].

Saldana et al. [101] studied the thermal stability of UFG copper with a consideration of the various defect structures. His results pointed to the possibility of using twins in simultaneous stabilizing and strengthening roles in microstructures [101].

2.3.5 The behaviours of dissolved atoms in SPD Al alloys

Atom probe microscopy has revealed different behaviours of dissolved atoms in SPD alloys [17-26]. The influence of the dissolved atoms in precipitation-strengthened aluminium alloys can be summarized as four cases:

If precipitates already exist before SPD processing, the pre-existing precipitates can be fragmented or partially dissolved. These phenomena are alloy-dependent and process-dependent. In Al-Cu [18-21] and Al-Cu-Mg based alloys [22], clear evidence of particle fragmentation and partial dissolution has been reported.

If no precipitates have been initially presented in alloys, the dissolve atoms can be redistributed and segregated to grain boundaries/dislocations (e.g. in AA7075 (Al-Zn-Mg-Cu) [24], AA6060 [23], AA6061 [25], AA7136 [26]). Studies on equilibrium grain boundary segregation on nanograined materials indicate that solute segregation reduces the grain boundary energy and stabilizes of crystalline defects [102, 103].

If SPD processing is carried out in the range between 100 °C to 200 °C, precipitation can occur during deformation. The reactions can be complex, correlated to the

formation of co-clusters and GP zones during SPD processing. It can lead to a further increase of hardness (i.e. AA6060 processed by HPT at 100 °C [23] and AA2024 processed by HPT at 100 °C [17]).

If an artificial heat treatment is applied to a heat treatable Al alloy after SPD processing at room temperature, a range of different phenomena can occur [27, 28, 99, 104, 105]. Due to recovery, the alloy can show softening, as revealed in an ECAP-processed 7075 Al alloy [99] and ARB-processed Al-2%Cu alloy [105]. At low ageing temperatures, the hardness remains almost constant in an SPD processed Al-Mg-Si alloy [104], but a further increase in hardness was achieved by artificial aging of an HPT-processed Al-Cu-Mg-Li (2091) alloy (aged at ~100 °C) [27] and an HPT-processed 7075 alloy (aged at ~70 °C) [28].

2.3.6 Superplasticity of UFG alloys

Superplasticity of polycrystalline materials refers to the ability to deform uniformly to a very high elongation (ε>500%) in tension without development of any incipient necking [106].

Attaining true superplastic flow through HPT processing has been proven to be quite difficult, especially by comparison with those processed by ECAP, where the processed billets are larger and more suitable for tensile testing. There are a limited number of reports documenting the occurrence of superplastic elongations in materials processed by HPT.

The first report of superplasticity in a material processed by HPT was for an Al-4%Cu-0.5%Zr alloy having an as-processed grain size of 300 nm and an elongation of 800% when tested at 773 K using an initial strain rate of 3×10^{-4} s^{-1} [1]. An HPT processed Al-3%Mg-0.2%Sc alloy exhibited an elongation of ~ 500% at 673 K with an initial strain rate of $3.3\cdot10^{-2}$ s^{-1} [16]. In an Al 2024 alloy, superplastic elongations were shown in both annealed and solution treated samples, with a maximum elongation of 570% at 673 K with an initial strain rate of $1.7\cdot10^{-3}$ s^{-1}[107]; whilst in a Mg-9%Al alloy, superplastic

ductility was achieved at a temperature of 473 K and an initial strain rate of $1.0 \cdot 10^{-3}$ s^{-1}, with a maximum measured elongation of 810% [108].

A model for the grain boundary sliding in superplasticity is depicted schematically in Fig. 2.11 [109]. The accommodating dislocations are able to glide through the blocking grain to impinge on the opposite grain boundary.

The flow mechanism leads to a strain rate, which is given by [106, 109, 110]:

$$\dot{\varepsilon} = A\frac{DGb}{kT}\left(\frac{b}{d}\right)^{p_s}\left(\frac{\sigma}{G}\right)^{n} \tag{2-10}$$

Where $\dot{\varepsilon}$ is the strain rate, D is the appropriate diffusivity (lattice or grain boundary), G is the shear modulus, b is the Burger's vector, k is the Boltzmann's constant, T is the test temperature, d is the grain size, p_s is the grain size exponent (usually 2 for lattice diffusion controlled flow and 3 for grain boundary diffusion controlled flow), n is the stress exponent, ~2, and σ is the applied stress. A is a dimensionless constant having a value of ~10 [111]. It is apparent that elongation can be greatly influenced by temperature as diffusivity is a temperature dependent factor. The test temperature is a key parameter when measuring the elongation of samples after HPT.

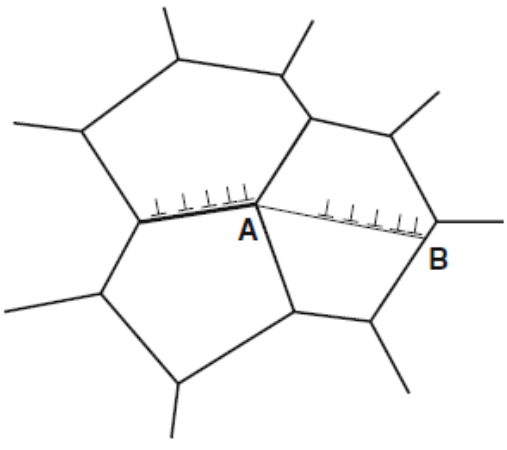

Fig. 2.11 Principles of a model for grain boundary sliding in superplasticity: dislocations move along the grain boundary and pile-up at the triple junction A, the stress concentration is removed by the nucleation of slip in the adjacent grain and these intragranular dislocations pile-up at B and climb into the grain boundary [109].

2.4 Modelling microstructural evolution of SPD processed samples

2.4.1 Modelling of dislocation generation and accumulation

In the classic theories, dislocations generate due to plastic deformation and migrate, which can be hindered by obstacles; new dislocations are generated by Frank-Read sources [92] to continue deformation. In the models developed by Mecking, Estrin and Kocks [112-114], the rate of accumulation of dislocations was described by:

$$\frac{d\rho}{d\gamma} = \frac{dL}{bda} = \frac{1}{bl} \tag{2-11}$$

where dL means the length of dislocation stored per area swept da, and l is a 'mean free path' [114].

A relation between flow stress τ and dislocation density ρ was established by Taylor [115] and well fitted by the data collected in a large number of publications [12, 13, 116-118]:

$$\tau = \alpha Gb\sqrt{\rho} \tag{2-12}$$

where G is the shear modulus and b is the magnitude of the Burgers vector. By differentiating Eq. (2-12), the dislocation accumulation rate can be given as

$$\tau\frac{d\tau}{d\gamma} = \frac{(\alpha Gb)^2}{2}\frac{d\rho}{d\gamma} \tag{2-13}$$

On the other hand, 'dynamic recovery' emphasizes the strong dependence on temperature and strain rate, indicating the net accumulation rate can be derived from Eq. (2-11) [114]:

$$d\rho = \frac{d\gamma}{bl} - d\rho_r \tag{2-14}$$

The second term presents dislocation density decrease due to annihilation. The relations of shear strain and the shear stress and their equivalent counterparts of polycrystalline metals in plastic deformation are provided by [119]:

$$\frac{d\sigma}{d\tau} = \frac{d\gamma}{d\varepsilon} = M \tag{2-15}$$

By integrating Eq. (2-14) [118], a quantitative expression is provided to reveal the relationship between average dislocation density in grains and micro strains:

$$\rho_{ig} = \left(blk_2\right)^{-1} - \left(\left(blk_2\right)^{-1} - \rho_0\right)e^{-k_2\varepsilon} \tag{2-16}$$

in which ρ_{ig} is the volume averaged dislocation density in the grains, ρ_0 is the initial dislocation density stored in the grain, ε is the strain, k_2 is a constant [118]. If the dislocation generation during straining is continuous, total volume averaged amount of dislocations generated per volumes is provided by [117]:

$$\rho_g = \left(\frac{K_A}{\alpha_1 MGb}\right)^2 \varepsilon \tag{2-17}$$

where K_A is a factor that incorporates the contribution of the solid solute atoms [117].

This model describes the dislocations generated with the induced strain and annihilation due to recovery; the net dislocations accumulated at grain boundaries strain the materials and increase the hardness. Eq. (2-17) indicates the dislocation generation due to strain, but it cannot fully explain the nonhomogeneous deformation in HPT. The dislocations in Eq. (2-17) are related to the SSDs, which will reach an effective saturation value during SPD. The descriptions of GNDs and SSDs are presented in the following Section 2.4.2.

2.4.2 Modelling of geometrically necessary dislocations

Physically-based models attribute strengthening at small dimensions to the existence of immobile dislocations [115]. In descriptions of dislocations in crystals, dislocations are termed into two different categories: geometrically-necessary dislocation (GND) and statistically-stored dislocations (SSD). In a preferred length scale of plastic deformation, the storage of SSDs mainly result from random trapping processing of mobile dislocations, while GNDs accommodate local orientation gradients. The strain gradient theories have been developed in dislocation mechanics since 1950s. Models have been established to calculate GNDs [95, 120].

The concept of an average dislocation density was first introduced Nye [120]. He expressed the dislocation density in terms of the number of dislocation lines crossing unit areas. Later, a physical basis for GND and SSD was provided by Ashby [95]. In Ashby's theory [95], both GND and SSD demonstrated their emergence in plastically inhomogeneous deformation.

As shown in Fig. 2.12, the strain gradient enhances the hardening effects and product GNDs, which was derived by [95]:

$$\rho_{GND} = \frac{1}{b}\frac{\partial \gamma}{\partial x_1} \tag{2-18}$$

where $\frac{\partial \gamma}{\partial X_1}$ is the gradients of plastic shear and b is the burger vector.

For cube-shaped particles of size d, the equation can be further expressed

$$\rho_{GND} = \frac{Cf\gamma}{bd} \tag{2-19}$$

where f is the volume fraction, and C is approximated 8.

For low-angle grain boundaries, the density of GNDs is simplified as [121, 122]

$$\rho_{GND} = \frac{\eta^b}{d} \tag{2-20}$$

where the plastic strain gradient is defined as η^b.

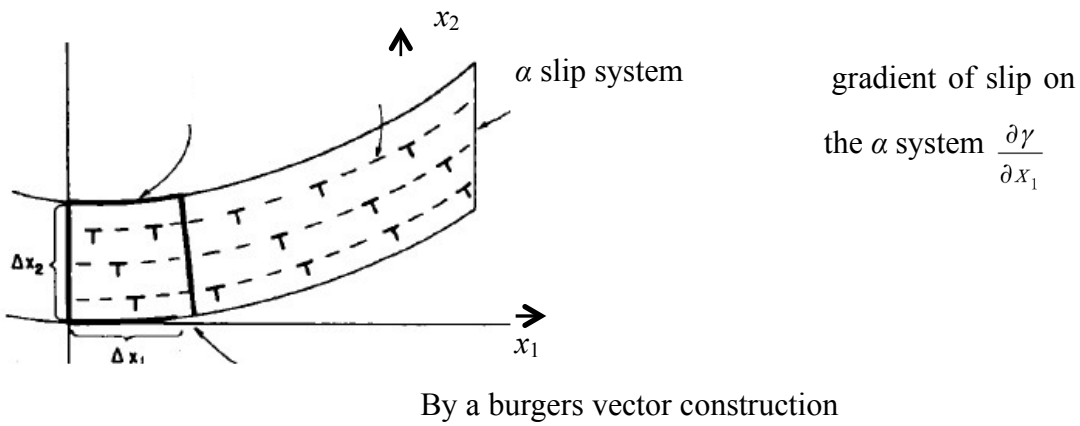

Fig. 2.12 Schematically measurement of GNDs in deformed materials.

According to the definition of GNDs, two characteristics of GNDs are indicated: firstly, GNDs do not directly contribute to plastic straining in the way the SSDs do, but they originate as a result of spatial plastic strain variations. In this case, the net Burgers

vector is non-zero [123]. Secondly, as a consequence of accommodating lattice curvatures, GNDs have equal orientations within a length scale substantially larger than their spacing, whereas the SSDs do not contribute to any spatial inhomogeneity at that length [123]. The measurements of SSD and GND densities are really based on the population of dislocations within a certain volume. This volume is denominated as the average representative volume element [124]. Within the volume, the SSDs cancel out at the continuum level, but GNDs locally accommodate a plastic strain gradient and reveal scale size effects [125-129].

In the crystal plasticity models [123, 130], both GND and SSD on all slip systems are considered to participate in mutual short-range interactions, which lead to the strength increase of metals. However, only GNDs rather than SSDs are responsible for the long-range contributions [123]. The GNDs bring additional residual stress, which counteract the local resolved shear stress and obstruct the crystallographic slip [122, 131].

2.5 Measurement of stored energy and dislocation densities

Microstructural modifications of materials processed by SPD can be analysed by a range of techniques. In this section we will review the theory behind two important techniques that produce quantitative data on stored energy and dislocation densities, differential scanning calorimetry (DSC) and X-ray diffraction (XRD). Both are used extensively in this project.

DSC is a thermal analytical technique to measure the difference in the amount of heat produced by a sample and a reference. This technique provides a direct calorimetric measurement of the energy released or absorbed when reactions occur in SPD samples during heating process at a constant heat rate. The principle and study of DSC on UFG metals and alloys processed by SPD will be reviewed in Section 2.6.1. In analysis of UFG materials, small grain size and microstrain are two main sources that cause profile broadening [132]. Section 2.6.2 reviews three models on XRD profile broadening.

2.5.1 Differential scanning calorimetry

DSC is widely used to investigate reactions in different materials. DSC measures the energy of the transformation process. The word ‘differential’ emphasises that measurements involve the determination the relative behaviour of a substance itself and a reference material [133].

There are two type of DSC: the heat flux DSC and the power compensation DSC. The working principles of the two methods are illustrated in Fig. 2.13 [134]. In the heat flux DSC, the signal derives directly from the difference in temperature between the sample and the reference and in that sense a heat flux DSC is similar to a DTA (differential thermal analysis). In power compensation DSC, the signal is related to differential heat provided to keep the sample and the reference to the same temperature. Only small amounts of sample are used in a typical experiment (the most common amount is between 2 and 20 mg), DSC is highly sensitive. However, a higher sensitivity does not

always mean that better results will be obtained. The baseline, heat capacity calibrations and sample preparations contribute to the accuracy and validity of a DSC thermal graph.

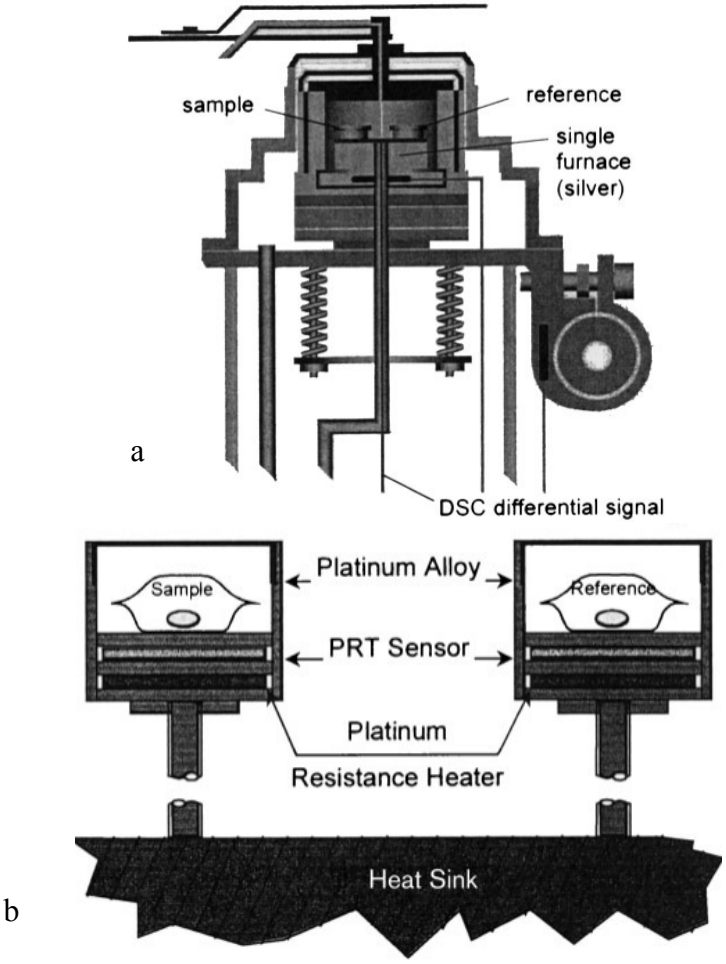

Fig. 2.13 DSC working principles (a) heat flux DSC, (b) power compensation DSC [134].

2.5.1.1 Baseline calibration

The ideal baseline for a system is a straight line without any slope. However, in real experimental runs, the experimental conditions, such as the flow rate of purge gases, the flow rate of coolant and the contamination of DSC cells, can be different from those of the calibration runs [135]. If the correct calibration is not performed for the experiments, the observed heat and temperature results will be different from the correct value. At the beginning of the experiments, the DSC instrument should be calibrated using the

melting enthalpy of standard samples (i.e. indium 28.4 J/g, tin 59.2 J/g or lead 23.2 J/g [135]).

In Al based alloys, the heat effects due to reaction will be of the same order of magnitude or smaller than heat effects due to the heat capacity difference between sample and reference [134]. A correction for the heat effect due to heat capacity difference is needed to be performed on the basis of the weights and a weighted average of heat capacities. The heat capacity difference in DSC [136] is

$$c_{\mathrm{p,s}}(T) = q\beta + c_{\mathrm{p,ref}}(T) \tag{2-21}$$

where q is the heat flow in DSC, β is the heating rate, $c_{\mathrm{p,s}}$, and $c_{\mathrm{p,ref}}$ are the heat capacities of a sample and a reference [136]. Derived from Eq. (2-21), a two point correction and three point correction have been developed to fit data. The method used in this study has been applied and validated for a range of light metal alloys. In the two point corrections the baseline fluctuations are considered to be linearly dependent on the temperature.

$$Q_{real} = Q_{measured} + a_{DSC}T + b_{DSC} \tag{2-22}$$

where the two parameters a and b can be obtained with knowledge of certain features of the curves. However, baseline drifts usually show a parabolic trend against temperature, T, due to baseline fluctuations and heat capacity, a second order polynomial function fit through these points is used to determine the heat flow.

$$Q_{real} = Q_{measured} + a_{DSC}T^2 + b_{DSC}T + c_{DSC} \tag{2-23}$$

2.5.1.2 Equivalent time calculation

The equivalent time of non-isothermal treatment (i.e. linearly heated at a constant heating rate in the power compensation DSC) allows comparison of the progress of a reaction when samples are exposed to different temperature paths. The transformation rate during a reaction is product of two functions, depending solely either on the temperature T, or on fraction transformed α [137, 138]:

$$\frac{d\alpha}{dt} = f(\alpha)k(T) \tag{2-24}$$

where the temperature dependent function $k(T)$ is assumed to follow an Arrhenius formula (Eq. (2-25)), and the fraction transformed function $f(\alpha)$ is assumed to follow the Johnoson-Mehl-Avriami equation (Eq. (2-26)) [139-141]:

$$k = k_0 \exp\left(-\frac{E}{RT}\right) \tag{2-25}$$

$$f(\alpha) = n(1-\alpha)\left[-\ln(1-\alpha)\right]^{1-1/n} \tag{2-26}$$

where R is the gas constant, E is the activation energy of the reaction, k_0 and n the constant, which need to be determined.

In the state variable approach, the fraction transformed in reactions is approximated by integrating the Eq. (2-24),

$$\int_{t=0}^{t_e} \frac{d\alpha}{f(\alpha)} = \int_{t=0}^{t_e} k(T)dt \tag{2-27}$$

As a result, the fraction transformation function on the left hand side of Eq. (2-27) is defined as a function solely depending on temperature with an Arrhenius expression. When the same amount of fractions are transformed in isothermal reaction at temperature T_{iso} and in non-isothermal reaction with temperature path $T(t)$, the equivalent time t_{eq} of non-isothermal reaction is given as [134]:

$$t_{eq} = \int_{t=0}^{t_e} \exp\left(-\frac{E}{RT(t)}\right) dt \exp\left(-\frac{E}{RT_{iso}}\right)^{-1} \tag{2-28}$$

where T_{iso} is the temperature of isothermal reactions.

For linear heating, the equation can be derived as

$$\int_{t=0}^{t_e} \exp(-\frac{E}{RT(t)})dt = \frac{E}{R\beta} \int_{y=y_f}^{\infty} \frac{\exp(-y)}{y^2} dy \tag{2-29}$$

where

$$y = \frac{E}{RT},\ y_f = \frac{E}{RT_f}$$

T_f is the temperature reached during the linear heating; β is the heating rate.

In order to obtain the equivalent time for linear heating, the integral $\int_{y=y_f}^{\infty} \frac{\exp(-y)}{y^2} dy$ is needed to be calculated. This temperature integral has been calculated using expansions of the integral in an infinite series [142-144]. The procedures for the derivation of the integral in DSC linear heating processes have been developed by Starink [145] using the Kissinger method [146, 147]. The approximation of equivalent time for DSC linear heating treatment leads to [134]:

$$t_{eq} \cong \frac{T_f}{\beta}\frac{RT_f}{E}\exp(-\frac{E}{RT_f})[\exp(-\frac{E}{RT_{iso}})]^{-1} \quad (2\text{-}30)$$

The Eq. (2-30) was used by Starink and Gregson in work on 8090 metal matrix composites [148]. In that work, samples were heated with heating rate β =10 K/min. The peak of the formation of semicoherent S phase was observed at 300 °C; the activation energy for the reaction of S phase is 107 kJ mol^{-1}. Eq. (2-30) predicted that if Al-Cu-Mg samples isothermal aged at 170 °C, it would take 30 hours to complete the same fraction of S transformation at 300 °C.

2.5.2 X-ray diffraction

X-ray diffraction peak profile analysis is a powerful technique for describing the microstructure of crystallite materials. X-ray diffraction peaks broaden when the crystal lattice are imperfect. Common sources contributed to the aberration from the ideal powder pattern include dislocations, microstress, internal stress, stacking faults, twinning, grain/subgrain boundaries, chemical heterogeneities, point defects, and precipitates [132]. Peak shift is related to the different types of internal stresses and planar faults. Small crystallite size and microstresses lead to peak broadening, however, stress gradients and dislocations can also cause profile broadening.

2.5.2.1 Principle of X-ray diffraction

In an XRD pattern, the intensities of permitted reflexions depend on the atomic groupings around the lattice. The relation between the structure amplitudes $F(hkl)$ and the observed relative intensities $I(hkl)$ is described by the Debye-Scherrer formula [149]:

$$I(hkl) = \frac{e^4 \lambda V_s}{32\pi m^2 c^4 R U^2} F^2(hkl) \cdot p \cdot \frac{1+\cos^2 2\theta}{\sin^2\theta\cos\theta} T \cdot A \quad (2\text{-}31)$$

where U is the cell volume, T is the temperature-correction factor, A is the absorption factor and p is the number of equivalent planes contributing to reflexion. The universal constants e, π, m and c have their conventional meanings [150, 151]. The Debye theory describes the how the different factors contribute to the breadth of X-ray diffraction peaks.

If the glancing angle of incidence θ equals the glancing angle of diffraction, and if the plane normal is coplanar with incident and reflected beam, all lattice points on the hkl plane must be in phase. This assumption leads to Bragg's law [152], which is

$$N_{hkl}\lambda = 2d_{hkl}\sin\theta \tag{2-32}$$

where d_{hkl} is lattice spacing between the parallel (hkl) planes, whilst N_{hkl} indicates the order of diffraction and λ is the wave length of the X-rays. The absence of certain reflexions indicates different lattice systems [153].

In principle, the experimental profile is the convolution of the instrumental profile and the intrinsic profile. The instrument broadening can never be eliminated because of the finite size of the source of X-rays and the finite width of specimen. The spread of wavelengths of X-rays $\lambda+\delta\lambda$ leads to the broadening of line at Bragg angle $\theta+\delta\theta$ [150]. In Bragg's equation, it is given by

$$2d_{hkl}\sin\left(\theta+\delta\theta\right) = \lambda+\delta\lambda \tag{2-33}$$

The simplified method to separate the intrinsic and instrumental profiles is based on assumptions that these profiles can be approximated by a bell-shape function such as Cauchy or Gaussian function [154]. The formations of these functions are summarized from Eqs.(2-34) to (2-36),

Cauchy-Cauchy

$$B_{\exp} = B_{\text{int}} + B_{ins} \tag{2-34}$$

Gaussian-Gaussian

$$B_{\exp}^2 = B_{\text{int}}{}^2 + B_{ins}{}^2 \tag{2-35}$$

Cauchy-Gaussian

$$\frac{B_{\text{int}}}{B_{\exp}} = 1 - \left(\frac{B_{ins}}{B_{\exp}} \right)^2 \tag{2-36}$$

where $B_{\exp}$, B_{int}, B_{ins} are integral breadth of experimental profile, intrinsic profile, and instrumental profile, respectively [154]. The intrinsic profile broadening is thought to attribute to either small crystallite size or microstress. Profile broadening due to small grain size was first observed and measured by Scherrer [155]:

$$D_{hkl} = \frac{K\lambda}{B_{hkl}\cos\theta} \tag{2-37}$$

where D_{hkl} is the crystallite size in the direction perpendicular to the lattice planes, h, k and l are the Miler indices of the planes being analysed, K is a numerical factor frequently referred to as the crystallite-shape factor, B_{hkl} is the width (full-width at half-maximum) of the X-ray diffraction peak in radians [151].

On the other hand, the profile broadening due to strain was first measured by Stokes and Wilson [156]:

$$\varepsilon = \frac{B_{hkl}}{4\tan\theta} \tag{2-38}$$

In reality, the experimental profile needs to be unfolded as size broadening component and strain broadening component at the same time. Three methods developed by

Williamson [157], Warren [158], and Rietveld [159] provide accurate ways of extracting size and strain information. These models on XRD profile broadening are presented in following Section 2.6.2.2 to Section 2.6.2.4.

2.5.2.2 Williamson-Hall Method

Williamson and Hall [157] assumed that both the size and the strain broadened profiles were Lorentzian components. Based on Cauchy-Cauchy approximation, the relationship between intrinsic integral breadth, strain and particle size effects was established [154, 160, 161],

$$B_{\text{int}} \cos\theta = \frac{K\lambda}{D} + f(\varepsilon)\sin\theta \tag{2-39}$$

or

$$\frac{B_{\text{int}} \cos\theta}{\lambda} = \frac{1}{D_v} + f(\varepsilon)\frac{\sin\theta}{\lambda} \tag{2-40}$$

where B_{int} is the integral breadth, λ is the wavelength of X-ray, θ is the Bragg angle, ε is the lattice strain, $f(\varepsilon)$ is a defined strain concerning function [154, 160, 161]. D_v is thought to be the volume weighted average domain size, which equal to D/K, D is the crystallite size in Eq. (2-39), K is the Scherrer constant [160]. By plotting $B_{\text{int}}\cos\theta$ versus $\sin\theta$ or plotting $B_{\text{int}}\cos\theta/\lambda$ versus $\sin\theta/\lambda$, the strain and the size component are obtained from the slope $f(\varepsilon)$ and intercept ($K\lambda/D$ or $1/D_{\text{v}}$), respectively.

Novelo-Peralta et al. [162] studied the XRD peak broadening due to the elastic effects caused by coherent precipitates in an Al-Mg-Cu alloy. The alloy was aged at 180 °C for 2 minutes (2M), 30 minutes (30M), 6 hours (6H), 3 days (3D) and 1 week (1W). The Williamson-Hall plot and the strain evolution during ageing are shown in Fig. 2.14 [162].

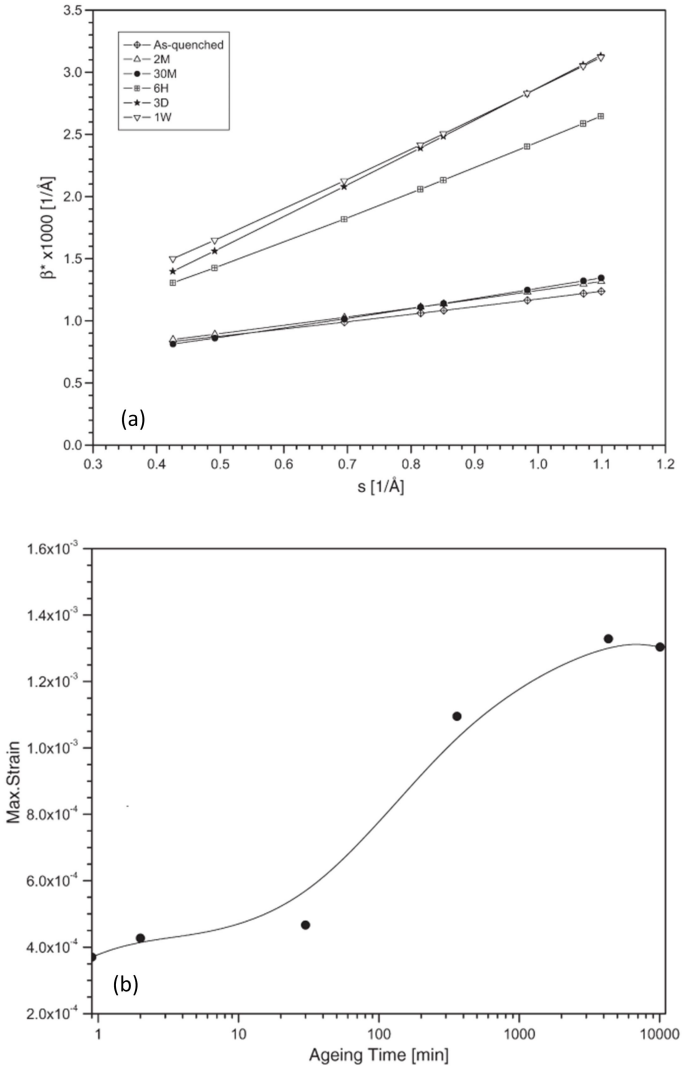

Fig. 2.14 (a) Williamson-Hall plots of Al-4.28Mg-0.68Cu (wt.%) alloy aged at 180 °C and (b) Max. Strain evolution as a function of ageing time [162].

2.5.2.3 Warren-Averbach Method

The Warren-Averbach method [158] was thought to be the first theory to describe the strain-induced Bragg peak broadening. By Taylor expansion of the Fourier coefficients of the peaks, the XRD profile of sample is expressed in the format of cosine and sine function [154, 163]:

$$f(s) \propto \sum_{L=-\infty}^{\infty} \{A(L)\cos[2\pi(s-s_0)L] + B(L)\sin[2\pi(s-s_0)L]\} \tag{2-41}$$

where $A(L)$ and $B(L)$ are the cosine and sine Fourier coefficient, respectively; L is the conjugate variable to s-s_0 in the real space and is interpreted as the column length of unit cells perpendicular to the diffracting plane corresponding to the Bragg peak [163].

In Warren-Averbach theory, the coefficients $A(L)$ is written as the product of a purely size-broadening term and a purely strain-broadening term [164]. A procedure has been developed to determine the individual size and strain contribution from measurements of two or more orders of the same Bragg reflection.

$$A = A^{\text{size}}(L)A^{\text{strain}}(s,L) \tag{2-42}$$

where $A^{\text{size}}(L)$ is an unknown size coefficient.

The strain coefficient is calculated as

$$A^{\text{strain}}(s,L) = \exp(-2\pi^2 s^2 L^2 < \varepsilon^2(L) >) \tag{2-43}$$

A logarithm function provides an effective way to measure strain and particle size broadening as [158],

$$\ln A(L,s) = \ln A^{size}(L) - 2\pi^2 s^2 L^2 < \varepsilon^2(L) > \tag{2-44}$$

where L is the Fourier length, which is defined as $L=na_3$, $a_3=\lambda/2(\sin\theta_1-\sin\theta_2)$, $<\varepsilon^2(L)>$ is the mean square strain, n is the integers staring from zero [158]. The slope of $\ln A(L)$ versus $2\pi^2 s^2 L^2$ gives the measurement of microstrain $<\varepsilon^2(L)>$. The domain crystallite size were calculated as [154]:

$$L_a = -\frac{A(0)}{\lim\limits_{L\to 0}\left(\frac{dA}{dL}\right)} \tag{2-45}$$

where L_a is the interpreted as an area averaged column length of unit cells. The Warren-Averbach analysis was carried out using the Bragg peak pairs i.e. (111)-(222) or (200)-(400). Fig. 2.15 shows the crystallite size of an as-extruded Al samples calculated from the reflection pair of (111)-(222) [154].

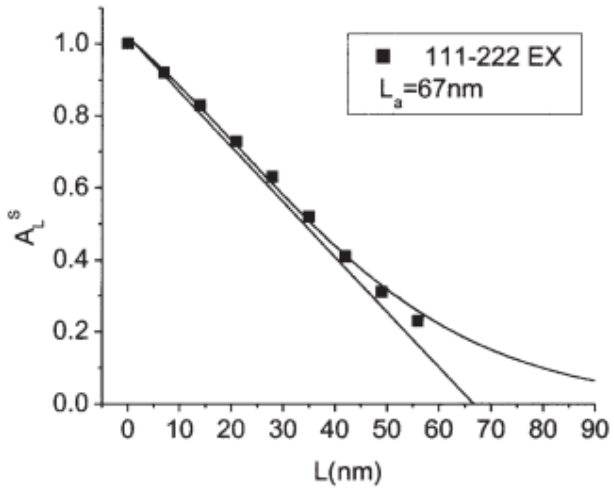

Fig. 2.15 Plot of Fourier size coefficients vs column length for as-extruded Al samples [154].

2.5.2.4 Rietveld Method

The Rietveld method is a full-pattern fit method. The objective of the Rietveld method is to determine and refine crystal structures by calculation. The model will be refined until the calculated pattern matches the experimentally observed pattern as close as possible. The peak profile is described as a Pseudo-Voigt (PV), Voigt or Pearson VII function. The model can be simplified as shown in Eq. (2-46) to Eq. (2-48) [165-167].

The residual function χ^2 to be minimize is given by

$$\chi^2 = \sum_i w_i (I_i^{\exp} - I_i^{calc})^2, w_i = \frac{1}{I_i^{\exp}} \tag{2-46}$$

where I_i^{calc} is determined by structure factor of cells, i.e. atoms in the asymmetric unit, symmetry equivalent positions, temperature factor [162, 167].

$$I_i^{calc} = S_F \sum_k L_k \left|F_k\right|^2 S(2\theta_i - 2\theta_k) P_k A + bg_i \tag{2-47}$$

in which

$$P_k = (r^2 \cos^2 \alpha + \frac{\sin^2 \alpha}{r})^{-3/2} \tag{2-48}$$

where P_k is denoted as the preferred orientation function; L_k is Lorentz-Polarization factor depending on the instrument (i.e. geometry, monochromator, detector, beam size and sample positioning). Profile shape function $S(2\theta_i - 2\theta_k)$ obeys Pseudo-Voigt function [168].

Profile shape function (PSF) is applicable over the whole range of diffraction angles [167]. Cagliotti formula (Eq. (2-51)), is the full width at half maximum (FWHM) as a function of θ for Gauss, pseudo Voigt and Pearson-VII function:

$$FWHM^2 = U \tan^2 \theta + V \tan \theta + W \tag{2-49}$$

where U, V, and W are free variable. U is the parameter most strongly associated with strain broadening. Crystallite size can be calculated from V and W.

The Rietveld method presents 3 main advantages over the Williamson-Hall method and Warren-Averbach method [169]: (a) crystal structure and microstructural parameters can be refined simultaneously by this method; (b) completely as well as partially overlapping reflections can be analysed with sufficient accuracy; and (c) Rietveld method takes into consideration the correction for preferred orientation if there is any.

Chapter 3 Materials and experimental procedures

3.1 Materials

Experimental work in this study was carried out on a commercial 2024-T351 Al-Cu-Mg alloy. The composition of this aluminium alloy is shown in Table 3-1. The T351 temper indicates the alloy has been solution treated, water quenched, and stretched to about 2~5% plastic deformation and then naturally aged. Table 3-2 shows the tensile properties of this type of Al alloy in the as-received condition. In order to relieve stress, some of the samples were re-solution treated at 495 °C for 30 minutes and naturally aged at room temperature.

Table 3-1 Composition of 2024-T351 Al-Cu-Mg alloy.

Elements	**Cu**	**Fe**	**Mg**	**Mn**	**Si**	**Zn**	**Others**	**Balance**
Composition (wt. %)	4.63	0.15	1.51	0.66	0.08	0.05	<0.05	Al
Composition (at. %)	2.1	0.07	1.8	0.35	0.08	0.02	<0.05	Al

Table 3-2 Tensile properties of 2024-T351 Al-Cu-Mg alloy.

Tensile Properties	Proof stress (0.2%), MPa	Ultimate tensile strength (UTS), MPa	Elongation (%)	Percent Stretch
Values	326	464	16.5	2.8%

3.2 HPT facility

The experiments were carried out at room temperature using a HPT facility in the Transport Systems Research Laboratory (TSRL) at the Faculty of Engineering and the Environment at the University of Southampton, shown in Fig. 3.1(a).

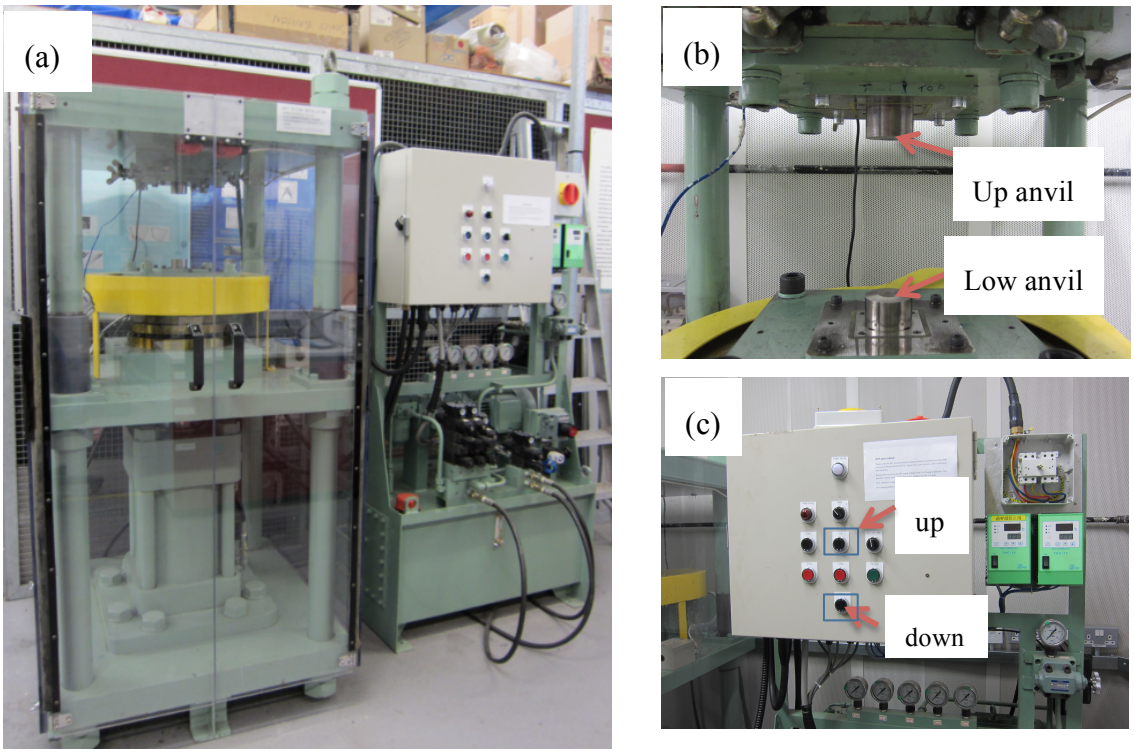

Fig. 3.1 High pressure torsion machine in TSRL lab at Southampton (a) overview of the HPT facility, (b) upper and lower anvils; (c) movement and speed control panel.

The facility consists of an upper and a lower anvil made from high strength tool steel (YXR3) (in Fig. 3.1 (b)). Each anvil contains a spherical cavity having a diameter of 10.0 mm and a height of 0.25 mm at the centre. Samples should be prepared with a diameter of 9.8 mm. The surfaces of both anvils are roughened and hardened using shot peening process. The upper anvil is fixed while the lower anvil rotates to introduce torsion straining. HPT processes can be controlled by the buttons on the panel (Fig. 3.1(c)). The thickness of the disks prepared for HPT was 0.85±0.03 mm after grinding

using 120, 400 and 800 grits. No lubricant was applied on the sample but some was applied on the anvil section adjacent to the samples.

3.3 HPT and heat treatment

3.3.1 HPT processes

Samples (2024Al-T351) were classified into two groups:

(1) Monotonic HPT, samples were clockwise rotated 1/8, ¼, 1, 3, 5 and 16 rotations, which are denoted as 1/8r-HPT, 1/4r-HPT, 1r-HPT, 3r-HPT, 5r-HPT and 16r-HPT. Due to the hardness saturation observed for samples processed by a higher number of rotations, 16 rotations were chosen as the maximum number of rotations [12-14]. To compare with torsional deformed samples, a sample was compressed under 6 GPa without any rotations.

(2) Single inverse HPT, the samples were first rotated clockwise 5 turns, and reversed 90°, 180° or 360° counter-clockwise, which are denoted as 5r-1/4r HPT, 5r-1/2r HPT and 5r-1r HPT.

3.3.2 Heat treatments

Because of microstructural inhomogeneity an HPT disc, the microhardness and XRD experiments need to be carried out on full disks. The DSC furnace is too small to hold a full-size HPT disc. Hence, artificial ageing on T351 samples and UFG samples are required to perform in an air-circulating furnace.

The samples were isothermal aged at 100 °C, 140 °C, 170 °C, 200 °C, 210 °C, 230 °C, 270 °C, and 400 °C. The dislocation densities of HPT samples after ageing were analysed using XRD at room temperature.

The equivalent time is taken into account for a sample isothermal heating up to ageing temperatures ([134] and see also 2.6.1.2). The relationship of time and temperature is illustrated in Eq. (2-32), with E approximated by the activation energy for diffusion of solute atom (Cu or Mg) as 107 kJ/mole [170], and a heating rate β of 10 °C/min. Thus the HPT sample is heat treated for the calculated equivalent time t_{eq} at the same temperature in the DSC curve (T_{iso}=T_f), e.g. a sample isothermal annealed at 210 °C for 2 minutes equivalent to that DSC linear heated up to 210 °C with a constant heat rate of 10 °C/min. The series of isothermal temperatures and the equivalent time are listed in Table 3-3.

Table 3-3 The isothermal temperatures T_{iso} and the equivalent time t_{eq}.

Isothermal heating temperature (^{o}C)	**The equivalent time (s)**
100	65
120	72
150	83
170	91
180	95
210	109
215	111
230	118
240	123
270	137
300	153
330	169
400	211

3.4 Hardness test

The disc-shaped samples were ground up to 4000-grit SiC paper and polished by using a 0.05μm colloidal silica suspension. These procedures were followed to eliminate oxide or other contaminations on the surface of samples and to obtain a mirror-like surface for Vickers hardness tests. The hardness tests were conducted immediately after heat treatment by using a standard HV test machine with a load of 500g for a dwell time of 15s.

A total of 9 hardness indents were made on a line across the disc centre on the surface of the samples. 6 lines were performed for each sample. The value of hardness at the same distance to the centre was calculated from the 6 indentations. Eq. (3-1) presents the calculation of Vickers hardness of each indentation. Prior to the hardness testing, the instrument had been calibrated and tested on the calibrated hardness standard sample.

$$H_V = \frac{2F \sin \frac{130\,\mathrm{deg}}{2}}{d_{HV}^{\ 2}} \tag{3-1}$$

where F is the applied load and d_{HV} is the measured average diameter of the indent. The average hardness and error bar are reported.

The standard deviation (STD) is taken for a set of indents as

$$STD = \sqrt{\frac{1}{N_{HV} - 1} \sum_{i=1}^{N_{HV}} \left(x_i^{HV} - \bar{x} \right)^2} \tag{3-2}$$

where N_{HV} is the number of indentations, and x_i^{HV} is the value of individual indentation, and $\bar{x}$ is the average value of indentations.

3.5 DSC

3.5.1 Sample preparation and baseline subtraction

Due to the inhomogeneous microstructures of a sample after HPT processing, DSC samples were punched at different positions in the discs. In Fig. 3.2 (a), disc-shaped samples, 5 mm in diameter by approximately 0.7 mm thick, were punched from the centre region. For the thermal performance at the periphery, the samples were also punched by approximately 3 mm in width from the periphery (Fig. 3.2 (b)).

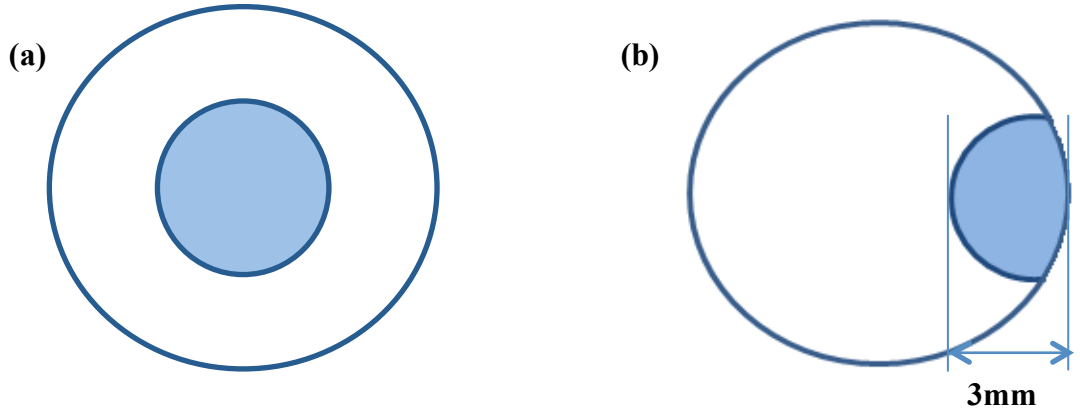

Fig. 3.2 Samples preparation (a) sample of 5 mm in diameter in the centre (b) sample of roughly 3 mm wide at the periphery.

DSC measurement was carried out on a power compensating Perkin-Elmer Pyris-1 calorimeter, using nitrogen gas as a protective atmosphere. An empty pure copper sample pan was used as a reference. Samples were performed from room temperature (25 °C) to 540 °C at a constant heating rate of 10 °C/min.

All DSC thermographs were corrected by subtracting a baseline obtained from a DSC run with an empty pan. A further correction was performed to correct for the baseline drift due to heat capacity difference and baseline fluctuations using a second order polynomial function (see Section 2.6.1). In this method, illustrated in Fig 3.3, three points on the DSC curves aid to identify the positions where no reaction occurs. The first point is readily defined as the initial part of DSC curve which is after the transient period and before the start of the first reaction (~70 °C in this case). The second middle

point is at the temperature where the transition from the first precipitation effect to its dissolution effect (i.e. ~300 °C for a 2024Al-T351 sample). The final point is at the temperature where all the precipitation and dissolution reactions are completed (i.e. ~500 °C corresponding to maximum heat flow between the final dissolution effect and the incipient melting).

The validity of these points was checked several times by re-solution treated (at 495 °C for 30 minutes), T351, naturally and artificially aged samples. In HPT processed samples, the middle point was chosen to balance the exothermic peaks of precipitation, co-clusters formation and dislocation annihilation. The selection of this middle point should be made to have the heat flows of precipitate dissolution (higher than 300 °C) overlap to curves of T351 or re-solution treated samples. An example (T351) for the second order polynomial correction is shown in Fig. 3.3. The heat released ΔQ is calculated by integrating the heat flow $\mathrm{d}Q/\mathrm{d}t$ (Q in J/(g·°C)) of peak over the temperature range from very beginning (the first point) to the end (the third point, ~ 500 °C). The original unit of heat flow is W/g. The three-point correction does not alter the position of the exothermic or endothermic peaks.

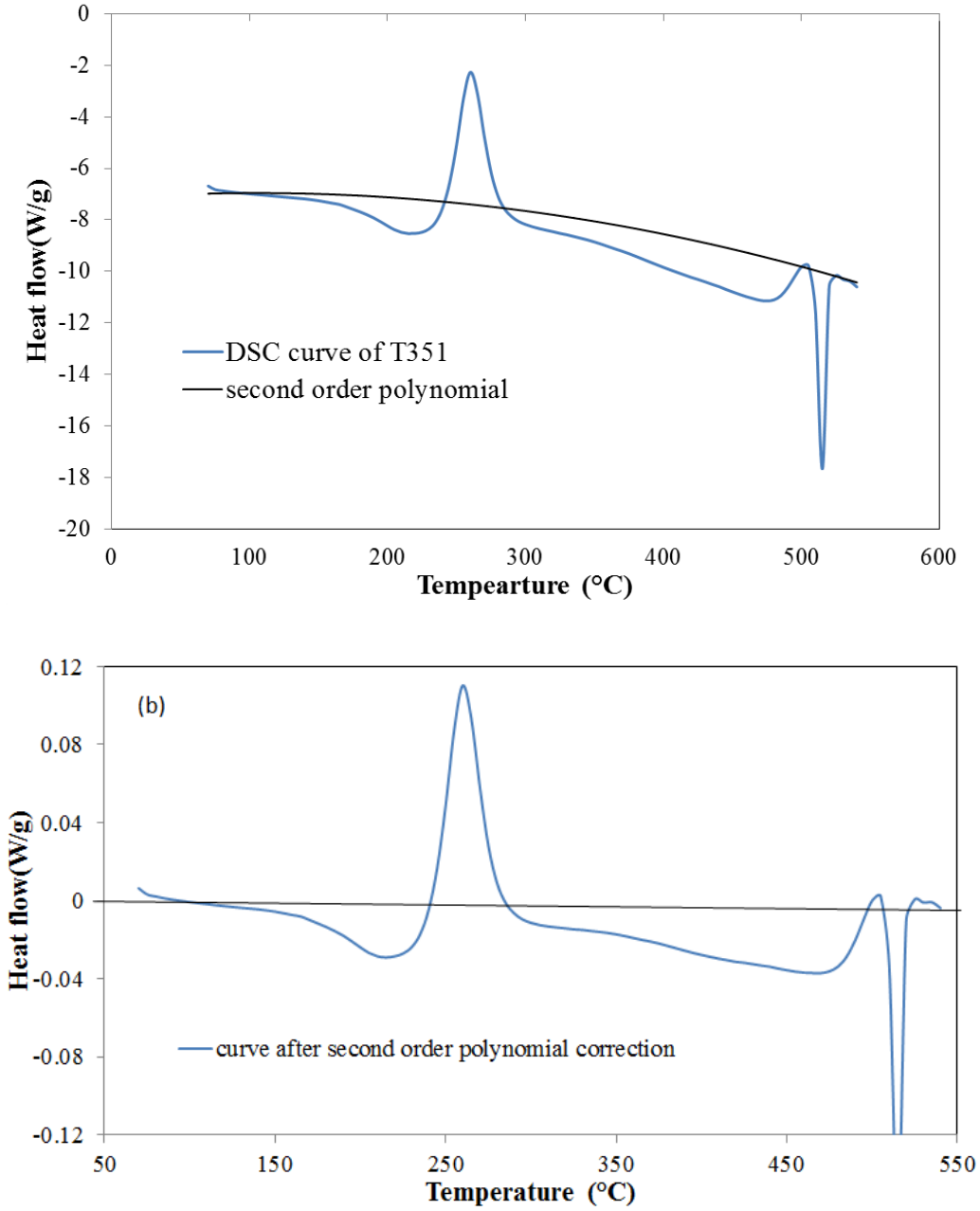

Fig. 3.3 A second order polynomial correction of DSC curve for 2024Al-T351 sample. (a) a curve after baseline subtraction (b) a curve after a second order polynomial correction.

3.5.2 Experimental accuracy

The accuracy of determination of DSC thermograms is influenced by environmental parameters (i.e. temperature, temperature fluctuations, humidity) as well as the characteristic factors of sample and the equipment (weight of sample, heating rate and heat capacity). Hence, in the present work, the experiments were performed at the same condition as those of the calibration runs. Nevertheless, an uncertainty of 1~2% in measured heat flows is common in DSC experiments [135]. The heat flow measured by DSC is influenced by heat capacity and kinetic components Eq. (3-3) [171].

$$\frac{dQ}{dt} = C_p \frac{dT}{dt} + f\left(T,t\right) \tag{3-3}$$

where C_p is determined by heat capacity and weight of sample and dT/dt is the heating rate.

To estimate accuracy in the present experiments, additional variations of baseline correction was performed to identify the heat flow difference (exothermic or endothermic effect) in the solid reaction in aluminium alloys (three point method, see Section 2.6.1). For example, the baselines of HPT deformed sample are very similar, see Fig. 3.4. The values of a and b in the baseline function Eq. (2-33), are very similar (Table 3-4). This indicates good reliability of the DSC data.

The small fluctuations of this second order polynomial baseline might lead to differences in exothermic or endothermic enthalpy measured by integrating the heat flow dQ/dt. One way to estimate this deviation is to approximate some other points around the standard three points where no reaction occurs. The mean value of stored energy and error bars are measured by repeating analysis on baseline correction. The results of stored energy determination and associated error bars are presented in Section 4.

Table 3-4 Calculation of baseline function of samples.

The number of rotations	1/4	1	5	16
a_{DSC}	-1.00E-05	-6.00E-06	-3.00E-06	-1.00E-05
b_{DSC}	0.003	0.0015	0.0007	0.0024
c_{DSC}	-4.34	-4.25	-4.25	-3.95

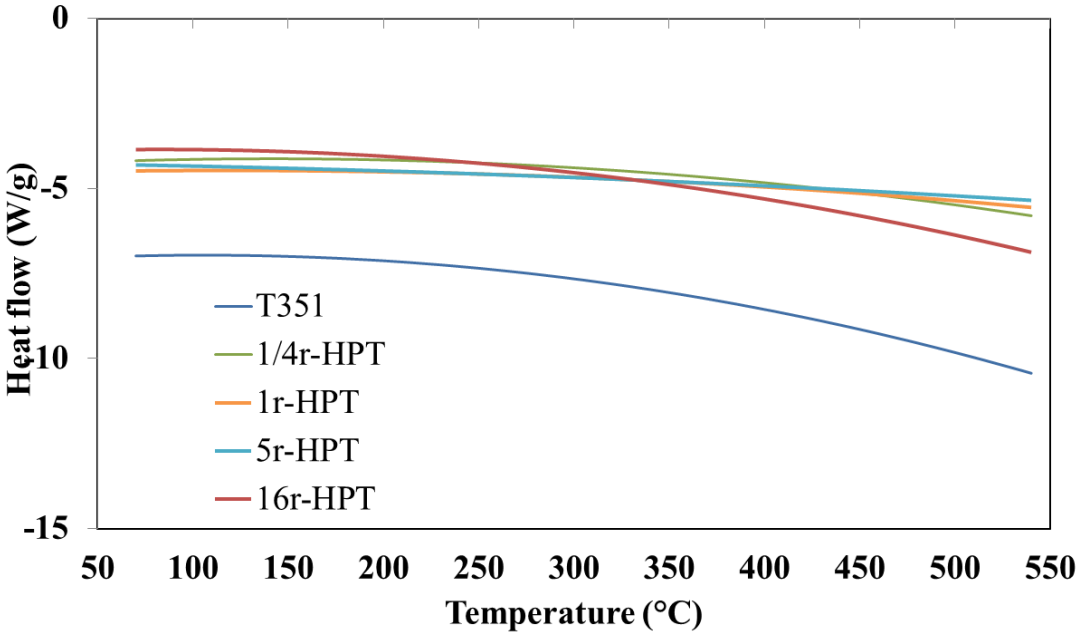

Fig. 3.4 Baseline of DSC traces via three point correction.

3.6 XRD

HPT processed samples were analysed by X-ray diffraction. Samples processed by different turns of HPT were measured using a Bruker D2 Phaser Diffractometer; while the HPT samples after isothermal heat treatments at different temperatures were examined using a Siemens D5000 X-ray Powder Diffractometer.

Samples must be in a form or size that can be inserted into or attached to the holder in XRD (<1 mm). Grinding and polishing were employed to get flat surfaces with a thickness of 0.7 mm. Samples were categorized into three groups: (1) the full disks, (2) the centre (blue areas, distance to centre $r < 2.5$ mm) and (3) the peripheral rings (green areas, 2.5 mm$< r < 5$ mm), see Fig. 3.5.

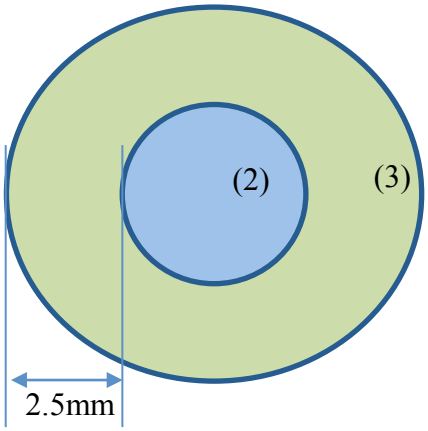

Fig. 3.5 XRD samples punched from HPT deformed discs.

To ensure good counting statistics throughout an X-ray powder diffraction pattern, the time per step should approximately compensate for the gradual decline in intensity with 2θ, because of the nature of the samples (i.e. scattering, pattern degrading, peak-broadening effects and the degree of peak overlap) [172, 173]. There should be at least 5 steps, but generally not more than ten) across the top of each peak, where step size =FWHM/5. FWHM presents the full width at half-maximum [173]. XRD were carried out on HPT-processed samples with 50 steps per degree and a count time of 1s per step

on the instruments equipped with a graphite monochromator using Cu Kα radiation. The slit lengths were both chosen 0.6 mm.

To reduce the errors and improve the accuracy, the data were collected by repeating runs. Experiments on HPT samples were performed 5 times to obtain one pattern. The data were saved as a format of raw or text, and analysed by DIFFRAC EVA software to identify the precipitates and peak shifts, corresponding to evolution of lattice parameters in SPD processing.

Profile broadening analysis due to grain refinements and dislocation densities were evaluated using Williamson-Hall [157] and Rietveld [159] methods. The principles of these methods were presented in Section 2.6.2.

The analysis of Rietveld full peak refinements were conducted in 'Materials Analysis using Diffraction' (MAUD) software. By optimizing calculating models step by step, the calculated curves were fixed to match experimental data. The optimizing conditions involve background and scale, basic phase, microstructure, crystal structure, texture and strain parameters. In MAUD, the conditions of source of radiation were set as α_1=1.5406 μm, α_2=1.54439 μm, weight ratio=0.5, while goniometer radius was set as 200.5 μm for D5000 X-ray Powder Diffractometer and 141 μm for Bruker D2 Phaser.

3.7 TEM

Transmission electron microscopy was performed on HPT processed samples using a JEOL 3100 TEM operated at 300 kV. The microstructural evolution due to different rotation strains was investigated by TEM on the periphery of ¼r-HPT, 1r-HPT and 5r-HPT. The coarsening of ultrafine grain in 5r-HPT samples was investigated after heating up to 210 °C and 300 °C and isothermal ageing for 109 s and 153 s, respectively (see Section 3.3.2), which are denoted as 5r-HPT-210 °C and 5r-HPT-300 °C.

Disks of 0.7 mm in thickness were mechanically ground with 800$^{\#}$SiC paper to 0.2 mm, further ground down to ~150 μm using finer grid papers (i.e. 1200$^{\#}$SiC and 4000$^{\#}$SiC). Circular samples of 3 mm in diameter were punched out at a position about 4 mm from

the centre of a disk (we term this peripheral areas, see Fig. 3.6). (Both sides of the sample surface were carefully ground, and circular samples for TEM examination were punched from this the central region (in the thickness direction) of the sample. Thus although microstructural inhomogeneity is presented in the thickness direction as all samples were examined at the same location in the thickness direction this can be ignored.) Subsequently, the samples were thinned to perforation using twin-jet electropolishing at -30 °C with an electrolyte solution of HNO_3: methanol=1:3 (in volume).

For each HPT condition, more than 20 bright field (BF) images from different locations were analysed to count as many grains as possible to provide good statistical significance. The grain size was measured using the modified line intercept method described in [117]. For TEM micrographs, intercept lengths were determined on random lines. In the measurement, only the grains with clear boundaries were taken into account (around 5-7 grains in one TEM figure). The grain size d was taken as d=1.455 $\bar{L}$, where $\bar{L}$ is the average line intercept, as the distribution of grain shapes is likely to resemble a Poisson-Voronoi distribution [174]. Selected area diffraction (SAD) patterns were taken with an aperture of ~1 μm^2. Ring pattern consisting of many dispersed spots were presented for UFG materials.

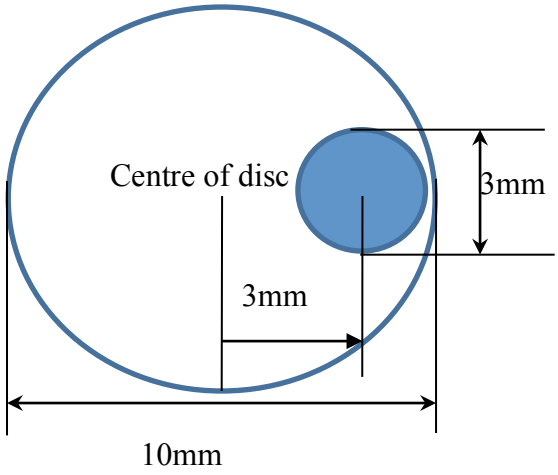

Fig. 3.6 TEM sample (blue) punched from the HPT processed disc.

3.8 APT

Atom probe tomography was carried out on samples processed by 1/4r-HPT, 5r-HPT, and HPT samples isothermal heat treated at 210 °C and 300 °C. Atom probe specimens in the form of sharp needles with an end radius of less than 100 nm were prepared from blanks with dimensions of $0.5 \times 0.5 \times 10\ mm^3$ using a standard two-stage electro polishing technique. The first stage used a solution of 25% perchloric acid in acetic acid at 15 V, whereas the second stage used an electrolyte of 5% perchloric acid in 2-butoxyethanol at 20 V.

APT analysis was carried out under an ultrahigh vacuum ($\sim 1 \times 10^{-8}$ Pa), UV laser pulsing energy of 40 pJ at the pulse repetition rate of 200 kHz and a specimen temperature of ~20-25 K using a local electrode atom probe (LEAP4000X SI®). In comparison with voltage pulsing at pulse fraction (ratio of the pulse voltage to direct current standing voltage) of ~20% [175], laser pulsing analysis improved analysis success rate. Reconstruction and visualization of atom probe tomography (APT) data was performed using the Imago Visualization and Analysis Software (IVAS^{TM} 3.6.2). The maximum separation algorithm was employed for cluster identification, with Mg, Si and Cu as clustering solutes and a separation distance of 0.5 nm [176, 177]. A minimum cluster size of $n = 2$ was employed to detect all extremely small solute clusters [177].

Chapter 4 Calorimetric studies on precipitation acceleration

This chapter presents calorimetric studies on solution treated, T351 and HPT deformed samples. In Section 4.1, the precipitation responses of the Al-Cu-Mg alloy are studied using DSC. Section 4.2 presents a calculation on stored energy due to SPD. Finally, in Section 4.3, a model is established to describe SPD processing accelerates S precipitation.

4.1 Results

4.1.1 Low strain Al-Cu-Mg alloy

Strain in an as-obtained T351 sample has been reported to be 2%~3% stretching [31]. The Hencky strain formula presented the relationship between equivalent strain and engineering strain:

$$\varepsilon = e - \frac{e^2}{2} + \frac{e^3}{3} \tag{4-1}$$

where the engineering strain e expressed as the ratio of total dimension l_H to the initial dimension L_H of the sample body:

$$e = \frac{l_H - L_H}{L_H} \tag{4-2}$$

As a result, equivalent strain of a sample processed by compression without any rotations in HPT instrument is calculated as 0.01. Samples with strain levels below ~0.1 will be referred to as the samples possessing a small deformation strain. (Strains are small in the context of SPD.)

In Fig. 4.1 (a), DSC thermograms of the Al-Cu-Mg alloy with small strains are shown, including solution-treated (i.e. strain free) samples, T351 samples, and compressed samples. Three main heat effects, marked A, B and C, (observed in the solution treated and T351 samples) are thought to be due to co-cluster dissolution, S phase precipitation and S phase dissolution, respectively [41]. The endothermic effect starting at about 500 °C and ending at about 520 °C is due to incipient melting of intermetallic phases in the 2024 Al alloy [10, 41, 65].

In Fig. 4.1 (b), the endothermic peak A shifts from 225 °C to a lower temperature, 210 °C, as samples were stretched (T351) or compressed. The endothermic areas A of a solution treated (ST) with 1-day aged sample or a solution treated with 7-day aged samples are lower and broader than those for other samples with low strains (i.e. T351, ST + compressed and T351+ compressed). The 7-day aged sample shows a lowest value in heat flow, indicating a larger heat effect corresponding to the dissolution of co-clusters or GPB zones [41, 65].

In Fig. 4.1 (c), a similar peak shift is observed for the exothermic peak B. The exothermic peaks of ST samples are located at 270 °C. The exothermic peak shifts to 260 °C for the T351 sample (stretched 2-3%), and to 255 °C for the ST-compressed or the T351-compressed sample. The heat flow of the T351 sample is ~0.02 W/g higher than the heat flow of the ST sample. This is consistent with other observations [11, 41]. In an Al-0.6Cu-4.2Mg (wt.%) alloy [11] and an Al-4.2Cu-1.5Mg-0.6Mn-0.08Si (AA2324) (wt.%) alloy [41], a peak due to S precipitation also shifts to a lower temperature when samples were 2% and 5% cold deformed. This indicates an acceleration of S precipitation. The dislocations introduced by stretching and compressing can act as preferential nucleation sites to facilitate nucleation of S phase.

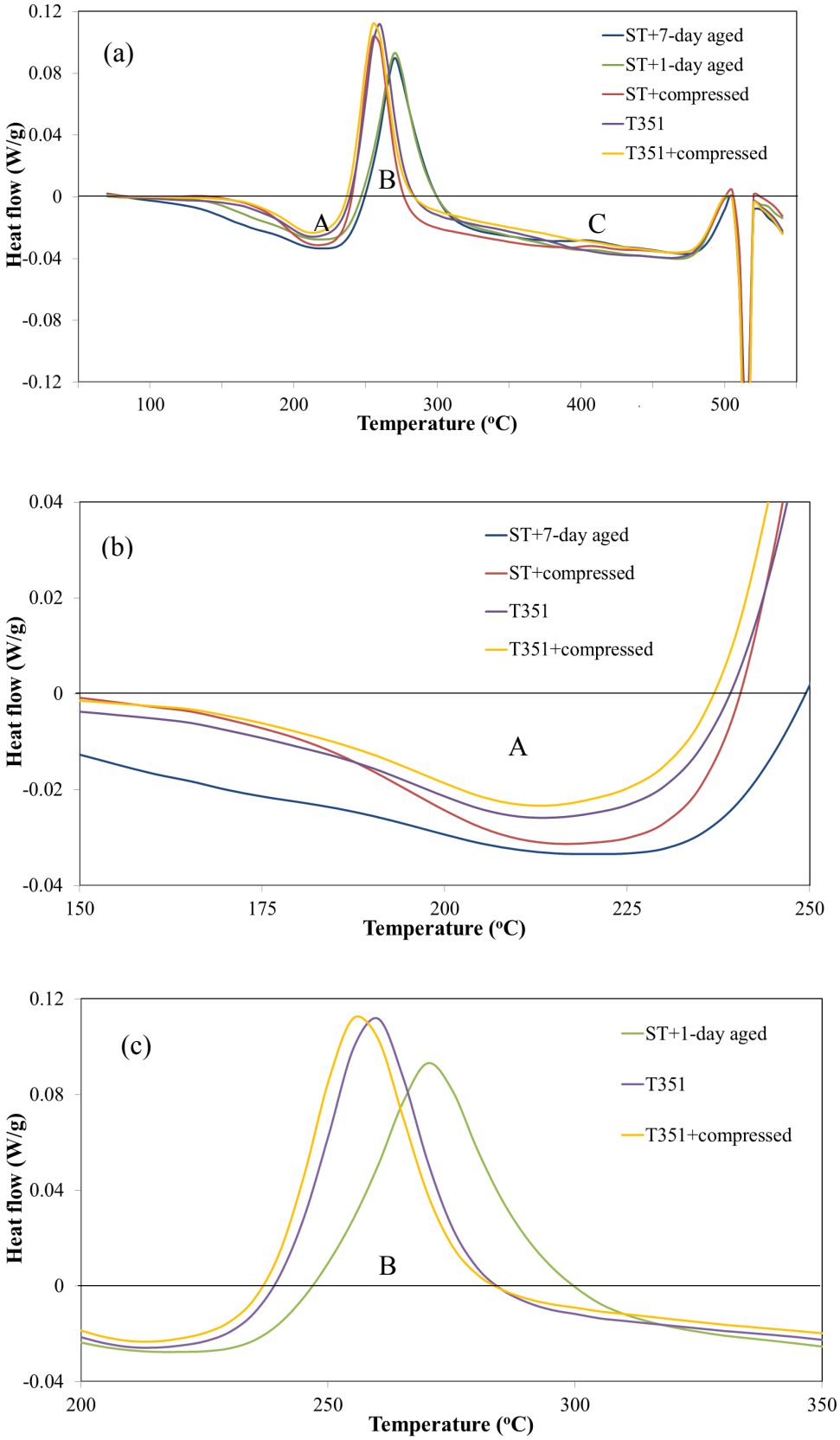

Fig. 4.1 (a) DSC thermograms (heating rate: 10 °C/min, from 50 °C to 540 °C) for T351, solution treated and 1-day/7-day aged samples, and compressed samples, (b) a comparison of endothermic peaks (c) a comparison of exothermic peaks.

4.1.2 Al-Cu-Mg alloy processed by monotonic HPT

The Al-Cu-Mg alloy was processed by monotonic HPT in clockwise direction at ambient temperature. For DSC experiments, samples were classified into two groups: central areas and peripheral areas (see Fig. 3.2). Table 4-1 illustrates the strain differences after HPT processes.

Table 4-1 The equivalent strain of samples after HPT processes (equivalent radius taken 1.25 mm for centre sample, and 3.75 mm for periphery sample).

Number of HPT rotations	**1/8**	**1/4**	**1**	**5**	**16**
Centre ε_{eq}	0.61	1.05	2.27	3.93	5.19
Periphery ε_{eq}	1.44	2.03	3.42	5.18	6.38

In Fig. 4.2, overlapping exothermic effects peaking at ~220 °C and ~240 °C starts to be observed in the DSC thermograph of a peripheral part of 1/4r-HPT sample (with an equivalent strain of 2), and were also observed in other HPT samples in Fig. 4.3 (a) and (b) with a larger strain (i.e. ε_{eq} >2). The effect peaking at 210 °C of 1/4r-HPT sample contributes only a small fraction of overall exothermic effects, while the peak at 240 °C contributes to the dominant effects.

However, for the HPT samples with equivalent strains lower than 2, only one single exothermic peak appears at 245 °C, shown in Fig. 4.2 (for instance the DSC curves of an 1/8r-HPT or an 1/4r-HPT centre sample). The single exothermic peak of the 1/8r-HPT peripheral sample (i.e. peaking at 240 °C) is 5 °C lower.

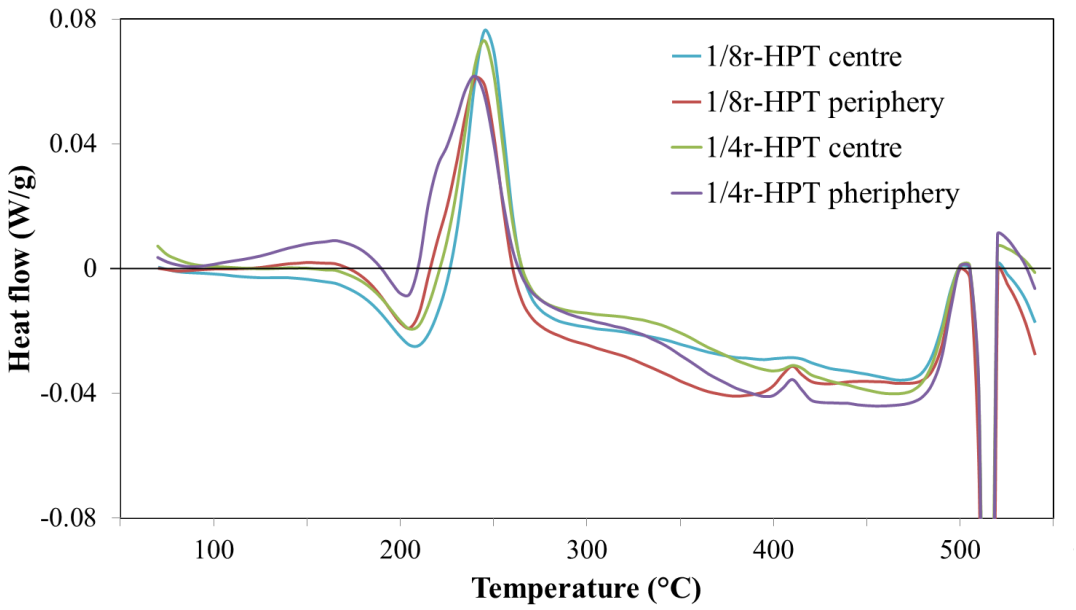

Fig. 4.2 Samples processed by small-rotation HPT (rotation number N<1).

DSC thermographs of samples processed by HPT for different rotations are shown in Fig. 4.3 (a) and 4.3 (b) for centre parts and edge parts of samples, respectively.

In Fig. 4.3 (a) and (b), endothermic effects (from 70 °C to 200 °C) prior to the exothermic regions (from 200 °C to 260 °C) are observed in samples with stain smaller than 2 (i.e. ST, T351, compression, 1/8r-HPT and 1/4r-HPT samples). In the samples processed by 1, 5 and 16r HPT, no endothermic effects are found at the same temperature. But instead, an exothermic peak appears prior to 200 °C, peaking at 170 °C, while a decrease in heat flow is observed at 200 °C in these samples.

Compared to the as-obtained T351 sample (non-HPT), the exothermic peak temperatures decrease to 210 °C for samples HPT processed up to 16 rotations. In region II, an overlapping of exothermic effects peaking at 210 °C and 240 °C appears in HPT processed samples with the rotation number larger than 1.

In Fig. 4.3 (a), there seems to be nearly no difference between the thermal effects of central areas in samples processed by 5 or 16 rotations in the region from 200 °C to 260 °C. But heat flows of both 5r- and 16r-HPT samples peaking at 210 °C are 0.01 W/g higher than peak heat flow of 1r-HPT sample.

In Fig. 4.3 (b), the peak heat flow at 210 °C for the peripheral areas of 1r-HPT, 5r-HPT, and 16r-HPT samples are 0.074 W/g, 0.092 W/g and 0.112 W/g. It presents an increasing trend with the increase of the rotation number. However, the heat flows of peaks at ~240 °C decrease with the increase of rotation number. The heat flow value is 0.031 W/g for the 16r-HPT sample, 0.055 W/g for the 1r-HPT sample, ~0.06 W/g for the 1/4r-HPT sample and ~0.06 W/g for the 1/8r-HPT sample. The identification of effects in this region will be presented in Section 4.2.

The exothermic effect between 200 and 300 °C is thought to be mainly due to the formation of S phase precipitates [41, 180]. Previous TEM studies by Wang et al. [41, 180] on Al-Cu-Mg based alloy (such as Al-2024 alloy or Al-2324 alloy) identified two types of S phase precipitates. The single peak in DSC thermograms for the T351 and the sample processed by water quenching and cold work (WQ+CW) can be thought to involve two overlapping reactions [41]. The two types of S precipitates in Al-Cu-Mg alloys were also confirmed by other investigators [42-44] with orientation of the two types rotated by 4~7° to the classic one. Type I and Type II S phase are essentially the same phase. Type I phase is semi-coherent with the Al matrix and can be easier accommodated with the strains at the interfaces with the matrix. In a WQ sample, the Cu and Mg remaining in solution will precipitate to form the Type II S phase, when the precipitation of Type I is not completed. It leads to two overlapping exothermic peaks appear between 200 °C and 300 °C in DSC thermograms [41, 180]. DSC exothermic peak of Type II S precipitates may not appear in these deformed samples subjected to small strains, such as T351 sample, solution treated sample, compressed sample and sample processed by 1/8r HPT. The absence of the second exothermic peak does not mean the absence of Type II S phases. In fact, the co-existence of two types of S phases in aluminium matrix was observed in some recent work [44].

Two exothermic peaks were observed in Fig. 4.3 (a) and (b) between 200 °C and 300 °C in samples processed by higher torsional deformation, the equivalent strain of which is larger than 200%. On increasing deformation, the DSC peaks shift to lower temperatures. These two peaks cannot be simply ascribed to the thermal effects of the two types of S precipitates. Even though Type I and Type II S phase co-exist in Al matrix in HPT samples, the transformation from Type I to Type II S phase is unlikely to cause a second exothermic peak. (Strain energy and interfacial energy are too small to cause a detectable second effect [180].) In reality, XRD pattern (Fig. 6.3) in Section

6.1.2 reveals the S precipitates appear in the 5r-HPT-240°C sample and 5r-HPT-300°C, but do not appear in the 5r-HPT-210°C sample. The XRD profile broadening analysis indicates a significant decrease of dislocation density can be correlated with the exothermic peaks at 210°C.

In fact, similar two exothermic peaks of DSC were also observed in other heat treatable SPD processed Al alloys. For example, DSC thermograms for an ECAP processed 7075 Al alloy [99] showed two peaks in the exothermic region (140~230 °C), which was due to the formation of the intermediate metastable phase η' and equilibrium phase η. At the first exothermic peak (140 °C), the hardness and dislocation density decreased significantly, while the grain size increased substantially. No direct evidence shows that the peak at 140 °C is due to the structural evolution, but the dislocations and strains in UFG samples have a great influence on the energy released in DSC thermograms [99]. The structural evolutions of ultra-fine grain 2024 Al alloy in DSC heating process in present work are similar to 7075 Al alloy. One possible explanation for the appearance of overlapping peaks could be the annihilation of dislocations and growth of grain size (see also Section 6.1).

In region III shown both in Fig. 4.3 (a) and (b), the endothermic effect between 265 °C and 500 °C is thought to be primarily due to dissolution of S phase [9, 178]. The relatively small exothermic effect is due to recrystallization which may appear superimposed on the larger exothermic effect due to S phase dissolution. These small exothermic effects appear around 400 °C in HPT-deformed samples (especially in a 1/8r-HPT or 1/4r-HPT sample). Similar phenomena were observed in a cast 2024 aluminium alloy subjected to ECAP, showing the exothermic peaks around 380 °C [179]. Ref. [179] attributed this exothermic peak at ~400 °C to recrystallization.

In summary, enthalpy changes are correlated to the microstructural evolutions of HPT-processed Al-Cu-Mg alloys. In DSC heating, the dislocation recovery occurred from 100 °C. The dislocation-cluster complexes (described in Chapter 5) formed at room temperature, and dissolved into the Al matrix from 170 °C to 200 °C. At 210 °C, the number of dislocations reduced significantly, while the S phase started to precipitate. As a result, the crystallite size (scattering domains) increases dramatically (Section 6.1.2). For samples heated up to 260 °C, the S precipitates dissolved, and grain growth occurred.

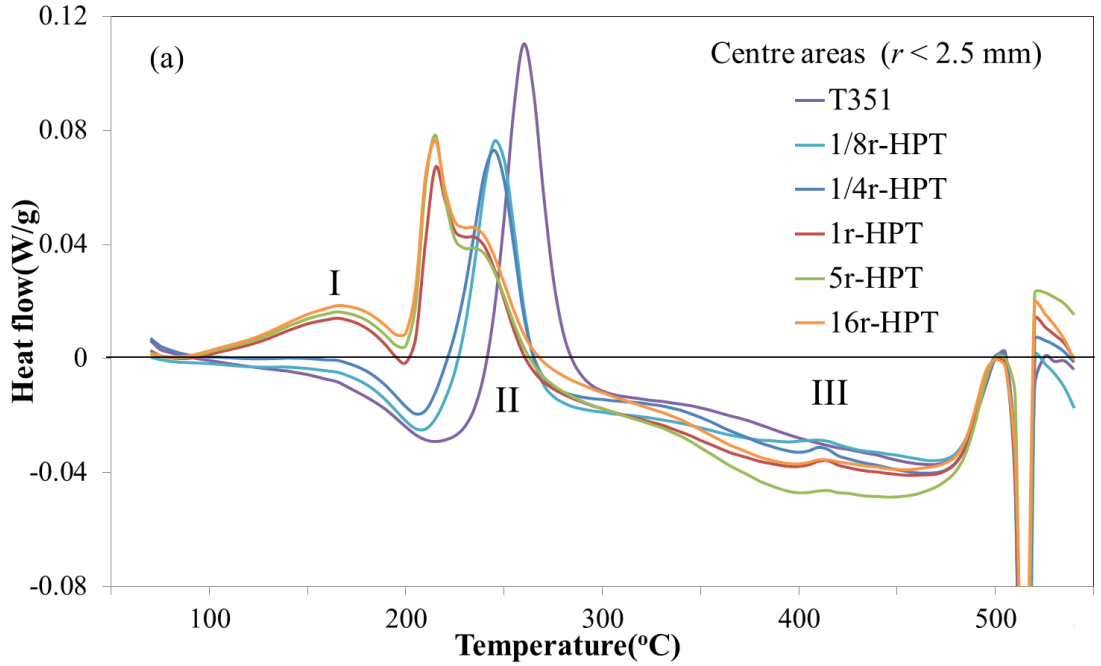

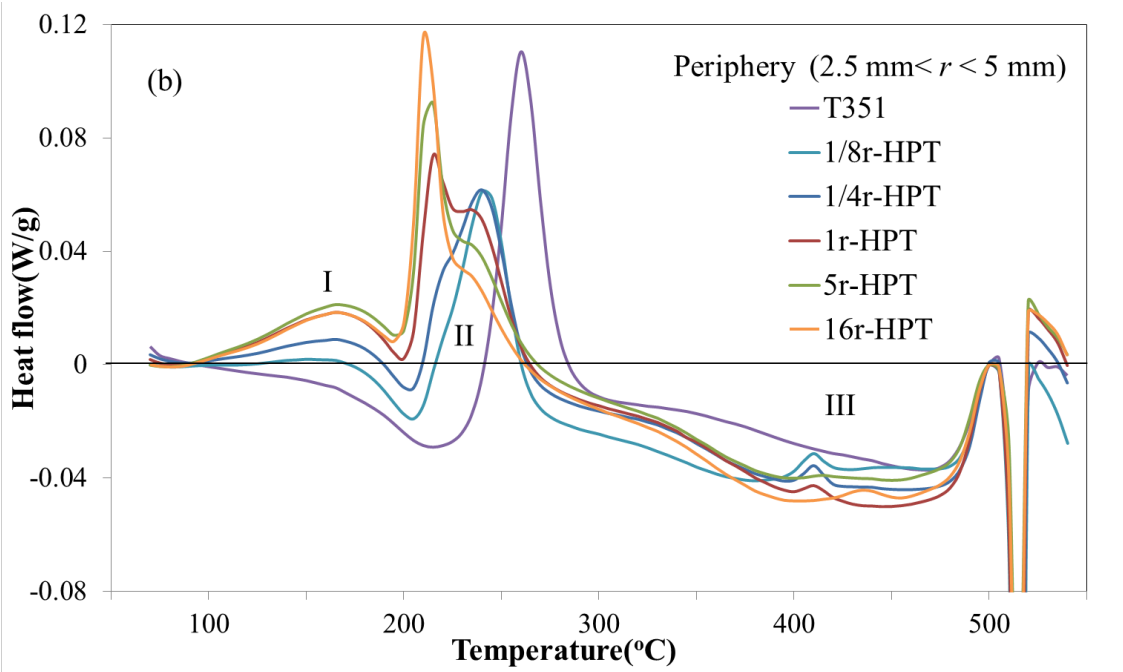

Fig. 4.3 DSC thermograms of samples after HPT processing for 1/8, 1/4, 1, 5 and 16 rotations (heat rate: 10 °C/min) (a) samples punched in central areas (r<2.5 mm); (b) samples punched in peripheral areas (2.5 mm <r < 5 mm).

4.2 A calculation of stored energy in DSC for HPT samples

Enthalpy due to the formation and dissolution of S phase in DSC is thought to be equal, because all S precipitates dissolve during the annealing process. As a result, the total enthalpy change during linear heating is associated with plastic deformation and co-cluster effects, with the assumption that the natural ageing does not generate much precipitation. Hence,

$$\Delta Q \cong \Delta H_d + \Delta H_{cl} \tag{4-3}$$

where ΔH_d is the energy stored in dislocations, and ΔH_{cl} is the enthalpy due to the clusters dissolution. Measurements of the total stored energy were performed by integrating the areas under DSC curves. The stored energy arises from all dislocations, the trapped solute atoms, and the formation of cluster-dislocation microstructures. The total evolved heat ΔQ (Table 4-2) is ascribed to the enthalpy from the reaction of dislocation annihilation and the reaction of clusters dissolution. (Missing data in the table are due to the fluctuation of baseline drift for some of the DSC experiments.)

Fig. 4.4 indicates that the evolved heat increases significantly as the number of rotations increases. The evolved heat then reaches its maximum value of around 14~16J/g after 5 rotations. Further plastic deformation through HPT (increasing number of rotations or choosing the position of DSC samples closer to the periphery) does not cause a further increase of evolved heat. This trend of evolved heat indicates the saturation of dislocations for the Al-Mg-Cu alloy subjected HPT is achieved after 5 revolutions. The relationship between stored energy and lattice defects (i.e. microstrain or dislocations, grain boundaries, solute/co-clusters segregation and interaction) introduced by HPT is modelled and discussed in Section 6.3.

Table 4-2 Energy change in DSC after HPT.

Condition	**Total energy (J/g)**
Annealing	-34.4 ±0.9
1/8r-HPT centre	-32.4±0.9
1/8r-HPT periphery	–
1/4r-HPT centre	-29.4±1.2
1/4r-HPT periphery	-27.9±1
1r-HPT centre	-23.4±0.7
1r-HPT periphery	-22.2±0.8
5r-HPT centre	-16.5±2
5r-HPT periphery	-14.3±2
16r-HPT centre	-14.2±0.5
16r-HPT periphery	-

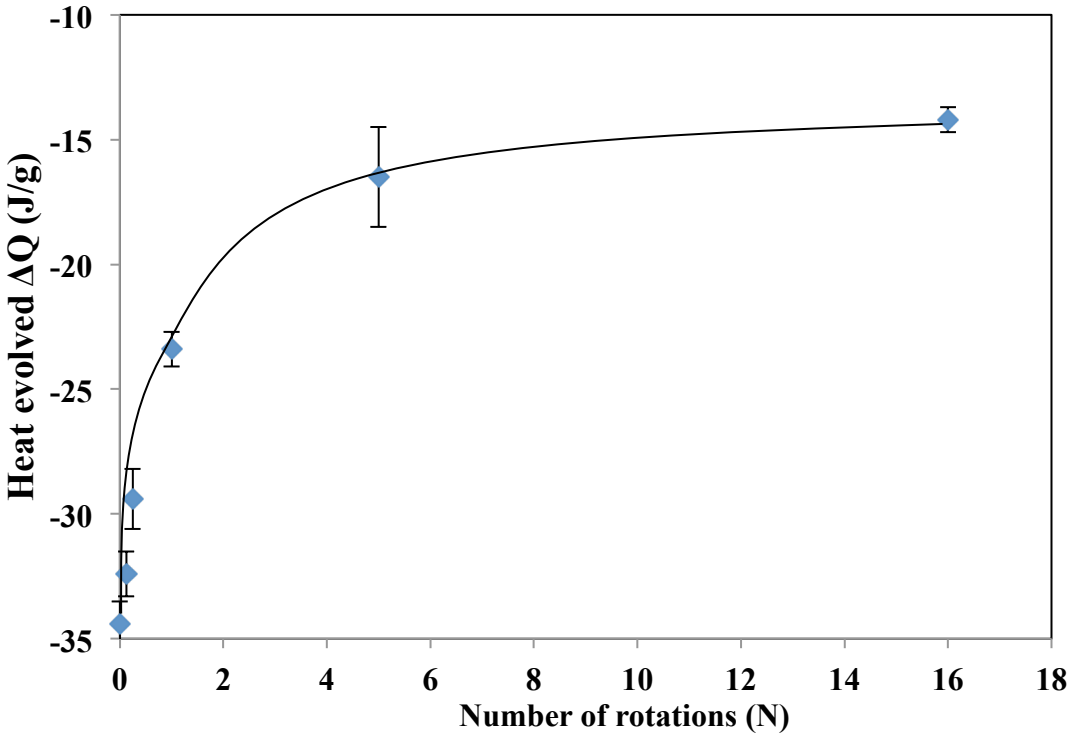

Fig. 4.4 Heat evolved from samples subjected to HPT of different turns.

4.3 A model predicting precipitation temperature for HPT samples

The DSC thermographs in Fig. 4.1 to Fig. 4.3 show that on increasing deformation, the peaks due to the formation of S phase shift to lower temperatures. This is thought due to the dislocations introduced by cold plastic deformation acting as nucleation sites for S precipitates, which accelerate the precipitation rate ([11] and see also Section 4.1). In this section a simple model for this shift is derived and tested.

Solid state reactions (i.e. precipitation and homogenisation) are considered to be diffusion controlled reactions. The typical diffusion distance of solute atoms s in an SPD sample is here simply assumed to be the typical distance between dislocations, which is given by [180, 181]

$$s = \frac{1}{\sqrt{\rho}} \tag{4-4}$$

The diffusion distance is generally given by [134, 145]

$$s = \sqrt{Dt} \tag{4-5}$$

where D is the diffusion coefficient which is given by Arrhenius term:

$$D = D_0 \exp\left(-\frac{E_D}{RT}\right) \tag{4-6}$$

where D_0 is the pre-exponential diffusion coefficient, E_D is the activation energy of diffusion, R, the gas constant .

The dislocation density stored in grains can be obtained from Kocks, Mecking and Estrin (KME) model [112-114] (see also Section 2.4.1), and is given by

$$\frac{\mathrm{d}\rho_{ig}}{\mathrm{d}\varepsilon} = (bl)^{-1} - k_2\rho_{ig} \tag{4-7}$$

where ρ_{ig} is the volume averaged dislocation density in the grains, ε is the strain, b is the Burgers vector, l is a constant associated with dislocation movement, k_2, a constant.

The first term in Eq. (4-7) is associated with the athermal storage of dislocations due to moving dislocations blocked by obstacles, whilst the second (decreasing) term is ascribed to the dislocation annihilation. Hence, the volume-averaged stored dislocation density is given by integrating Eq. (4-7) [118],

$$\rho = (blk_2)^{-1} - \left((blk_2)^{-1} - \rho_0\right)e^{-k_2\varepsilon} \tag{4-8}$$

The dislocation saturation has been considered in the calculation of the equivalent strain in Eq. (2-6).

By combining Eqs. (4-4) to (4-6), the relationship between peak temperature of S phase precipitation T and the equivalent strain ε introduced by cold work is then established as

$$\rho = \frac{1}{D_0 t}\exp\left(\frac{E_D}{RT}\right) = \left(blk_2\right)^{-1} - \left(\left(blk_2\right)^{-1} - \rho_0\right)e^{-k_2\varepsilon} \tag{4-9}$$

where t is the diffusion time of precipitation during linear heating, which is measured as equivalent time of isothermal ageing and is given by Eq. (2-30) (see also Section 2.5.1.2).

$$t_{eq} = \int_{t=0}^{t_e} \exp(-\frac{E}{RT(t)})dt[\exp(-\frac{E}{RT_{iso}})]$$

The model is used to predict the peak temperature of S phase formation T (°C) on increasing strain ε in the HPT processed Al-Cu-Mg alloy. The diffusion coefficient D_0 and the activation energy E_D were obtained from data fitting. The initial dislocation density ρ_0 has very little influence on the predictions, and is taken as 10^{13} m^{-2}, which is a typical value for annealed Al [118, 157, 182] and is also close to the value obtained from XRD annalysis of an annealed Al-2024 alloy in present work (see Section 5.1.2). In Table 4-3, the dislocation density after HPT for Al-2024 in the present work is close to that of Al-1050 in Ref [182]. Hence, the constant associated with dislocation movement is taken from work on SPD Al-1050 alloy as 5 [118], and the constant k_2 is given as 1.86 [118].

Table 4-3 Parameter values used in model.

Parameters	Value	units	Refs
D_0	$3 \cdot 10^{-4}$	m^2/s	This work by fitting
E_D	127	kJ/mol	This work by fitting
R	8.314	J/(K·mol)	[134]
b	0.286	nm	A constant for Al alloys
l	≈5	μm	4.5 for Al-1200, 5.6 for Al-1050 [118]
k_2	1.86		Fitting in [118]
ρ_0	$\approx 1 \cdot 10^{13}$	m^{-2}	[118, 157, 182] and this work
t	Equivalent time of isothermal ageing		
T	Measured in this work from the experimental peak temperature		

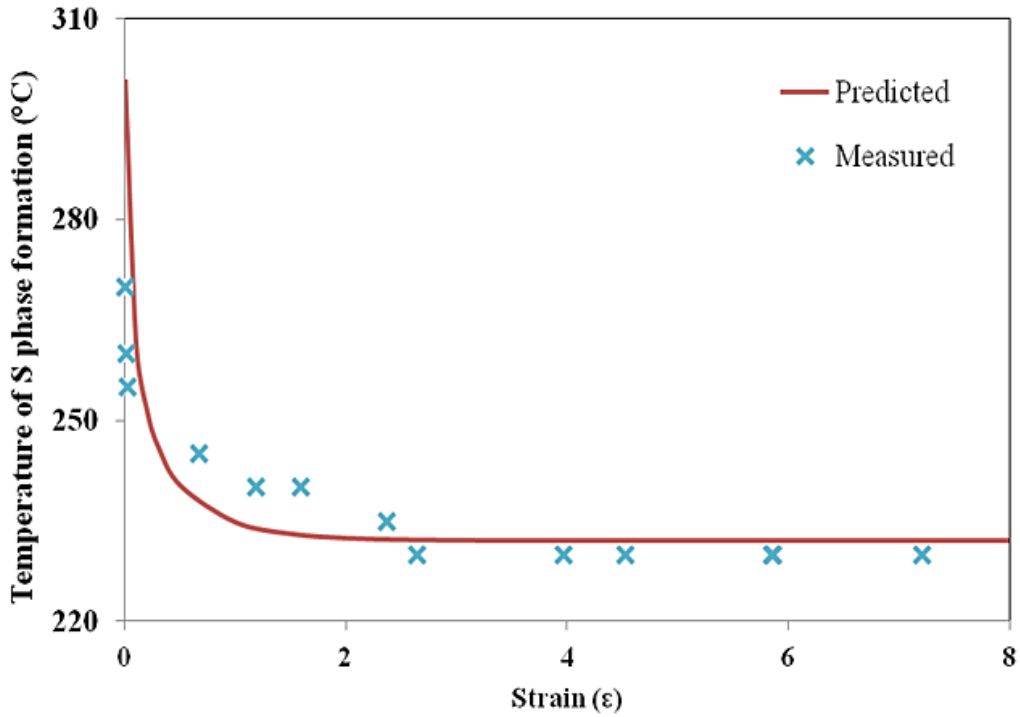

Fig. 4.5 Predicted and measured peak temperatures due to S phase formation as a function of equivalent strain in SPD Al-2024.

Fig. 4.5 shows that the peak temperature of S phase predicted by present model is generally in line with measured data on Al-2024, and the model broadly captures the correct trend on increasing strain. The predicted peak temperature fits the measured temperature to 240 °C (the 2nd peak in the overlapping exothermic region between 200 and 260 °C in Fig. 4.3(a) and (b)) with a higher torsional deformation (>200%, i.e. 1r-HPT, 5r-HPT and 16r-HPT). The fitted activation energy (127 kJ/mole) and the diffusion coefficient D_0 ($3 \cdot 10^{-4}$ m^2/s) are close to that in literature (Table 4-4) [170].

Table 4-4 A tabulation of diffusion data [170].

Diffusing Species	Host Metal	D_0 (m^2/s)	Activation Energy Q_d	
			kJ/mol	eV/atom
Al	Al	2.3×10^{-4}	144	1.49
Cu	Al	6.5×10^{-5}	136	1.41
Mg	Al	1.2×10^{-4}	131	1.35

4.4 Summary

Calorimetric studies on HPT-processed samples show overlapping exothermic peaks in the range of 200 °C to 260 °C, indicating two dominant thermal effects (i.e. S precipitation and microstructural recrystallization) during DSC heating. The calculation on enthalpy change during DSC heating illustrates an increasing trend of stored energy with an increase in rotation number.

The exothermic peaks shift to a lower temperature, indicating SPD accelerates S precipitation. A model from solute diffusion and dislocation generation/annihilation function fits the measured peak temperatures in DSC thermograms with a good accuracy.

However, the calorimetric study is an indirectly technique, the microstructural evolutions were characterized by other techniques, i.e. XRD, TEM and APT, which are presented in Chapter 5 and Chapter 6.

Chapter 5 Microstructural evolution and strength of an UFG Al-Cu-Mg alloy processed by HPT

In this Chapter, the microstructural evolution of the UFG Al-Cu-Mg alloy processed by HPT was measured by Vickers hardness, XRD and TEM. Solute segregation of HPT-processed samples at grain boundaries and dislocations was observed using APM. In Section 5.2, various strengthening mechanisms are considered to predict the ultra-high strength after HPT processing.

5.1 Results

5.1.1 Vickers hardness of samples processed by HPT for various rotations

Vickers hardness was measured on 6 lines across the disc centre. Each average value was taken at the positions with the same distance to the centre. Fig. 5.1 shows the distribution of the Vickers microhardness of T351 and HPT-deformed samples against distance from the centre of discs.

Strain is inhomogeneous and the equivalent (von Mises) strain increases with the distance to the centre, reaching the maximum value at the edge regions. The hardness of HPT-processed samples is higher than that of as-obtained T351 sample. The hardness of HPT-processed samples increases with distance from the centre of disk as well as the increasing numbers of rotations. 1/8r-HPT and 1/4r-HPT show a similar distribution of Vickers hardness, which is about 166 HV in the centre and 200~206 HV in the peripheral areas. The hardness of HPT discs in the peripheral regions is reasonably similar after 1, 3, 5 and 16 rotations, tending towards a saturation value of 260 HV. In

centre areas (where the distance to the centre< 2 mm), the hardness increases gradually with the number of rotations.

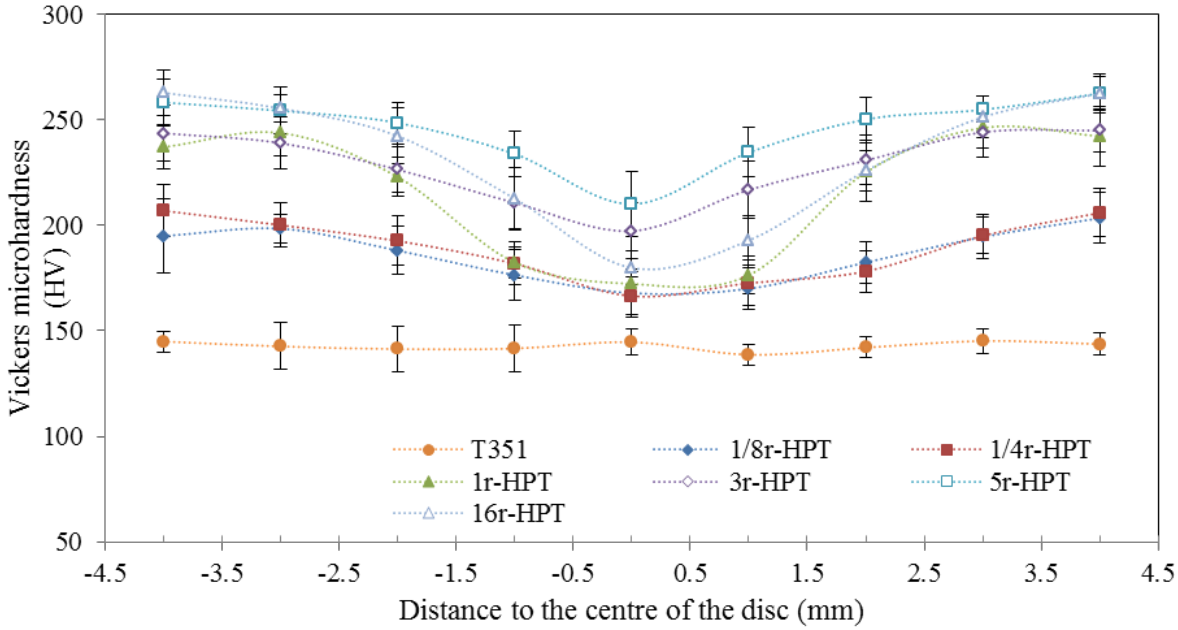

Fig. 5.1 Microhardness distribution versus distance to the centre of HPT discs at various rotations at ambient temperature.

5.1.2 X-ray diffraction analysis

Vickers hardness for HPT-processed samples in Fig. 5.1 indicates the inhomogeneous microstructure across the diameter of each disc after HPT. The patterns of full disks, central areas and edge areas were illustrated in Fig. 5.2 (a) to (c). The 5 main peaks are due to the Al planes (111), (200), (220), (311) and (222). Compared to the XRD profile of T351 sample, the profile broadening is observed in the patterns of samples processed by HPT. There is a baseline shift in lower angle (<35°) for HPT-processed samples in centre areas (see Fig. 5.2 (b)), which is probably due to small size of the samples.

It is known that small grain size and internal microstrains are the two main sources contributing to X-ray profile broadening [132], and the dislocation density ρ can be calculated from the lattice microstrain, $<\varepsilon^2>^{1/2}$ [99, 181] by:

$$\rho = \frac{2\sqrt{3}\left\langle \varepsilon^2 \right\rangle^{\frac{1}{2}}}{D_c b} \tag{5-1}$$

where D_c is the average crystallite size (related to coherently scattering domains, i.e. the mean size of dislocation free domains [182]); the dislocation density ρ should be regarded as an average value over the volume studied.

Two methods were developed to calculate the lattice defects in samples processed by a series of HPT rotations, including Williamson-Hall plots [157], and Rietveld full peak refinement [159].

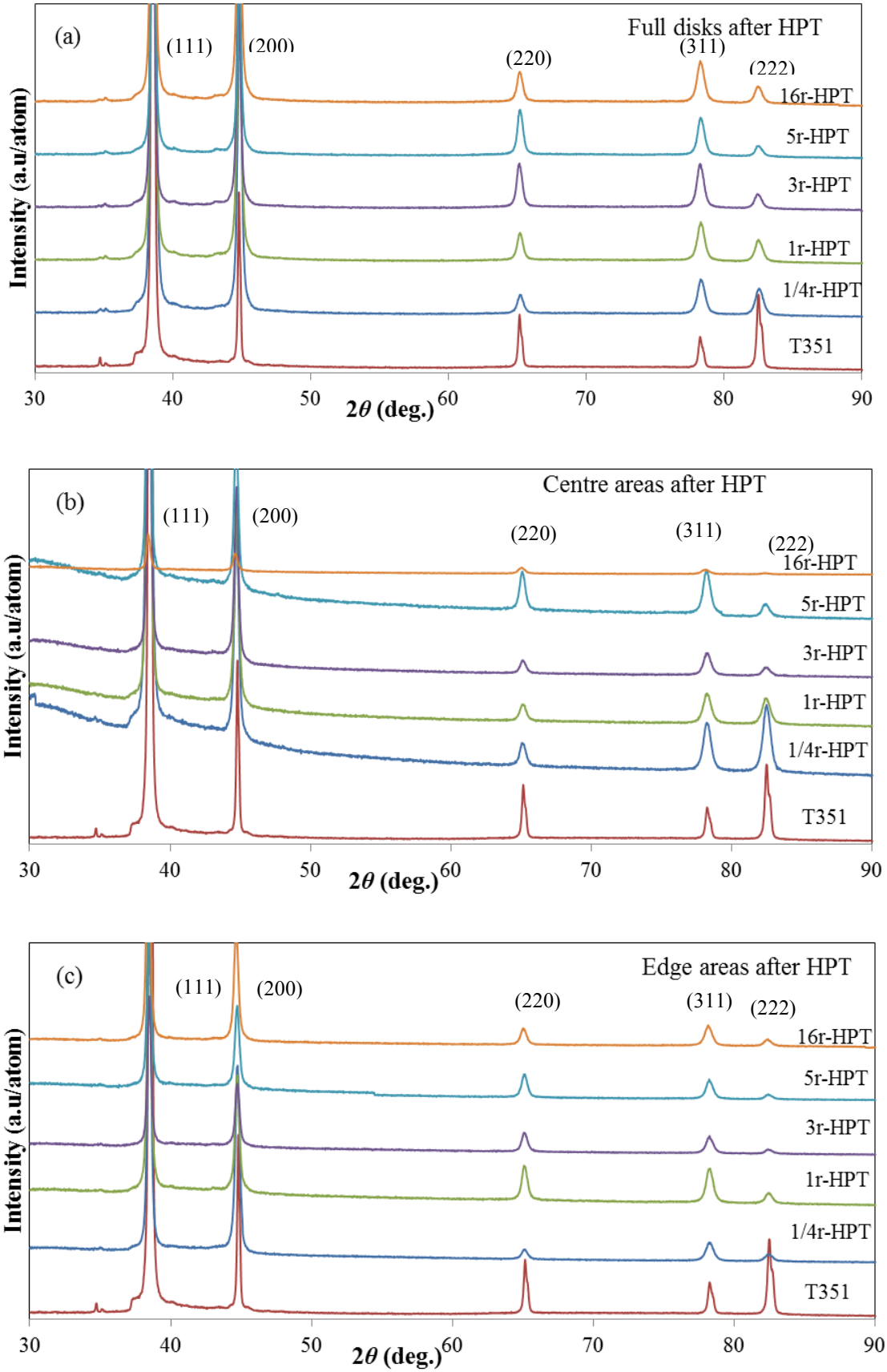

Fig. 5.2 The X-ray diffraction patterns of the alloy at T351 and that deformed by HPT for ¼, 1, 3, 5 and 16 rotations: (a) full disks; (b) centre areas; (c) edge areas.

5.1.2.1 Williamson-Hall method

On the assumption that both size and strain broadened profiles are Lorentzian components, the full width at half maximum (FWHM) of a XRD profile [157] can be expressed as Eq. (2-40), which is

$$\frac{B_{\text{int}}\cos\theta}{\lambda} = \frac{1}{D_C} + f(\varepsilon)\frac{\sin\theta}{\lambda}$$

where D_C is the crystallite size, $f(\varepsilon)$ is a defined function equals to 2ε [160-162].

In commercial diffractometers, the environmental broadening, such as slit width, wavelength width of the Cu resource $K\alpha_1$ and $K\alpha_2$, were extracted prior to strain or size broadening. B_{int} was obtained by subtracting instrumental broadening using Gaussian-Gaussian relationship [154] (Eq. (2-35) in Section 2.6.2.1), which is:

$$B_{\text{exp}}^2 = B_{\text{int}}^2 + B_{\text{ins}}^2$$

where B_{exp}, B_{int}, B_{ins} are the integral breadth of experimental profile, intrinsic profile, and instrumental profile, respectively [154].

Taken $K=\sin\theta/\lambda$, and $\Delta K=B_{\text{int}}\cos\theta/\lambda$, the Williamson-Hall plots of HPT-processed samples are illustrated in Fig. 5.3 (a) to Fig. 5.3 (c). The figures refer to the whole disks, central areas and edge areas, respectively. In HPT-deformed samples, an increase in the value of slopes indicates an increase in microstrains in Al matrix, while an increase in the value of intercept suggests a decrease of crystallite sizes. The dislocation densities calculated from Eq. (5-1) and crystallite size of an Al-Cu-Mg T351 alloy processed by HPT for different rotations are shown in Fig. 5.4 (a) to Fig. 5.4 (b).

In Fig. 5.4 (a), the average crystallite size of full disks decreases generally from ~500 nm at T351 to ~110 nm after 1/4r-HPT, further decreases to ~40 nm and stays at a

similar value as the number of rotations increases. Crystallite sizes of HPT samples in centre areas and edge areas present similar trends to the full disks. The only differences are shown in magnitude (see Fig. 5.4 (b) and Fig.5.4 (c)). The average crystallite sizes of HPT-processed samples are slightly larger in centre areas, which presents an approximated value ~50 nm for HPT-processed samples with rotation number larger than 1 (i.e. 3r-HPT, 5r-HPT or 16r-HPT). However, the average crystallite sizes of HPT samples are smaller in edge areas, ~30 nm.

The dislocation density increases significantly after the sample is subjected to HPT deformation for ¼ rotations (i.e. $\sim 1.0 \times 10^{14}\ m^{-2}$ for the full disks, $\sim 0.8 \times 10^{14}\ m^{-2}$ for centre areas). It is clear seen from Fig. 5.4 (a) that a further slight increase in dislocation density (up to $\sim 1.1 \times 10^{14}\ m^{-2}$) occurs as the sample subjected to 5 rotations HPT (5r-HPT) deformation. The dislocation densities for the edge areas of samples processed by 1r-HPT or higher rotations present relatively higher values, $\sim 1.2 \times 10^{14}\ m^{-2}$.

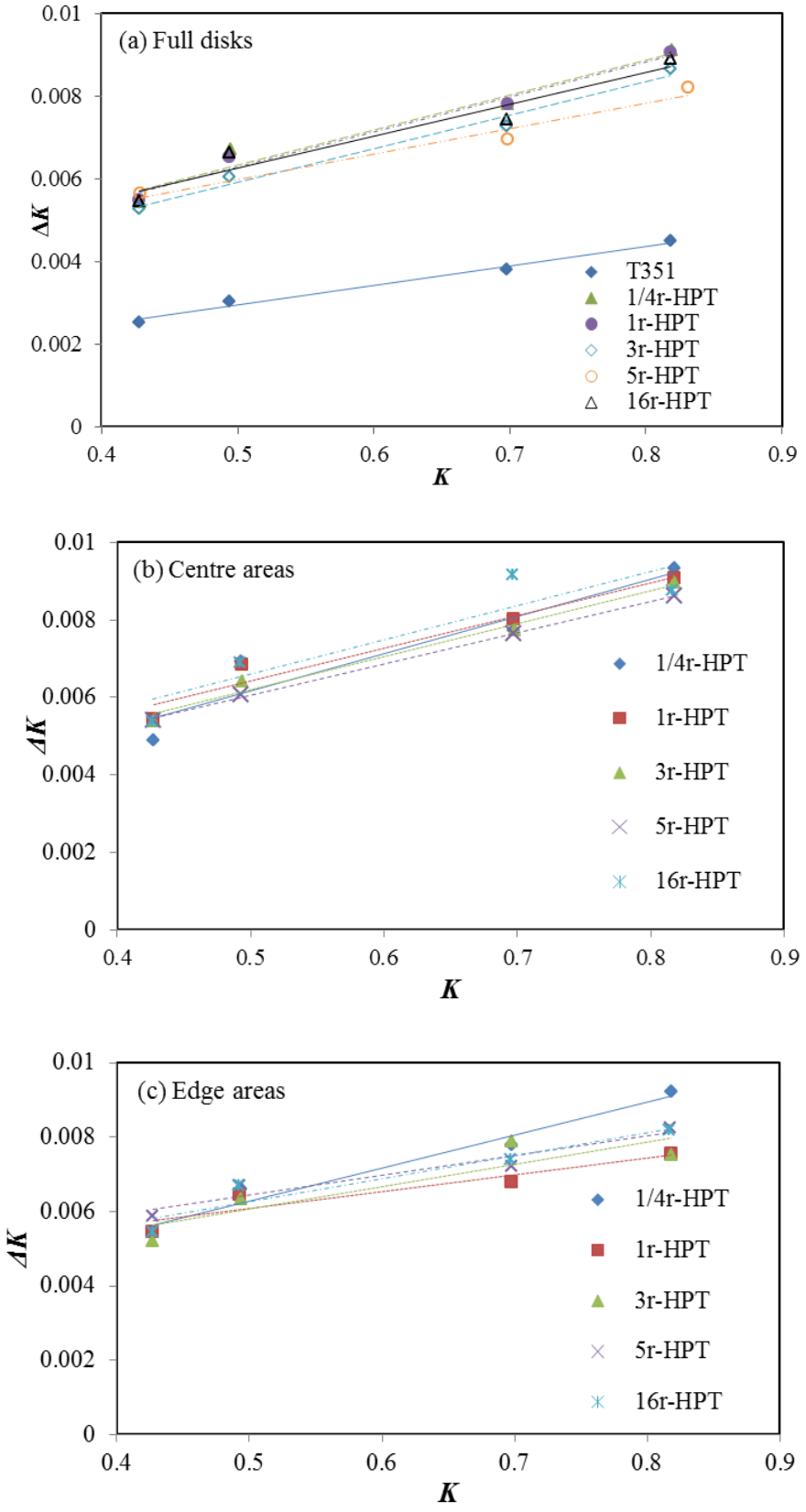

Fig. 5.3 Plots of different HPT-deformed Al-Cu-Mg samples for determination of the average crystallite size and microstrain via Williamson-Hall plots: (a) full disks; (b) centre areas; (c) edge areas.

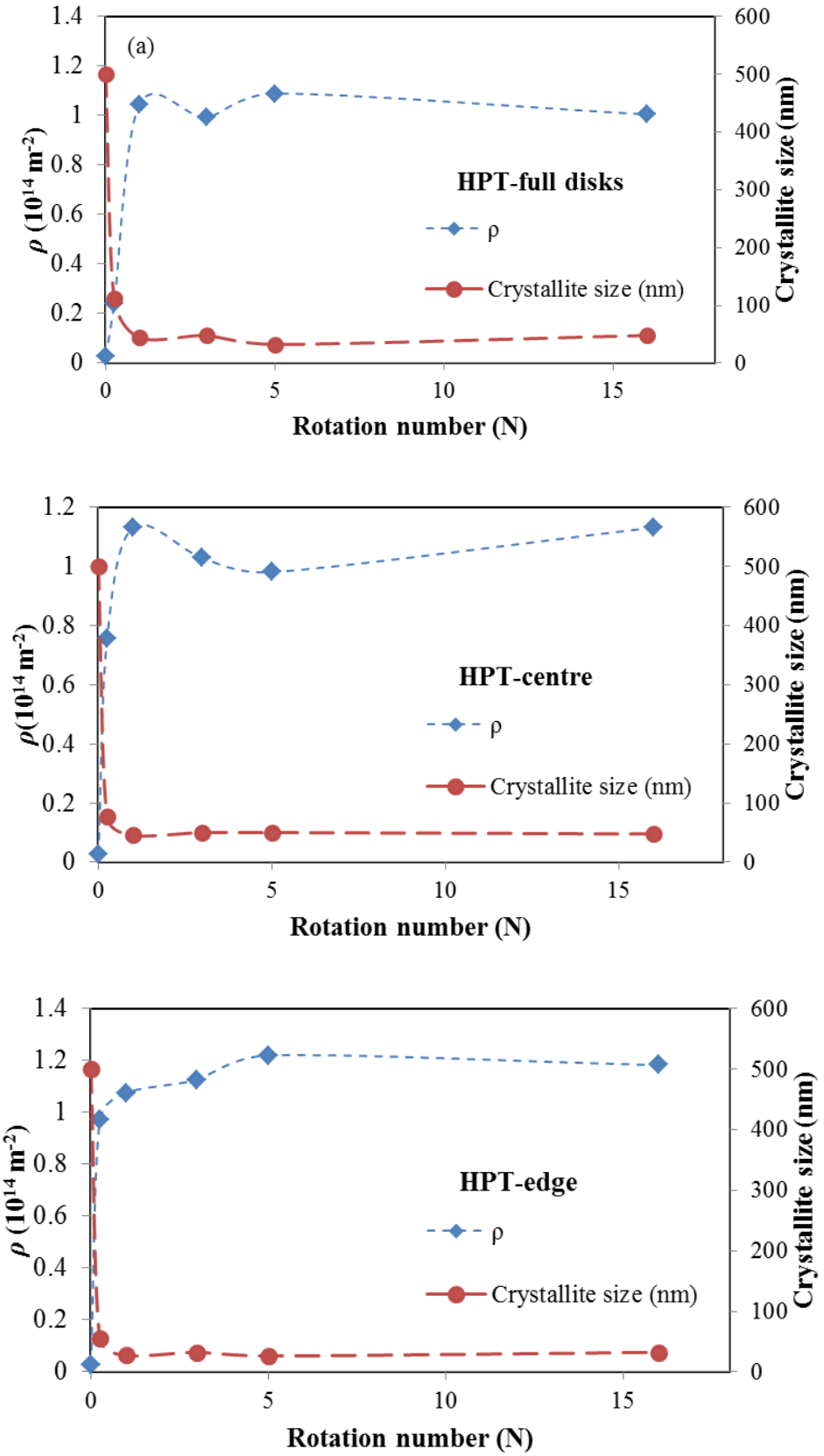

Fig. 5.4 The crystallite size (coherently scattering domains) and average dislocation density determined by Williamson-Hall produce plotted as a function of the number of HPT rotations: (a) full disks; (b) centre areas; (c) edge areas.

5.1.2.2 Rietveld method

Rietveld whole profile fitting was applied on XRD data of T351 and HPT-deformed samples by the pseudo-Voigt function [167]. The calculation was based on the crystallographic structure models, which also took into account the sample and instrumental broadening effects. The fitting to the measured XRD pattern is performed by a least-square calculation, which minimises the residual between calculated and measured data. this is programmed directly by using 'MAUD' [173].

When a good match of the peak positions has approached, the other profile parameters, *i.e.* peak width or peak asymmetry as a function of 2θ, will be refined. Taken the FWHM as a Gaussian component, the peak shape as a function of 2θ is modelled with the equation derived by Caglioti et al [183]. Instrumental parameters simulated from 'MAUD' are illustrated in Table 5-1. Examples of Rietveld full pattern fitting using 'MAUD' software are illustrated in Fig. 5.5 (a) 3r-HPT sample and (b) 5r-HPT sample.

The differences between central areas and edge areas are very small. In this section, the crystallite size and dislocation density from edge-area samples will be used in the strength predicting model (see Section 5.2). Fig. 5.6 shows the evolutions of dislocation density and crystallite size in the edge areas of the alloy subjected to different rotations. The dislocation density increases significantly up to 2.5×10^{14} m^{-2} after 1/4r-HPT processing and is about constant at 3.3×10^{14} m^{-2} when processed 1r-HPT or more. The crystallite size decreases to 60 nm for 1/4r-HPT and further decreases to ~50 nm for higher rotations. Compared to the dislocation densities in Fig. 5.4 (c), the dislocation densities calculated from Rietveld refinement are higher than those from Williamson-Hall method, and the crystallite sizes in Rietvled method are larger in HPT deformed samples.

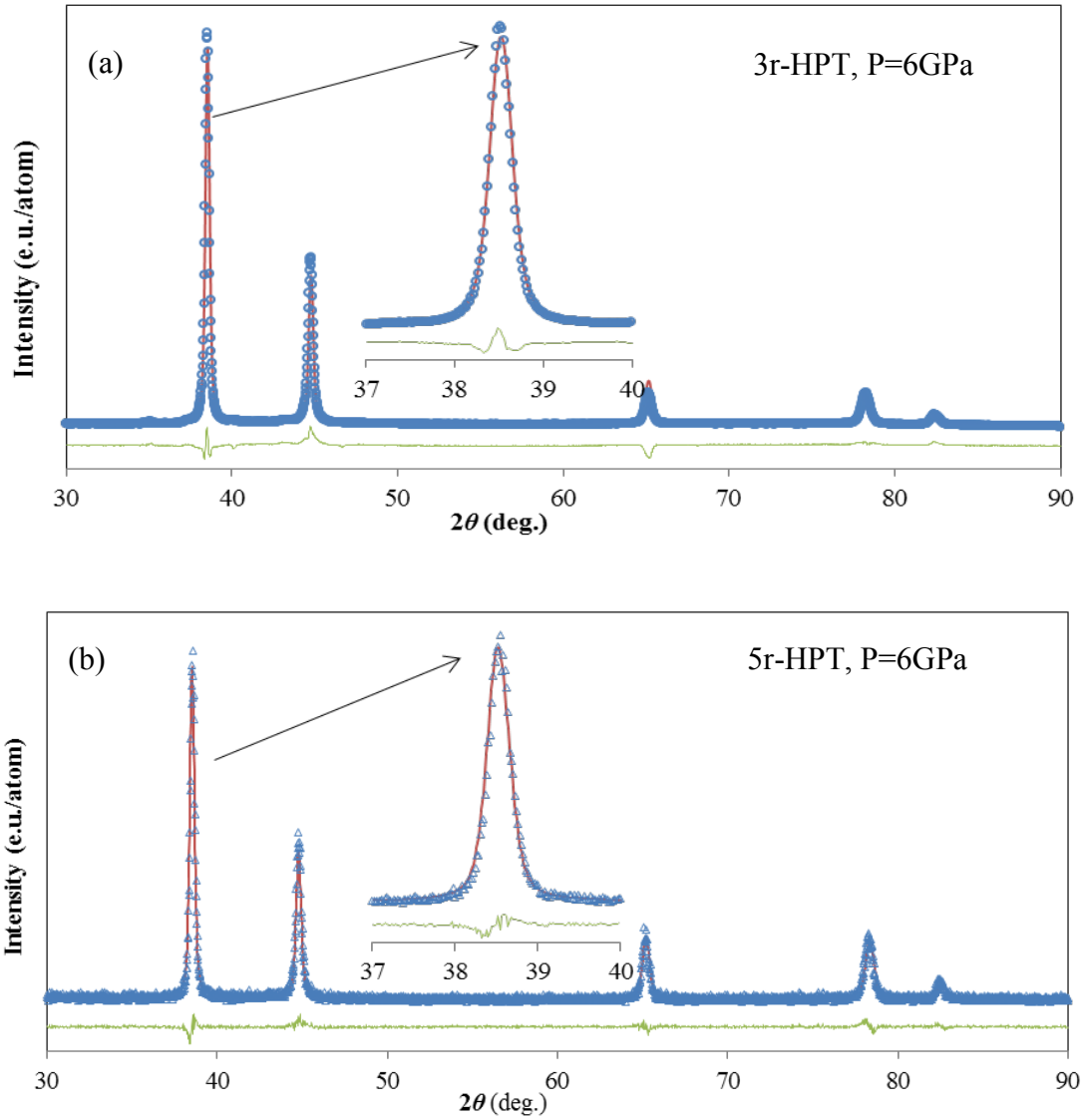

Fig. 5.5 Rietveld analysis fits for X-ray diffraction pattern of 3r-HPT (a) and 5r-HPT sample (b). Experimental data of 3r-HPT and 5r-HPT are shown as circles in (a) and triangles in (b), respectively; and the refined simulated patterns are shown as continuous solid line. The difference between experimental data and fitted simulated pattern is shown as continuous line under each diffraction pattern.

Table 5-1 Instrumental parameters simulated from 'MAUD'.

Instrumental parameters	**U**	**V**	**W**	**Gaussianity coefficient 1**	**Gaussianity coefficient 2**
Value	1.969	-6.416	0.6634	-198.7	6.676

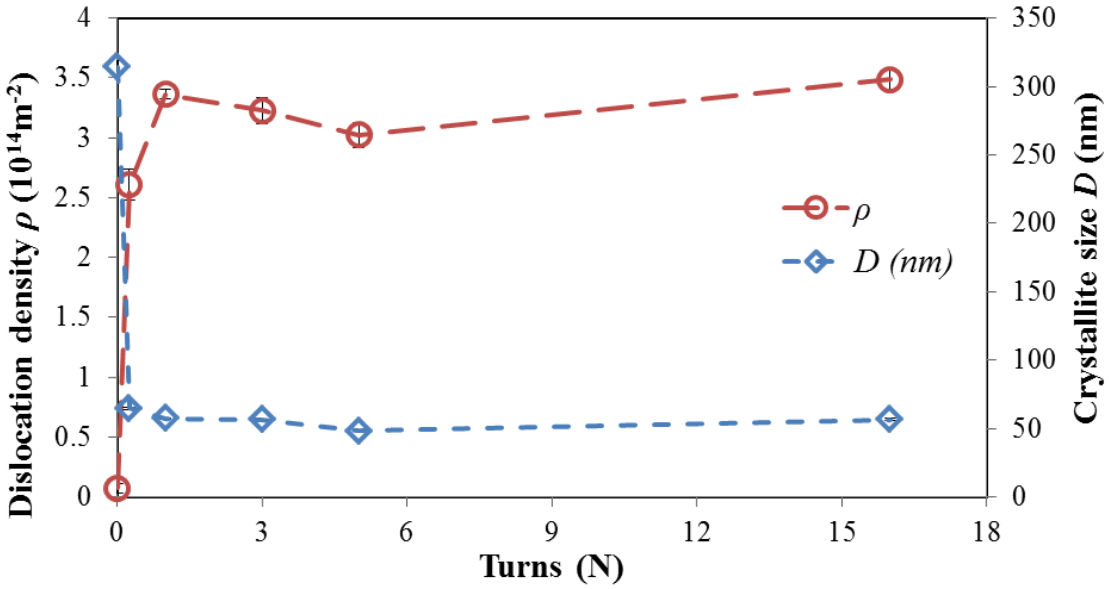

Fig. 5.6 The crystallite size (coherently scattering domains) and average dislocation density determined by Rietveld full pattern refinement plotted as a function of the number of HPT rotations.

A higher dislocation density has been evaluated by XRD in edge areas of HPT deformed samples. The saturated value indicates the microstructural homogeneity. The findings show a reasonable correspondence with Vickers hardness and the equivalent strains in these areas are nearly the same. But in Williamson-Hall plots, the small grain size and the strain broadened profiles are thought to be Lorentzian factors. The broadening components are linear added to each other. In Rietveld method, (i.e. [161, 162, 184, 185]), the profile broadening due to microstrain is thought to be a Gauss component. Hence, the dislocation densities calculated from Williamson-Hall plots are smaller than those obtained from Rietveld method.

5.1.3 Transmission electron microscopy

TEM micrographs obtained at positions at ~4 mm from the centre of disks after ¼r-HPT, 1r-HPT and 5r-HPT processing are shown in Fig. 5.7 to Fig. 5.9, respectively. There is very little difference in grain sizes in the outer regions of 1r-HPT and 5r-HPT disks. High dislocation densities within some of the ultrafine grains were observed in a 5r-HPT sample (see Fig. 5.9 (a)). With an aperture of ~1 μm^2, a ring pattern consisting of many dispersed spots, as shown in Fig. 5.8 (c) and Fig. 5.9 (b), signifies the formation of high-angle grain boundaries with many grains in multiple orientations. More spots appear in Fig. 5.9 (b) than those in Fig. 5.8 (c) suggest more grains with different orientations for 5r-HPT sample within the aperture area.

The average grain sizes are measured using the modified line intercept method described in [117]. Averaging over 20 TEM micrographs provided a line intercept grain size of 177$\pm$35 nm after ¼ rotation, 145$\pm$35 nm after 1 rotation and 157$\pm$30 nm after 5 rotation, respectively. The grain size distribution of the HPT processed samples was illustrated in Fig. 5.7 (d), Fig. 5.8 (d) and Fig. 5.9. (c), respectively.

After HPT processing the average grain sizes measured by TEM were in the range of ~120-200 nm but these size are about 3-times higher than the mean crystallite sizes of ~40-60 nm determined using XRD profile broadening analysis. This discrepancy is now well-established in observations of materials processed by SPD [186, 187]. The TEM grain size can only be observed as grain misorientations of larger than 15° with a bright mass-thickness contrast. But the crystallite size is the size of scattering domains, which are dislocation free domains. Thus, the crystallite size determined from XRD corresponds essentially to the mean size of any subgrains or dislocation cells and the mean size is generally smaller than the conventional grain size measured using TEM micrographs [186-188].

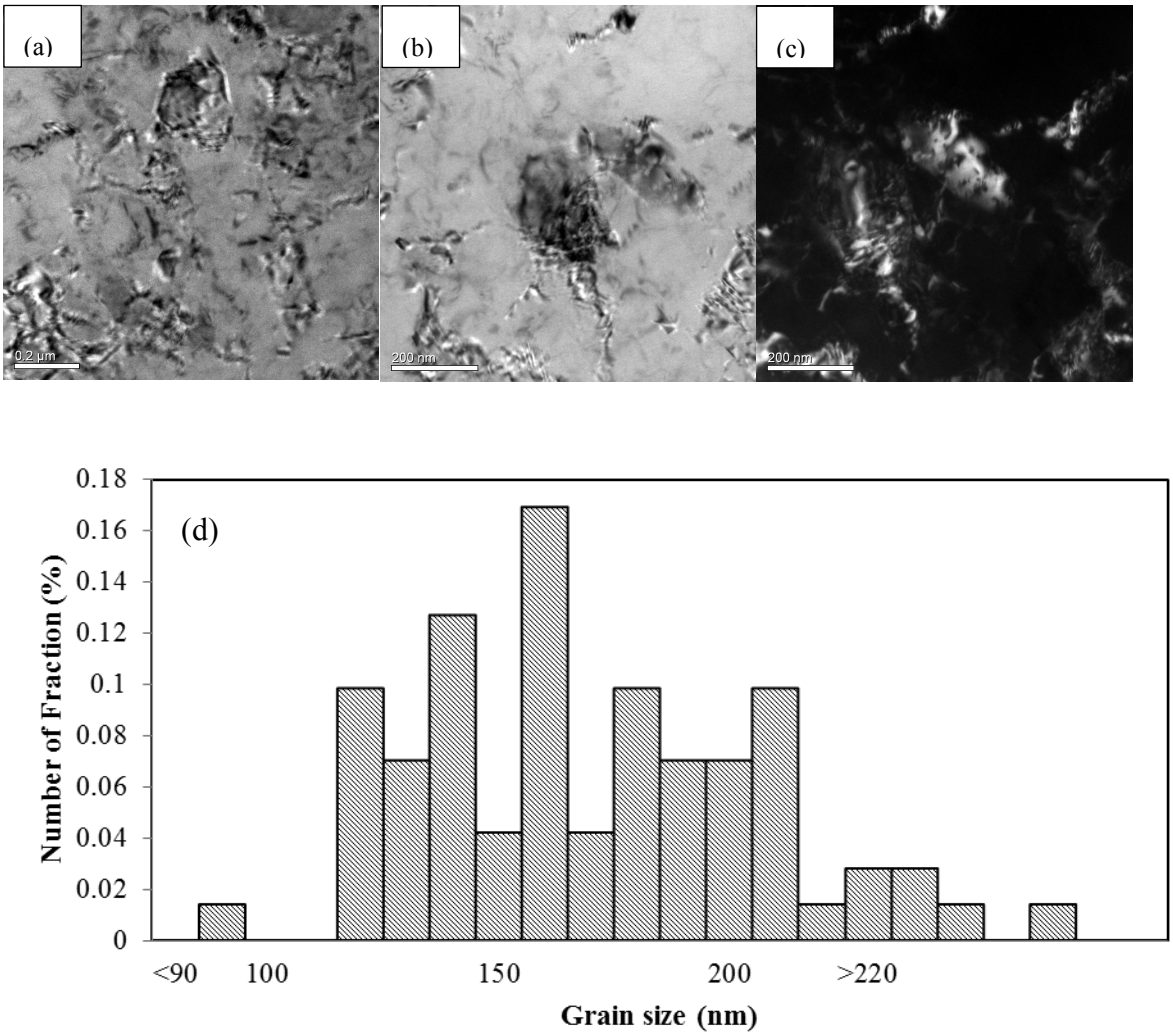

Fig. 5.7 TEM micrographs showing the structural evolution of the Al-Cu-Mg alloy after 1/4r-HPT, (a) and (b) bright field images, and (c) a dark field image, (d) grain size distribution.

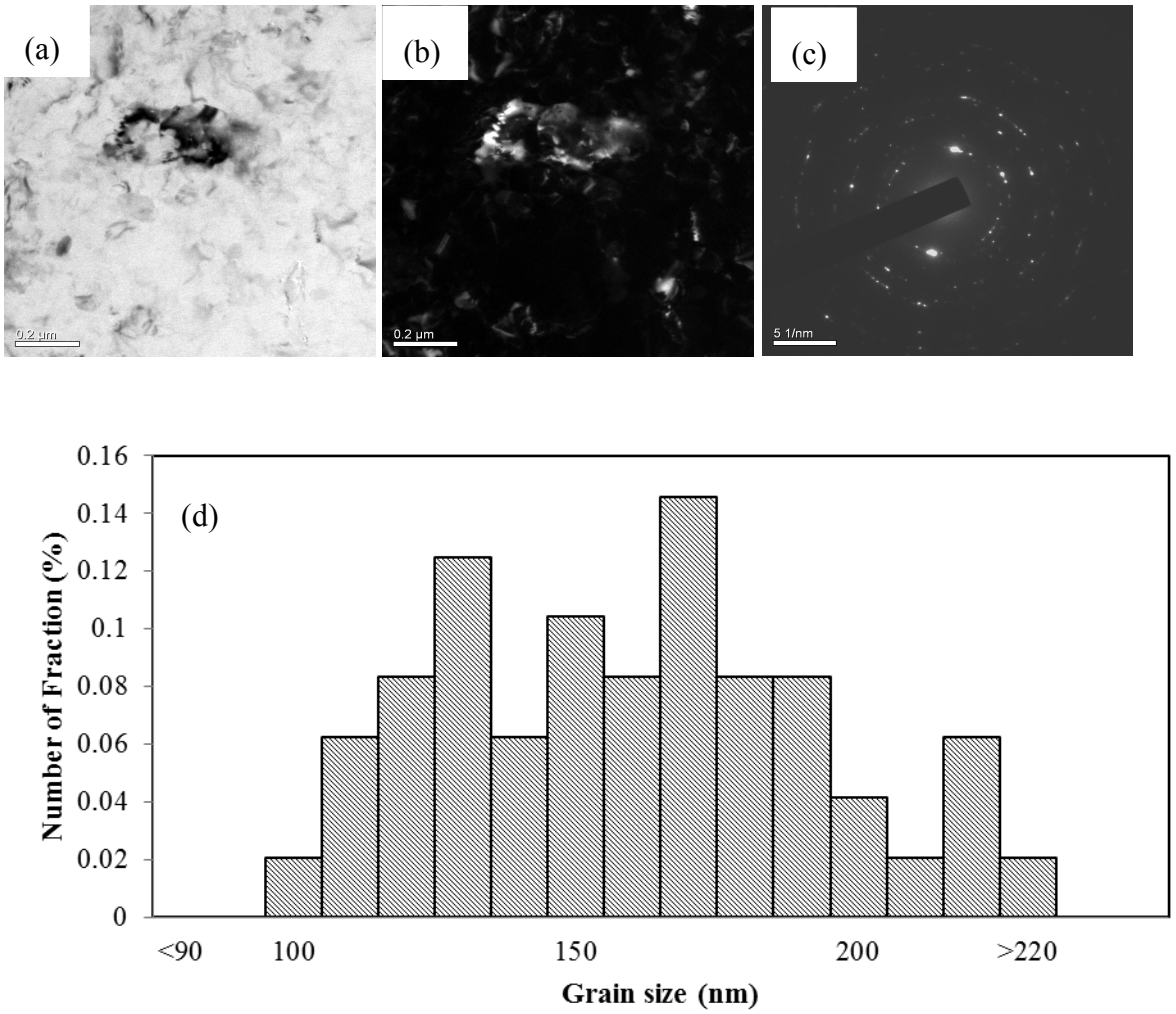

Fig. 5.8 TEM micrographs showing the structural evolution of the Al-Cu-Mg alloy after 1r-HPT, (a) bright image (b) dark image (c) select area diffraction (d) grain size distribution.

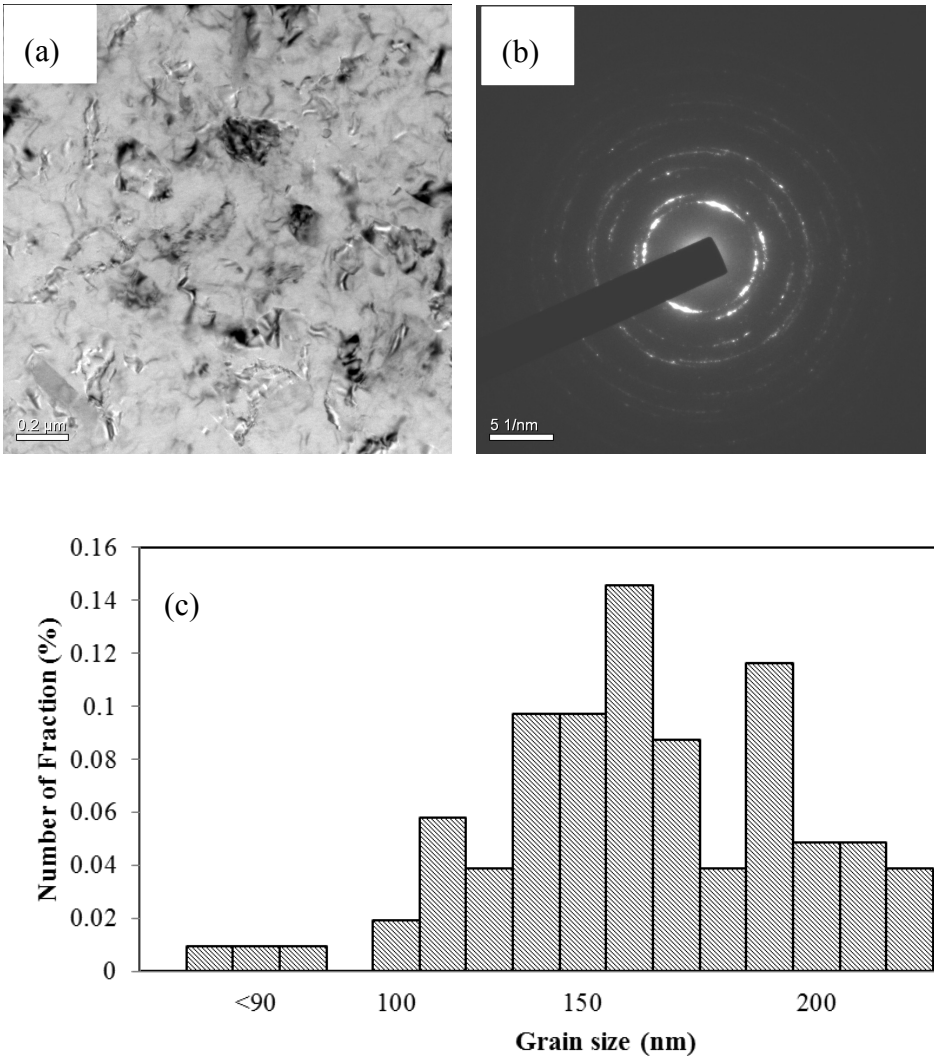

Fig. 5.9 TEM micrographs showing the structural evolution of the Al-Cu-Mg alloy after 5r-HPT, (a) bright image (b) select area diffraction (c) grain size distribution.

5.1.4 Atom probe microscopy

Fig. 5.10 (a)-(c) shows atom maps of Mg, Cu and Si for a sample processed by 1/4r HPT. The analysis volume contains only 2 sections of grain boundaries (GBs), here marked GB1 and GB2. Both Mg and Cu are seen to segregate at the grain boundaries. The total number density of solute clusters in the volume in Fig. 5.10 is identified as 1.90×10^{26} m^{-3}. Mg-Cu co-clusters are the dominant type of detected clusters, with density 1.06×10^{26} m^{-3}. Quantitative measurement of the composition profiles of GB1 in the 1/4r-HPT Al-Cu-Mg alloy is shown in Fig. 5.10 (e). It appears that peak Mg concentration of GB1 is 2.40 at% and peak Cu concentration is lower, ~1.90 at%.

The Cu and Si atom maps of the 5r-HPT sample (Fig. 5.11 (b)-(c)) presents the preicipitate-free zones near grain boundaries, while Fig. 5.11 (a) illustrates a nearly random distribution of Mg atoms. Thus, it is proposed that in this sample GBs only enrich with Cu and Si, with no clear segregation of Mg. This is because segregation characteristic in grain boundaries depends strongly on the nature of each GB, i.e. disorientation angle of GBs, tilt and rotation of the grain (see also [23, 26]). The nearest-neighbour analysis in Fig. 5.11 (e) and (f) confirms that Cu and Si develop non-random distributions slightly more strongly than Mg atoms, because of the clustering of Cu-Mg and Si-Mg, which segregate to GBs. The detected solute clusters have an overall number density of 1.99×10^{26} m^{-3}, with Mg-Cu co-clusters being dominant with a number density of 1.07×10^{26} m^{-3} (see Table 5-2).

The overall number density of solute clusters increases slightly as the number of rotations increased. The average Mg/Cu ratio in clusters is around 1 after 1/4r-HPT, and it increases slightly to 1.15 after 5r-HPT processing.

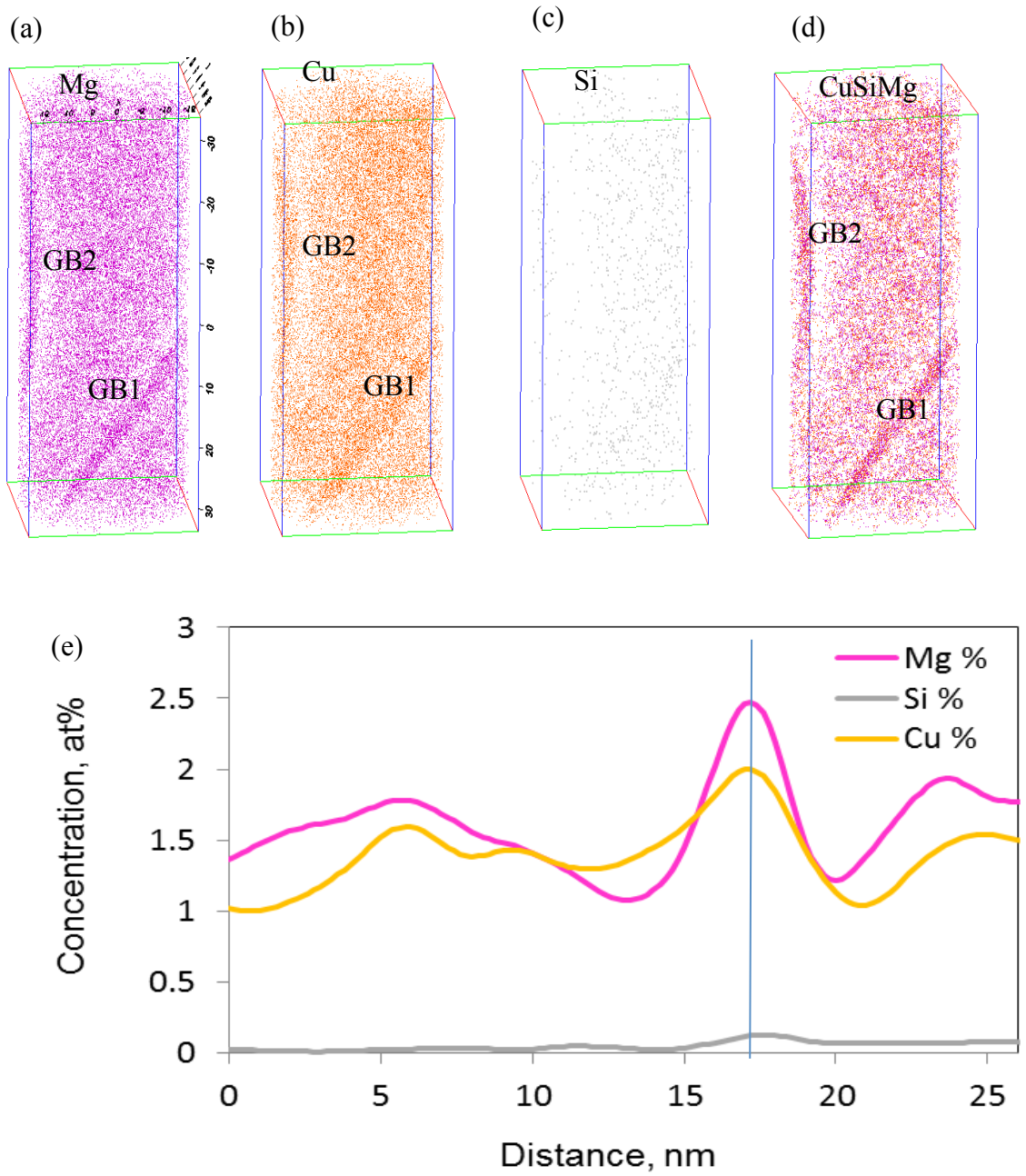

Fig. 5.10 Single-element atom maps of one 1/4r-HPT Al-Cu-Mg sample (a) Mg map, (b) Cu map, (c) Si map and (d) CuSiMg map; (e) composition profiles of GB1 measured using a selection box with the z-axis parallel to grain boundary plane normal.

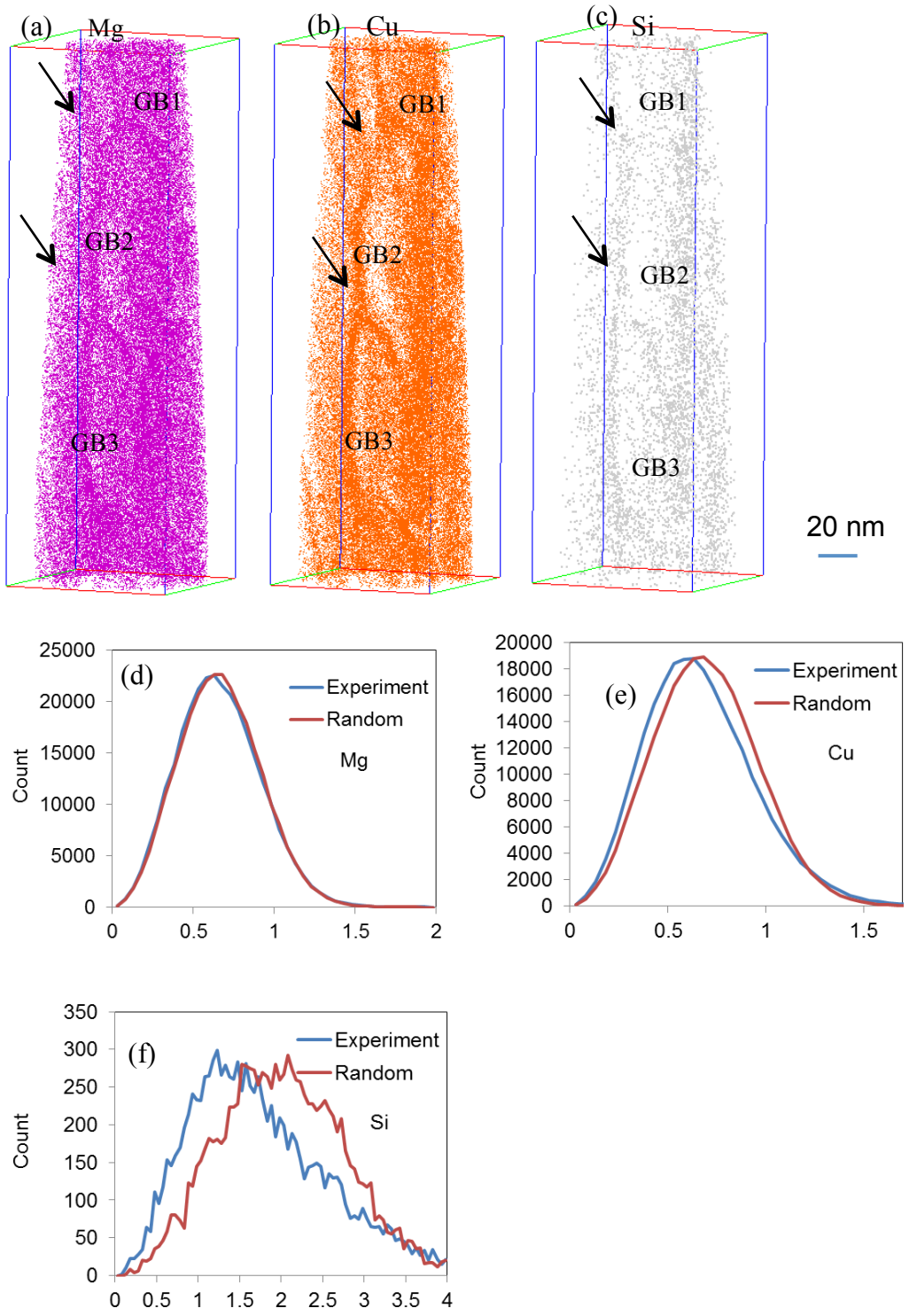

Fig. 5.11 Single-element atom maps of one 5r-HPT Al-Cu-Mg sample (a) Mg map, (b) Cu map, (c) Si map; (d) (e) (f) near-neighbour distribution of Mg, Cu and Si, respectively.

Table 5-2 Number densities of detected clusters in Al-4.3Cu-1.5Mg-0.08Si wt.% processed by ¼ rotation and 5 rotations of HPT at room temperature.

HPT rotations	No. density $\times 10^{26} m^{-3}$				Alloy composition (at.%)	
	All	Mg-Cu	Cu-Cu	Mg-Mg	Mg	Cu
1/4	1.90	1.06	0.34	0.42	1.67	1.69
5	1.99	1.07	0.37	0.45	1.71	1.49

5.2 A model predicting strength of the alloy after HPT

In heat-treatable Al alloys, because of the increase in lattice defects introduced by SPD, the redistribution of solute atoms [24-26] or the fragment of pre-existing precipitations [18-21] can occur. In the Al-Cu-Mg T351 alloy, the ratio of Cu to Mg is close to 1. Cu-Mg co-clusters disperse randomly in the Al matrix. Fig. 5.10 shows that Cu-Mg clusters segregate to grain boundaries in a sample processed by 1/4r-HPT. Similar segregation phenomena were investigated in other SPD Al alloys at room temperature [24, 25]. In previous studies on solution treated Al-Cu-Mg alloys (i.e. [38, 39, 46, 53, 56, 189-191]), co-clusters strengthening are thought to be domain mechanism that causes the rapid hardening in the early stage of precipitation. In this SPD processed Al-Cu-Mg alloy, the segregated clusters will act as obstacles which hinder the movements of dislocations, and pin up the dislocation walls and grain boundaries. Thus, in addition to dislocation strengthening and grain boundary strengthening, short range order strengthening (due to clusters) also contribute to overall strengthening. The strength of an SPD processed Al alloy can be much higher than pure Al due to the clusters effects. A model is established in this section to explain these multi-strengthening mechanisms.

5.2.1 General model structure

The yield strength of a polycrystalline metal is related to the critically resolved shear stress (CRSS) of the grains and the grain boundary strengthening, with an expression of the type [13, 118, 192, 193]:

$$\sigma = \Delta\sigma_{gb} + M\Delta\tau_{tot} \tag{5-2}$$

$\Delta\sigma_{gb}$ is the yield strength increment due to the grain boundaries; M is an orientation factor (often termed the Taylor factor), which is related to texture and the orientation of the tensile axis relative the main axes of the worked specimen [192, 193]; $\Delta\tau_{tot}$ is the CRSS of the grains. We will consider the various strengthening mechanisms in the below.

5.2.2 Critically resolved shear stress of the grains

Within a grain in a ternary (or higher order) alloy that has been work-hardened, $\Delta\tau_{tot}$ is determined by a range of mechanisms and nanoscale features. Within these grains, the resistance against deformation (i.e. resistance against the movement of dislocations) is due to the interactions of the moving dislocations with obstacles in the form of other dislocations (primarily those introduced by the prior work hardening), various types of clusters, precipitates and solute atoms. If we consider a ternary heat treatable aluminium alloy (for instance an Al-Mg-Cu alloy), atoms of type A (for instance Mg) and type B (for instance Cu) dissolve in a lattice of host metal M (the fcc Al-rich phase) after solution heat treatment and on low temperature ageing, some (or most) of the solutes can form clusters. Fig. 5.12 (a) illustrates how a dislocation moving on a slip plane encounters co-clusters, i.e. 4-atom co-clusters intersecting the slip plane (see also [57, 194, 195]). Fig. 5.12 (b) illustrates this from a different orientation (looking down onto a slip plane), now with also a small number of stationary dislocations present (resulting

from a small amount of prior deformation). This shows the moving dislocation will pass through the co-clusters and those dislocations. On passing of one dislocation through the A-B co-cluster, the A-B bonds will be destroyed and some will be retained [57]. After SPD processing, a large number of dislocations are stored in the grain, as illustrated in Fig. 5.12(c).

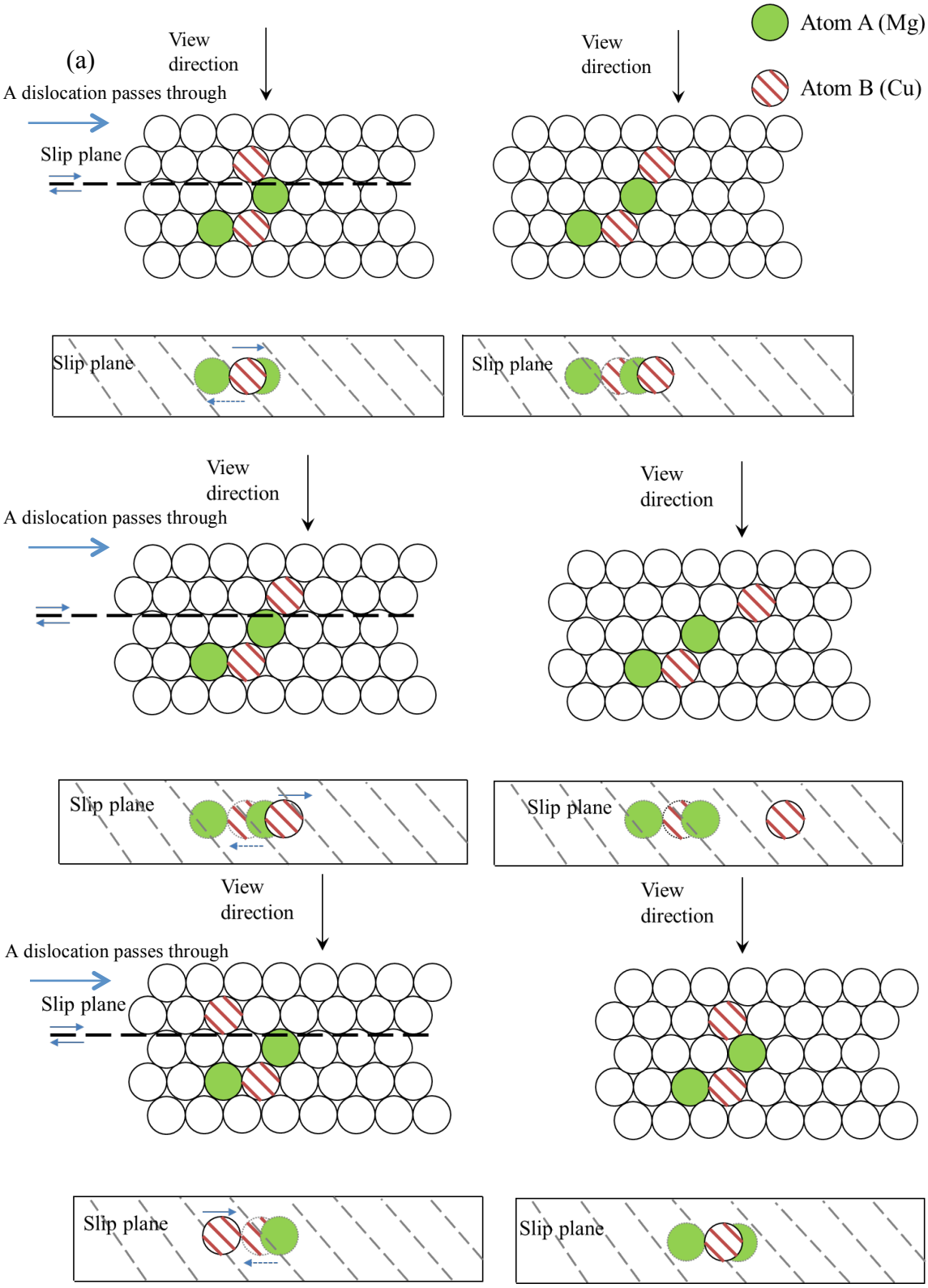
(a)
A dislocation passes through
Slip plane
View direction
Atom A (Mg)
Atom B (Cu)
Slip plane
Slip plane
View direction
View direction
A dislocation passes through
Slip plane
Slip plane
View direction
View direction
A dislocation passes through
Slip plane
Slip plane
Slip plane

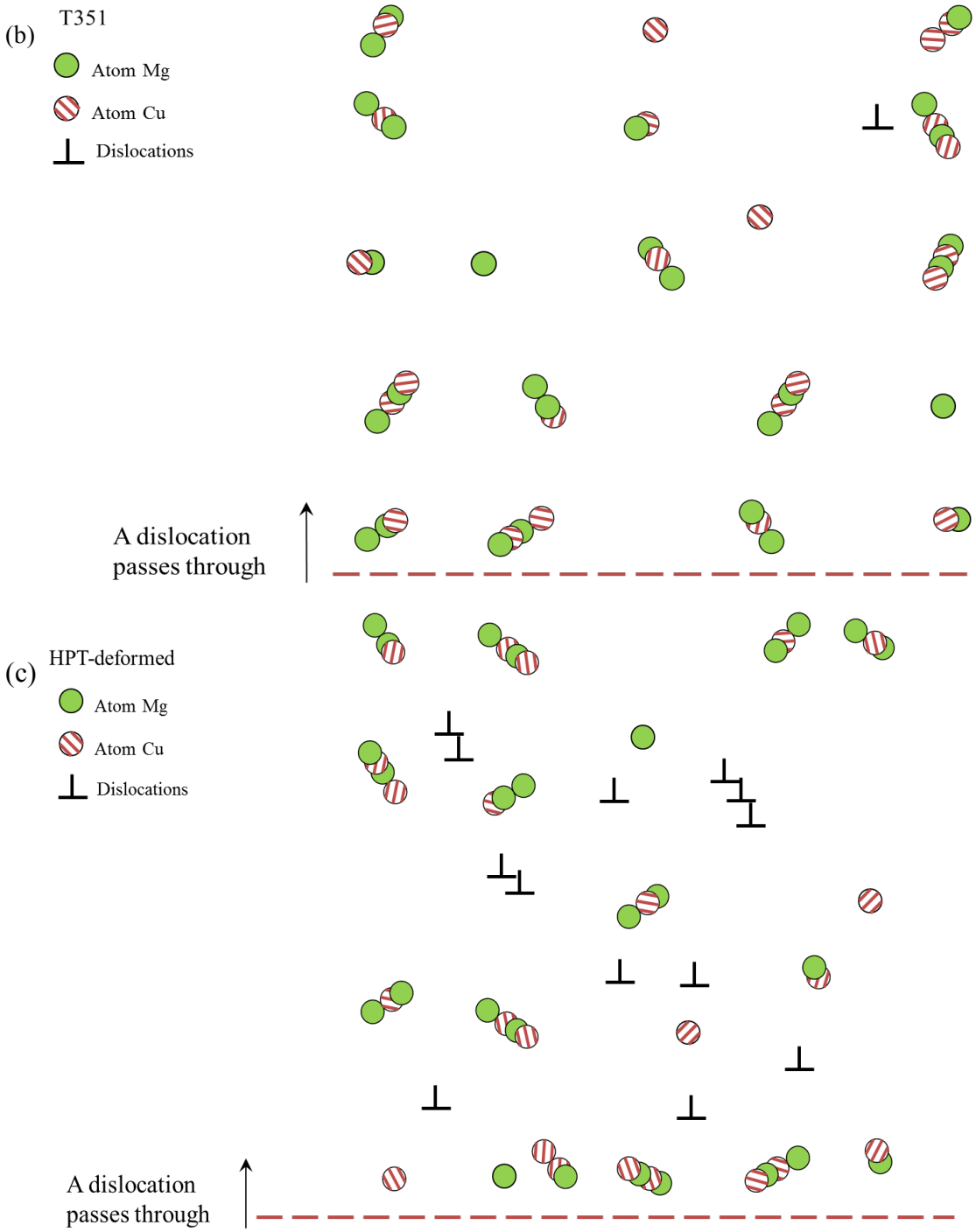

Fig.5.12 (a) Schematic illustrations of (a) co-clusters and a slip plane in a (111) plane of an FCC lattice with a 2-atom co-cluster (left) and 4-atom co-cluster (right), the view direction is the direction employed in (b) and (c); (b) simplified view of a moving dislocation with clusters, solutes and (a low density of) dislocation intersecting the slip plane in its path (illustrating the situation in an Al-Cu-Mg alloy with limited pre deformation); (c) simplified view of a moving dislocation with clusters, solutes and a high density of dislocations intersecting the slip plane in its path (resembling a SPD processed Al-Cu-Mg alloy).

In the present model five contributions to CRSS of grains will be considered: the intrinsic CRSS, $\Delta\tau_0$; the contribution due to dislocations, $\Delta\tau_d$; the contribution due to solid solution contribution, $\Delta\tau_{ss}$; the contribution due to co-clusters $\Delta\tau_{cl}$, which involves a short range order strengthening component, $\Delta\tau_{SRO}$ and a modulus strengthening component, $\Delta\tau_m$. Here, a linear approximation of the superposition of these five contributions is used [116-118, 193]:

$$\Delta\tau = \Delta\tau_0 + \Delta\tau_d + \Delta\tau_{ss} + \left(\Delta\tau_{SRO} + \Delta\tau_m\right) \tag{5-3}$$

The intrinsic strength of pure Al is very low, and to account for the small contributions of Mn, Fe, and Si impurities, $\Delta\tau 0$=10 MPa is taken [192, 193].

The increment of CRSS is due to both statistically stored dislocations and geometrically necessary dislocations and is given by [117, 196].

$$\Delta\tau_d = \alpha_1 Gb\sqrt{\rho_T} = \alpha_1 Gb\sqrt{\rho_{SSD+}\rho_{GND}} \tag{5-4}$$

where α_1 is an empirical constant ranging from 0.2-0.5 [128], in aluminium alloys this value is usually taken as 0.3 [118], which is applied in the present model. G is the shear modulus (taken as 26 GPa), b is the Burgers vector.

The increment in CRSS due to solid solution strengthening $\Delta\tau ss$ is assumed to be described by [50, 192].

$$\Delta\tau_{ss} = \sum k_j c_j^p \tag{5-5}$$

where k_j are the factors describing the strengthening due to the individual elements and c_j are the concentrations of the alloying elements (i.e. Cu and Mg) in solid solution and p is a constant, which is assumed to be 1 (see Ref [50, 197, 198]). We would want to note that solution strengthening is very much a minor effect and has no substantive influence on the analysis, providing only 0.5 to 1 % of the predicted strength of HPT processed alloys.

The co-cluster strengthening is taken to be due to short range order strengthening and modulus hardening where the former is the dominant effect in typical Al alloys [57, 194]. The work consumed in deforming the lattice through movement of dislocations hampered by co-clusters equals the change in energy related to short range order per unit area on slip planes in Al matrix [57, 199], i.e.:

$$\Delta\tau_{\mathrm{SRO}} = \frac{\gamma_{\mathrm{SRO}}}{b} \tag{5-6}$$

where γ_{SRO} is the change in energy per unit area on slip planes on the passing of one dislocation. Ref. [57] provides a detailed calculation on the change in area density of A-B nearest neighbour bonds crossing the slip plane on passing of one dislocation, which is simplified as

$$\rho_{A-B}\left(n_d=0\right)-\rho_{A-B}\left(n_d=1\right)=\frac{4}{\sqrt{3}b^2}\frac{2}{3}\left(y_A+y_B\right) \tag{5-7}$$

where $\rho_{\mathrm{A\text{-}B}}$ (n=0) and $\rho_{\mathrm{A\text{-}B}}$ (n=1) are the area density of A-B nearest neighbour bonds crossing the slip plane $\{111\}$ before and after passage of one dislocation; $\Delta H_{\mathrm{A\text{-}B}}$ is the enthalpy of the nearest neighbour bond; y_{A} and y_{B} are the amount of A and B atoms in the co-clusters, respectively. Although further dislocation movement will cause further changes in density of clusters, the first dislocation experiences the greatest resistance due to clusters [57, 194]. Hence, the short range order strengthening due to co-clusters can be approximated as [57]:

$$\Delta\tau_{SRO}=\frac{\gamma_{SRO}}{b}=\frac{\Delta H_{A-B}}{b}\left[\rho_{A-B}\left(n_d=0\right)-\rho_{A-B}\left(n_d=1\right)\right]=C_{SRO}\frac{\Delta H_{A-B}}{b^3}\left(y_A+y_B\right) \tag{5-8}$$

Clusters possess an elastic modulus that is different to the matrix which will result in an additional strengthening mechanism. This modulus strengthening mechanism is difficult to deal with in theory but simplified treatment has been developed in a range of works [57, 194, 200]. The CRSS due to difference in shear modulus is approximated as

$$\Delta\tau_m=\frac{\Delta\mu}{4\pi\sqrt{2}}f^{\frac{1}{2}} \tag{5-9}$$

$$\mu_{\mathrm{cl}} = \frac{m\mu_M + a\mu_A + b\mu_B}{m + a + b} \tag{5-10}$$

where f is the volume fraction of the clusters, $\Delta\mu$ is the difference in shear modulus between surrounding metallic phase and clusters, with the average cluster ($M_mA_aB_b$) modulus, μ_{cl}, expressed as a weighted average of the pure substances in Eq. (5-15) [57]. The cluster average modulus is 29.6 GPa (using μ_{Al}=26.2, μ_{Cu}=48.3, μ_{Mg}=17.3 GPa from [170], with compositions given in the same reference), providing $\Delta\mu$ = 3.4 GPa.

5.2.3 Strengthening due to grain refinement

In recent works [201, 202], a power-law dependence of yield or flow stress on grain size was expressed as follows

$$\sigma = \sigma_0 + k_{HP} d^{-x'} \tag{5-11}$$

where d is the grain size, σ_{o} and k_{HP} are material constant, the exponents are reported to be in the range from 0 to1 for different classes of materials [201, 202]. Analysis of data for a number of metals and alloys has revealed that the typical values of exponent *x'* range from 0.6 to 1 for fcc metals, whilst they are around 0.5 or less for bcc metals, and 0.2 or even zero for ceramics [203]. To date, there is no theory fully explaining such experimental exponents. Taylor forest hardening [115] gives *x'*=1/2, which has been applied by a large number of strengthening behaviours in coarse-grained metals in the traditional Hall-Petch relation [79]. On the other hand, theory based on the fundamental physics of yield and plastic deformation by dislocations [78, 204] implies a exponent of 1, which provides

$$\Delta\sigma = \frac{k}{d} \tag{5-12}$$

where the value of k is correlated to intrinsic materials factors [95, 117, 118], in general proportional to shear module and Burgers vector, Gb.

$$\Delta\sigma_{\mathrm{gb}} = \alpha_2 Gb\left(\frac{1}{d}\right) \tag{5-13}$$

where α_2 is a constant, d is the grain size.

5.2.4 Hardness/ strength ratio of deformed Al alloys

Either yield strength or ultimate tensile strength (σ_{UTS}), or both, can be approximated by Vickers hardness through.

$$\sigma = \frac{HV}{C} \tag{5-14}$$

where C is a constant, which is usually taken as ~3 in a number of works [13, 14, 118, 205-207]. For our Al-Cu-Mg alloy, $HV_{T351}/3$ is 467 MPa, which is close to σ_{UTS} of the alloy. In SPD processed metals and alloys that strengthen as a result of SPD, the work-hardening ability of materials decreases strongly with increasing deformation, and the yield strength σ_y is approximately equal to σ_{UTS} [207]. In our assessment of the strengthening model we will thus take strengths from Vickers hardness test as σ = HV/ 3.

5.2.5 Modelling results and further refinement of model

The model has been described above to predict the yield strengths of the samples, using the microstructure data in the Section 5.1 combined with data of constants and parameters available in the literature. The model parameters are provided in Table 5-3. In this model, we use the grain sizes determined by TEM, which for HPT samples are on average 3 times larger than the crystallite sizes obtained from XRD line broadening analysis. (For 3r-HPT and 16r-HPT no TEM data is available and the grain size was estimated as 3 times the measured crystallite size.) Dislocation densities are taken from the Rietveld XRD line broadening analysis in Section 5.1.2.2. The amounts of Cu and Mg in the co-clusters y_{Cu} and y_{Mg} in the model are determined using the analysis of thermodynamics presented in [57]; i.e. the stoichiometry of the clusters is considered fixed such that $y_{Cu} : y_{Mg} = 1$. The analysis in Ref. [20] shows that that for the present Al-

Cu-Mg alloy, at the present low temperature ageing of the samples before and after HPT (all at room temperature), the Mg dissolved in the Al-rich phase (i.e. not forming clusters) is $3x10^{-3}$ at%, (which is virtually negligible) and its Cu content is 0.3 at%. The latter contributes to solid solution strengthening through $\Delta\tau_{ss.}$ The effective volume of the clusters for in the modulus hardening is calculated using the approach described in [57].

Table 5-3 Parameter values used in the model

Parameters	**Value**	**Equations**	**Refs.**
M	2.6	(5-2)	[192, 193]
$\Delta\tau_0$	10 MPa	(5-3)	[192, 193]
α_1	0.3	(5-4)	[118]
G	26 GPa	(5-4), (5-13)	[118]
k_{Cu}	10.5	(5-5)	[50, 197, 198]
k_{Mg}	5	(5-5)	[50, 197, 198]
y_{Cu}	1.8 at.%	(5-7), (5-8)	See text and [57]
y_{Mg}	1.8 at.%	(5-7), (5-8)	See text and [57]
b	0.286 nm	(5-4),(5-6),(5-7),(5-8),(5-13)	[192, 193]
α_2	2	(5-13)	[117]
C	3	(5-14)	[118] [14] [13] [205] [206] [207]

The results of the model predictions are presented in Fig. 5.13 (green triangles). In this figure the predictions are compared with measured HV/3 (blue diamonds), with HV determined in the peripheral areas (distance to centre> 3 mm) was used.) In all samples

the cluster hardening is the main strengthening effect. The model broadly captures the trends, but the predicted yield strengths of HPT processed samples are about 150 MPa lower than strengths measured from Vickers hardness. Clearly the model presented above, which is based on non-interacting superposition of strengthening effects in cluster-hardened undeformed ternary alloys and classical work hardening through dislocations and grains boundaries, underestimates strength in the present HPT processed cluster-hardened alloy. To include interaction between HPT-induced defects and clusters we propose the below extension to the model.

The model effectively assumes that solute atoms and dislocations produce separate and distinct strengthening effects (see Fig. 5.12 (b) and (c)). However, atomic probe analysis of samples processed by 1/4r-HPT (Fig. 5.10) and 5r-HPT (Fig. 5.11) indicates solute clusters segregated to dislocations and grain boundaries, which can provide an additional strengthening mechanism. These dislocation-solute interactions reduce the Gibbs free energy of the defect through decreasing the enthalpy associated with it (see e.g. [208]), producing a more stable state (see schematic illustration in Fig. 5.14). These dislocation-solute complexes form a stronger barrier to movement of dislocations, through a mechanism that is similar to the cluster strengthening by short range order: when a dislocation passes through these solute-dislocation obstacles, it causes a higher enthalpy change. We may represent this here by modifying Eq. (5-13) as follows:

$$\Delta\tau_{SRO} = C\frac{\Delta H_{\text{A-B-dis}}}{b^3}(y_A + y_B) \tag{5-15}$$

where $\Delta H_{\text{A-B-dis}}$ is the average enthalpy of the various types of A-B-dislocation clusters:

$$\Delta H_{\text{A-B-dis}} = f_1\Delta H_{\text{A-B}} + f_2\Delta H_{\text{A-dis}} + f_3\Delta H_{\text{B-dis}} + f_4\Delta H_{(\text{A-B})_n\text{-dis}} \tag{5-16}$$

where f_1 to f_4 are the fraction of A-B cluster, fraction of A segregated to dislocations, fraction of B segregated to dislocations, and fraction of A-B co-clusters segregated to dislocations, respectively; $\Delta H_{\text{A-B}}$ is the enthalpy of A-B co-clusters in M matrix, $\Delta H_{\text{A-dis}}$, $\Delta H_{\text{B-dis}}$ the enthalpy of single atom A or B located at dislocations (disordered Al matrix),

$\Delta H_{(A\text{-}B)n\text{-}dis}$ the enthalpy of co-clusters located at dislocations (disordered Al matrix). $\Delta H_{A\text{-}B\text{-}dis}$ increased as compared to $\Delta H_{A\text{-}B}$.

The latter modification has been employed by adjusting $\Delta H_{A\text{-}B\text{-}dis}$ to obtain the best possible fit between data and model. The results presented in Fig. 5.13 (red crosses) show an excellent correspondence with the measured HV/3 data for all samples over the range of HPT processing applied for 1 rotation or more. $\Delta H_{A\text{-}B\text{-}dis}$ in this fit is 49.5 kJ/mole, which compares to $\Delta H_{Cu\text{-}Mg}$ = 34.5 kJ/mole [57].

For ¼ rotation the fit with $\Delta H_{A\text{-}B\text{-}dis}$ = 49.5 kJ/mole overestimates the strength, and the model without cluster-dislocation complexes provides a good fit (i.e. with $\Delta H_{Cu\text{-}Mg}$ = 34.5 kJ/mole). Apparently, for these low deformations, the amount of dislocations present after HPT and the amount of dislocation movement during HPT is too low to allow the formation of significant cluster-dislocation complexes. Most of the Cu and Mg in the 1/4r-HPT sample then present in Cu-Mg clusters that are not related to HPT dislocations. In that sense the 1/4r-HPT sample is similar to the 2024-T351 sample.

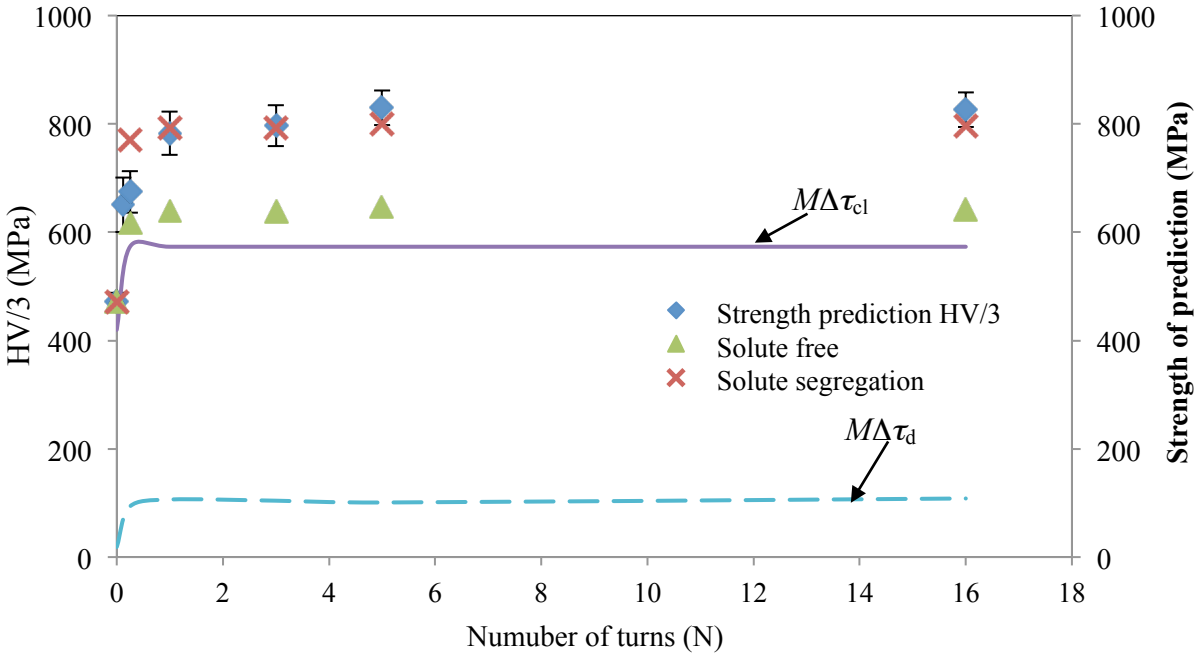

Fig. 5.13 HV/3 (♦) compared with model predictions of strength using 2 model variants: the case for solutes and clusters being separated from defects (grain boundaries and dislocations) (▲) and for clusters being associated with defects providing an enhanced strengthening effect (×). Also plotted are the two main strengthening effects in the HPT processed materials due to cluster-defect complexes ($M\Delta\tau_{cl}$) and strengthening due to dislocations ($M\Delta\tau_{d}$).

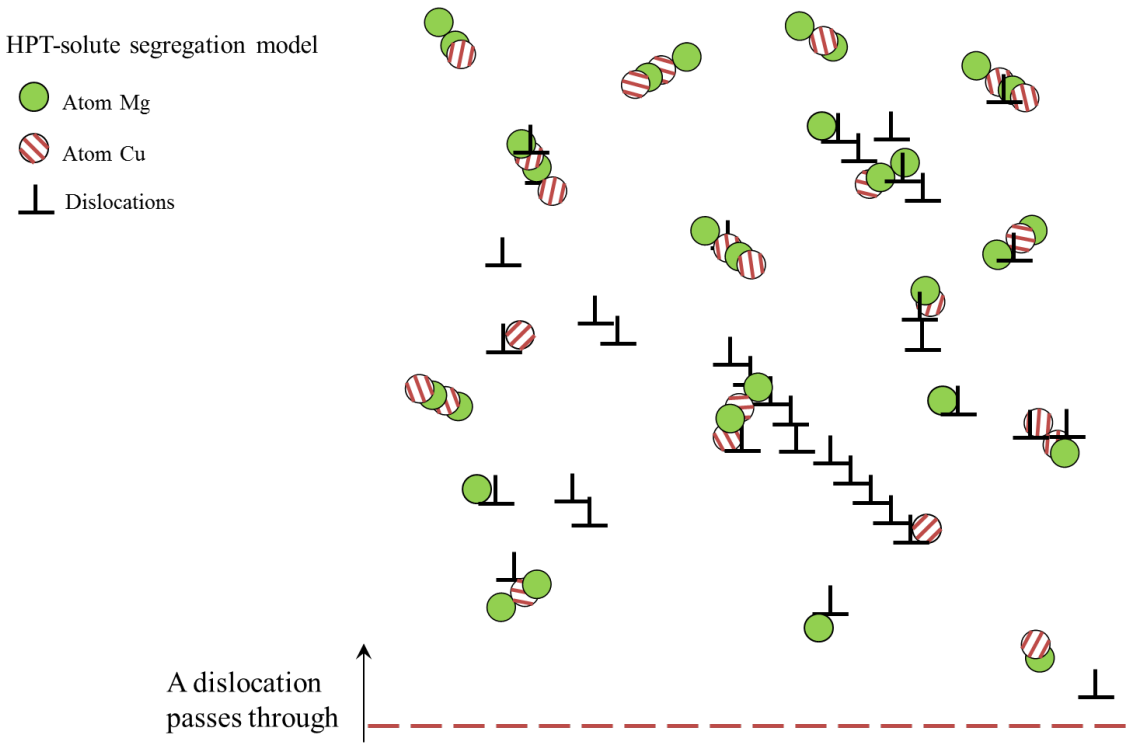

Fig. 5.14 Schematic illustration (schematic) of a moving dislocation with clusters, solutes, dislocations and dislocation-cluster complexes intersecting the slip plane in its path (illustrating the situation in an SPD processed Al-Cu-Mg alloy).

5.2.6 Verifying the model

The model of cluster strengthening in the absence of clustering on defects provides an explanation for a range of observations in ternary and higher order alloys. For example, the strength of conventionally processed, coarse-grained, underaged Al-Cu-Mg and Al-Mg-Si alloys were accurately presented by a model in which cluster strengthening is the dominant strengthening mechanism [57, 194]. However, the model cannot fully explain the strengthening in the present SPD-processed Al alloys, and, as shown in the Section 5.2.5 a modification taking into account the changed enthalpy related to cluster-defect interaction is required to provide an accurate model that is consistent with strength and microstructure data. In fact it is well known that solutes and various types of defects

interact and cluster together, including vacancy-solute clusters [209] and dislocation-solute clusters [210, 211], leading to a reduction of overall grain-boundary Gibbs free energy and a stabilization of ultrafine-grained microstructures [103, 208, 212, 213]. Thus this model modification is justifiable and required.

The interaction between dislocations and solute can be described by thermodynamic models, incorporating enthalpy and entropy terms [57, 194]. In line with this, in our strength model modification we introduced a new parameter, $\Delta H_{\text{A-B-dis}}$, which for the present alloy was determined by fitting to be 49.5 kJ/mole. (At present we are not considering the entropy related to this interaction; it is thought that at room temperature this effect is negligible.) This $\Delta H_{\text{Cu-Mg-dis}}$ accounts for the different fractions of Cu-Mg clusters in Al matrix, solute atoms segregated to dislocations and Cu-Mg clusters segregated to dislocations. The proportions of each part may be adjustable, because the amount of atoms/clusters segregated to dislocations or grain boundaries can be different between HPT-processed samples subjected to different rotations (see Fig. 5.10 and Fig. 5.11). We avoid focusing on the proportion of $\Delta H_{\text{Cu-Mg-dis}}$ correlated to the various types of solute-defect interactions and clustering, and instead adjust $\Delta H_{\text{Cu-Mg-dis}}$ to obtain a single averaged $\Delta H_{\text{Cu-Mg-dis}}$ (see also [209-211] and [103, 208, 213]). Fig. 5.13 shows this works well providing the HPT is conducted for one rotation or more. Apparently the one rotation of HPT is sufficient to reach conditions in which relative proportions of the different solute-defect interactions and their contribution to $\Delta H_{\text{Cu-Mg-dis}}$ are stationary on further deformation. We believe that the reduced strength at very low deformations (less than 1 HPT turn) is due to the mobility of solute atoms (which is enhanced by deformation induced vacancy generation) and the movement of dislocations being too limited to form substantial dislocation-cluster complexes.

The $\Delta H_{\text{Cu-Mg-dis}}$ value of 49.5 kJ/mole is larger than an enthalpy determined from the 5×5×1 and 6×6×1 supercell calculation in a GPB structure [51], suggesting that the Cu-Mg-defect cluster complexes are quite stable. In fact with this value of $\Delta H_{\text{Cu-Mg-dis}}$, the defect-cluster complexes in the SPD materials can be more stable than some of the intermediate precipitates, and the solute atoms captured in the cluster-defect complexes will not transform to GPB zones or intermediate precipitates on ageing, unless changes elsewhere in the material (away from the cluster-defect complexes) changes this local situation. On continuous heating these cluster-defect complexes would be more stable than the co-clusters present in solution treated and aged Al-Cu-Mg alloys. To validate

this we performed differential scanning calorimetry on the HPT processed alloys at heating rate 10 °C/min. This confirmed that whilst for similar Al-Cu-Mg alloys in solution treated and room temperature aged condition a strong endothermic effect due to co-cluster dissolution occurs from about 140°C with an endothermic maximum at 220 °C [50], for the present (solution treated, RT aged, HPT processed and subsequently RT aged) samples, no endothermic effect is detected in this temperature range. The present analysis of cluster-defect complexes suggests that only dislocation movement and annihilation at elevated temperature and/or the formation of stable phases would be able to cause the dissolution of these cluster-defect complexes.

Our understanding of cluster segregation to grain boundaries and dislocations rests on 3DAP data and the statistical analysis of that data. When APM is performed on the ultrafine-grained Al-Cu-Mg alloy, a wide range of cluster types and compositions (Table 5-2) are generally detected, which may seem at variance with the present model. However, the APM data is based on statistical analysis of the locations of atoms that are detected at a detection rate of about 50~55% [23, 194], and hence many of the the two-atom or four-atom types (based on A-B dimers) that are illustrated in Fig. 5.12 (a) cannot be identified individually. For each dimer present in the alloy, the APM experiment with cluster identification algorithm can provide 4 outcomes: if both atoms in the dimer are detected the result can be the detection of the A-B dimer, if only A is detected the outcome is a single dissolved atom A, if only B is detected the outcome is a single dissolved atom B, and if both atoms are go undetected then nothing is detected. Similarly, for 4 atoms clusters, a range of possible outcomes can occur. This leads both to an underestimate of the amount of clusters as well as an overestimate of the variety of cluster compositions [194]. The APT data does confirm that the Cu:Mg ratio of atoms in the cluster is very close to unity, which is consistent with the model.

5.3 Summary

The microstructures and mechanical properties of the Al-Cu-Mg alloy are significantly changed through HPT. The rotations less than 1 cause a substantial grain refinement and introduce a large number of dislocations with an inhomogeneous microstructure, whilst the higher rotations lead to a further grain refinement and a further increase of dislocation density with a more homogeneous microstructure. Mg and Cu segregate strongly at the grain boundary of the Al-Cu-Mg alloy processed by 1/4-rotation HPT at room temperature. Si appeared selectively segregated at some of the GBs.

The microhardness of T351 sample increases dramatically as a result of microstructural evolution during HPT processing. In addition to dislocation strengthening and grain refinement strengthening, a high density of Cu-Mg co-clusters is thought to be the dominant strengthening mechanism in the HPT-processed Al-Cu-Mg alloy. However, as presented in the model, the explanation of individual strengthening mechanisms cannot predict the increase of strength well. A new concept of the multiple interactions between co-clusters and dislocations leading to complex solute-defect clusters is introduced to explain the further increase in strength.

The fitting $\Delta H_{\text{Cu-Mg-dis}}$ is determined to be 49.5 kJ/mole. It suggests the solute-defect clusters are more stable than some of the intermediate precipitates such as GPB zones, and indicates only dislocation movement and annihilation at elevated temperature and/or the formation of stable phases would be able to cause the dissolution of these cluster-defect complexes.

Chapter 6 Thermal stability of an UFG Al-Cu-Mg alloy processed by HPT

The solute atom or cluster redistribution in the Al-Cu-Mg alloy processed by HPT has been presented in Chapter 5. The solute atoms are thought to act as obstacles which hinder the movements of dislocations, and pin up the dislocation walls and grain boundaries. The microstructures can be stabilized by segregated clusters.

This chapter presents the thermal stability of the UFG Al-Cu-Mg alloy during DSC heat treatment. The microstructural evolutions and the solute/co-clusters behaviours during DSC heating were studied using XRD, TEM and APT. The Hall-Petch relationship and the lattice parameter misfits are discussed in Section 6.2. In the final Section 6.3, a model is established to predict the stored energy in the UFG Al-Cu-Mg alloy processed by various rotations of HPT.

6.1 Results

6.1.1 DSC heating and Vickers hardness

DSC thermographs of T351 and the 5r-HPT samples on the edge area are chosen to illustrate in Fig. 6.1. As also presented in Chapter 4, DSC thermogram of the T351 sample has an endothermic reaction at a temperature range between 100 and 240 °C; while the thermograph of the 5r-HPT sample has a small exothermic reaction up to 170 °C. The heat flow of the 5r-HPT sample drops slightly around 195 °C. Both T351 and HPT processed samples have exothermic reactions at intermediate temperatures and an endothermic reaction in the temperature ranges of 285-500 °C and 265-500 °C, respectively. The overlapping exothermic peaks in the 5r-HPT sample indicate the two

domain exothermic effects in this region: microstrain annihilation and S precipitation (see Chapter 4). The thermal stability of UFG microstructures can be studied on samples heating up to various temperatures in DSC curves.

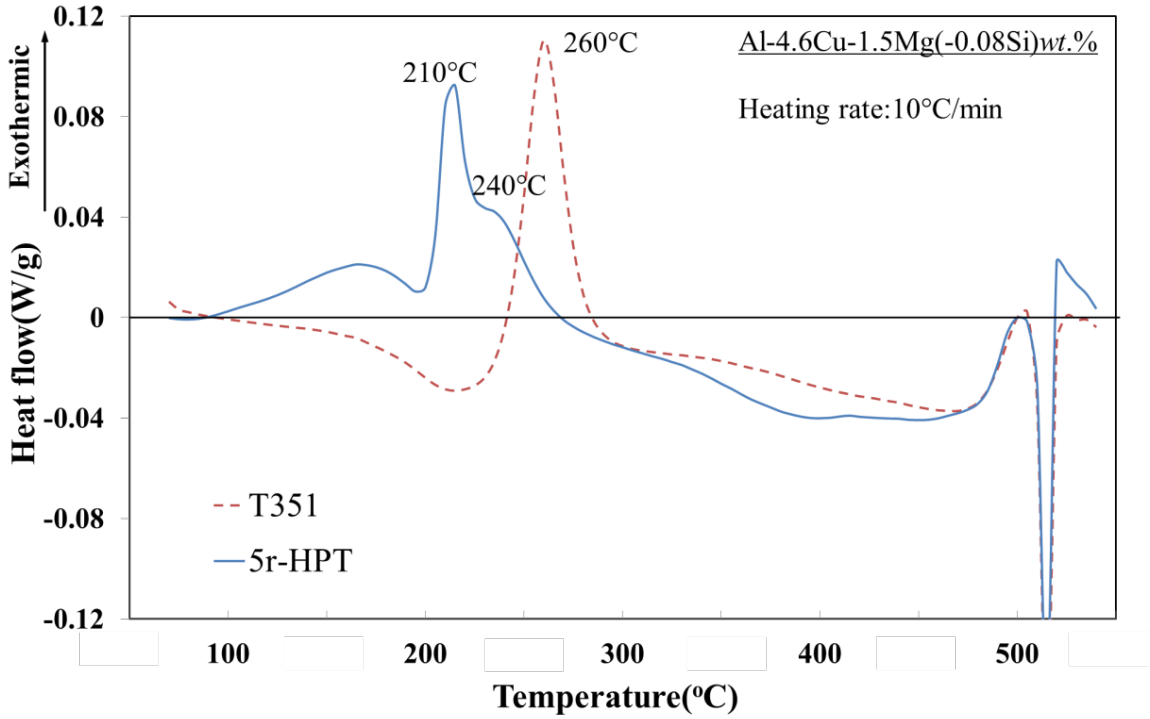

Fig. 6.1 DSC curves for T351 and 5r-HPT Al-Cu-Mg samples.

The hardness evolution during DSC annealing with heating rate of 10 °C/min is shown in Fig. 6.2. This figure shows that the microhardness increases significantly after HPT processing at room temperature: Vickers hardness of the HPT sample (243 HV) is ~70% higher than that of T351 sample (142 HV). On heating, the hardness of the HPT-processed sample first increases slightly from 243 HV (room temperature) to 263 HV at 140 °C. In general, the microhardness changes for both samples are limited on heating in the range of 140 °C~200 °C.

The microhardness of the 5r-HPT sample decreases significantly as the sample is heated beyond 210 °C, and for the T351 sample the decrease in hardness occurs from 260 °C onwards. The small increase in hardness after heating to 260 °C is thought to be due to S precipitation [41, 189]. The microhardness of both samples present similar values

after heating to 300 °C and higher temperatures. This indicates the initial ultrafine-grained microstructure produced by HPT has coarsened and dislocations have been annealed out.

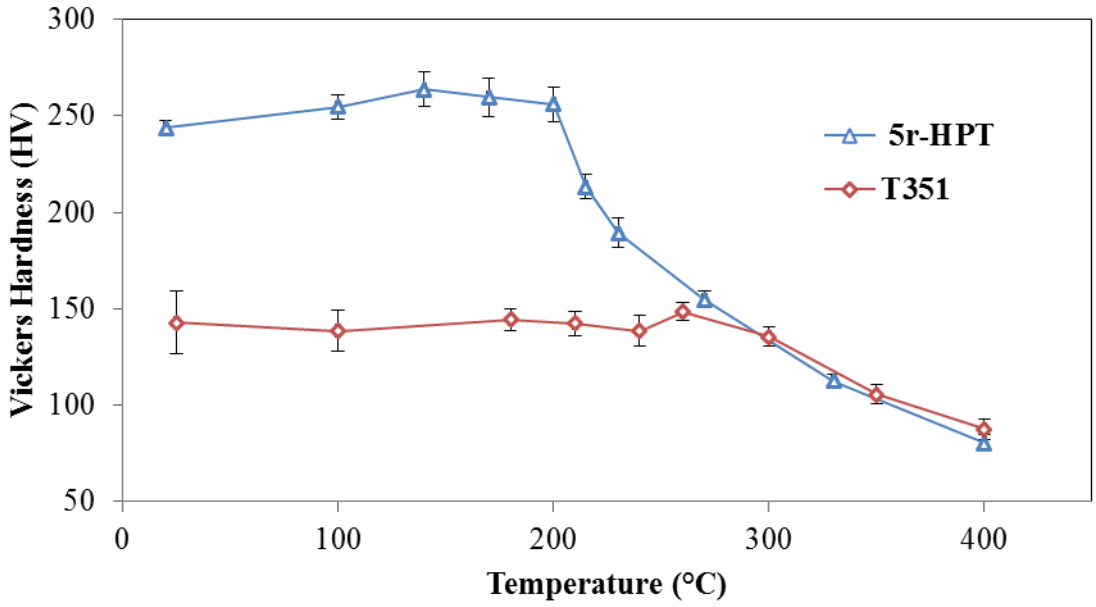

Fig. 6.2 Vickers hardness of T351 and 5r-HPT samples during DSC linear heating annealing

6.1.2 X-ray diffraction

The XRD patterns of 5r-HPT samples heated to various temperatures are shown in Fig. 6.3. As indicated in this figure, peaks due to the S precipitates were observed in the 5r-HPT samples annealed up to 240 °C and 300 °C. The difference in peak relative intensity in XRD results indicates HPT processing changed the texture of the alloy significantly. A similar observation has been found in HPT processed AA6060 via transmission Kikuchi diffraction maps [23]. The broadening of the aluminium phase peaks of HPT-processed samples indicates lattice imperfections are introduced, predominantly from dislocations and (additional) grain boundaries. Rietveld whole profile fitting [159, 173] was applied on XRD data using the 'MAUD' software [165, 166, 214]. The calculation processes are similar to the method described in Section 5.1.2.2.

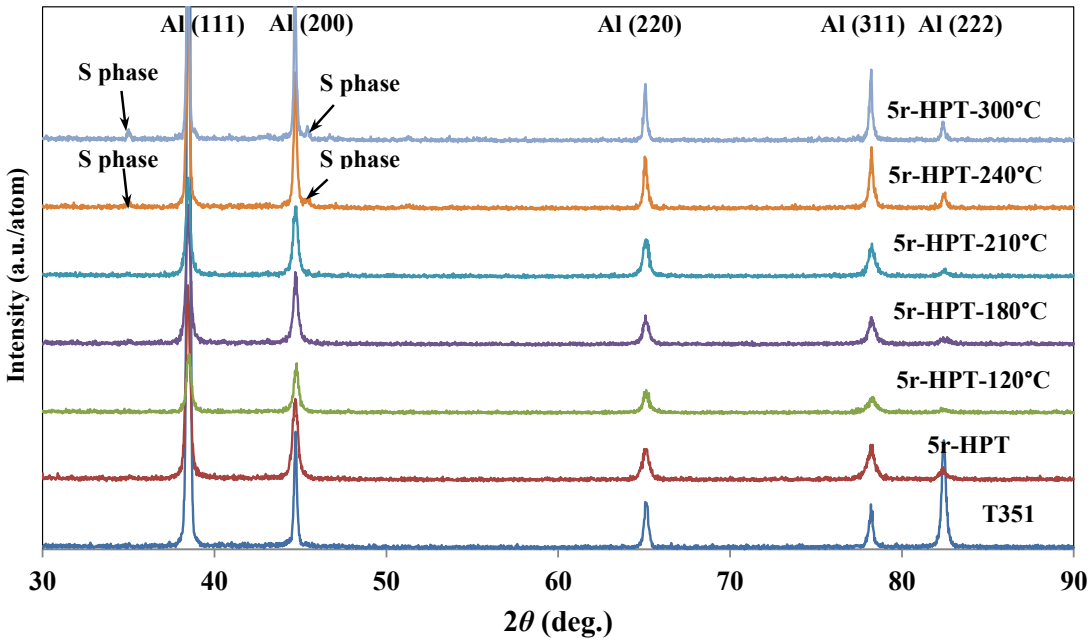

Fig. 6.3 XRD patterns of T351 and the 5r-HPT samples equivalent annealed up to varying temperatures with a heating rate of 10 °C/min. The diffraction plane indices of aluminium are indicated in the figures.

In the Rietveld refinement, the microstrain and crystallite size were optimized simultaneously, and results are shown in Fig. 6.4. The microstrain of 5r-HPT sample increases from 0.0018 at room temperature to 0.0021 as heating at 120 °C. This small increase is possibly due to cluster effects, which corresponds to the small exothermic effects peaking at 170 °C in DSC thermogram (Fig. 6.1). A significant decrease of microstrain is observed after heating beyond 120 °C. The value of microstrain approaches 0.0007 at 300 °C, which is close to the as-obtained T351 sample (0.0009) at room temperature. The crystallite sizes when heating to temperatures up to 210 °C stay constant at 60~70 nm, while it increases significantly to 310 nm when heating to 300 °C. The combination of reducing microstrain and increasing crystallite size are key contributing factors for the hardness decrease in the corresponding temperature range.

According to Eq. (5-1), the dislocation densities were calculated from measured microstrain and crystallite size. The evolution of dislocation density is shown in Fig. 6.5. It shows an increase from 3.29×10^{14} m^{-2} at room temperature to 3.42×10^{14} m^{-2} at

120 °C. The decrease in dislocation density appears to occur in two stages: (I) 120 °C-210 °C; (II) above 210 °C. In the stage I, the dislocation density decreases gradually and approaches a value of 2.31 $\times 10^{14}$ m^{-2} at 210 °C, while the hardness keep unchanged, shown in Fig. 6.2. In the stage II, both the dislocation density and hardness show a significant decrease. The slope of decreasing trend is steeper in this stage.

At 210 °C, an exothermic peak is shown in DSC thermgram (Fig. 6.1), and simultaneously the hardness decreases significantly (Fig. 6.2). This phenomenon is consistent with the decrease of dislocation density (Fig. 6.5) and the increase of crystallite size (Fig. 6.4). The exothermic peak at 210 °C is thought to due to growth of crystallite size, the annihilation of dislocations, and S precipitation. Some tiny S precipitates would exist in Al matrix even though Bragg reflection peaks correlated to S precipitates were not observed in Fig. 6.3.

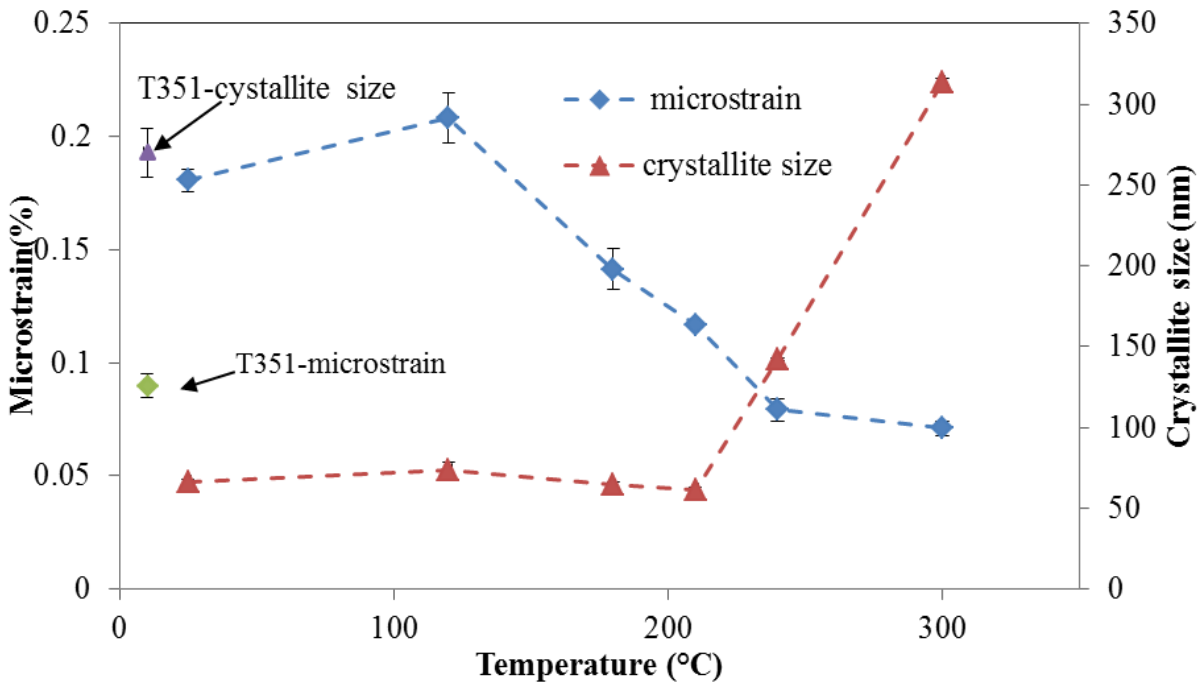

Fig. 6.4 Microstrain and crystallite size evolutions of 5r-HPT sample during the equivalent isothermal annealing at different temperature.

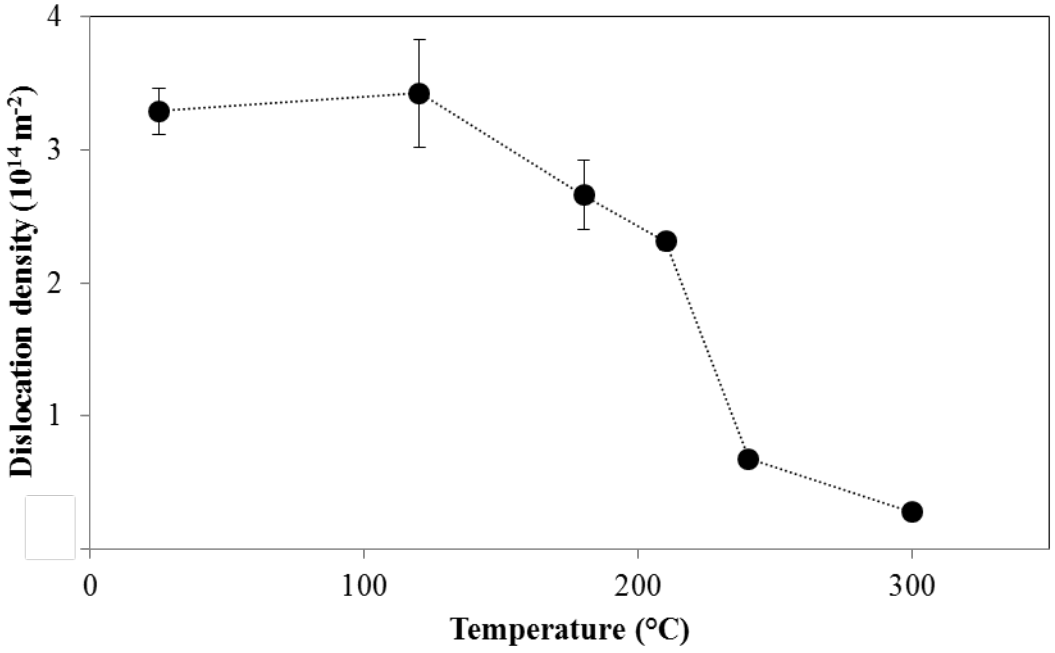

Fig. 6.5 Dislocation density evolutions of the 5r-HPT sample after isothermal annealing equivalent to DSC linear heating at 10 °C/min, as determined from the crystallite size and microstrain.

6.1.3 Transmission electron microscopy

From TEM images Fig. 6.6 (a-c), the average grain sizes of 5r-HPT samples and those after heating to 210 °C and 300 °C can be obtained. The average grain sizes at about 4 mm from the centre of the disks were measured, using the modified line intercept method described in Section 3.7. The statistic average grain sizes were obtained based on more than 20 TEM images. The average grain size of 5r-HPT sample is 157±30 nm ($\bar{L}$=108 nm), and it appears to increase slightly to 169±30 nm ($\bar{L}$=116 nm) on heating to 210 °C. With an aperture of ~1 μm^2, a ring pattern consisting of many dispersed spots, as shown in Fig. 6.6 (a), signifies the formation of high-angle grain boundaries with many grains in multiple orientations. The SAD pattern of the 5r-HPT sample DSC heated to 210 °C (5r-HPT-210 °C) indicates a decrease of dislocation density and subgrain boundaries. The grain size of 5r-HPT-300 °C is 250±40 nm. The grain size of SPD-processed materials determined by TEM is generally several times larger than the crystallite size (or coherently scattering domain size) obtained by X-ray line profile

analysis [186, 188]. The grains confined by high-angle boundaries are subdivided into subgrains and/or cells. The misorientation angle between cells is low (1-2°) therefore there is no measurable contrast difference between them in the type of TEM micrographs used to obtain an overview of grain structure [188].

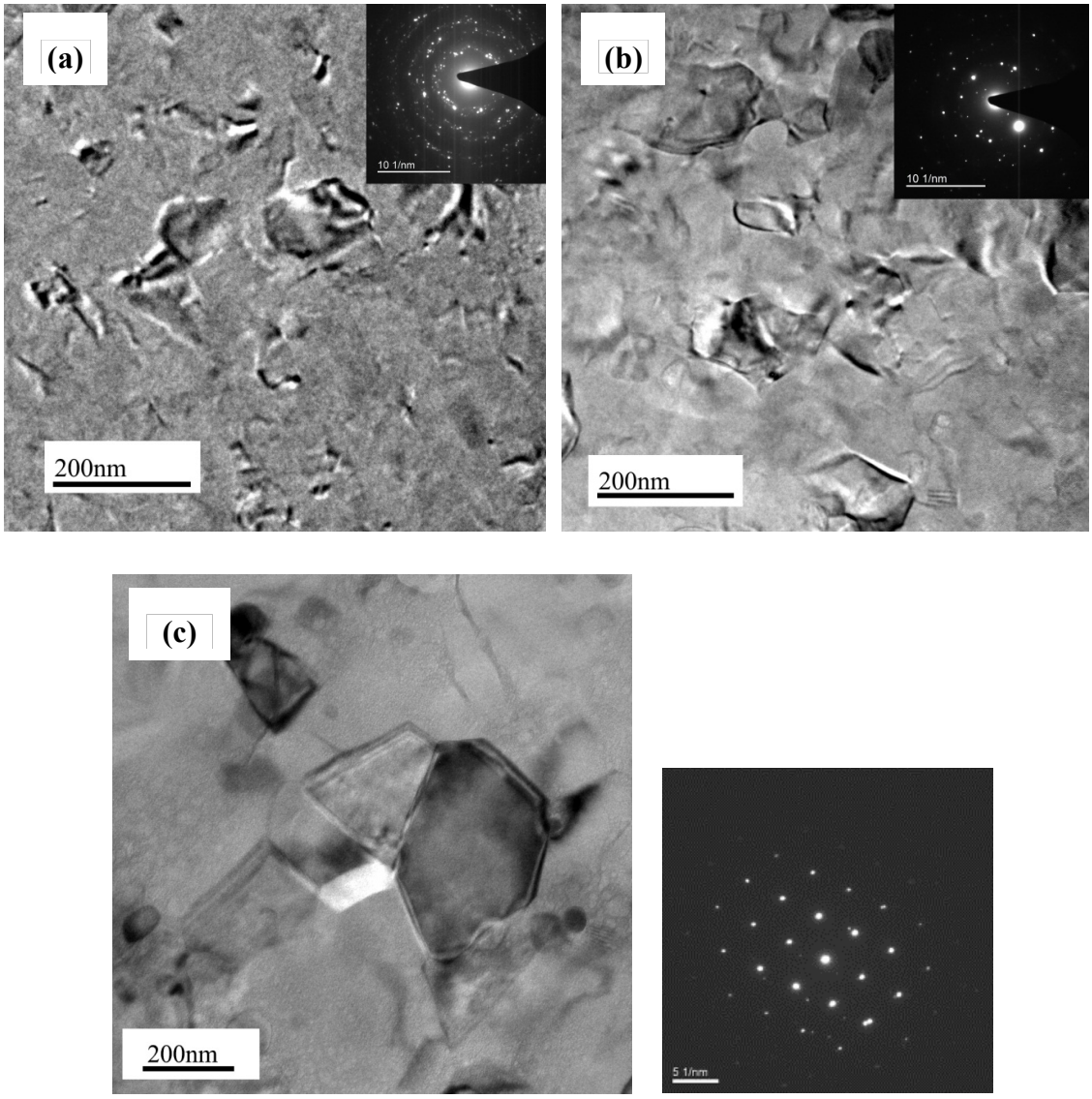

Fig. 6.6 TEM bright field images of 5r-HPT samples in as HPT processed condition (a); and after heating to 210 °C (b); after heating to 300 °C (c). The corresponding selected area diffraction patterns are at the top-right corner. (Samples (a) and (b) were operated using a Philips CM200 field emission gun TEM, while sample (c) was operated using a JEOL 3100 TEM).

6.1.4 Atom probe microscopy

The HPT processed sample and samples subsequently subjected to equivalent annealing have been analysed using APM. Cu, Mg and Si distributions of 5r-HPT sample have been illustrated in Fig. 5.11 in Chapter 5, whilst Cu, Mg and Si distributions of 5r-HPT-210 °C sample and 5r-HPT-300 °C sample are shown in Fig. 6.7 to Fig. 6.8, respectively.

In Fig. 5.11, APT analysis of the 5r-HPT sample reveals significant solute segregation to grain boundaries (see black arrows in the figures). The solute-enriched features in this volume element involve: (i) a segment of grain boundary; (ii) a uniform distribution of fine scale solute-rich clusters (containing up to 50 solute atoms) with a number density of 1.99×10^{26} m^{-3} (as determined from the total number of solute clusters identified in the analysed volume). The vast majority of the segregants are Mg and Cu, and a small but a significant minor concentration of Si was also evident in corresponding atoms maps.

Fig. 6.7 shows Mg, Cu and Si atom maps of an analysed volume of a 5r-HPT sample heated to 210 °C (after removing single clusters <9 atoms). This volume contains three grain boundaries and some small precipitates. It illustrates a similar solute enrichment of Cu, Mg and Si as those of grain boundary segments in Fig. 6.7 (a), while dislocations segregated with solutes are observed at the right bottom of each map. The total number density of solute clusters in this volume is identified as 1.11×10^{26} m^{-3}. The number density of Mg-Cu co-clusters decreases significantly from 1.06×10^{26} m^{-3} after HPT processing to 0.60×10^{26} m^{-3} after subsequent heating to 210 °C. Fig. 6.7 (b) shows that the concentrations of Mg and Cu at grain boundary are 1.8 at.% and 1.9 at.%, respectively. However, the concentrations of Mg at 5 nm to the boundary are much lower about 0.6 at.% and 1.2 at.%; and the concentration of Cu at 5 nm to the boundary are 0.5 at.% and 1.1 at.%.

The XRD results show that on heating up to 300 °C, coarse S phase precipitates are formed, whilst the grain size increases significantly. Fig. 6.8 shows one coarse S precipitate as well as a thin grain boundary line on the bottom side. The measured

composition of the coarse particle indicates a ratio of Al:Cu:Mg equalling 2:1:1, which approaches the stoichiometry of S phase (Al_2MgCu). On heating, the total cluster number density decreased significantly to 2.42×10^{25} m^{-3}, while it shows a decrease of Cu-Mg co-cluster density to 1.22×10^{25} m^{-3}.

Previous APM work on a solution treated and aged 2024 aluminium alloy showed that solute clusters firstly formed during ageing by aggregation of the main alloying elements Cu and Mg, along with the minor elements Si and Zn [176]. In the present HPT-deformed samples, the clustering phenomenon is similar. The main alloy elements Mg and Cu concentrate along the grain boundaries or dislocation walls together with the minor element Si. The size of the nano-precipitates increases as the annealing temperature increases. Coarser precipitates were found in the sample heated to 300 °C (Fig. 6.8 (b)).

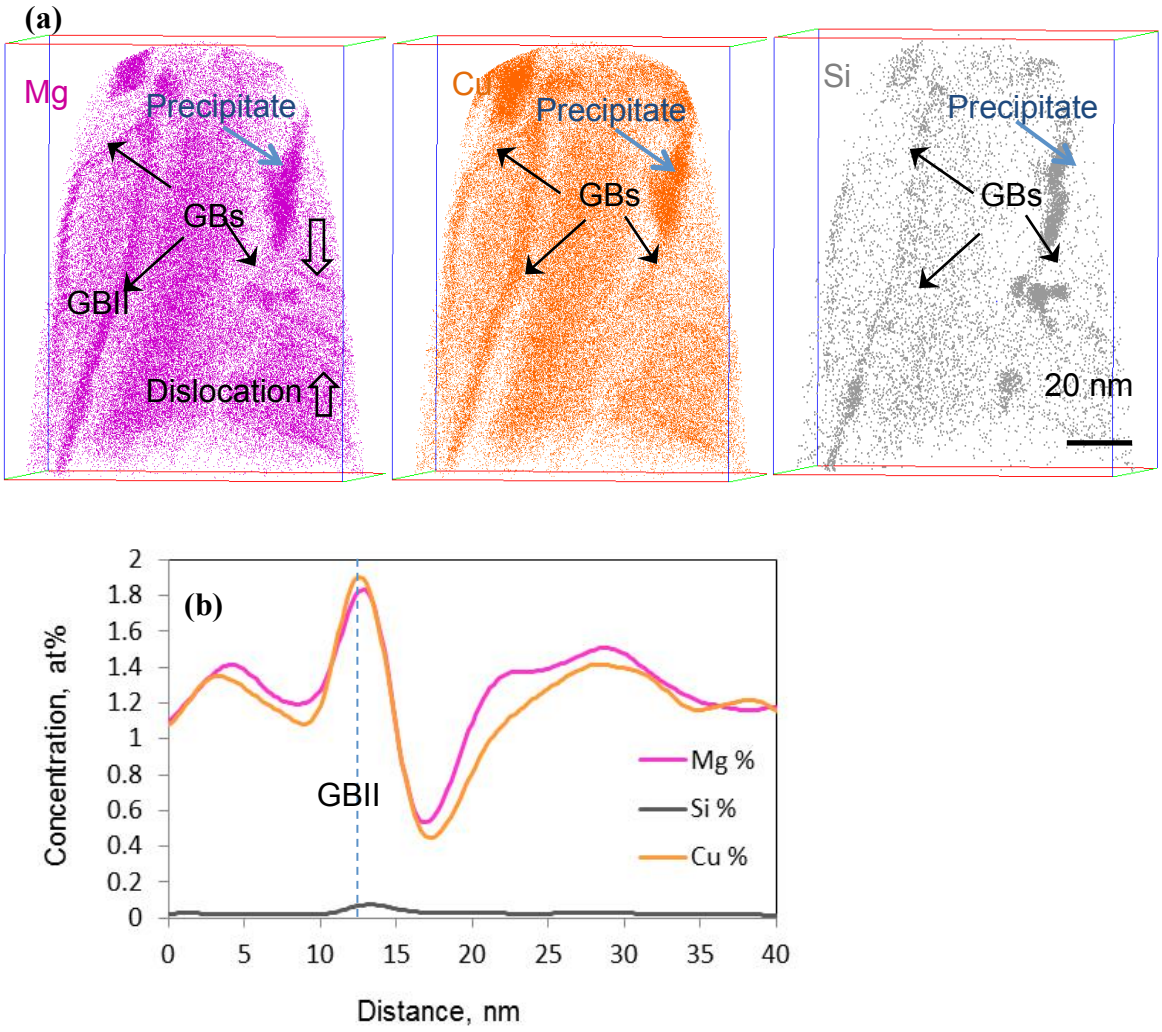

Fig. 6.7 3DAP of 5r-HPT sample annealing at 210°C (a) Mg, Cu and Si atom maps (b) Mg, Cu and Si profiles measured using an analysis box with its z-axis parallel to the plane normal of the grain boundary.

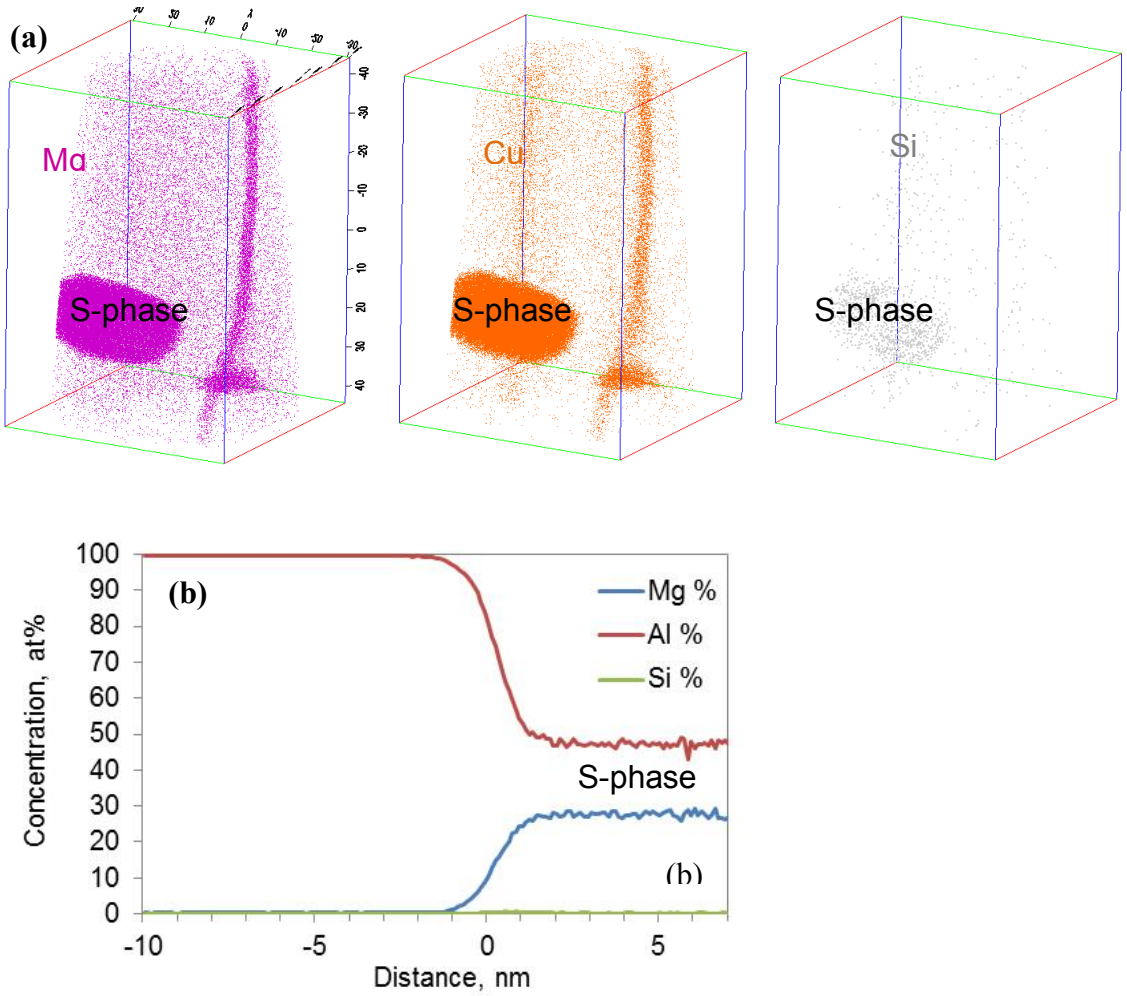

Fig. 6.8 (a) Mg, Cu and Si atom maps of 5r-HPT Al-Cu-Mg alloy aged at 300°C (b) concentration of Al, Mg, and Si (Cu in the balance).

6.2 Discussion

During the annealing of the ultrafine-grained Al-Cu-Mg alloy processed by HPT at a constant rate of 10 °C/min, the recrystallization started at 210 °C, and around this temperature S/S' precipitation started. The hardness of 5r-HPT sample is always higher than that of T351 until 260 °C (Fig. 6.1), indicating a good thermal stability. This is thought due to the presence of clusters, cluster-defect complexes or nano-precipitates, which hinder the movement of dislocations in grain boundaries and therefore further retain the fine grain sizes. Fig. 6.8 shows S particles at the grain boundaries.

In recent work [196], it is shown that the increment of hardness and grain refinement of pure metals due to SPD can be explained quantitatively by a model that incorporates dislocations in the grain and by grain boundaries, with the former providing the main contribution. Due to the existence of alloying elements, the ultrafine-grained Al alloys have the potential to achieve a higher strength, as the clusters segregate to grain boundaries. The discussion in Section 6.2.1 presents the relationship between grain size and hardness on the basis of Hall-Petch equation. The calculation of lattice parameter misfits in Section 6.2.2 presents the alloying element effects and indicates solute segregation after HPT.

6.2.1 Discussion on Hall-Petch relation

It is known that most nanocrystallite materials do not obey the Hall-Petch relation (if d<50 nm, the conversional microcrystalline limit) [83, 206, 215]. A complicated issue is whether the ‘grains size’ can be taken as the size determined by TEM or the crystallite size of coherently scattered domains as determined from X-ray line broadening analysis. The Hall-Petch relation is a semi-empirical formula, in which the value of the Hall-Petch constant k_{HP} will be greatly influenced by grain size measurement method. The XRD crystallite sizes in Section 5.1.2 and Section 6.1.2 present similar trends to TEM grain sizes described in Section 5.1.3 and Section 6.1.3, respectively: in HPT processing

the grain size decreases significantly, while the grain size increases in the subsequently DSC heating. The magnitudes of grain size measured by TEM are approximately 3 times the magnitudes of crystallite size measured by XRD.

To understanding of the Hall-Petch relation, HV vs $D^{-1/2}$ is plotted using crystallite size data obtained from XRD profile broadening. The Hall-Petch plot in Fig. 6.9 is clearly not linear. In the coarse grain region ($D^{-1/2}$ <3500 $m^{-1/2}$) the hardness increases with the decrease of grain size, but in the ultrafine grain region ($D^{-1/2}$ >3500 $m^{-1/2}$, where the k_{HP} appears to be negative) the hardness decreases with the decrease of grain size. Furthermore, a misfit in hardness is shown in the red circle. It is clear from the present work and a range of other works (i.e. [113, 117, 118, 196, 216, 217]) that grain boundary strengthening is not the dominant strengthening effect in nanoscale materials.

The Hall-Petch type plot in Fig. 6.9 cannot be interpreted in terms of grain boundary strengthening mechanisms. Instead, the effect for nanoscale grain size is dominated by the combination of Cu-Mg co-clusters and dislocations.

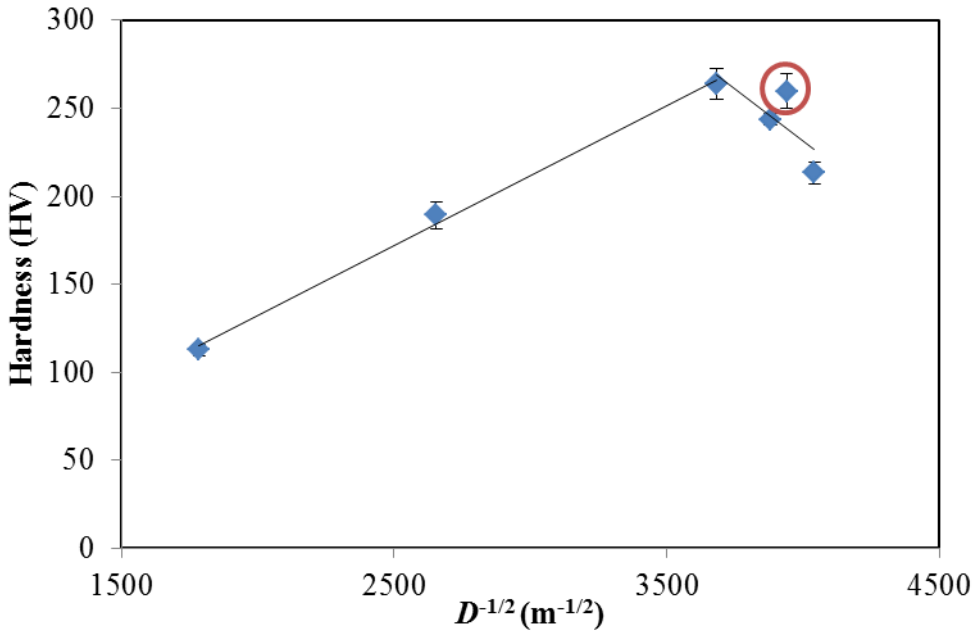

Fig. 6.9 Hall-Petch plot, Hv vs. $D^{-1/2}$ for 5r-HPT samples annealing up to different temperature. D is the crystallite size measured from XRD.

6.2.2 The lattice parameter misfits

The XRD analysis shows that HPT processing significantly affects the crystal lattice parameter *a* of the Al-Cu-Mg alloy, reducing from *a*=4.0523 Å in the T351 condition to *a*=4.0510 Å after 5r-HPT processing. Both values of T351 and 5r-HPT samples are larger the lattice parameter of pure Al 4.0495 Å (as given in the PDF-ICDD database and the Ref. [185]). The lattice parameter of Al-Mg-Cu alloys is directly linked to the amount of Mg and Cu in solid solution [218]. The dissolved Cu and Si atoms in the Al matrix decrease the lattice parameter, while the dissolved Mg atoms increase the lattice parameter. An example showing Mg dissolving effect in recent SPD research [219]:1 at.% Mg resulted in a change of *a* by 0.0046 Å, while 1.6 at.% loss of Mg after HPT caused a decrease of 0.0073 Å in Al-Mg alloys.

In Al-Cu-Mg(-Si) alloys, the lattice parameter change owing to different elements can't be taken simply as the sum of the independent contributions, but the solute-solute interactions need to be taken into account [218]. In the case of Cu-Mg interactions, it is assumed that the interactions are proportional to the virtual concentration of S (Al_2CuMg) phase. Consequently, the maximum lattice parameter shifts in the Al-(1-*x*) at.%Cu-2*x* at.% Mg alloy [220] was equalled 0.00006 nm for *x*=1/3. Hence, the interaction term $\Delta a^{i}_{\text{Cu-Mg}}$ can be approximated by

$$\Delta a^{i}_{\text{Cu-Mg}} = -\left[\text{Al}_2\text{CuMg}\right] \times 0.009 \text{ nm} \tag{6-1}$$

where [Al_2CuMg] is the virtual concentration of Al_2CuMg in the Al matrix, i.e. [Al_2CuMg]=[Cu] when [Cu]<[Mg] or [Al_2CuMg]=[Mg] when [Cu]≥[Mg].

In present study for the Al-Cu-Mg (-Si) alloy, the Mg-Si interaction also has an influence on lattice parameter change. It is assumed that for Mg-Si interactions, a relationship to that for Cu-Mg holds. It correlates to the Mg_2Si phase. The interaction term $\Delta a^{i}_{\text{Mg-Si}}$ can be approximated by Eq. (6-2) [218].

$$\Delta a^{i}_{\text{Cu-Mg}} = -\left[\text{Mg}_2\text{Si}\right] \times 0.026 \text{ nm} \tag{6-2}$$

where $[Mg_2Si]$ is concentration in Al matrix. Because [Mg] is much larger than [Si], $[Mg_2Si]$ equals to [Si], with the maximum value as 0.08 at.%.

Neglecting interaction among three atoms Cu, Mg and Si, lattice parameter changes owing to dissolved atoms are calculated from

$$\frac{\Delta a_{\text{Al}}}{a^{0}_{\text{Al}}} = p_{\text{Cu}} x_{\text{Cu}} + p_{\text{Mg}} x_{\text{Mg}} + p_{\text{Si}} x_{\text{Si}} + \frac{\Delta a^{i}_{\text{Cu-Mg}} + \Delta a^{i}_{\text{Mg-Si}}}{a^{0}_{\text{Al}}} \tag{6-3}$$

where x_{Cu}, x_{Mg}, x_{Si} are the concentrations of Cu, Mg and Si atoms in Al matrix; p_{Si} and p_{Cu} are the Vegard constant describing the effects of dissolved Si and Cu atoms on Al lattice parameter in binary alloys Al-Si or Al-Cu; $p_{\text{Mg}}(x_{\text{Mg}})$ is the non-linear function describing the effect of dissolved Mg atoms on Al lattice parameter [218].

In SPD processing, the lattice parameter will change as a result of solute segregation to subgrain boundaries/dislocation walls. The lattice parameter changes from T351 to 5r-HPT can be approximated by

$$\frac{\Delta a_{\text{SPD}}}{a^{0}_{\text{Al}}} = \frac{\Delta a^{\text{HPT}}_{\text{Al}} - \Delta a^{\text{T351}}_{\text{Al}}}{a^{0}_{\text{Al}}} = p_{\text{Cu}}\left(x^{\text{HPT}}_{\text{Cu}} - x^{\text{T351}}_{\text{Cu}}\right) + p_{\text{Mg}}\left(x^{\text{HPT}}_{\text{Mg}} - x^{\text{T351}}_{\text{Mg}}\right) + p_{\text{Si}}\left(x^{\text{HPT}}_{\text{Si}} - x^{\text{T351}}_{\text{Si}}\right) + \frac{\Delta a^{seg}_{\text{Cu-Mg}} + \Delta a^{seg}_{\text{Mg-Si}}}{a^{0}_{\text{Al}}} \tag{6-4}$$

Since no S precipitate was found in 5r-HPT XRD pattern (Fig. 6.3) and in APM mapping (Fig. 5.11 (a)), the overall solute concentrations of the Al-2.1Cu-1.8Mg-0.08Si (at.%) alloy is assumed to be unchanged during HPT processing. As a result, the lattice parameter changes due to HPT processing are thought to be only associated to the last term in Eq. (6-5),

$$\Delta a_{\text{SPD}} \approx \Delta a^{seg}_{\text{Cu-Mg}} + \Delta a^{seg}_{\text{Mg-Si}} \tag{6-5}$$

where $\Delta a^{seg}_{Cu\text{-}Mg}$ and $\Delta a^{seg}_{Mg\text{-}Si}$ are lattice parameter changes due to Cu-Mg cluster segregation and Mg-Si cluster segregation. Hence, the lattice parameter changes during SPD processing, Δa_{SPD}, equal to -0.00158 Å.

For a T351 sample, the value of a was measured to be 4.0523 Å, while that of 5r-HPT was 4.0510 Å (in Fig. 6.10).

$$\Delta a_{SPD} = \Delta a_{Al}^{HPT} - \Delta a_{Al}^{T351} = (a_{Al}^{HPT} - a_{Al}^{0}) - (a_{Al}^{T351} - a_{Al}^{0}) = a_{Al}^{HPT} - a_{Al}^{T351} \tag{6-6}$$

where $a_{Al}{}^{0}$, $a_{Al}{}^{T351}$ and $a_{Al}{}^{HPT}$ are lattice parameters of a pure Al, a T351 and a 5r-HPT sample, respectively. Eq. (6-6) suggests Δa_{SPD}=-0.0013 Å.

The XRD measured data shows a good correspondence to the lattice parameter changes in calculation. The small deviation (0.00028 Å) is probably caused by the interactions among Cu, Si and Mg atoms and other solute atoms. The lattice defects caused by dislocations and vacancies may also contribute to this deviation.

The formation of nano-precipitates (mainly Al_2CuMg) at 210 °C suggests a strong integration term $\Delta a^{i}_{Cu\text{-}Mg}$ in Eq. (6-2), and concentrations of Mg (x_{Mg}) and Si (x_{Si}) atoms in Al matrix is very small (≈0). Hence the lattice parameter changes owing to nano-precipitates are obtained from

$$\frac{\Delta a_{Al}^{HPT\text{-}210°C}}{a_{Al}^{0}} \approx p_{Cu}x_{Cu} + \frac{\Delta a_{Cu\text{-}Mg}^{HPT\text{-}210°C}}{a_{Al}^{0}};\ \ p_{Cu}x_{Cu} + \frac{-[Al_2CuMg]\times 0.009nm}{a_{Al}^{0}} \tag{6-7}$$

where p_{Cu} is the Vegard constant, 0.118 [221]; x_{Cu}, concentration of Cu in Al matrix at 210 °C, i.e. x_{Cu}=[Cu]-[Mg]=0.0031; the virtual concentration of Al_2MgCu, [Al_2MgCu]=[Mg]. The lattice parameter change of a 5r-HPT-210 °C sample in this model is 0.00199 Å.

The measured lattice parameter change of an HPT-processed sample in XRD experiments is presented as:

$$\Delta a_{210°C} = \Delta a_{Al}^{HPT\text{-}210°C} - \Delta a_{Al}^{T351} = (a_{Al}^{HPT\text{-}210°C} - a_{Al}^{0}) - (a_{Al}^{T351} - a_{Al}^{0}) = a_{Al}^{HPT\text{-}210°C} - a_{Al}^{T351} \quad (6\text{-}8)$$

where $a_{Al}^{HPT\text{-}210°C}$ is the lattice parameter of a 5r-HPT sample heating up to 210 °C. The measured lattice parameter change is 0.0020 Å (Fig. 6.10). This perfect correspondence provides a solid proof of the occurrence of S precipitation at 210 °C.

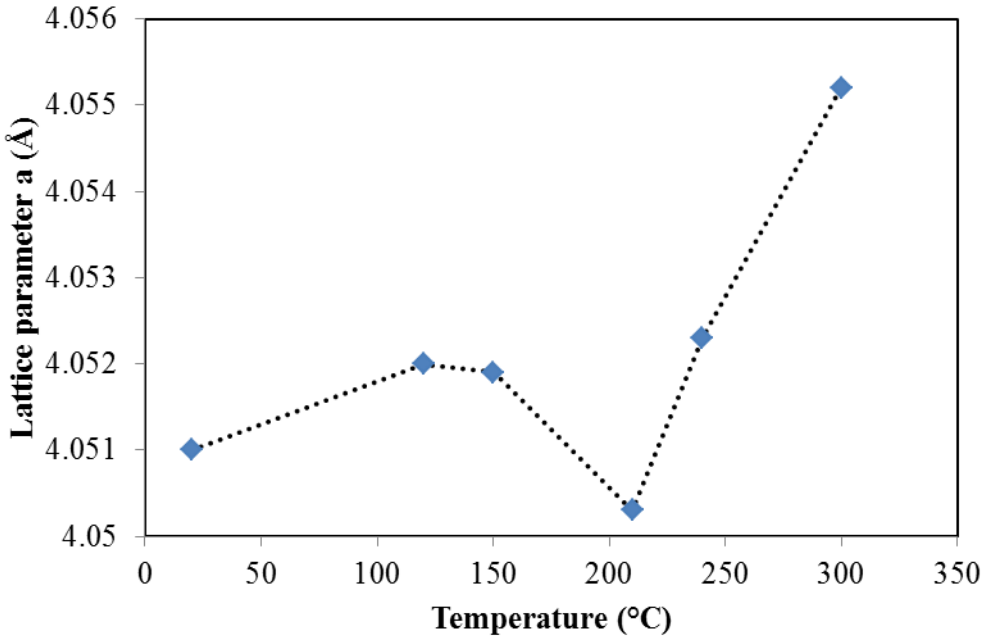

Fig. 6.10 The evolution of lattice parameters *a* during the equivalent isothermal heating from XRD pattern

In Fig. 6.10, the small increase of *a* (Δa=0.0010 Å) during heating from 25 °C to 120 °C and to 150 °C can be due to a decrease in dislocation density. The segregated clusters may dissolve at 150 °C, reducing the Cu-Mg and Mg-Si interaction term $\Delta a^{i}_{Cu\text{-}Mg}$ and $\Delta a^{i}_{Mg\text{-}Si}$.

The lattice parameter of 5r-HPT sample heat treated up to 120 °C (4.0520 Å) and 150 °C (4.0519 Å) are still smaller than that of T351 (4.0523 Å) without HPT deformation. The significant decrease of *a* at 210 °C corresponds to exothermic peak in DSC thermogram (Fig. 6.1). The lattice parameter at 210 °C (4.0503 Å) is even smaller than that of 5r-HPT sample at ambient temperature.

Hence, the exothermal effects at 210 °C (Fig. 6.1) are thought due to a combination of different contributions, including at least three components: dislocations annealing, small grain growth and nano-precipitation. There may be other additional components that may enhance the thermal effects at 210 °C, i.e. the dislocation-precipitate interactions/grain boundary-precipitate interactions, causing a distinction of two overlapping peaks at 210 °C and 240 °C.

6.3 A model predicting stored energy in HPT sample

6.3.1 General model structure

The DSC thermograms indicate a substantial enthalpy release for the samples processed by HPT. Lattice strain (microstrain) and the small crystallite size are thought to be dominant causes for the increased enthalpy. The enthalpy released during DSC heating implies the occurrence of the recovery of lattice defects created by HPT in association with grain coarsening. In practice the changes in enthalpy are closely correlated to changes in Gibbs free energy [134, 222-224], thus the discussion on enthalpy in DSC is valid for the Gibbs free energy as well.

The enthalpy released in DSC incorporates at least four components: (i) the enthalpy due to dislocations annihilation, ΔE_{dis}, (ii) the enthalpy due to grain coarsening and grain rotation, ΔE_{gb}, (iii) the enthalpy associated with the co-clusters (atomic short range order), ΔE_{cl}, and (iv) the enthalpy due to solute desegregation ΔE_{deg} ,which is too small to be neglected, (<~0.5 J/g [222]).

An expression of the total enthalpy changes is presented as

$$\Delta E = \Delta E_{dis} + \Delta E_{gb} + \Delta E_{cl} \quad \cdots\cdots \quad (6\text{-}9)$$

In the below we will assess how these different components contribute to the total enthalpy change.

6.3.2 Stored energy measured in DSC

Fig. 4.3 shows an overall trend of the enthalpy released in DSC for samples processed by various HPT rotations. The lattice stored energy is thought to be the enthalpy differences between HPT samples and full annealing samples, if taken the full annealing sample as a standard reference, which is

$$\Delta E = \Delta E_{\text{HPT}} - \Delta E_{\text{annealling}} \tag{6-10}$$

The DSC measured stored energy linearly increase with the equivalent strain is shown as blue diamonds in Fig. 6.11.

6.3.3 Enthalpy due to dislocation annihilation

The Vickers hardness is generally expressed as Eq. (5-14)

$$H_V = C\sigma_y$$

The strength increase due to presence of solid solution, dislocations inside the grain and precipitation are incorporated in the total shear stress Eq. (5-2),

$$\Delta\sigma = M\Delta\tau$$

In conversional CRSS theory, the interaction between defects and solute atoms/co-clusters has not been taken into consideration (see also Section 5.2.2). The dislocation strengthening is thought to be one of the dominant strengthening components (see also

[13, 118, 192, 193]), the strengthening due to dislocation density is expressed by Eq. (5-4), which is

$$\Delta\tau_d = \alpha_1 Gb\sqrt{\rho}$$

where α_1 is an empirical constant, usually taken as 0.3 [118], which is applied in the present model. *G* is the shear modulus, *b* is the Burgers vector.

With the combination of Eq. (5-2), Eq. (5-4) and Eq. (5-14), dislocation density in HPT can be broadly approximated by

$$\rho = \left(\frac{H_V}{CM\alpha_1 Gb}\right)^2 \tag{6-11}$$

The enthalpy due to dislocation annihilation is evaluated in Eq. (6-12), suggesting the total stored energy of random dislocations [222, 225, 226]:

$$E = \rho \mathrm{g}\frac{Gb^2}{4\pi\kappa}\ln\frac{R_e}{r_0} \tag{6-12}$$

where κ equals 0.67~1, due to the fraction of screw or edge dislocations in the UFG sample. R_e and r_0 are the outer and inner cut off radii of the dislocations, respectively; r_0 is approximated by b/2 , whilst R_e is evaluated from the measurements, which is expected to lie between the value of distance between dislocations and the cell size [223, 225].

Thus, the relationship between hardness and stored energy is derived as

$$E_D = \frac{1}{4\pi\kappa}\ln\frac{R_e}{r_0}\cdot\frac{1}{G}\left(\frac{H_V}{CM\alpha_1}\right)^2 \tag{6-13}$$

Eq. (6-13) provides an easy way to calculate the stored energy directly from hardness in engineering. This formula shows a good consistence with the stored energy relationship established in [227]:

$$E_D \cong \frac{\left(M\alpha HV/3\right)^2}{G} \tag{6-14}$$

where G is the shear modulus, M is the Taylor factor, and the constant α is approximated as 0.5 for Al.

The parameters applied in the model are listed in Table 6-1. Fig. 6.11 illustrates the predicted enthalpy due to accumulated dislocations. The upper line (light blue cross) is for screw dislocations (κ=0.67); and the lower line (red square) is for edge dislocations (κ=1). With a dependency of fraction of screw or edge dislocation, the dislocation stored energy is predicted within the region between the lines in blue and red in Fig. 6.11. The enthalpy due to dislocations increases as the strain increases.

Table 6-1 Parameter values used in the model

Parameters	Values	Ref
C	~3	[117, 205]
M	2.6	[13, 117]
G	26 GPa	[13, 117]
κ	0.67~1	[223, 225]
r_0	0.143 nm	[228]
α_1	~0.3	[95]
R_e	50~60 nm	Cell size detected from XRD, also been exanimated by dislocation distances (using Eq. (4-3))

6.3.4 Enthalpy due to grain/subgrain boundaries

The enthalpy release due to grain coarsening and grain rotation for low-angle grain boundaries can be estimated from the Read-Shockley relationship [118, 227, 229],

$$\Delta E_{gb} = \frac{\left[\gamma_m \left(\frac{\bar{\theta}}{\theta_m}\right)\left(1 - \ln\left(\frac{\bar{\theta}}{\theta_m}\right)\right)\right]}{d_{SG}} \tag{6-17}$$

where γ_m and θ_m are the boundary energy and the maximum misorientation angle of low-angle boundaries, $\bar{\theta}$ is the average misorientation angle and d_{SG} is the average subgrain diameter [227]. γ_m is taken as 0.3 J/m^2 [227, 230]. Analysis of $\bar{\theta}$ data on a number of severely plastically deformed Al alloys [17, 231, 232] has shown that $\bar{\theta}$ can be approximated well by [13, 118, 134]:

$$\frac{\bar{\theta}}{\theta_m} = 1 - \left(\left(k_1 \varepsilon\right)^{n_1} / \eta + 1\right)^{-\eta} \tag{6-18}$$

where the exponent n_1 is equal to 1, $\overline{\theta_m}$ is the maximum value that average misorientation angle can take 15°. Here, to simplify the equation, we take k_1 equal to 1 and η is assumed to be 0.3 [118]. In the Read-Shockley model, the grain misorientation must be very small. In XRD profile broadening analysis, the crystallite size is the size of coherently scattering domain, the grain orientations of which must be the same. The misorientation between scattering domains are very small; and therefore, the crystallite domains are considered to be low-angle grains. Hence, subgrain grain diameters in Eq. (6-17) are assumed to be equivalent with crystallite size. The enthalpy correlated to grain boundary recrystallization is plotted as purple balls in the bottom of Fig. 6.11. Its contribution is very small (~2 J/g) as compared to the enthalpy change due to dislocation annihilation.

6.3.5 Solute-defect interaction and further refinement of model

The store energy evaluated in DSC is much higher than the enthalpy due to dislocation annihilation and grain coarsening for samples processed by HPT to a very high strain. A possible explanation is the formation of a more stable solute-defect complex structure, which hinders the movement of dislocations and further increases the strength (see also Section 5.2). Solute atoms segregate to grain boundaries after HPT processing (see Fig. 5.11), and tend to form nanoprecipitates along grain boundaries/dislocation walls during DSC heating (see Fig. 6.7). The formation of nanoprecipitate destroys the solute-defect complexes, and leads to a decrease in strength and stored energy.

The presence of clusters (like the Mg-Cu co-clusters in Al-Cu-Mg samples) is associated with stored energy [57, 194]. APT study indicates the number density of Cu-Mg co-clusters decreases significantly during annealing. The stored energy due to formation of cluster-defect complexes can be calculated as

$$\Delta E_{\text{cl}} = (n_0 - n_1)\Delta H_{\text{cl-dis}} \tag{6-19}$$

where n_0 and n_1 are the number density of clusters before and after annealing. In an Al-Mg-Cu alloy, the major enthalpy of the nearest neighbour bond is $\Delta H_{\text{cl-dis}}$= 49.5 kJ/mole, which has been fitted in Section 5.2.5. In analysing APM data, the detection efficiency leads to an underestimate of the number of clusters ([233, 234] and also presented in Section 5.2.6). The detection efficiency is taken as 0.55 for the measurement of stored energy due to short range effect of solute-defect complexes. The green triangle in Fig. 6.11 presents a predicted total enthalpy correlated with all parameters, dislocations, grain boundaries and solute-defect stable complexes.

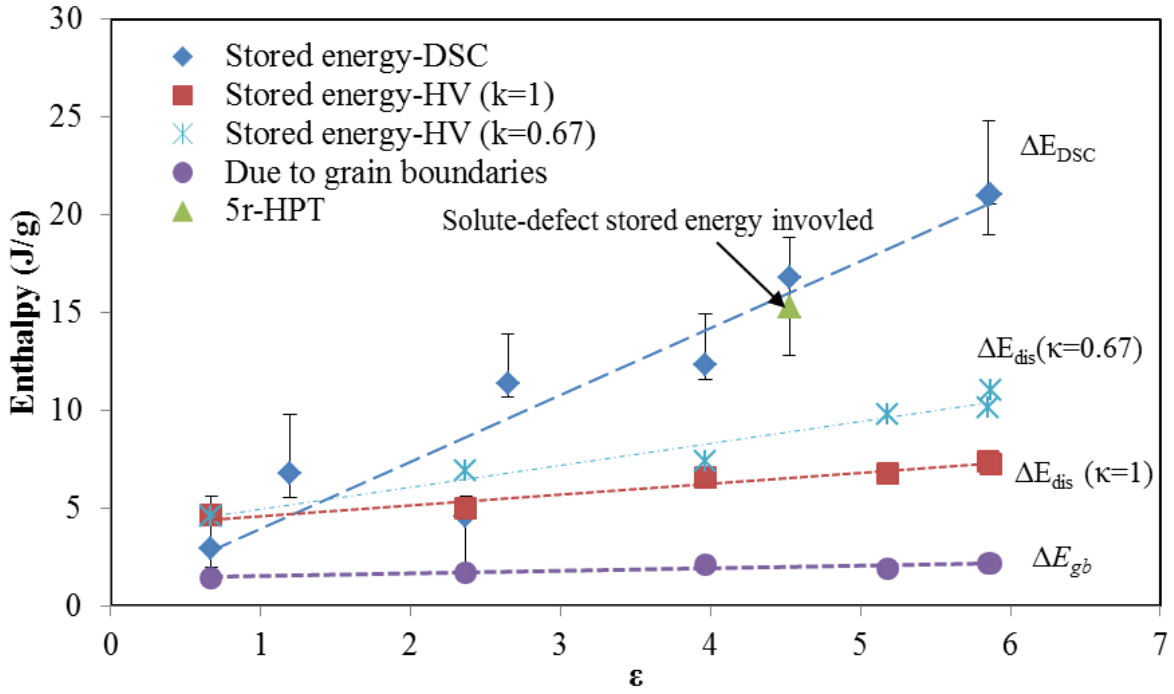

Fig. 6.11 Predictions of stored energy in UFG Al-Cu-Mg alloy processed by HPT

6.3.6 Verifying the model

The predicted total stored energy of 5r-HPT sample in Fig. 6.11 shows a good correspondence with the enthalpy measured by DSC. But accurate value for the stored energy cannot be calculated because no substantial APT data for samples processed by HPT and heat treated at 300 °C are available.

Besides, some uncertainties need to be kept in mind for the calculations of stored energy in the model above. Enthalpy due to dislocation annihilation is approximated on the basis of hardness measurements. In addition, some other strengthening mechanisms in UFG Al-Cu-Mg alloys (i.e. solid solution contribution, a modulus strengthening component, a short range order strengthening component, and grain refinement) also co-exist but they haven't been considered in the model. It will overestimate the individual component of stored energy due to dislocation annihilation, but underestimate the stored energy correlated to the interaction between solute/cluster and dislocations. The calculation in Section 6.3.5 provides an approximated calibration.

6.3.7 A refinement of model

The classic theories describe the dislocation behaviours in SPD alloys as: a large number of dislocations generate due to cold plastic deformation, pre-existed dislocations move and travel through the crystal until being blocked by an obstacle (i.e. another dislocation, grain boundaries, solute atoms/clusters, or a second short range phase particle). The dislocations are stored in grains, while new dislocations can be generated to continue the deformation [117, 118] (see also Section 2.4.1). In the second stage, the accumulated dislocations will form the subgrain boundaries, of which grains will rotate and increase misorientation angle between the adjacent grains.

The moving dislocations will either be mobile in the grain, be accumulated at grain boundaries or be stuck by solute atoms, clusters, or second phase particles within grains. Thus the changes in the numbers of dislocations are described as

$$\rho_{\text{gen}} = \rho_{\text{GB}} + \left(\rho_{\text{G}} + \rho_{\text{S}}\right) \tag{6-20}$$

where ρ_{gen}, ρ_{GB}, ρ_{G} and ρ_{S} are dislocation densities generated in grains, accumulated in grain boundaries, mobile within grains, and immobile due to short range order phase particles.

No matter which formation it tends to be, the energy initially added for alloy deformation is equal to the sum of enthalpy for dislocation generation and enthalpy due to the rotation of the grains, forming the grain boundary misorientation. The total stored energy is thought be given as

$$\Delta E = \Delta E_{gen} + \Delta E_{gb} \tag{6-21}$$

where ΔE_{gen} is the enthalpy due to initial dislocation generation, and ΔE_{gb} is the enthalpy due to grain rotations.

A total dislocation density generated since the start of deformation is expressed by [117],

$$\rho_{\text{gen}} = \left(\frac{K_A}{\alpha_1 MGb} \right)^2 \varepsilon \tag{6-22}$$

where K_A is a factor incorporates the contribution of the solid solute atoms, G the shear modulus, M the Taylor factor, α_1 the constant, b the Burger vector, ε the equivalent strain in HPT deformation [117]. The model in Section 2.4.1 describes the density of dislocations generated during deformation up to a stain of 5%. Here, we make the assumption that the total number of dislocations generated in SPD regime (strains>3) is given by the same equation. The key element in this model is the value K_A, which increase linearly with the amount of Mg dissolved in the Al-rich phases for a range of solution-treated Al-Mg-Cu alloys [235], as Mg addition drastically increases the dislocation density [188]. For spherical obstacles in an alloy with dissolved alloying elements i, at concentration x_i, K_A is given by

$$K_A = C_2 G M^{\frac{1}{2}} b^{\frac{1}{2}} \left(\left[\frac{f}{2r} \right]^2 + \sum \left[B_i x_i \right]^2 \right)^{\frac{1}{4}} + K_A^0 \tag{6-23}$$

where B_i are constants, K_A^0 is the contribution due to generation of dislocations unrelated to geometrical or chemical obstacles. The fitting has been performed by Starink et al [117], indicating the value K_A in Al-2.1Cu-1.8Mg-0.08Si (at.%) alloy is ~410 MPa. The value of K_A has been measured to be 430 MPa by uniaxial tensile or compression test for this Al alloy.

In this refinement, the solute-dislocation effect has been taken into consideration for dislocation generation. The intrinsic stored energy of a dislocation unit is related to Eq. (6-12) and given as

$$E_{gen} = \rho_{gen} \mathrm{g} \frac{Gb^2}{4\pi} f(v) \ln \frac{R_e}{r_0} \tag{6-24}$$

where a small adjustment on proportion of screw and edge dislocations, which is expressed as a function of Poisson's ratio $f(v)$ [230],

$$f(v) = \frac{1 - v/2}{1 - v} \tag{6-25}$$

where v is taken as 0.3. The stored energy predicted by this refinement model is plotted as orange triangle in Fig. 6.12. It shows an excellent agreement with the DSC measured enthalpy.

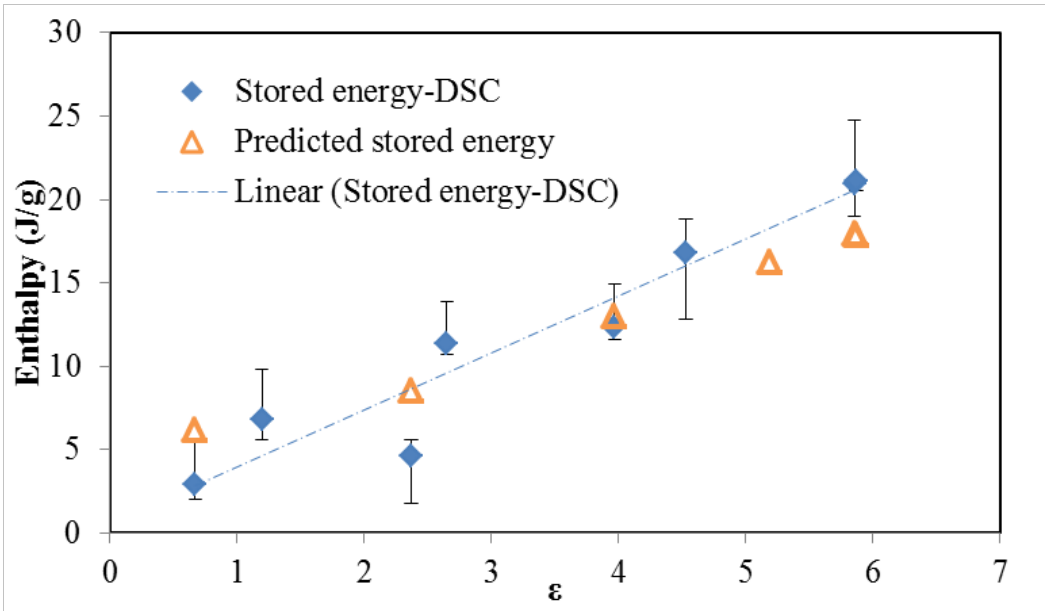

Fig. 6.12 A prediction in stored energy for the refined model in UFG Al-Cu-Mg alloy processed by HPT.

6.4 Summary

In this chapter, the microstructural modification of UFG Al-Mg-Cu alloy samples during DSC heating has been studied.

The changes of microstructures in DSC heating incorporates dislocation recovery, recrystallization of ultrafine grain microstructures, desegregation of solute atoms, formation of nano S precipitate, and precipitate coarsening.

At 210 °C, crystallite size increases and dislocation density decreases. As nano precipitates are observed in APM significantly, the exothermic effects around 210 °C are thought to be due to a combination of different contributions, including at least three components: dislocation annealing, grain growth and nano scale precipitation.

The UFG Al-Cu-Mg matrix shows a high thermal stability caused by the pinning effect of the numerous segregated atoms and small precipitates.

The existence of solute-defect complexes reduces overall Gibbs energy and increases the stored energy for UFG Al-Cu-Mg alloy processed by HPT. The refined model in Section 6.3 shows a good correspondence in stored energy prediction.

Chapter 7 Influence of reversal strain during HPT on strengthening and microstructures in an Al-Cu-Mg alloy

HPT is different from other SPD processes. The microstructural inhomogeneity of HPT has been studied in Section 5.1.1. In HPT processing, strain gradients are imposed by torsion deformation in the radial direction. Dislocation theory suggests that the plastic flow strength of materials depends not only on the magnitude of strain but also on the gradient of strain.

Some basic questions haven't been solved in previous chapters, i.e.: how do the original grains fragment into much smaller structural units? How do the strain gradients affect the refinement processes? DSC and XRD studies on reversal-rotation HPT provide answers to these questions. In this chapter, the studies on DSC, hardness in DSC heating, and XRD quantitative analysis are presented in the result section. Section 7.2 schematically illustrates the mechanism of grain refinement and the influences of strain gradients. Section 7.3 presents a model on strain gradient plasticity for samples processed by SR-HPT.

7.1 Results

7.1.1 DSC analysis on single reversal HPT Al-Cu-Mg alloy

Disks were processed by single reversal HPT of 90°, 180° and 360° in the counter-clockwise direction following 5r-HPT deformation. Samples were punched in the centre region with 5 mm in diameter or punched in the edge region, where distance to the centre is between 2.5 mm to 5 mm. DSC was performed by heating the samples from 25 °C to 540 °C at a constant heating rate of 10 °C/min. Following the equivalent

isothermal heat treatment at different temperature in DSC thermographs, Vickers hardness test were performed on SR-HPT samples using a load of 500 g. XRD was conducted on samples punched from the centre and the edge areas of the samples.

Fig. 7.1 (a) shows the DSC thermographs of the centre area in SR-HPT samples. There seems no difference in exothermic effect A (peaking at ~170 °C) between these SR-HPT samples. The decrease in heat flow at 200 °C is caused by the dissolution of cluster-defect complexes. This indicates the reversal strains contribute very little to the formation or redistribution of clusters-dislocation complexes. The overlapping exothermic regions B and C are thought predominantly due to dislocation annihilation, grain/subgrain recovery and the precipitation of S phase (see also Chapter 5). The heat flow of exothermic peak B decreases with the increasing of the inverse rotation number. The magnitudes of heat flow peaking B are nearly the same for samples processed by ½ and 1 inverse rotation. However, the heat flow of exothermic peak C presents an inverse trend, which increases with the increasing inverse rotation number. The magnitudes of heat flow peaking C are close to each other for the 5r-HPT sample and the sample processed by a ¼ inverse rotation.

Fig. 7.2 (b) illustrates the DSC thermographs of SR-HPT samples in the edge areas. The magnitudes of the heat flow peaking B are much higher than those of heat flow peaking at C. The peak magnitudes B decrease with the increase of the inverse rotations. The heat flow peaking B decreases very slightly with the increasing of inverse rotation number, i.e. the blue solid line (5r-HPT) and the red break line (5r-1/2r-HPT). But there are few differences in curves between samples processed by an 1/2r inverse HPT and 1r inverse HPT, indicating the saturation of dislocations and no strain gradients in these edge regions. The microstructures of HPT samples become homogeneous in the periphery of discs after processing a high number of rotations [1] (see also Section 5.1).

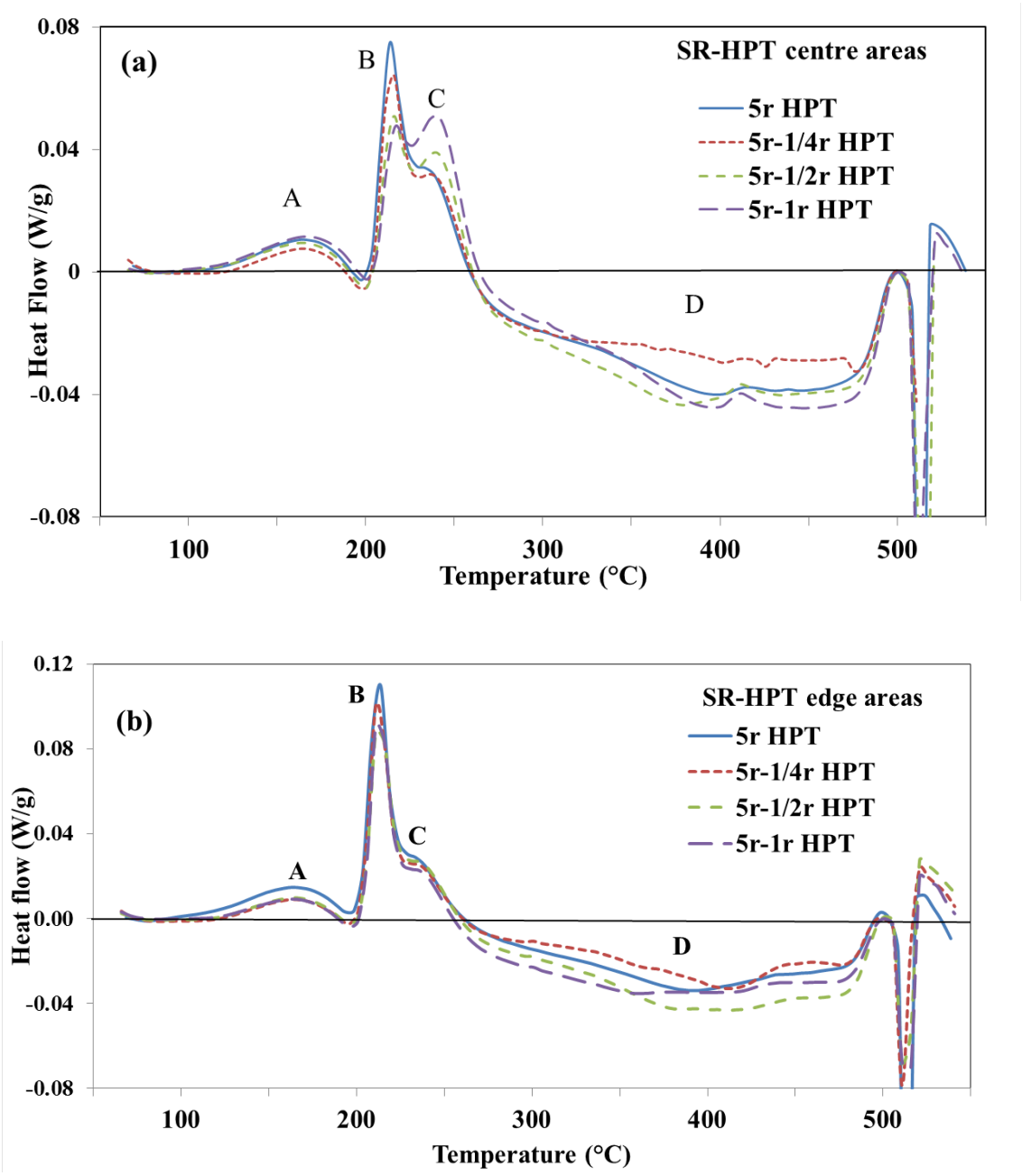

Fig. 7.1 DSC traces of 5r-HPT deformed samples subjected to inverse rotations of 1/4, 1/2 and 1 rotation, respectively, (a) centre areas (b) edge areas.

7.1.2 Vickers hardness test

Vickers hardness tests were carried out on samples subjected to small inverse rotations and the subsequent heat treatment. In Fig. 7.2, there are some slight differences in hardness of samples processed by SR-HPT and subsequent DSC heat treated up to 200 °C. The hardness of each sample decreases dramatically when heating temperatures above 200 °C.

For the 5r-HPT sample, the hardness increases slightly to 253HV at 140 °C and stays unchanged until 200 °C. In the 5r-1/4r HPT sample, the hardness first decreases to 235 HV at 140 °C then increases again to 259 HV at 200 °C. The hardness of the 5r-1/2r HPT sample approaches its maximum value of 278 HV at 170 °C, and decreases a little at a higher temperature. For the 5r-1r HPT sample, the evolution of hardness in DSC heat treatment at a series of temperatures is nearly the same as the hardness of a 5r-HPT sample.

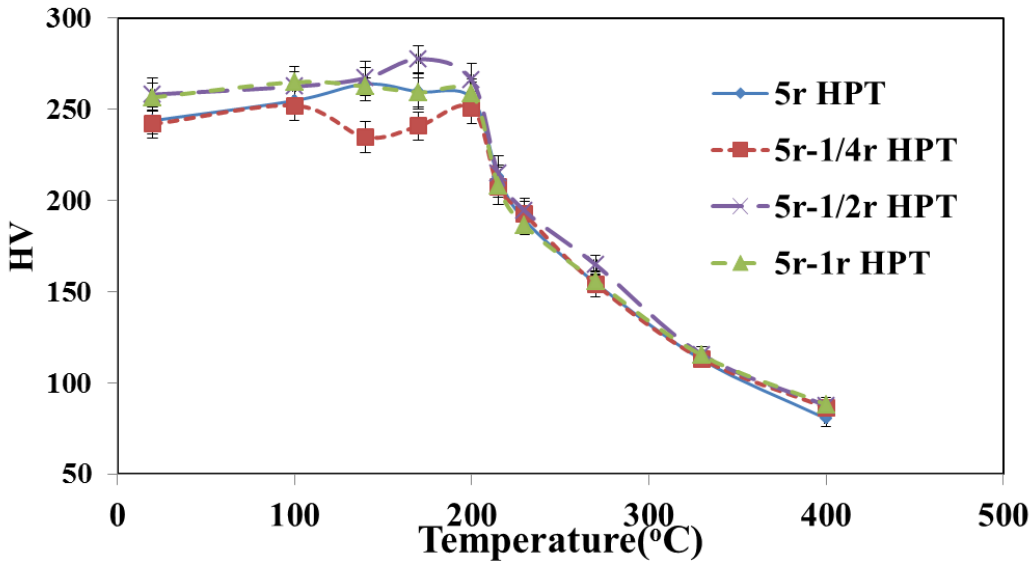

Fig. 7.2 Hardness of 5r-HPT samples with 0, ¼, 1/2 and 1 rotation in the opposite direction.

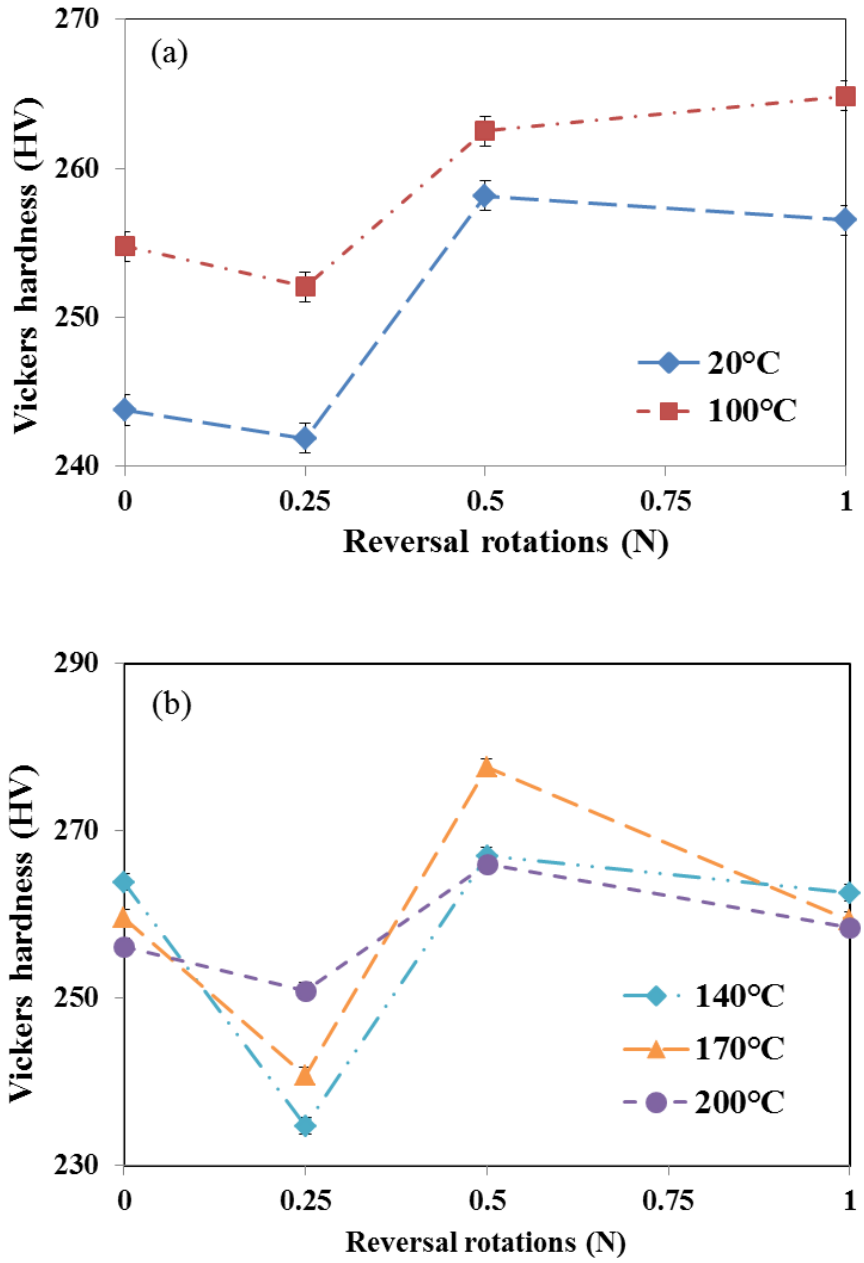

Fig. 7.3 Hardness evolutions due to reversal HPT at (a) 20, 100°C; (b) 140, 170 and 200°C.

Fig. 7.3 shows the hardness evolution due to single reversal- HPT (SR-HPT) deformation and followed by DSC heat treatments up to 20, 100, 140, 170 and 200 °C. Both figures present similar trends for samples heat treated at various temperatures. The hardness first decreases when subjected to an ¼-inverse rotation. Subsequently, it increases to the maximum value for the ½ inverse rotations. The hardness shows a good

correspondence to DSC heat flow evolution at 210 °C, especially for those samples in the central areas (see Fig. 7.1).

7.1.3 X-ray diffraction analysis

The XRD patterns of SR-HPT samples are classified in three groups (full disks, centre areas, and edge areas). Fig. 7.4 shows the full disk patterns of SR-HPT samples. The differences are small, but the profile broadening analysis using Willamson-Hall plots (in Fig. 7.5) for all disks in the centre and edge indicates an evolution of the average crystallite size and microstrains after inverse rotations, see Fig. 7.6.

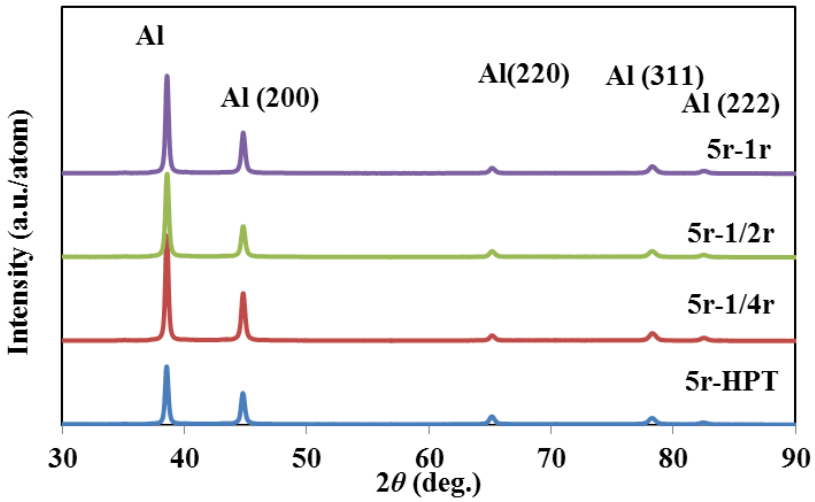

Fig. 7.4 The X-ray diffraction patterns of 5r-HPT samples were processed by HPT reversal ¼, ½ and 1 rotations.

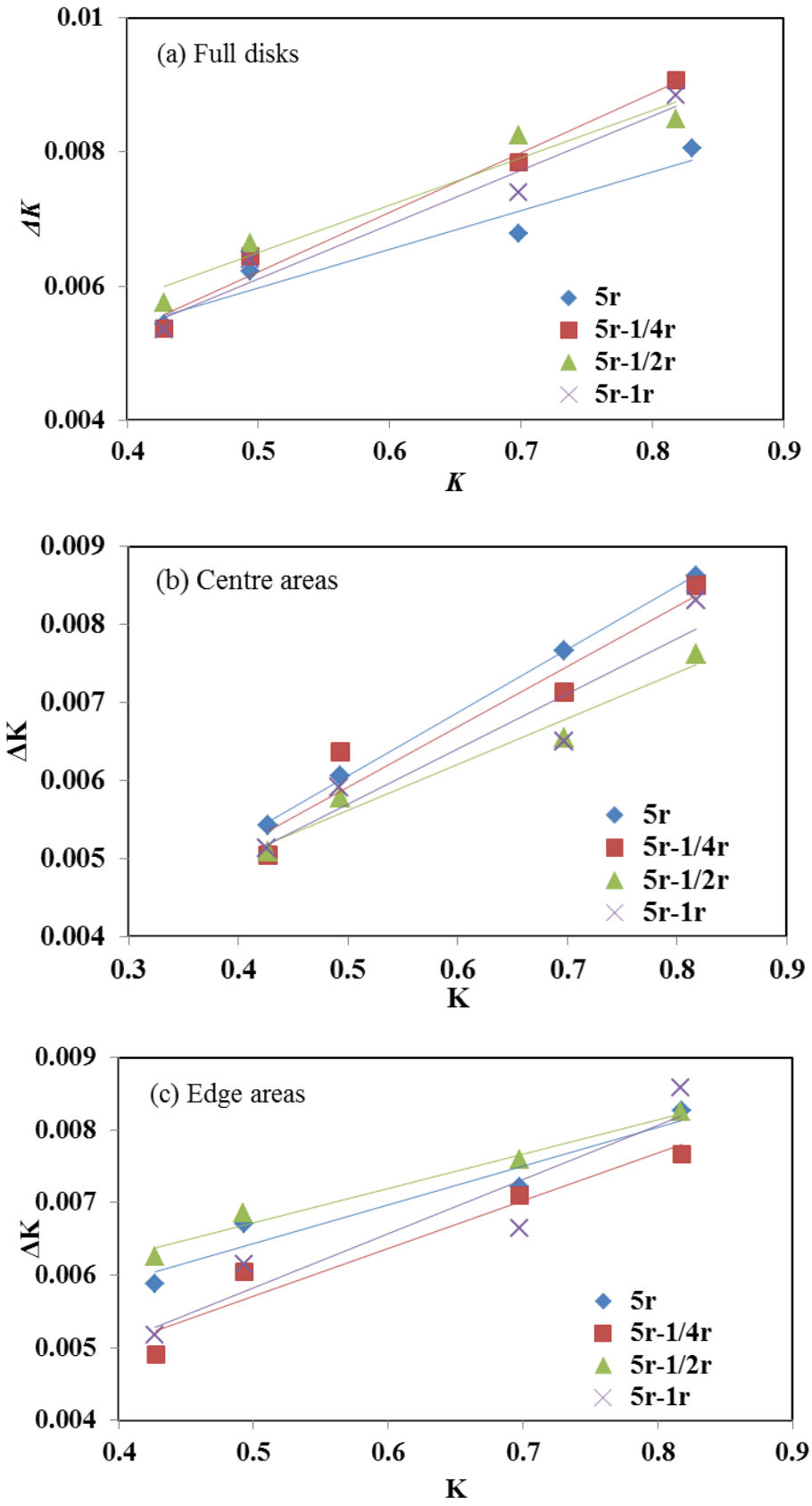

Fig. 7.5 Williamson-Hall plots of 5r-HPT Al-Cu-Mg samples followed by 1/4, ½ and 1 inverse rotations (a) full disks; (b) centre areas; (c) edge areas.

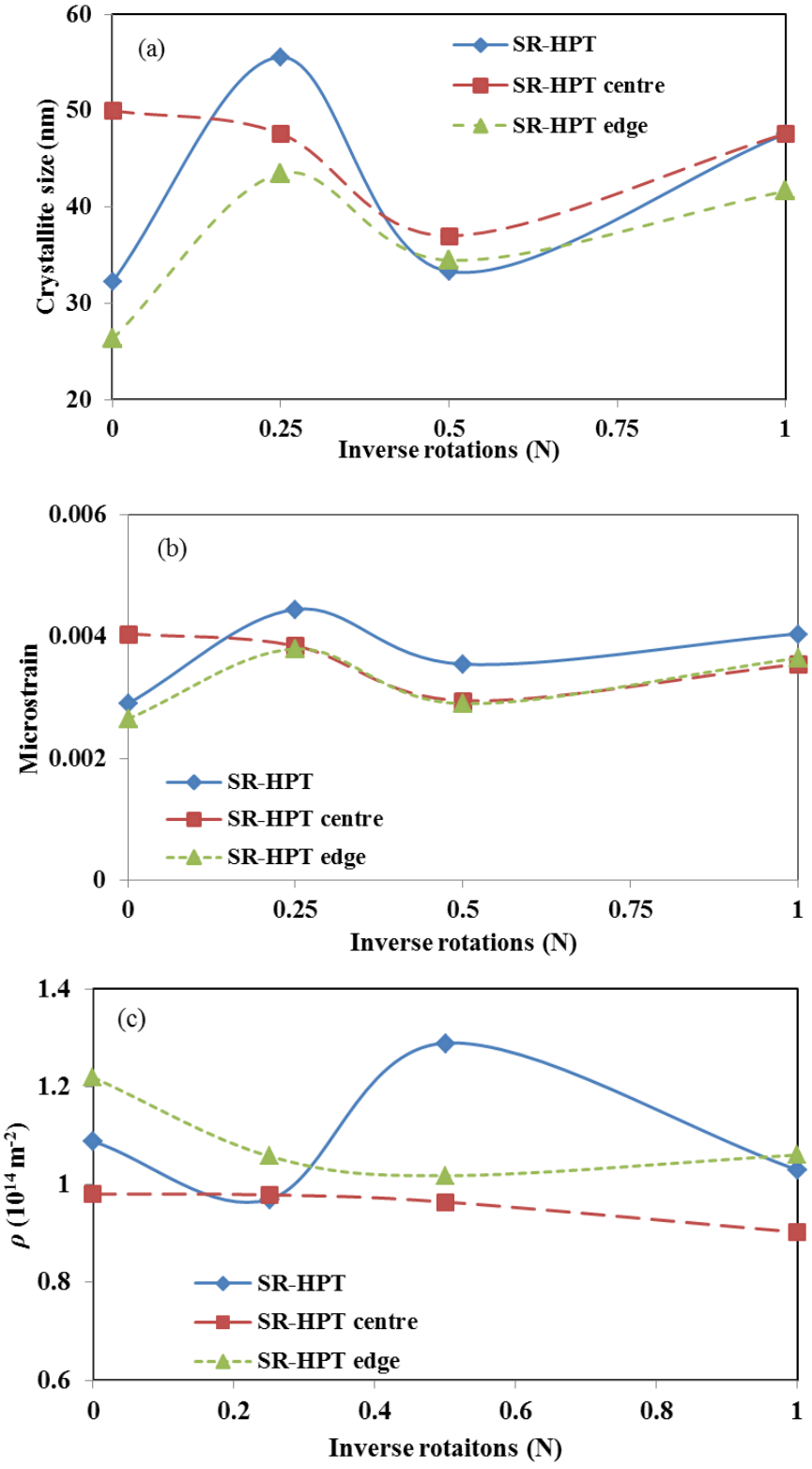

Fig. 7.6 Microstructure evolutions of 5r-HPT samples processed by ¼, 1/2, and 1 inverse rotations (a) crystallite sizes (b) microstrains (c) dislocation densities.

In Fig. 7.6 (a), the crystallite sizes of 5r-HPT samples in both centre and edge areas present similar trends. They first increase when processed by an ¼ inverse rotation, then decrease when processed by inverse rotation up to ½ turn. Finally, the crystallite sizes increase again when processed using 1 inverse rotation. The trend of average crystallite size for the whole disk is the same as the edge sample. Similar trends for the SR-HPT samples in centre and edge areas are observed for microstrain in Fig. 7.6 (b).

The dislocation densities of full disks in Fig. 7.6 (c) show an opposite trend for reverse rotations: it first decreases to $1x10^{14}$ m^{-2} for a ¼ inverse rotation; then increases to $1.3x10^{14}$ m^{-2} when processed by ½ inverse rotation, and finally decreases a little for 1 inverse rotation. For a 5r-1/4r HPT sample, the increase of microstrain increases the number of dislocations. But these dislocations accumulate to form subgrain boundaries and narrow the scattering domains, leading to a decrease in crystallite size.

The dislocation densities and crystallite sizes of full disk have been quantitatively analysed using Rietveld full peak refinement and programed by software 'MAUD' (see also Section 5.1.2). In Fig. 7.7, the dislocation densities of samples processed by SR-HPT are nearly the same. The crystallite size reveals a similar trend as Vickers hardness.

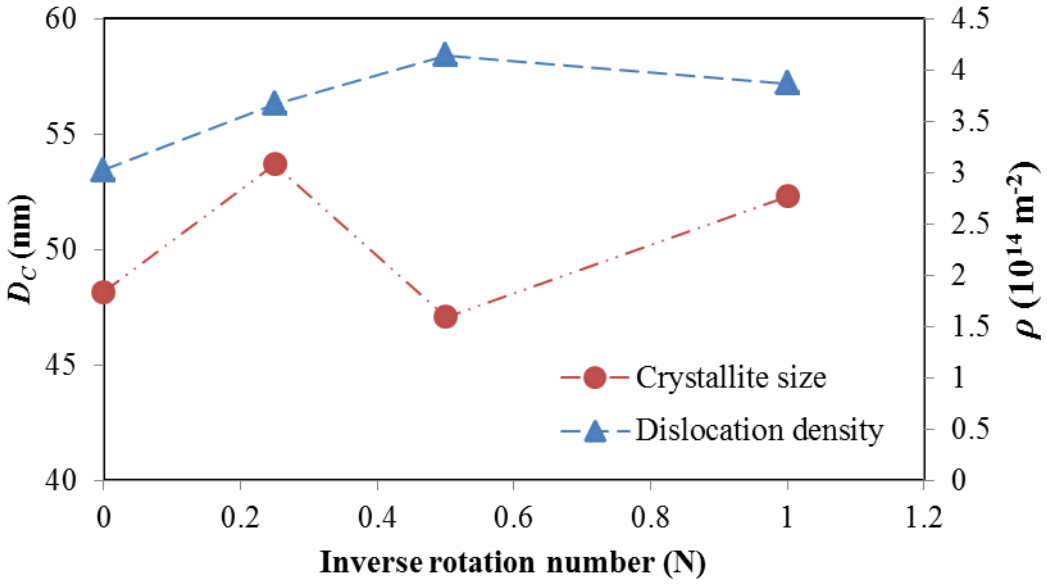

Fig. 7.7 Microstructure evolutions of 5r-HPT samples processed by ¼, 1/2, and 1 inverse rotations by Rietveld XRD full peak refinement.

7.2 Mechanism of microstructural evolution in SR-HPT

The trends of microhardness evolutions for 5r-HPT Al-Cu-Mg samples processed by small inverse HPT rotations and subsequent post-HPT annealing are similar. The trends of crystallite size and dislocation density show good correspondences with Vickers hardness: the Vickers hardness decreases with an increase of crystallite size as well as a decrease of dislocation density.

The microstructural evolution in SR-HPT is probably due to geometrically necessary dislocations, which accommodate the lattice curvature. In HPT samples, strain in the centre of the disks should be zero and increases as the distance to the centre increases (according to Eq. (2-9) to Eq. (2-11)). This appearance of strain gradient along the radius of HPT disc generates GNDs.

In XRD profile analysis, the scattering domain size of a 5r-1/4r HPT sample is larger than that of a 5r-HPT and a 5r-1/2r HPT sample (shown in Fig. 7.6 (a) and Fig. 7.7); simultaneously, an increase of microstrain is also observed in a 5r-1/4r HPT sample (see Fig.7.6 (b)). A possible mechanism can be explained the observation is illustrated in Fig. 7.8, which combine the dislocation pile-up mechanism [236, 237] and the core and mantle mechanism [88, 95, 206, 238, 239]:

In those core and mantle models (i.e. [88, 95, 206, 238, 239]), the deformation within a grain is composed of two parts: (1) the grain interior, ‘core’ and (2) the grain-boundary region, ‘mantle’. In the grain interior (core), slip system S is activated, corresponding to easy glide; dislocations slip to grain boundaries (Fig. 7.9 (a) at initial stage). In the grain boundary mantle region, the moving dislocations will be accumulated, interact with other pre-stored dislocations. The orientation of slip plane may change, lead to cross-slip of dislocations. The subgrain boundary (mantle) region becomes thicker with the decrease of grain size and reduction of resistance within grain interior (core) (Fig. 7.9 (a) at 5r-HPT).

For samples processed by ¼ inverse rotation (Fig. 7.9 (b)), a small inverse strain gradient $-d\gamma_2/dr$ is added, reducing the number of dislocations in the ‘core’. This inverse strain gradient $-d\gamma_2/dr$ may activate another slip system S2, and release the dislocations

in ‘mantle’ region. As a result, the relative scattering domains are enlarged, as the subgrain boundaries become thinner [240, 241]. The released dislocations from subgrain boundaries will move back to grain region and increase the lattice microstrain in the grain interior.

If the inverse rotation continues, an increasing of inverse strain gradient is (Fig. 7.9 (c)). The dislocations in system S2 will continue to move to the grain boundaries on the other sides. Due to cross-slip, the slip orientation may change to S3. As a result, the dislocation density will decrease in the region of grain interior (core). The mantle region will enlarge while the stress within the core decreases. Due to this mechanism, the lattice strain decreases and the scattering domains become smaller. The XRD profile analysis reveals that the crystallite size of 5r-HPT decreases.

If the inverse rotation continues moving on, the dislocations can present a series of cycle behaviours, changing to different slip system and reducing (or increasing) the scattering domain. We can except that the hardness and microstructure of the samples processed by inverse HPT can be the equivalent to 5r-HPT samples.

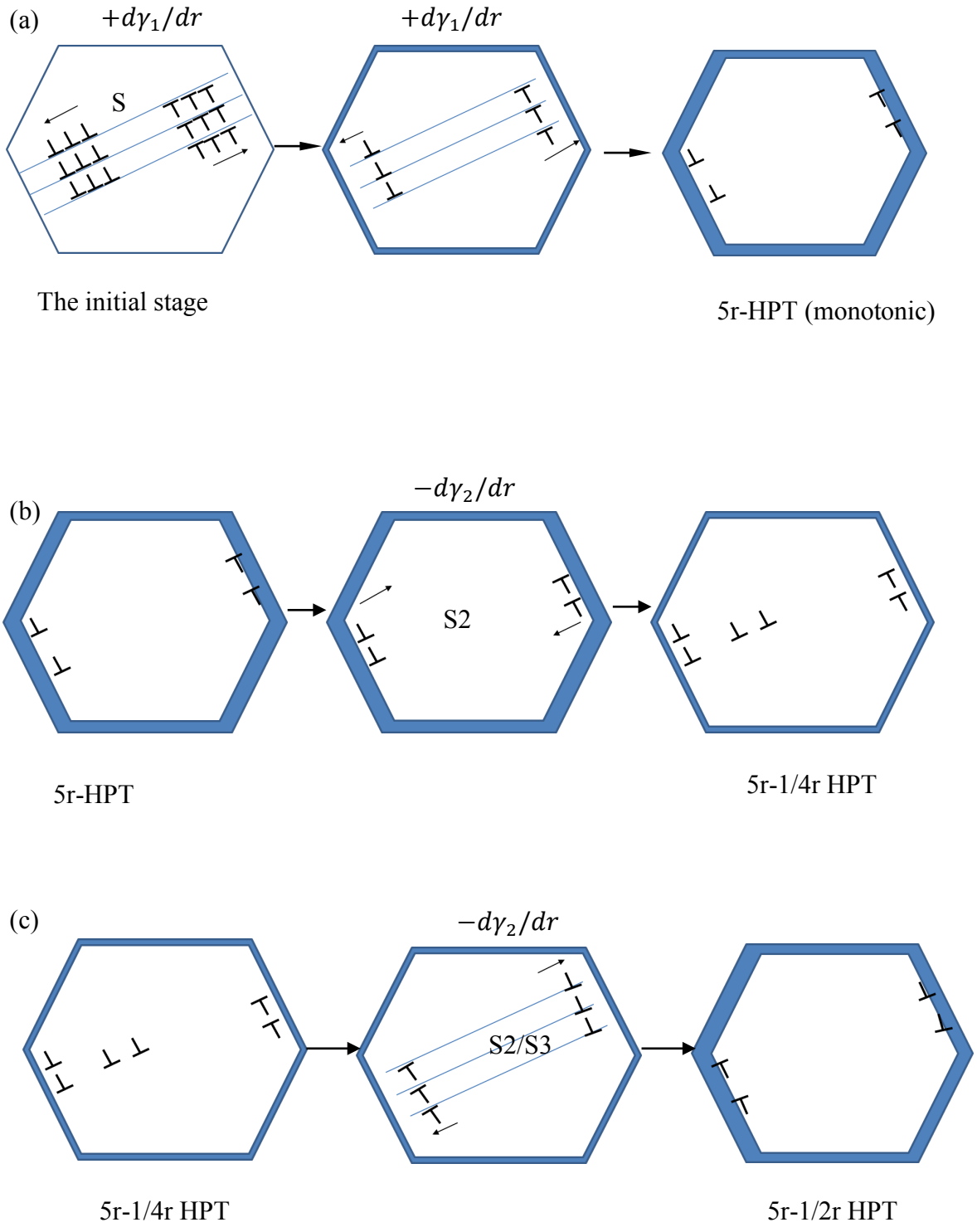

Fig. 7.8 Schematic illustration of a combination mechanism of 'core and mantle' and 'dislocation pile-up' model

7.3 Strain gradient plasticity modelling of SR-HPT processing

7.3.1 A prediction on strength

The yield strength of an HPT Al alloy can be approximated from the Vickers hardness, which has been modelled in Section 5.2.4, which is simply presented as [13, 14, 118, 205-207]:

$$\sigma = \frac{HV}{3}$$

We assume that the strengthening mechanisms for reversal HPT samples are the same as those processed by monotonic HPT deformation, which incorporates dislocation strengthening, $\Delta\tau_d$, grain boundary strengthening, $\Delta\sigma_{gb}$, solute strengthening, $\Delta\tau_{ss}$, short range order strengthening, $\Delta\tau_{SRO}$ and modulus strengthening, $\Delta\tau_m$.

The grain size of reverse HPT is assumed to be 3 times the crystallite size obtained from Rietveld XRD profile broadening analysis. The enthalpy associated with cluster-defect complexes $\Delta H_{Cu\text{-}Mg\text{-}dis}$ is taken as 49.5 kJ/mole (as determined in Section 5.2.5). Using the model derived in Section 5.2, the predicted yield strength is plotted in Fig. 7.9.

Fig. 7.9 indicates a good correspondence in yield strength (mostly within 20MPa) between that evaluated from Vickers hardness and that derived from the strengthening model which incorporates 5 strengthening components. The somewhat poorer prediction for the 5r-1/4r HPT sample can be probably due to reverse strain gradients, which will be discussed in next section.

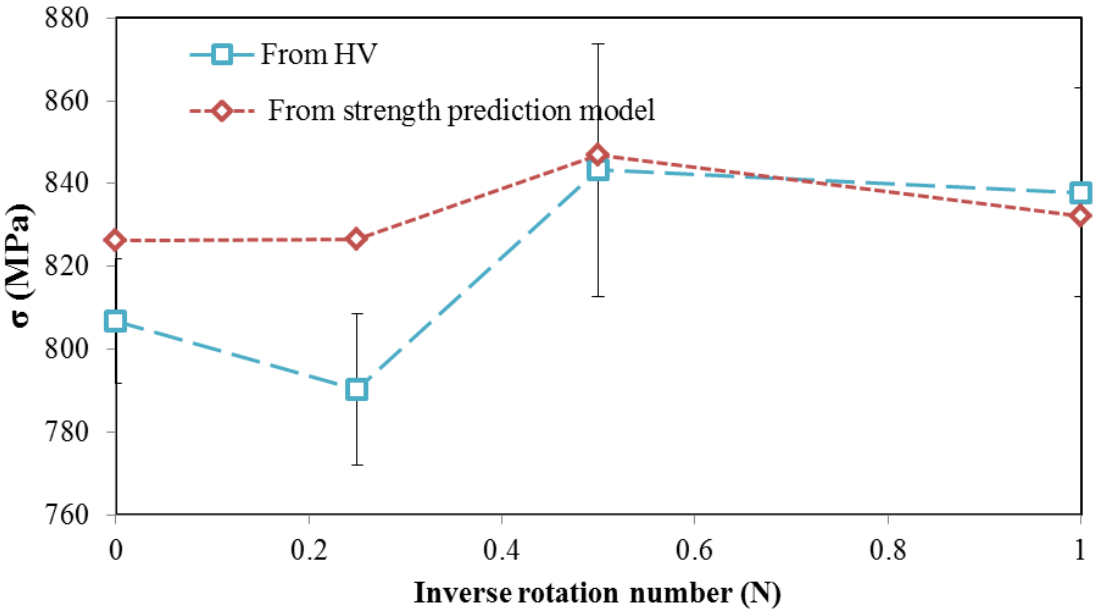

Fig. 7.9 Comparison of model predictions of strength and HV/3.

7.3.2 Strain gradient plasticity modelling of SR-HPT

Dislocation hardening is thought to be due to the combined presence of GNDs associated with strain gradient and SSDs associated with a plastic strain. In HPT inhomogeneous deformation, $\Delta\tau_d$, was given as (see Eq. (5-4))

$$\Delta\tau_d = \alpha_1 Gb\sqrt{\rho_T} = \alpha_1 Gb\sqrt{\rho_{SSD+}\rho_{GND}}$$

In Section 5.2 and Section 7.3.1, the total dislocation density, ρ_T values, are taken from XRD line broadening analysis , neglecting the details of GNDs and SSDs.

The dislocations caused by plastic strain incorporate two components, the cell interior and the cell walls (see also Section 7.2). Hence, ρ_{SSD} can be obtained using the rule of mixtures [217, 242],

$$\rho_{SSD} = f_s\rho_w + (1-f_s)\rho_c \tag{7-1}$$

where f_s is the volume fraction of cell walls, ρ_c and ρ_w are dislocation density in the cell interior and in the cell walls.

However, the presence of GNDs leads to additional storage of defects which can provide additional macroscopic strengthening caused by short range interaction, when they are cut by glide dislocations [125, 126]. It was suggested by Ashby that GND density is related to the absolute value of the equivalent plastic strain gradient (see also Section 2.4.2), given as follow:

$$\rho_{GND} = M \frac{\left\| \nabla \varepsilon^p \right\|}{b} \tag{7-2}$$

where ε^p is the equivalent plastic strain, M is Taylor factor as denoted before.

The equivalent plastic strains in HPT disc are cylindrically symmetric. The strain gradients are imposed by torsion (see Fig. 7.10 [243]), and according to Eq. (2-11), the strain gradient is derived as

$$\left\| \nabla \varepsilon^p \right\| = \frac{\partial \varepsilon}{\partial r} = \frac{\partial \varepsilon}{\partial \gamma} \cdot \frac{\partial \gamma}{\partial r} = \frac{2}{\sqrt{3}} \frac{\frac{1}{8}\gamma\left(1+\gamma^2\right)+1}{\left(1+\gamma^2\right)^{\frac{1}{2}}+\gamma} \cdot \frac{2\pi}{h} N \tag{7-3}$$

where γ is the local shear strain, the distance to the center is r (see Fig. 7.11 [243]). γ can be calculated using Eq. (2-9) (see also Section 2.3.1). N and h are rotation number and the thickness of samples are denoted in Section 2.3.1. In SR-HPT processing, the samples were first rotated clockwise up to 5 turns, and inverse rotated counter-clockwise for ¼, ½ and 1 turns. The hardness (Fig. 7.3 (a)) and the predicted strength (Fig.7.9) of the 5r-1r HPT sample are slightly higher than 5r-HPT sample. This indicates the inverse rotation (1r) leads to a further grain refinement as compared to the 5r-HPT sample.

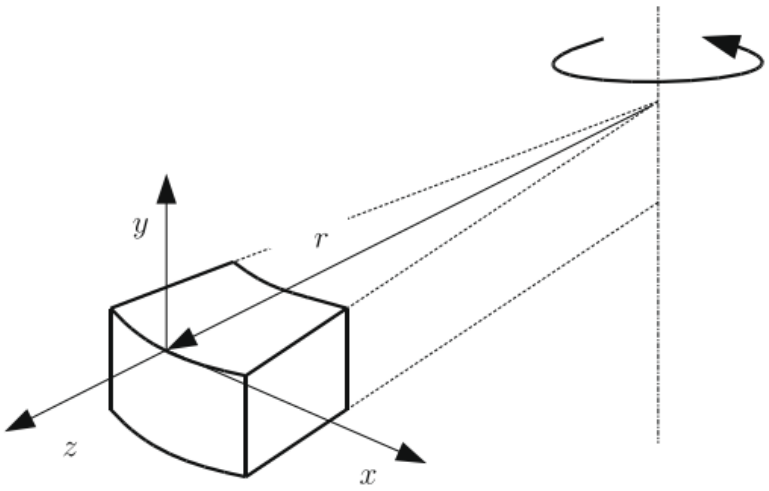

Fig. 7.10 A volume element exposed to HPT [243]

Section 7.2 presents the cyclic reversal mechanical behaviors of the Al-Cu-Mg alloy processed by HPT are due to the introduction of inverse strain gradient $-d\gamma_2/dr$, which leads to a decrease of dislocations (i.e. SSDs) within cell interiors and an increase in thickness of the cell walls. In Eq. (7-3), the density of GNDs can be reduced when processed by a ¼ inverse rotation. This is consistent with the phenomena presented in Fig. 7.9, in which the magnitude of flow stress σ predicted from Vickers hardness is smaller than that predicted from strength models.

The reduction in geometrically necessary dislocations may lead to a decrease of strengthening due to short-range interactions between GNDs or GND-solute complexes, when a glide dislocation passes by. The magnitude of $\Delta H_{\text{Cu-Mg-dis}}$ in Eq. (5-15) needs to be adjusted due to the changes in the GNDs components.

7.4 Summary

In present study, the Vickers hardness of samples in SR-HPT processing first decreases for a quarter inverse rotation and increases for a half inverse rotation. The crystallite size presents a similar trend.

The XRD profile broadening analysis quantitatively evaluated the crystallite size and microstrain in SR-HPT samples. The results are explained by a model based on introduction of inverse strain gradient and GNDs generation.

The strength prediction model shows a consistent trend for hardness and corresponding strengthening components, i.e. dislocation density, crystallite size and solute-dislocation complexes. The changes in exothermic peak at 210 °C show a consistent trend: the higher heat flow, the smaller the crystallite size.

Chapter 8 Discussion on the solute effects in the UFG Al-Cu-Mg alloy

An ultrahigh strength of the Al-Cu-Mg alloy is obtained via high-pressure torsion. The strength of the Al-Cu-Mg alloy processed by HPT is higher than the strength of the pure aluminium processed by HPT with the same pressure and same rotations (i.e. 40 HV, the high pure aluminium, 5r-HPT, P=6 GPa [72]). The alloying elements play an important role in microstructural modification of alloys, and have a significant effect on their mechanical properties. This chapter discusses the behaviours of solute atoms in the UFG Al-Cu-Mg alloy. In Section 8.1, the intrinsic trends of solute segregation and its relation to thermodynamics are presented. Section 8.2 discusses the influence of solute atoms or clusters in microstructural thermal stability. Finally, Section 8.3 summarizes the potential influences of microstructural modification with the trace addition of Si.

8.1 Trends of grain boundary segregation in UFG materials: relations to free energy

Solute segregation on grain boundaries has been shown in APM (Section 5.1.4 and Section 6.1.4). This section describes solute migration within the framework of statistical thermodynamics.

Several models related to the interaction of solute atoms with crystallite defects indicates the solute atoms segregate at the defect if site energies are lower than that at random distribution [177, 191, 244-246]. In ternary M-A-B alloys (in the present work Al-Cu-Mg), solute atoms A and B distribute either at grain boundary, or in the grain interior matrix. In Wagner's definition of surface excess [247] and Kirchheim's

derivation [208, 213], the solute excess at defects (i.e. dislocations, grain boundaries, vacancies) for solute atom A and atom B dissolved in matrix M is

$$\left.\frac{\partial \gamma}{\partial \mu_A}\right|_{V,T,a,n_M} = -\Gamma_A \tag{8-1}$$

$$\left.\frac{\partial \gamma}{\partial \mu_B}\right|_{V,T,a,n_M} = -\Gamma_B \tag{8-2}$$

where γ is the surface energy, μ_A and μ_B are the chemical potential of solute atom A and atom B dissolved in a constant number n_M of material matrix M, Γ_A and Γ_B are the solute excess at defects for solute atom A and atom B. Eq. (8-1) and Eq. (8-2) predict interface energy for a positive excess and an increase of chemical potential of A and B. The solute atoms reveal a trend to concentrate at the grain boundaries to reduce the surface energy γ. The surface energy in a closed system M-A-B is

$$\gamma = \gamma_0 + \Gamma_A\left[\Delta H_{seg-A} - T\Delta S_{seg-A}\right] + \Gamma_B\left[\Delta H_{seg-B} - T\Delta S_{seg-B}\right] + \Gamma_{A-B}\left[\Delta H_{A-B} - T\Delta S_{A-B}\right] \tag{8-3}$$

where γ_0 is the non-segregated grain boundary free energy, $\Delta H_{\text{seg-A}}$ and $\Delta H_{\text{seg-B}}$ are the enthalpy changes, $\Delta S_{\text{seg-A}}$ and $\Delta S_{\text{seg-B}}$ are the entropy changes, associated with the segregation of a solute atom from a matrix site into a grain-boundary site [248]. $\Gamma_{\text{A-B}}$ is the co-cluster excess at defects. The $\Delta H_{\text{A-B}}$ and $\Delta S_{\text{A-B}}$ are the enthalpy and entropy changes associated with the formation of co-cluster A-B.

When $\left[\Delta H_{seg-A} - T\Delta S_{seg-A}\right] < 0$ and $\left[\Delta H_{seg-B} - T\Delta S_{seg-B}\right] < 0$, solute segregation to grain boundaries is favoured, and γ decreases. The formation of A-B clusters is also favoured as A-B near-neighbour bonds have negative interaction energies (i.e. $\Delta H_{\text{A-B}}<0$, Cu-Mg formation in Al-Cu-Mg alloys reduces ~-30 kJ/mole for 4-atom equilibrium structure [79]). This is the basis of the thermodynamic mechanism for cluster segregation.

The strengthening prediction model in Section 5.2 indicates the multiple interactions between co-clusters and dislocations lead to the formation of complex solute-defect clusters, which cause a further increase of strength (due to the short-range order strengthening mechanism). Hence, the third term on right hand side of Eq. (8-3) needs to be changed as

$$\gamma = \gamma_0 + \Gamma_A \left[\Delta H_{seg-A} - T\Delta S_{seg-A}\right] + \Gamma_B \left[\Delta H_{seg-B} - T\Delta S_{seg-B}\right] + \Gamma_{A-B}\left[\Delta H_{A-B-dis} - T\Delta S_{A-B-dis}\right] \quad (8\text{-}4)$$

where the average enthalpy of the various types of A-B-dislocation clusters is expressed in Eq. (5-16), given as:

$$\Delta H_{A-B-dis} = f_1 \Delta H_{A-B} + f_2 \Delta H_{A-dis} + f_3 \Delta H_{B-dis} + f_4 \Delta H_{(A-B)_n-dis}$$

The segregation of atom A and atom B has been considered in the first and the second terms in Eq. (8-4), the fraction f_2 and f_3 are zero in above equation. Thus, the enthalpy $\Delta H_{\text{A-B-dis}}$ and the entropy $\Delta S_{\text{A-B-dis}}$ of clusters at grain boundaries are given as:

$$\Delta H_{A-B-dis} = \Delta H_{A-B} + \Delta H_{(A-B)_n-dis} \quad (8\text{-}5)$$

$$\Delta S_{A-B-dis} = \Delta S_{A-B} + \Delta S_{(A-B)_n-dis} \quad (8\text{-}6)$$

The fitting in Section 5.2 is determined $\Delta H_{\text{Cu-Mg-dis}}$ to be -49.5 kJ/mole, which is lower than $\Delta H_{\text{Cu-Mg}}$. Thus, the formation of cluster-dislocation complexes leads to a further decrease of the surface energy γ.

Due to the decrease of surface energy, the overall difference in Gibbs energy (in Eq. 8-1 and Eq. 8-2) of solute atoms at GBs and the Gibbs energy of solute atoms inside the grain become smaller. If this Gibbs energy difference approaches zero, there is no longer a driving force for solute atom to segregate to grain boundaries, a metastable equilibrium is reached.

The amount of segregated solute atoms is also determined by the surface area. The Gibbs free energy can be written as [103, 249]:

$$G = \sum \mu_i n_i + \gamma a \tag{8-7}$$

where n_i is the amount of component i, (A or B), a is the surface area. At constant pressure and temperature, the change in free energy is given as

$$dG = \gamma da \tag{8-8}$$

Consequently, the Gibbs free energy increases as the surface area increases in nano-grained materials. As a result, an increasing number of solute atoms are required to act as excess solute, segregate at the GBs and further reduce the surface energy γ. Finally, the overall free Gibbs energy is reduced to reach a stable equilibrium state in thermodynamics, and the solute atoms segregated at grain boundaries approach their saturated amount.

8.2 The effects of solute atoms on thermal stability

The potential of solute segregation to grain boundaries has been discussed in Section 8.1 on the basis of the Gibbs adsorption theorem [208, 213]. The addition of solute atoms to grain boundaries can lower the grain-boundary energy. This reduction of the excess grain-boundary free energy provides a reduction in driving force for grain growth in ultrafine-grained metals and alloys. The equation is given as [248]

$$P = \frac{C\gamma}{r} \tag{8-9}$$

where C is a numerical constant, r is the radius of curvature, which is proportional to the grain size.

The driving force can be very large since the grain size decreases to ultrafine scale or nano scale. However, the grain boundaries can be pinned by the solute atoms. The pinning effect reduces grain growth at elevated temperature. The grain growth velocity, v. is controlled by the activation energy and the annealing temperature [250].

$$v = M_v \exp\left(-\frac{Q_m}{RT}\right)\frac{C\gamma}{r} \tag{8-10}$$

where M_v is a constant associated with the grain boundary mobility, Q_m is the activation energy. If the annealing temperature is high, the mobility of dislocation can be thermally activated; and the pinning force resisting boundary motion will be overcome. The grain growth velocity decreases with the increase of grain size.

The solute-boundary pinning mechanism is used to explain the microstructural evolution of UFG samples in DSC heat processes in this PhD project. When heating is conducted between 100 °C to 210 °C in DSC, the crystallite size is nearly the same (Fig. 6.4). The interior dislocations anneal within grains, thus the dislocation density decreases slightly, shown in Fig. 6.5. This indicates the UFG microstructures are retained during DSC heat treatment. Due to the annihilation of grain interior dislocations, co-cluster segregation phenomenon (Fig. 6.7) became easier to observe in HPT-processed Al-Cu-Mg alloy samples.

When heating up to 210 °C, the crystallite size increases significantly (Fig. 6.4) and the dislocation density decreases dramatically (Fig. 6.5). It reveals that the pinning force resisting boundary motion is overcome, and the grain- or subgrain-boundary dislocations anneal at 210 °C. Then the defect-cluster complexes dissolve and tend to transform to nano-scale precipitates (illustrated in Fig. 6.7). The microstructures can also be retained by the precipitates. However, the S precipitates become coarsened in these types of heat treatments, leading to a smaller pinning effect for dislocation mobility.

In Fig. 8.1, the room temperature hardness of samples subjected to HPT and T351 in the present work are compared to the same alloy subjected to water quench (WQ) only, water quench and cold work (WQ-CW), slow water quench and cold work (SWQ-CW) [251]. The hardness of the HPT-deformed sample (240~260 HV) is much higher than the others (by 100HV to 150HV). The hardness increases on heating from 25 °C to 170 °C and change little up to 210 °C. The phenomenon can be explained as the boundary pinning effect [248, 252, 253], which hinders the movement of dislocations during the DSC annealing. When heating from 210 °C to 300 °C, the hardness of the 5r-HPT sample is still higher than other samples (i.e. WQ, WQ-CW, SWQ-CW and T351). As indicated in DSC thermographs (Fig. 4.1 and Fig. 4.3) and XRD patterns (Fig. 6.3), the S phase forms in this temperature range. The higher hardness in the temperature range of 210 °C to 300 °C is probably due to the pinning effect of nano precipitates.

In summary, due to the existence of alloying elements, UFG microstructures are retained to a higher temperature; and the ultrahigh strength of the Al-Cu-Mg alloy is also retained.

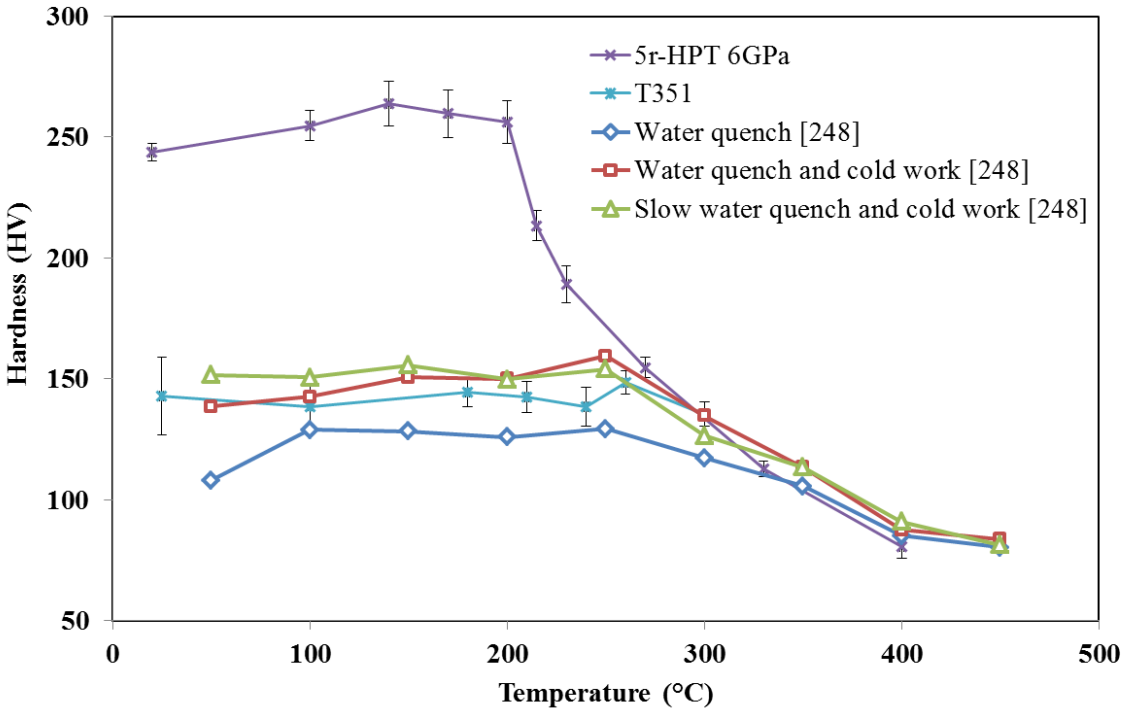

Fig. 8.1 Temperature hardening curve of 2024 alloy subjected to (1) 5r-HPT (6GPa, T351), (2) T351, (3) water quench only [251], (4) water quench and cold work (10%) [251], (5) slow water quench (80 °C) and cold wold (10%) [251].

8.3 Effect of Si on UFG Al-Cu-Mg alloy

The trace additions of alloying elements, such as Ag and Si, have marked effects on the age hardening Al-Cu-Mg alloys [46, 53, 254-257]. The presence of Si atoms modifies the GPB zones and the precipitation sequences, as the θ and σ were also observed in alloys containing 0.5 wt.% Si [256, 257]. The age hardening curves of Al-Cu-Mg alloy were raised with the addition of Si over the entire time scale, particularly with a noticeable increase in plateau hardness [254, 256]. The addiction of Si is of great importance to improve mechanical properties.

The Al-Cu-Mg alloy in present study contains trace Si, Fe and Mn, as list in Table 3-1. The alloy investigated in this PhD project contains very limited amount (0.08 wt.%) of Si, which was observed to segregate to grain boundaries (Fig. 5.10 and Fig. 5.11) and precipitates (Fig. 6.7 and Fig. 6.8) in APM. Si was also found in Mn-containing dispersoids, as shown in Fig. 8.2 (c). (The particle in Fig. 8.2 (d) BF-TEM image is the Mn-containing dispersoids, which is similar to the TEM images in Ref. [258, 259]). Si can dissolve in constituent phases and dispersoids and thereby the Si supersaturation can be considerably reduced. Mukhopadhyay [258] pointed out that nucleation of σ phase required a critical minimum supersaturation of Si in the solid solution, and the σ nucleate close to the Mn-bearing dispersoids. Although the σ phase has not been found in the UFG Al-Cu-Mg sample studies in recent works [12, 27, 260, 261], it is not possible to present that these particles simply were not there.

The calculation on lattice parameter misfits in Section 6.2.2 suggests that the lattice parameter, a, is changed due to the trace addition of Si. The Mg-Si interaction leads a decrease of the Mg concentration to form S phase (Al_2CuMg). As a result, the lattice parameters are changed when the concentrations of dissolved atoms are different. The lattice parameter of an HPT-processed sample is smaller than that of the T351sample, which is probably due to the solute segregation. The lattice parameter decreases at 210 °C as the formation of S phase reduce the dissolved atoms in Al matrix. However, the magnitude of lattice parameter of the 5r-HPT-210 °C sample is larger than the pure

Al sample. This is attributed to the addition of Si and other trace elements, as well as Cu left in Al matrix.

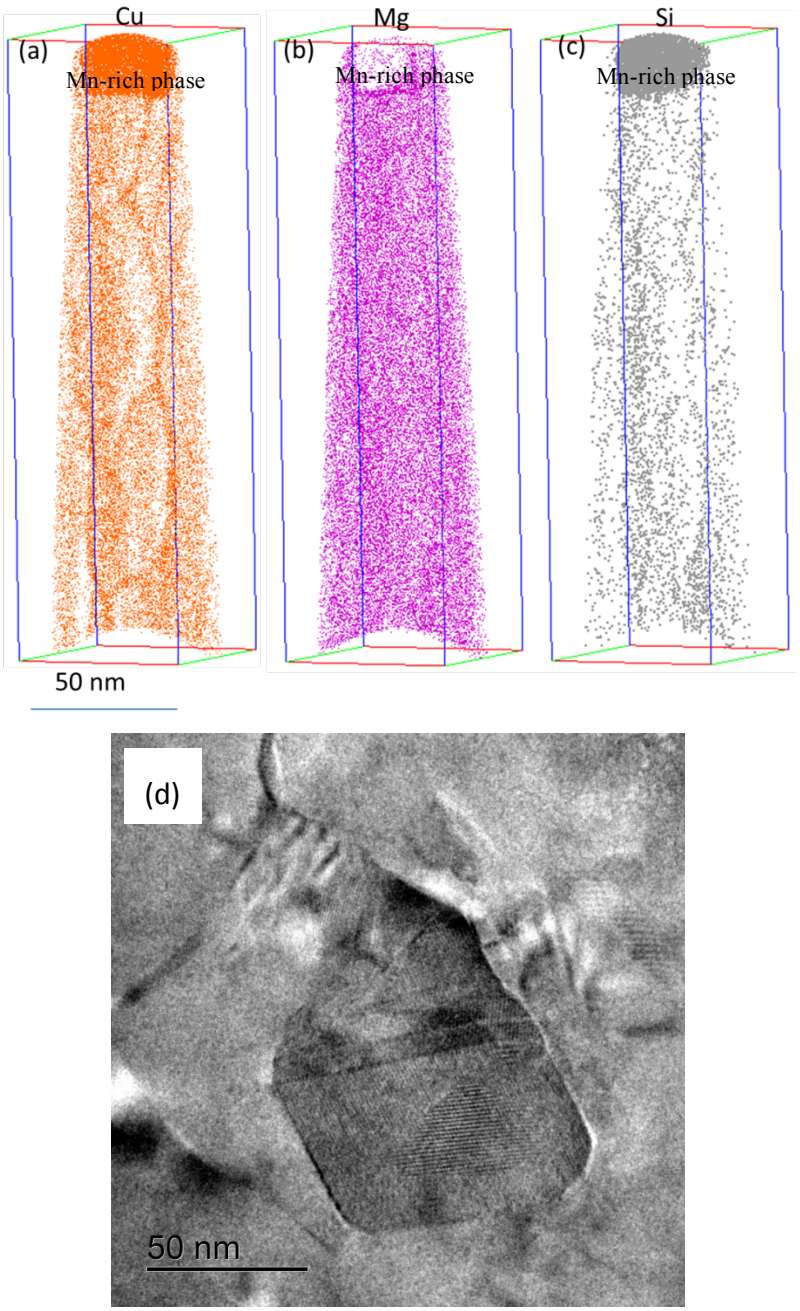

Fig. 8.2 Single-element atom maps (a)-(c) of 5r-HPT Al-Cu-Mg sample that contains the Mn-rich phase on the top: (a) Mg map, (b) Cu map, (c) Si map; (d) TEM bright field image of 5r-HPT sample contains Mn-rich phase.

Chapter 9 Conclusions and future work

9.1 Conclusions

The strength of age-hardenable Al-Cu-Mg alloys processed by SPD depends on the presence of dislocations, grain boundaries, and short range order phases. In this thesis, the UFG microstructure of Al-Cu-Mg alloy has been examined after HPT and after heat treatment at various temperatures.

DSC thermographs of HPT-processed samples show a single exothermic effect peaking at 170 °C, and overlapping exothermic effects peaking at 210 °C and 240 °C. DSC exothermic peak shifts suggest an acceleration of S precipitation. A probable explanation is presented as more nucleation sites are introduced by a substantial number of dislocations in SPD processing. A model describes solute diffusion and dislocation generation/annihilation; it fits the measured peak temperatures in DSC thermograms with a good accuracy.

The hardness of the Al-Cu-Mg alloy is greatly improved (by 100 HV) due to HPT. The distribution of hardness is nonhomogeneous, higher at the edge region and lower at the centre region, particularly for samples subjected to small rotations. Grain size in TEM decreases to 180 nm for 1/4r-HPT and ~150 nm for higher HPT rotations (i.e. N>1). Quantitative analysis on XRD profile broadening shows the crystallite size (coherent scattering domain size) decreases dramatically to ~60 nm while the dislocation density increase up to a saturated value ~$3x10^{14}$ m^{-2} after HPT processing. The hardness increases with an increase of dislocations and grain refinement.

For samples processed by DSC heating treatment, the hardness presents a slight increase up to 170 °C with a value of 263 HV, and a decrease starts at 210 °C and continues to a series of higher temperatures. The grain size of a 5r-HPT-210 °C sample (~150 nm) is nearly the same as that of a 5r-HPT sample, but an increase is observed for a 5r-HPT-300 °C sample with ~250 nm in magnitude. The analysis of XRD profile broadening

reveals that at 210 °C the crystallite size increases significantly while the dislocation density decreases. Thus the decrease of strength results from dislocation annihilation and grain coarsening.

APM shows that both before and after HPT the alloy contains a high density of clusters, which are predominantly of the Cu-Mg co-cluster type. The solute atoms segregate to grain boundaries and dislocations in HPT processing. The interactions between dislocations and Cu-Mg clusters leading to complex solute-defect clusters further increase the strength and reduce the free energy of Al matrix.

A strength model and a stored energy model are established to explain the strengthening behaviours of the Al-Cu-Mg alloy caused by cluster-dislocation complexes:

The strength model indicates that short range order due to these clusters is the dominant strengthening mechanism. The increase in dislocation density evaluated from XRD line broadening provides a significant strengthening (about 10% of the strength of HPT processed samples). The grain size strengthening is the 3rd most potent strengthening mechanism in the HPT processed ternary Al-Cu-Mg alloy.

Through fitting, $\Delta H_{\text{Cu-Mg-dis}}$ is determined to be 49.5 kJ/mole, which suggests the solute-defect clusters are more stable than some of the intermediate precipitates such as GPB zones. Through fitting of $\Delta H_{\text{Cu-Mg-dis}}$ a good strength prediction for samples processed by single reversal HPT is obtained.

The stored energy model indicates the solute/co-cluster segregation leading to a further increase of stored energy. The increases in dislocation density contribute to the increase of overall stored energy, while grain size stored energy also takes account as the 3rd most potent contribution.

The solute-defect clusters not only increase the strength and reduce Gibbs free energy, but also present a positive effect on dislocation generation and accumulation. The formation of solute-defect clusters produces obstacles that block the migration of dislocations, pins dislocations at grain boundaries, and leads to a higher thermal stability of the UFG microstructures.

SR-HPT processing involves torsion in one direction followed by a smaller torsion in the opposition direction. A small reversal of ¼ rotation reduces hardness, while a

reversal of ½ rotation increases hardness. XRD profile broadening analysis reveals the crystallite size of 5r-HPT sample increases when processed by ¼ reversal rotation. The crystallite size of 5r-1/2r-HPT sample is larger than that of 5r-1/4r-HPT sample. These behaviours and other effects are interpreted in terms of the introduction of inverse strain gradient and GNDs.

9.2 Future work

Because of the grain refinements and the dislocation accumulation in severe plastic deformation, an ultrahigh strength is obtained in alloys. The alloying elements in Al alloys contribute to a further increase of strength. APT analysis indicates solute atoms/clusters segregate to grain boundaries for heat treatable Al alloys (i.e. [24-26] and also this thesis). However, the microstructures and the composition of these clusters or nano precipitates along the grain boundaries or dislocations have not been clearly clarified by microstructure tomography. It will be an interesting subject to study microstructures and compositions of these nanoscale clusters or precipitations in specific along the grain boundaries using a powerful high-angle annular dark-field scanning transmission electron microscopy (HAADF-STEM) in the future. This analysis will contribute to a more clear understanding of the fundamental theory on dislocation-cluster interaction and strengthening mechanisms in SPD processing.

A number of models with different variants have been developed in this thesis. Some of them need to be further studied, tested and expended. In the stored-energy predicting model (see section 6.3), the energy due to solute-defect interaction was calculated by using the number density of Cu-Mg co-clusters obtained in APM (i.e. 5r-HPT sample and 5r-HPT-300°C). APM experiments should be better to carry out on other samples processed by different-rotation of HPT and the subsequent heat treatment. The overall trend of stored energy can be justified by microstructural investigation of solute-defect complexes (e.g. Section 6.3.5).

Due to strain gradient introduced by HPT processing, the microstructural inhomogeneity appears in an HPT disc along the radius. A fairly good prediction on

strength and crystallite size of samples processed by inverse HPT rotations was presented in Section 7.2. GNDs and SSDs were used to explain the reversal mechanical properties in SR-HPT. However, it is still unclear how the inhomogeneous strain is specifically related to the inhomogeneous microstructure and microhardness. Microstructural investigation needs to be further studied, e.g. TEM, EBSD or APM. Apart from the experimental work, a proper finite element model can be built to better understanding the HPT processing.

The trace additions of Si, Fe and Mn can modify the microstructures and thereby play an important role in mechanical properties of Al-Cu-Mg alloys. The future work can include the analysis on microstructural modification and properties evolution by adding different amount of trace elements in UFG Al-Cu-Mg alloys processed by HPT.

The HPT is an efficient way to produce UFG materials without introducing impurities; however, its applications are limited by the dimension of the samples. The technique development to produce a larger UFG sample is worth considering in the future.

Reference

[1] A.P. Zhilyaev, T.G. Langdon, Progress in Materials Science, 53 (2008) 893-979.

[2] J. Mühlbach, P. Pfau, K. Sattler, E. Recknagel, Zeitschrift für Physik B Condensed Matter, 47 (1982) 233-237.

[3] L. Peraldo Bicelli, B. Bozzini, C. Mele, L. D'Urzo, International Journal of Electrochemical Science, 3 (2008) 356-408.

[4] H. Fecht, E. Hellstern, Z. Fu, W. Johnson, Metallurgical and Materials Transactions A, 21 (1990) 2333-2337.

[5] Y. Saito, H. Utsunomiya, N. Tsuji, T. Sakai, Acta Materialia, 47 (1999) 579-583.

[6] Z. Horita, T. Fujinami, T.G. Langdon, Materials Science and Engineering A, 318 (2001) 34-41.

[7] P.W. Bridgman, Journal of Applied Physics, 14 (1943) 273-283.

[8] E.A. Starke Jr, J.T. Staley, Progress in Aerospace Sciences, 32 (1996) 131-172.

[9] M.J. Starink, J.L. Yang, Aluminium Alloys 2006: Innovation Through Research and Technology,Proc. of the 10th Intern. Conf. on Aluminum Alloys, 2006, pp. 251-258.

[10] S.C. Wang, M.J. Starink, International Materials Reviews, 50 (2005) 193-215.

[11] P. Ratchev, B. Verlinden, P. De Smet, P. Van Houtte, Acta Materialia, 46 (1998) 3523-3533.

[12] J. Zhang, N. Gao, M.J. Starink, Materials Science and Engineering: A, 527 (2010) 3472-3479.

[13] J. Zhang, N. Gao, M.J. Starink, Materials Science and Engineering: A, 528 (2011) 2581-2591.

[14] J. Zhang, M.J. Starink, N. Gao, W. Zhou, Materials Science Forum, (2010) 809-814.

[15] A.P. Zhilyaev, K. Oh-ishi, T.G. Langdon, T.R. McNelley, Materials Science and Engineering: A, 410–411 (2005) 277-280.

[16] G. Sakai, Z. Horita, T.G. Langdon, Materials Science and Engineering: A, 393 (2005) 344-351.

[17] R. Vafaei, M.R. Toroghinejad, R. Pippan, Materials Science and Engineering: A, 536 (2012) 73-81.

[18] Z. Liu, X. Chen, X. Han, Y. Gu, Materials Science and Engineering: A, 527 (2010) 4300-4305.

[19] Z. Liu, S. Bai, X. Zhou, Y. Gu, Materials Science and Engineering: A, 528 (2011) 2217-2222.

[20] W. Huang, Z. Liu, M. Lin, X. Zhou, L. Zhao, A. Ning, S. Zeng, Materials Science and Engineering: A, 546 (2012) 26-33.

[21] M. Murayama, Z. Horita, K. Hono, Acta Materialia, 49 (2001) 21-29.

[22] W. Lechner, W. Puff, B. Mingler, M.J. Zehetbauer, R. Würschum, Scripta Materialia, 61 (2009) 383-386.

[23] G. Sha, K. Tugcu, X.Z. Liao, P.W. Trimby, M.Y. Murashkin, R.Z. Valiev, S.P. Ringer, Acta Materialia, 63 (2014) 169-179.

[24] P.V. Liddicoat, X.-Z. Liao, Y. Zhao, Y. Zhu, M.Y. Murashkin, E.J. Lavernia, R.Z. Valiev, S.P. Ringer, Nat Commun, 1 (2010) 63.

[25] G. Nurislamova, X. Sauvage, M. Murashkin, R. Islamgaliev, R. Valiev, Philosophical Magazine Letters, 88 (2008) 459-466.

[26] G. Sha, L. Yao, X. Liao, S.P. Ringer, Z. Chao Duan, T.G. Langdon, Ultramicroscopy, 111 (2011) 500-505.

[27] S. Lee, Z. Horita, S. Hirosawa, K. Matsuda, Materials Science and Engineering: A, 546 (2012) 82-89.

[28] A. Deschamps, F. De Geuser, Z. Horita, S. Lee, G. Renou, Acta Materialia, 66 (2014) 105-117.

[29] D.R. Askeland, P.P. Phule, Thomson Learning, 2006.

[30] J.R. Davis, ASM specialty Handbook: Aluminum and Aluminum Alloys, ASM Int., USA, 1993.

[31] I.J. Polmear, Light Alloys: From Traditional Alloys to Nanocrystals, Elsevier/Butterworth-Heinemann, 2006.

[32] J.R. Davis, Corrosion of Aluminum and Aluminum Alloys, Asm International, 1999.

[33] T.F. Morgeneyer, School of Engnieering Sciences, Faculty of Engineering, Science and Mathematics, University of Southampton, Southampton, 2008.

[34] A. Wilm, Metallurgie, 8 (1911) 225–227.

[35] Y.A. Bagaryatsky, Dokl.Akad. S.S.S.R., 87 (1952) 559-562.

[36] J.M. Silcock, J.Inst.Metals, 89 (1960) 203-210.

[37] H.-C. Shih, N.-J. Ho, J. Huang, Metallurgical and Materials Transactions A, 27 (1996) 2479-2494.

[38] S.P. Ringer, K. Hono, T. Sakurai, I.J. Polmear, Scripta Materialia, 36 (1997) 517-521.

[39] S.P. Ringer, K. Hono, I.J. Polmear, T. Sakurai, Applied Surface Science, 94–95 (1996) 253-260.

[40] A. Charai, T. Walther, C. Alfonso, A.M. Zahra, C.Y. Zahra, Acta Materialia, 48 (2000) 2751-2764.

[41] S.C. Wang, M.J. Starink, Acta Materialia, 55 (2007) 933-941.

[42] G.B. Winkelman, K. Raviprasad, B.C. Muddle, Acta Materialia, 55 (2007) 3213-3228.

[43] J. Majimel, G. Molenat, F. Danoix, O. Thuillier, D. Blavette, G. Lapasset, M.J. Casanove ¶, Philosophical Magazine, 84 (2004) 3263-3280.

[44] M.J. Styles, C.R. Hutchinson, Y. Chen, A. Deschamps, T.J. Bastow, Acta Materialia, 60 (2012) 6940-6951.

[45] L.F. Monfoldo, Aluminium alloys: structure and properties, Butterworths and Co., London, 1976.

[46] S.P. Ringer, T. Sakurai, I.J. Polmear, Acta Materialia, 45 (1997) 3731-3744.

[47] L. Reich, S.P. Ringer, K. Hono, Philosophical Magazine Letters, 79 (1999) 639-648.

[48] C. Wolverton, Acta Materialia, 49 (2001) 3129-3142.

[49] L.F. Davin, University of Oxford, 2004.

[50] M.J. Starink, N. Gao, L. Davin, J. Yan, A. Cerezo, Philosophical Magazine, 85 (2005) 1395-1417.

[51] L. Kovarik, S.A. Court, H.L. Fraser, M.J. Mills, Acta Materialia, 56 (2008) 4804-4815.

[52] A.M. Zahra, C.Y. Zahra, C. Alfonso, A. Charaï, Scripta Materialia, 39 (1998) 1553-1558.

[53] S.P. Ringer, K. Hono, I.J. Polmear, T. Sakurai, Acta Materialia, 44 (1996) 1883-1898.

[54] S.P. Ringer, S.K. Caraher, I.J. Polmear, Scripta Materialia, 39 (1998) 1559-1567.

[55] L. Kovarik, P.I. Gouma, C. Kisielowski, S.A. Court, M.J. Mills, Acta Materialia, 52 (2004) 2509-2520.

[56] M.J. Starink, N. Gao, J.L. Yan, Materials Science and Engineering A, 387-389 (2004) 222-226.

[57] M.J. Starink, S.C. Wang, Acta Materialia, 57 (2009) 2376-2389.

[58] S.C. Wang, M.J. Starink, Materials Science and Engineering A, 386 (2004) 156-163.

[59] F. Cuisiat, P. Duval, R. Graf, Scripta Metallurgica, 18 (1984) 1051-1056.

[60] R. Kent, V. Horn, Properties, physical metallurgy and phase diagrams, American society for metals, Metals Park, Ohio, 1968.

[61] H. Perlitz, A. Westgren, The crystal Structure of Al8Si6Mg3Fe, Almqvist & Wiksell, 1942.

[62] R. Kilaas, V. Radmilovic, Ultramicroscopy, 88 (2001) 63-72.

[63] V. Radmilovic, R. Kilaas, U. Dahmen, G.J. Shiflet, Acta Materialia, 47 (1999) 3987-3997.

[64] J. Yan, Materials Research Group, School of Engineering Sciences, Faculty of Engieering, Science and Mathematics, University of Southampton, Southampton, 2006.

[65] N. Gao, L. Davin, S.C. Wang, A. Cerezo, M.J. Starink, Mater. Sci. Forum, 396-402 (2002) 923-928.

[66] M. Kawasaki, R.B. Figueiredo, T.G. Langdon, Acta Materialia, 59 (2011) 308-316.

[67] Y.Z. Tian, S.D. Wu, Z.F. Zhang, R.B. Figueiredo, N. Gao, T.G. Langdon, Acta Materialia, 59 (2011) 2783-2796.

[68] M.V. Degtyarev, T.I. Chashchukhina, L.M. Voronova, A.M. Patselov, V.P. Pilyugin, Acta Materialia, 55 (2007) 6039-6050.

[69] R.Z. Valiev, R.K. Islamgaliev, I.V. Alexandrov, Progress in Materials Science, 45 (2000) 103-189.

[70] A. Vorhauer, R. Pippan, Scripta Materialia, 51 (2004) 921-925.

[71] G.B. Rathmayr, R. Pippan, Acta Materialia, 59 (2011) 7228-7240.

[72] C. Xu, Z. Horita, T.G. Langdon, Acta Materialia, 55 (2007) 203-212.

[73] A.P. Zhilyaev, G.V. Nurislamova, B.K. Kim, M.D. Baró, J.A. Szpunar, T.G. Langdon, Acta Materialia, 51 (2003) 753-765.

[74] K. Edalati, Z. Horita, Scripta Materialia, 64 (2011) 161-164.

[75] K. Edalati, Z. Horita, Acta Materialia, 59 (2011) 6831-6836.

[76] K. Edalati, Z. Horita, Materials Transactions, 51 (2010) 1051-1054.

[77] A.J.E. Foreman, M.J. Makin, Philosophical Magazine, 14 (1966) 911-924.

[78] M. Institute of, S. Faraday, Symposium on internal stresses in metals and alloys, London, 1948.

[79] E.O. Hall, Proceedings of the Physical Society. Section B, 64 (1951) 747.

[80] J.R. Cahoon, W.H. Broughton, A.R. Kutzak, MT, 2 (1971) 1979-1983.

[81] R.Z. Valiev, F. Chmelik, F. Bordeaux, G. Kapelski, B. Baudelet, Scripta Metallurgica et Materialia, 27 (1992) 855-860.

[82] M. Furukawa, Z. Horita, M. Nemoto, R.Z. Valiev, T.G. Langdon, Acta Materialia, 44 (1996) 4619-4629.

[83] A. Loucif, R.B. Figueiredo, T. Baudin, F. Brisset, R. Chemam, T.G. Langdon, Materials Science and Engineering: A, 532 (2012) 139-145.

[84] C.A. Schuh, T.G. Nieh, T. Yamasaki, Scripta Materialia, 46 (2002) 735-740.

[85] C.E. Carlton, P.J. Ferreira, Acta Materialia, 55 (2007) 3749-3756.

[86] C.S. Pande, R.A. Masumura, R.W. Armstrong, Nanostructured Materials, 2 (1993) 323-331.

[87] H. Hahn, P. Mondal, K. Padmanabhan, Nanostructured Materials, 9 (1997) 603-606.

[88] H. Margolin, Acta materialia, 46 (1998) 6305-6309.

[89] L. Proville, B. Bakó, Acta Materialia, 58 (2010) 5565-5571.

[90] E. Nembach, Scripta Materialia, 36 (1997) 1409-1413.

[91] S.M. Jeon, J.K. Park, Acta Materialia, 44 (1996) 1449-1455.

[92] F.C. Frank, W.T. Read, Jr., Physical Review, 79 (1950) 722-723.

[93] J.S. Koehler, Physical Review, 86 (1952) 52.

[94] U. Messerschmidt, M. Bartsch, Materials Chemistry and Physics, 81 (2003) 518-523.

[95] M.F. Ashby, Philosophical Magazine, 21 (1970) 399 - 424.

[96] S. Brinckmann, T. Siegmund, Y. Huang, International Journal of Plasticity, 22 (2006) 1784-1797.

[97] R.K. Islamgaliev, F. Chmelik, R. Kuzel, Materials Science and Engineering: A, 234–236 (1997) 335-338.

[98] R.K. Islamgaliev, F. Chmelik, R. Kuzel, Materials Science and Engineering: A, 237 (1997) 43-51.

[99] Y.H. Zhao, X.Z. Liao, Z. Jin, R.Z. Valiev, Y.T. Zhu, Acta Materialia, 52 (2004) 4589-4599.

[100] J. Gubicza, S.V. Dobatkin, E. Khosravi, A.A. Kuznetsov, J.L. Lábár, Materials Science and Engineering: A, 528 (2011) 1828-1832.

[101] C. Saldana, A.H. King, S. Chandrasekar, Acta Materialia, 60 (2012) 4107-4116.

[102] J. Weissmüller, Nanostructured Materials, 3 (1993) 261-272.

[103] R. Kirchheim, Acta Materialia, 50 (2002) 413-419.

[104] E. Cerri, P. Leo, Materials Science and Engineering: A, 410–411 (2005) 226-229.

[105] N. Tsuji, T. Iwata, M. Sato, S. Fujimoto, Y. Minamino, Science and Technology of Advanced Materials, 5 (2004) 173-180.

[106] Z. Horita, T.G. Langdon, Scripta Materialia, 58 (2008) 1029-1032.

[107] S.V. Dobatkin, E.N. Bastarache, G. Sakai, T. Fujita, Z. Horita, T.G. Langdon, Materials Science and Engineering: A, 408 (2005) 141-146.

[108] M. Kai, Z. Horita, T.G. Langdon, Materials Science and Engineering: A, 488 (2008) 117-124.

[109] M. Kawasaki, T. Langdon, Journal of Materials Science, 42 (2007) 1782-1796.

[110] E. Schafler, R. Pippan, Materials Science and Engineering A, 387-389 (2004) 799-804.

[111] K.-T. Park, H.-J. Lee, C.S. Lee, W.J. Nam, D.H. Shin, Scripta Materialia, 51 (2004) 479-483.

[112] H. Mecking, U.F. Kocks, Acta Metallurgica, 29 (1981) 1865-1875.

[113] Y. Estrin, H. Mecking, Acta Metallurgica, 32 (1984) 57-70.

[114] U.F. Kocks, H. Mecking, Progress in Materials Science, 48 (2003) 171-273.

[115] G.I. Taylor, Proceedings of the Royal Society of London. Series A, Containing Papers of a Mathematical and Physical Character, 145 (1934) 388-404.

[116] M.J. Starink, A. Deschamps, S.C. Wang, Scripta Materialia, 58 (2008) 377-382.

[117] M.J. Starink, X.G. Qiao, J. Zhang, N. Gao, Acta Materialia, 57 (2009) 5796-5811.

[118] X.G. Qiao, N. Gao, M.J. Starink, Philosophical Magazine, 92 (2011) 446-470.

[119] R. Pippan, High-Pressure Torsion – Features and Applications, Bulk Nanostructured Materials, Wiley-VCH Verlag GmbH & Co. KGaA, 2009, pp. 217-233.

[120] J. Nye, Acta metallurgica, 1 (1953) 153-162.

[121] Y. Huang, S. Qu, K.C. Hwang, M. Li, H. Gao, International Journal of Plasticity, 20 (2004) 753-782.

[122] H. Mughrabi, Materials Science and Engineering A, 387-389 (2004) 209-213.

[123] L.P. Evers, W.A.M. Brekelmans, M.G.D. Geers, Journal of the Mechanics and Physics of Solids, 52 (2004) 2379-2401.

[124] A. Gupta, D.J. Steigmann, Mathematical Methods in the Applied Sciences, 35 (2012) 1799-1824.

[125] N.A. Fleck, G.M. Muller, M.F. Ashby, J.W. Hutchinson, Acta Metallurgica et Materialia, 42 (1994) 475-487.

[126] N.A. Fleck, J.W. Hutchinson, Strain Gradient Plasticity, in: W.H. John, Y.W. Theodore (Eds.) Advances in Applied Mechanics, Elsevier, 1997, pp. 295-361.

[127] J.Y. Shu, N.A. Fleck, Journal of the Mechanics and Physics of Solids, 47 (1999) 297-324.

[128] H. Gao, Y. Huang, W.D. Nix, J.W. Hutchinson, Journal of the Mechanics and Physics of Solids, 47 (1999) 1239-1263.

[129] Y. Huang, H. Gao, W.D. Nix, J.W. Hutchinson, Journal of the Mechanics and Physics of Solids, 48 (2000) 99-128.

[130] L.P. Evers, D.M. Parks, W.A.M. Brekelmans, M.G.D. Geers, Journal of the Mechanics and Physics of Solids, 50 (2002) 2403-2424.

[131] H. Mughrabi, Materials Science and Engineering: A, 317 (2001) 171-180.

[132] T. Ungár, Scripta Materialia, 51 (2004) 777-781.

[133] N. Gao, M.J. Starink, T.G. Langdon, Materials Science and Technology, 25 (2009) 687-698.

[134] M.J. Starink, International Materials Reviews, 49 (2004) 191-226.

[135] D. Chen, A. Green, D. Dollimore, Thermochimica Acta, 284 (1996) 429-433.

[136] A. Zahra, C. Zahra, R. Castanet, G. Jaroma-Weiland, G. Neuer, Journal of Thermal Analysis and Calorimetry, 38 (1992) 781-788.

[137] J. Málek, Thermochimica Acta, 267 (1995) 61-73.

[138] M.J. Starink, Journal of Materials Science, 32 (1997) 4061-4070.

[139] W.A. Johnson, R.F. Mehl, Trans. Aime, 135 (1939) 396-415.

[140] M. Avrami, The Journal of Chemical Physics, 7 (1939) 1103-1112.

[141] M. Avrami, The Journal of chemical physics, 9 (1941) 177-184.

[142] P. Murray, J. White, Clay Minerals, 2 (1955) 255-264.

[143] A.W. Coats, J.P. Redfern, Nature, 201 (1964) 68-69.

[144] C.D. Doyle, Nature, 207 (1965) 290-291.

[145] M.J. Starink, Thermochimica Acta, 404 (2003) 163-176.

[146] H.E. Kissinger, Analytical chemistry, 29 (1957) 1702-1706.

[147] H.E. Kissinger, Journal of Research of the National Bureau of Standards, 57 (1956) 217-221.

[148] M.J. Starink, P.J. Gregson, Materials Science and Engineering: A, 211 (1996) 54-65.

[149] P. Debye, P. Scherrer, Nachrichten von der Gesellschaft der Wissenschaften zu Göttingen, Mathematisch-Physikalische Klasse, 1916 (1916) 1-15.

[150] A.R. Stokes, X-ray diffraction by polycrystalline materials, The Insititute of Physics,UK, 1960.

[151] H.P. Klug, L.E. Alexander, X-ray diffraction procedures for polycrystalline and amorphous materials, Wiley, 1974.

[152] W.H. Bragg, W.L. Bragg, X rays and crystal structure, Bell, 1915.

[153] H.S. Peiser, X-ray diffraction by polycrystalline materials, Institute of Physics, 1955.

[154] Z. Zhang, F. Zhou, E. Lavernia, Metallurgical and Materials Transactions A, 34 (2003) 1349-1355.

[155] A.L. Patterson, Physical Review, 56 (1939) 978-982.

[156] A.R. Stokes, A.J.C. Wilson, Mathematical Proceedings of the Cambridge Philosophical Society, 38 (1942) 313-322.

[157] G.K. Williamson, W.H. Hall, Acta Metallurgica, 1 (1953) 22-31.

[158] B.E. Warren, Progress in Metal Physics, 8 (1959) 147-202.

[159] H.M. Rietveld, Journal of Applied Crystallography, 2 (1969) 67-71.

[160] E. Hosseini, M. Kazeminezhad, Materials Science and Engineering: A, 526 (2009) 219-224.

[161] P. Mukherjee, A. Sarkar, P. Barat, S.K. Bandyopadhyay, P. Sen, S.K. Chattopadhyay, P. Chatterjee, S.K. Chatterjee, M.K. Mitra, Acta Materialia, 52 (2004) 5687-5696.

[162] O. Novelo-Peralta, G. González, G.A. Lara-Rodríguez, Materials Characterization, 59 (2008) 773-780.

[163] B. Marinkovic, R.R.d. Avillez, A. Saavedra, F.C.R. Assunção, Materials Research, 4 (2001) 71-76.

[164] C.E. Kril, R. Birringer, Philosophical Magazine A, 77 (1998) 621-640.

[165] L. Lutterotti, S. Gialanella, Acta Materialia, 46 (1998) 101-110.

[166] M. Ferrari, L. Lutterotti, Journal of Applied Physics, 76 (1994) 7246-7255.

[167] R.A. Young, D.B. Wiles, Journal of Applied Crystallography, 15 (1982) 430-438.

[168] F. Sanchez-Bajo, F.L. Cumbrera, Journal of Applied Crystallography, 30 (1997) 427-430.

[169] J. Ghosh, S.K. Chattopadhayay, A.K. Meikap, S.K. Chatterjee, Journal of Alloys and Compounds, 453 (2008) 131-137.

[170] C.J. Smithells, E.A. Brandes, G.B. Brook, Smithells' metals reference book, Butterworth-Heinemann, 1992.

[171] T.M.V.R. de Barros, R.C. Santos, A.C. Fernandes, M.E.M. da Piedade, Thermochimica Acta, 269–270 (1995) 51-60.

[172] I. Madsen, R. Hill, Advances in X-Ray Analysis., 35 (1991) 39-47.

[173] L.B. McCusker, R.B. Von Dreele, D.E. Cox, D. Louer, P. Scardi, Journal of Applied Crystallography, 32 (1999) 36-50.

[174] A. Thorvaldsen, Acta Materialia, 45 (1997) 587-594.

[175] G. Sha, A. Cerezo, Acta Materialia, 52 (2004) 4503-4516.

[176] G. Sha, R.K.W. Marceau, X. Gao, B.C. Muddle, S.P. Ringer, Acta Materialia, 59 (2011) 1659-1670.

[177] R.K.W. Marceau, G. Sha, R.N. Lumley, S.P. Ringer, Acta Materialia, 58 (2010) 1795-1805.

[178] I.N. Khan, M.J. Starink, J.L. Yan, Materials Science and Engineering: A, 472 (2008) 66-74.

[179] N. Gao, M.J. Starink, S.C. Wang, C. Xu, T.G. Langdon, in: Y.T. Zhu, T.G. Langdon, Z. Horita, M.J. Zehetbauer, S.L. Semiatin, T.C. Lowe (Eds.) TMS Annual Meeting, Minerals, Metals, and Materials Society, Warrendale, USA, 2006, pp. 223-230.

[180] Y. Estrin, H. Kim, Journal of Materials Science, 42 (2007) 9092-9096.

[181] Y. Estrin, Journal of Materials Processing Technology, 80-81 (1998) 33-39.

[182] M. Murashkin, A. Kil'mametov, R. Valiev, The Physics of Metals and Metallography, 106 (2008) 90-96.

[183] G. Caglioti, A. Paoletti, F.P. Ricci, Nuclear Instruments, 3 (1958) 223-228.

[184] J. He, J. Ye, E.J. Lavernia, D. Matejczyk, C. Bampton, J.M. Schoenung, Journal of Materials Science, 39 (2004) 6957-6964.

[185] A.L. Ortiz, L. Shaw, Acta Materialia, 52 (2004) 2185-2197.

[186] J. Gubicza, I. Schiller, N.Q. Chinh, J. Illy, Z. Horita, T.G. Langdon, Materials Science and Engineering: A, 460–461 (2007) 77-85.

[187] T. Ungar, J. Gubicza, G. Ribarik, A. Borbely, Journal of Applied Crystallography, 34 (2001) 298-310.

[188] J. Gubicza, N.Q. Chinh, Z. Horita, T.G. Langdon, Materials Science and Engineering: A, 387–389 (2004) 55-59.

[189] S.C. Wang, F. Lefebvre, J.L. Yan, I. Sinclair, M.J. Starink, Materials Science and Engineering: A, 431 (2006) 123-136.

[190] S.P. Ringer, B.T. Sofyan, K.S. Prasad, G.C. Quan, Acta Materialia, 56 (2008) 2147-2160.

[191] R.K.W. Marceau, G. Sha, R. Ferragut, A. Dupasquier, S.P. Ringer, Acta Materialia, 58 (2010) 4923-4939.

[192] S.C. Wang, Z. Zhu, M.J. Starink, Journal of Microscopy, 217 (2005) 174-178.

[193] M.J. Starink, S.C. Wang, Acta Materialia, 51 (2003) 5131-5150.

[194] M.J. Starink, L.F. Cao, P.A. Rometsch, Acta Materialia, 60 (2012) 4194-4207.

[195] M.J. Starink, International Journal of Materials Research, 103 (2012) 942-947.

[196] M.J. Starink, X. Cheng, S. Yang, Acta Materialia, 61 (2013) 183-192.

[197] H.R. Shercliff, M.F. Ashby, Acta Metallurgica et Materialia, 38 (1990) 1789-1802.

[198] Ø. Ryen, B. Holmedal, O. Nijs, E. Nes, E. Sjölander, H.-E. Ekström, Metallurgical and Materials Transactions A, 37 (2006) 1999-2006.

[199] P.A. Flinn, Acta Metallurgica, 6 (1958) 631-635.

[200] P. Gomiero, Y. Brechet, F. Louchet, A. Tourabi, B. Wack, Acta Metallurgica et Materialia, 40 (1992) 857-861.

[201] D.J. Dunstan, A.J. Bushby, International Journal of Plasticity, 40 (2013) 152-162.

[202] D.J. Dunstan, A.J. Bushby, International Journal of Plasticity, 53 (2014) 56-65.

[203] S. Korte, W.J. Clegg, Philosophical Magazine, 91 (2010) 1150-1162.

[204] H. Brooks, American Society for Metals, Metals Park, OH, (1952) 20.

[205] X.G. Qiao, M.J. Starink, N. Gao, Acta Materialia, 58 (2010) 3690-3700.

[206] M.A. Meyers, A. Mishra, D.J. Benson, Progress in Materials Science, 51 (2006) 427-556.

[207] P. Zhang, S.X. Li, Z.F. Zhang, Materials Science and Engineering: A, 529 (2011) 62-73.

[208] R. Kirchheim, Acta Materialia, 55 (2007) 5129-5138.

[209] K.T. Aust, R.E. Hanneman, P. Niessen, J.H. Westbrook, Acta Metallurgica, 16 (1968) 291-302.

[210] A. Cottrell, Report of a Conference on Strength of Solids, 1948, pp. 30-36.

[211] H. Suzuki, Science reports of the Research Institutes, Tohoku University. Ser. A, Physics, chemistry and metallurgy, 4 (1952).

[212] T. Chookajorn, H.A. Murdoch, C.A. Schuh, Science, 337 (2012) 951-954.

[213] R. Kirchheim, Acta Materialia, 55 (2007) 5139-5148.

[214] L. Lutterotti, S. Matthies, H. Wenk, Proceeding of the Twelfth International Conference on Textures of Materials (ICOTOM-12), NRC Press Ottawa, Canada, 1999, pp. 1599.

[215] T.D. Shen, R.B. Schwarz, S. Feng, J.G. Swadener, J.Y. Huang, M. Tang, J. Zhang, S.C. Vogel, Y. Zhao, Acta Materialia, 55 (2007) 5007-5013.

[216] N. Hansen, Acta Metallurgica, 25 (1977) 863-869.

[217] Y. Estrin, A. Molotnikov, C.H.J. Davies, R. Lapovok, Journal of the Mechanics and Physics of Solids, 56 (2008) 1186-1202.

[218] M.J. Starink, V.M.F. Abeels, P. van Mourik, Materials Science and Engineering: A, 163 (1993) 115-125.

[219] R.Z. Valiev, N.A. Enikeev, M.Y. Murashkin, V.U. Kazykhanov, X. Sauvage, Scripta Materialia, 63 (2010) 949-952.

[220] D. Poole, H. Axon, Journal of the Institute of Metals, 80 (1952) 599-604.

[221] M.J. Starink, P. Mourik, B.M. Korevaar, MTA, 24 (1993) 1723-1731.

[222] M. Verdier, I. Groma, L. Flandin, J. Lendvai, Y. Bréchet, P. Guyot, Scripta Materialia, 37 (1997) 449-454.

[223] A. Rohatgi, K.S. Vecchio, Materials Science and Engineering: A, 328 (2002) 256-266.

[224] A. Varschavsky, E. Donoso, Journal of Thermal Analysis and Calorimetry, 48 (1997) 1229-1248.

[225] G. Guiglionda, A. Borbély, J.H. Driver, Acta Materialia, 52 (2004) 3413-3423.

[226] A. Varschavsky, E. Donoso, Materials Letters, 31 (1997) 239-245.

[227] M. Taheri, H. Weiland, A. Rollett, Metallurgical and Materials Transactions A, 37 (2006) 19-25.

[228] M.J. Starink, A.M. Zahra, Acta Materialia, 46 (1998) 3381-3397.

[229] Y. Huang, F.J. Humphreys, Acta Materialia, 47 (1999) 2259-2268.

[230] F. Zhou, X.Z. Liao, Y.T. Zhu, S. Dallek, E.J. Lavernia, Acta Materialia, 51 (2003) 2777-2791.

[231] X.G. Qiao, M.J. Starink, N. Gao, Materials Science and Engineering: A, 513-514 (2009) 52-58.

[232] E.A. El-Danaf, M. Baig, Materials Science and Engineering: A, 565 (2013) 301-307.

[233] G. Sha, H. Möller, W.E. Stumpf, J.H. Xia, G. Govender, S.P. Ringer, Acta Materialia, 60 (2012) 692-701.

[234] M.K. Miller, Journal of Microscopy, 186 (1997) 1-16.

[235] Z. Zhu, M.J. Starink, Materials Science and Engineering: A, 489 (2008) 138-149.

[236] G.D. Hughes, S.D. Smith, C.S. Pande, H.R. Johnson, R.W. Armstrong, Scripta Metallurgica, 20 (1986) 93-97.

[237] C. Pande, R. Masumura, R. Armstrong, Nanostructured materials, 2 (1993) 323-331.

[238] M. Ashby, R. Verrall, Acta Metallurgica, 21 (1973) 149-163.

[239] D.J. Benson, H.-H. Fu, M.A. Meyers, Materials Science and Engineering: A, 319–321 (2001) 854-861.

[240] H.H. Fu, D.J. Benson, M.A. Meyers, Acta Materialia, 49 (2001) 2567-2582.

[241] M.A. Meyersm, E. Ashworth, Philosophical Magazine A, 46 (1982) 737-759.

[242] R. Lapovok, F.H. Dalla Torre, J. Sandlin, C.H.J. Davies, E.V. Pereloma, P.F. Thomson, Y. Estrin, Journal of the Mechanics and Physics of Solids, 53 (2005) 729-747.

[243] J. Kratochvíl, M. Kružík, R. Sedláček, Acta Materialia, 57 (2009) 739-748.

[244] J.W. Gibbs, H.A. Bumstead, W.R. Longley, The collected works of J. Willard Gibbs, Longmans, Green and Company, 1928.

[245] A. Cottrell, Dislocation and plastic flow in crystals, Clarendon Press Oxford, 1953.

[246] Y. Nagai, M. Murayama, Z. Tang, T. Nonaka, K. Hono, M. Hasegawa, Acta Materialia, 49 (2001) 913-920.

[247] C. Wagner, Mathematisch-Physikalische Klasse, 3 (1973).

[248] K.A. Darling, B.K. VanLeeuwen, C.C. Koch, R.O. Scattergood, Materials Science and Engineering: A, 527 (2010) 3572-3580.

[249] F. Liu, R. Kirchheim, Scripta Materialia, 51 (2004) 521-525.

[250] C. Krill Iii, H. Ehrhardt, R. Birringer, Zeitschrift für Metallkunde, 96 (2005) 1134-1141.

[251] T.S. Parel, S.C. Wang, M.J. Starink, Materials & Design, 31, Supplement 1 (2010) S2-S5.

[252] K.W. Liu, F. Mücklich, Acta Materialia, 49 (2001) 395-403.

[253] S.J. Li, Y.W. Zhang, B.B. Sun, Y.L. Hao, R. Yang, Materials Science and Engineering: A, 480 (2008) 101-108.

[254] K. Raviprasad, C.R. Hutchinson, T. Sakurai, S.P. Ringer, Acta Materialia, 51 (2003) 5037-5050.

[255] A. Zhu, B.M. Gable, G.J. Shiflet, E.A. Starke Jr, Acta Materialia, 52 (2004) 3671-3679.

[256] C.R. Hutchinson, S.P. Ringer, Metallurgical and Materials Transactions A, 31 (2000) 2721-2733.

[257] S. Abis, P. Mengucci, G. Riontino, Philosophical Magazine A, 70 (1994) 851-868.

[258] A.K. Mukhopadhyay, Metallurgical and Materials Transactions A, 33 (2002) 3635-3648.

[259] M. Gazizov, R. Kaibyshev, Journal of Alloys and Compounds, 527 (2012) 163-175.

[260] R. Zheng, Y. Sun, K. Ameyama, C. Ma, Materials Science and Engineering: A, 590 (2014) 147-152.

[261] L.H. Su, C. Lu, L.Z. He, L.C. Zhang, P. Guagliardo, A.K. Tieu, S.N. Samarin, J.F. Williams, H.J. Li, Acta Materialia, 60 (2012) 4218-4228.